Author:
Robinson, Joshua F

Title:
Quasi-equilibrium approaches to the high-density liquid

University of Bristol

Doctoral Thesis

Quasi-equilibrium approaches to the high-density liquid

Author:
Joshua F. Robinson

Supervisor:
Prof. C. P. Royall

A dissertation submitted to the University of Bristol in accordance with the requirements for award of the degree of Doctor of Philosophy in the Faculty of Science, H. H. Wills Physics Laboratory.

August 2019

47,303 words

Abstract

This dissertation describes an investigation into methods for advancing understanding of liquids at high densities, where dynamical processes become highly non-trivial. Specifically, we address structure in supercooled liquids approaching their glass transition, and the kinetics of nucleating the stable crystal phase. In both cases we describe the liquid using equilibrium physics, even though the system is metastable and not strictly in equilibrium. The first three results chapters focus on the supercooled liquid, while the final results chapter addresses nucleation.

In the first part comprising three chapters, we combine geometric techniques with liquid state theory to develop an approach for treating complex many-particle local structures inside the bulk hard sphere liquid. We introduce the *morphometric approach*, a liquid state theory based on integral geometry, as a means of calculating many-body correlation functions. We argue for the morphometric approach from several routes, and derive multiple specific theories for hard spheres including one suitable for producing accurate correlation functions. We later derive the morphometric approach for hard spheres from first-principles using the virial series. This places the approach on more rigorous ground, and suggests routes to extending the theory as part of a controlled expansion.

With the resulting many-body correlation functions, we are able to predict the concentrations of complex many-particle structures in the bulk liquid; these results are of particular relevance to theories of supercooled liquids and glasses. We find a bimodality in the energy landscape for hard sphere local structures, where fivefold symmetric structures appear lower in free energy than fourfold symmetric structures. In addition, we develop similar techniques for predicting the thermodynamic barriers to dynamical processes inside the bulk system. The solution to the overarching problem of predicting structure formation inside a bulk system has potential to advance study of self-assembly, nucleation and protein folding in aqueous environments.

In a final part we address nucleation of salt crystals in drying aerosol droplets, of particular relevance to climate models and industrial spray drying applications. Treating the droplet in the continuum limit, we solve the diffusion equation with moving boundary conditions. By comparison with experimental data we are able to assess the accuracy of classical nucleation theory, with mixed success depending on the system.

Dedicated to all of the cats of the internet, whose rheological properties inspired this delve into liquids.

Acknowledgements

First and foremost, I want to thank my supervisor, Paddy, for being the reason that any of this happened at all, for being a crucial check on my natural impulse to be *too* focused on details and for the fact that I now see beautiful (pink) icosahedra every time I close my eyes. I thank him for giving me the freedom to develop my ideas, and for his remarkable degree of patience when that led to me studying six particles for four years.

It has now been several years since Paddy gave me the 'humble' task of solving the glass transition once and for all. Having failed spectacularly at this, I hope we can collectively agree that the real glass transition was the friends we made along the way. In particular, all of the cave-dwellers (and countless mice) of G.39 who survived the water features, two fumigations and Paddy. The forces of darkness may have stolen our toaster, but they never broke our spirit*. I will treasure these memories, and your friendship, until the end of my days.

I owe a great debt to Francesco Turci for dedicating far more time than I deserve to discuss my work. I honestly don't think I could have done this without his consistent, valuable input throughout.

I would like to express my gratitude to our collaborator Roland Roth, for founding the Bristol's White Bear institute, conjuring up the initial idea for my project with Paddy and providing guidance along the way. Additionally, I am deeply grateful to our collaborators in chemistry for what turned out to be a fun and fruitful project: Flo Gregson, Rachel Miles and Jonathan Reid. I especially thank Flo for doing the experiments which made this collaboration possible, and for providing valuable feedback on my initial attempts at describing them in chapter 7.

Special thanks go out to Bob Evans, who showed interest in my work from the very beginning, for the many stimulating discussions about liquid state theory over the years. I must also thank him for the constructive feedback he gave on an early draft of the paper underlying parts of chapters 4 and 5. I recall he described me as "completely mad" afterwards, which I *think* was a compliment, so I must additionally thank him for inadvertently suggesting an 'insanity defence' to rely upon in my viva.

I am very grateful to the organisers and lecturers at the Boulder School in Condensed Matter and Materials Physics 2017. This school influenced my development as a statistical physicist in a myriad of ways. Notably, I found myself referring back to the phenomenological lectures by Gilles Tarjus while writing chapter 3.

Financially, I acknowledge the European Research Council under the FP7 / ERC Grant Agreement No. 617266 "NANOPRS" and Paddy for finding ways to support me after this ran out.

I have learned that research is an almost constant uphill struggle, with the occasional false summit. My most heartfelt appreciation goes out to all my friends and colleagues who made the struggle worthwhile. I would particularly like to thank Kate Oliver, Nick Wood and Max Meissner for keeping me sane in difficult times, and Kirsty Wynne for teaching me perspective and the meaning of a 'false summit'. Last, and certainly not least, I owe my deepest gratitude to all the close friends and family members who were there for me every step along the way.

*After all, we had the science to do that.

Author's declaration

I declare that the work in this dissertation was carried out in accordance with the requirements of the University's Regulations and Code of Practice for Research Degree Programmes and that it has not been submitted for any other academic award. Except where indicated by specific reference in the text, the work is the candidate's own work. Work done in collaboration with, or with the assistance of, others, is indicated as such. Any views expressed in the dissertation are those of the author.

SIGNED: .....Joshua F. Robinson..... DATE: .....30/08/19.....

Significant contributions:

[1] J. F. Robinson et al., "Morphometric approach to many-body correlations in hard spheres", Phys. Rev. Lett. **122**, 068004 (2019).
[2] F. K. A. Gregson et al., "Drying kinetics of salt solution droplets: water evaporation rates and crystallization", J. Phys. Chem. B **123**, 266 (2019).
[3] J. F. Robinson et al., "Many-body correlations from integral geometry", Phys. Rev. E **100** (2019) `10.1103/physreve.100.062126`.
[4] J. F. Robinson et al., "Morphological thermodynamics for hard bodies from a controlled expansion", arXiv: 1910.11836 (2019), Submitted to Phil. Mag..
[5] J. F. Robinson et al., "Nucleation kinetics in drying sodium nitrate aerosols", arXiv: 1911.06212 (2019), Submitted to J. Chem. Phys..
[6] F. K. A. Gregson et al., "Studies on crystal nucleation rates in evaporating sodium nitrate aerosol droplets", in preparation.

Other contributions:

[7] C. P. Royall et al., "The race to the bottom: approaching the ideal glass?", J. Phys. Condens. Matter **30**, 363001 (2018).

"*Keep cool, never freeze.*"

– Hellmann's® mayonnaise.

Contents

List of Figures

List of Tables

Chapter 1

Introduction

> I'm being quoted to introduce something, but I have no idea what it is and certainly don't endorse it.
>
> Randall Munroe, *XKCD*, (2018).

It is a matter of some debate over what is precisely meant by "soft matter", and how to demarcate the various systems studied. In introducing this field one normally takes a deep breath, then lists the vast range of topics studied, before drawing inferences over what their quintessential features are; this is an inherently subjective procedure so the boundaries of the field are necessarily fuzzy. In this vein, soft matter encompasses foams, gels, dispersions, liquid crystals, polymer solutions, polymer melts, granular materials, complex plasmas, active matter and many more systems of fundamental, practical and aesthetic importance. A widely proposed definition to unify these disparate topics postulates that a soft matter system possesses energy scales accessible to fluctuations [9], whether this involves spontaneous thermal fluctuations in passive systems or those due to driving forces in active systems. In each example, the interactions involved are weak enough relative to the source of fluctuations that flow is possible, though the physical processes and chemistry involved can become arbitrarily complex allowing for incredible diversity of phenomena. In some sense, this idea is best captured with *vaguer* statements, driving a prominent worker in the field to describe soft matter as "liquids with bits in them" [10].

As a rule of thumb, increasing the size of the constituent components in soft matter systems results in more complex interactions and a greater diversity of phenomena; the various systems are arranged in a loose hierarchy of complexity in Fig. 1.1, with molecular systems at the bottom and living things at the top. In the context of this hierarchy, the deepest and most universal questions then reside at the level of the simplest liquid[1]. Unsurprisingly, liquids have been thoroughly explored in their long history of study, though fundamental open questions remain concerning their dynamical behaviour at high densities. To initiate this discussion we will introduce *the* archetypal model for simple liquids: hard spheres.

[1] By which we mean those formed by the noble gases at high densities.

The hard sphere interaction energy is simply defined by forbidding any

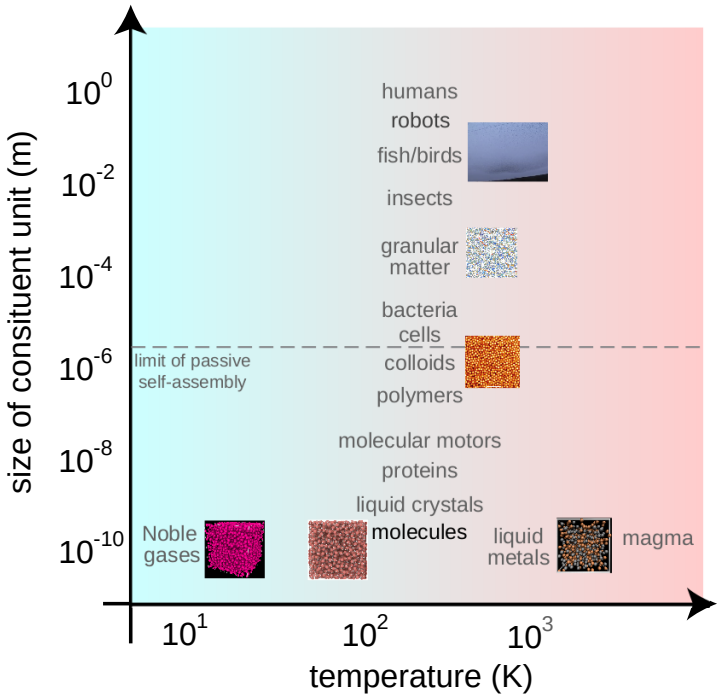

Figure 1.1: The various systems studied in soft matter, featuring an impressive range of length and temperature scales. Every system possesses features in common with liquids, if not actually a liquid themselves. Small systems can be dynamically driven through entirely passive sources, with temperature being the prototypical example in thermal systems. By contrast, larger systems require active sources of fluctuations to self-assemble, from e.g. external driving forces in granular matter or chemical reserves in living systems. Image courtesy of Ref. [8].

configurations where spheres mutually overlap[2], that is

$$u(r) = \begin{cases} \infty & r < \sigma \\ 0 & \text{otherwise,} \end{cases} \tag{1.1}$$

where σ is the diameter of the each sphere. No chemical bonds are possible in the absence of any attractions so this represents a kind of *zeroth-order* approximation to real fluids; nonetheless, atoms and molecules do feature sharp short-ranged repulsions so this is a reasonable starting point. Furthermore, this oversimplified model has historically, and counterintuitively, represented the frontiers in our understanding of real liquids.

To illustrate the above we consider the van der Waals equation of state for real gases. This *mean-field theory* characterises a system of N particles contained in a volume V as

$$\frac{p + a\frac{N^2}{V^2}}{k_B T} = \frac{N}{V - bN} \tag{1.2}$$

where p is the pressure, k_B is the Boltzmann constant, T as temperature, and with a, b as perturbations from the ideal gas law due to the interactions. We have written this equation such that the left-hand side contains *liquid-like* modifications to the pressure due to the attractions, whereas the right-hand side contains *gas-like* perturbations from the reduction in the accessible volume due to short-range repulsions. Introducing the (number) density $\rho = N/V$ allows (1.2) to be rewritten more simply as

$$\frac{\beta p}{\rho} = 1 + (b - \beta a)\rho + \mathcal{O}(\rho^2) \tag{1.3}$$

where $\beta = (k_B T)^{-1}$. Setting $a = b = 0$ recovers the ideal gas law as expected. It was widely believed that improvements to van der Waals'

[2] I like to imagine them as ideal billiard balls, without any dissipative forces so they continue to bounce off one another forever.

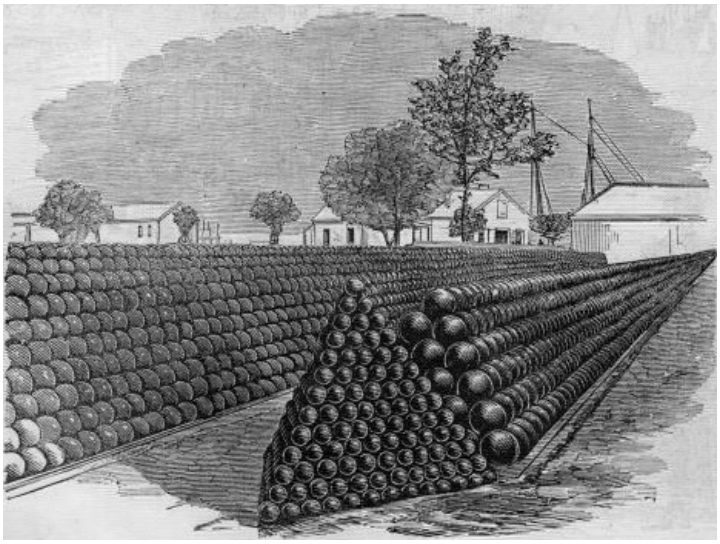

Figure 1.2: Sketch of cannonball piles at Fortress Monroe. The stacking structure is an example of close packing, the densest arrangement of hard spheres in three dimensions. The ball positions are consistent with sites of a face-centred cubic lattice, similar to that seen in crystal structures. Image by Stacy, *Harper's weekly* (1861)

theory would require sophisticated treatments of the *attractions*, however history has shown that it was the treatment of the *repulsions* which were lacking [11–13]. Simple liquids can to a large extent be considered as weak perturbations to the hard sphere model; as such, the left-hand side of (1.2) is reasonably accurate, but the right-hand side must be refined to account for the non-trivial effects of exclusion [12].

As the foundational model for liquids, hard spheres serve as a good touchstone for progress (and controversies) within liquid state physics and, by extension, soft matter. We will focus our discussion of established properties on the hard sphere phase diagram. As the hard sphere potential (1.1) is everywhere zero or divergent, temperature has no effect[3] on the thermodynamics and we say the system is *athermal*. The phase diagram is thus one-dimensional with state point specified solely by density ρ[4]. For convenience, and to emphasise the geometric nature of hard spheres, it is usual to work with a normalised density: the *volume fraction*, the volume of space occupied by the spheres i.e.

$$\eta = \rho\omega_d \left(\frac{\sigma}{2}\right)^d, \tag{1.4}$$

where ω_d is the volume of a d-dimensional ball of unit radius e.g. $\omega_3 = 4\pi/3$. From its definition we know the volume fraction must be bounded from above by $\eta < 1$ where all space would be perfectly tiled, although in practice tighter upper bounds can be placed from the constraints of spherical packings. The largest density achievable without causing spheres to overlap is called the *close packing* limit, and in $d = 3$ corresponds to the face centred cubic (FCC) lattice (Fig. 1.2), occurring at $\eta_{\mathrm{CP}} = \pi/(3\sqrt{2}) \sim 0.74$. This happens to coincide with a crystal structure observed in real systems, so by analogy we might postulate the existence of a thermodynamic phase transition separating this ordered state from the disordered state around the dilute limit $\eta \to 0$ where ideal gas behaviour is recovered.

Written in terms of volume fraction, the van der Waals equation (1.2) for d-dimensional hard spheres adopts the simpler form[5]

$$\frac{\beta p}{\rho} = \frac{1}{1 - 2^{d-1}\eta} \tag{1.5}$$

[3] The velocities will be trivially rescaled by temperature, but this will not affect the static structure.

[4] Or equivalently the pressure, itself connected to ρ by the equation of state.

[5] The coefficient of 2^{d-1} in this form can be obtained by recognising that leading-order corrections to the ideal gas law involves the *excluded volume*, i.e. that excluded to the centre of a test particles which modifies the occupied volume by 2^d by doubling the radius. This has to be divided by two to avoid double

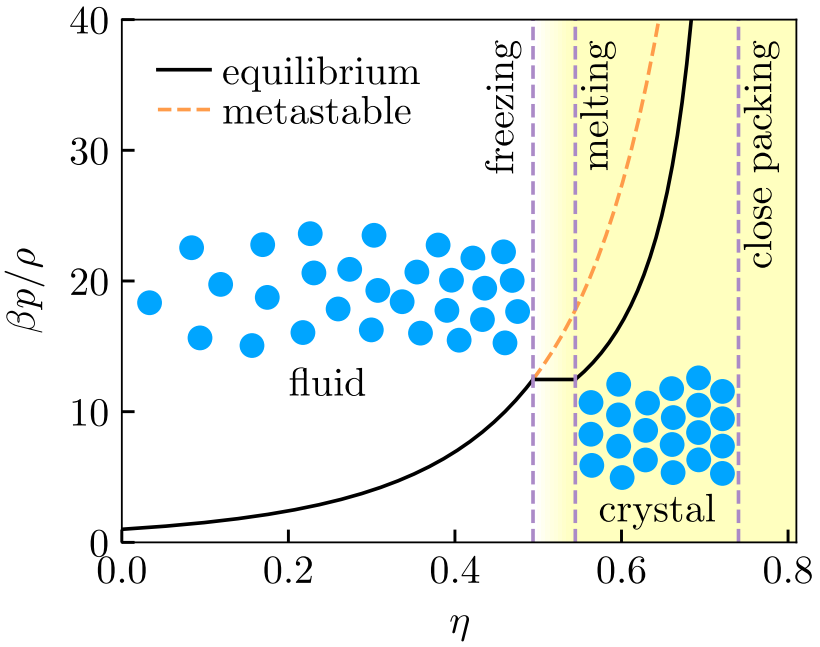

Figure 1.3: The hard sphere equation of state in $d = 3$ in terms of volume fraction, including the metastable branch. The one-dimensional phase diagram is overlaid, with the volume fractions of freezing and melting taken as $\eta_f \sim 0.494$ and $\eta_m \sim 0.545$ respectively [14]. Close packing occurs at $\eta_{\rm CP} \sim 0.74$. The equations of state were adapted from Refs. [15–17].

where we recognised that $a = 0$ because hard spheres have no attractions. This theory features no singularities until $\eta = 2^{1-d}$ where the pressure diverges, so it predicts no thermodynamic phase transitions and contradicts the existence in $d = 3$ of a close packing limit at $\eta_{\rm CP} \sim 0.74$ well above the value of 0.25 predicted by (1.5). By contrast, the actual phase diagram (Fig. 1.3), determined from simulations [14, 18, 19] and colloidal experiments [20], shows that the hard sphere system remains a liquid[6] up to $\eta_f \sim 0.494$ whereupon it undergoes a freezing transition to an ordered phase with an accompanying melting transition at $\eta_m \sim 0.545$ [14]. This result was not immediately accepted by the community, even though these simulation studies are generally considered definitive in hindsight [21].

In everyday scenarios crystallisation typically occurs as one lowers temperature, and the classroom explanation posits that the crystal is favoured due to *attractions* between molecules. In the absence of any attractions in hard spheres, we find that *entropy* must drive crystallisation. Part of the reason people could not believe that the crystal is entropically favoured, is because we often (mistakenly) identify entropy as a measure of disorder making it counterintuitive for an ordered phase to be favoured. In reality entropy is more subtle: the crystal may be more ordered than the liquid, with a lower *configurational* entropy, however entropy includes other contributions. At high densities, the penalty paid for being locked into the crystal is offset by a *vibrational* entropy, because each particle has more available space for motion. The net entropic effect leads to the crystal being favoured over the liquid at high densities, giving the phase diagram that we know today (Fig. 1.3).

A similar effect is seen in balls floating on water as in e.g. peas boiling in a saucepan or shade balls covering a reservoir (Fig. 1.4). The hard interactions between the balls causes[7] them to 'crystallise' at high densities as can been seen in the figure. Strictly speaking these are not crystals in the sense of long-range *translational* order, instead they are said to possess long-range

[6] Strictly speaking there is no distinction between a liquid and a gas phase in hard spheres because the phase diagram does not have a critical point. As such, to be precise we should refer to the isotropic phase as a *fluid*. However, we will always be focusing on the high density fluid, which serves as the starting point for descriptions of real liquids, so we can justify using 'liquid' and 'fluid' interchangeably.

[7] In an attempt to find an everyday example, I have taken liberties with the interaction being purely hard; I suspect that floating balls feature effective attractions because of *hydrodynamic* interactions at the water surface.

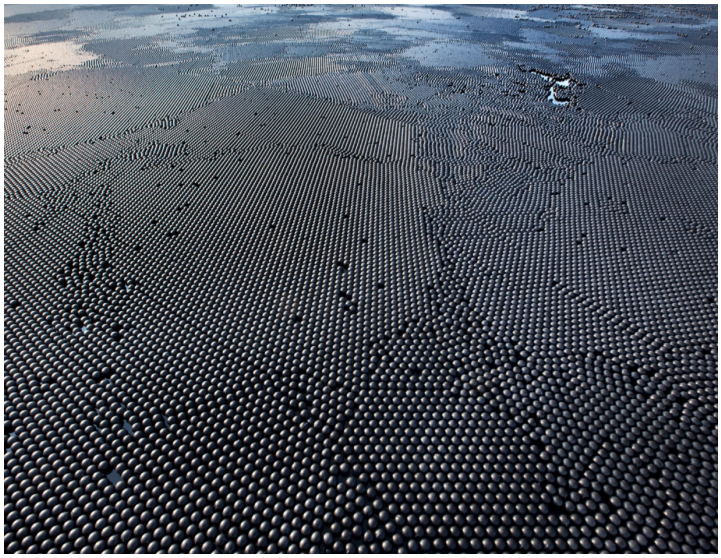

Figure 1.4: Shade balls covering the Los Angeles reservoir to cool the water, preventing evaporation, and inhibit harmful light-activated chemical reactions at the water surface. As macroscopic objects these balls interact as hard spheres, and they spontaneously form long-ranged orientational order seen as hexagonal domains. This is reminiscent of crystallisation in atomic systems. Image by Gerd Ludwig, *National Geographic* (2007).

orientational order. This subtlety emerges because the floating balls are confined to the water surface making them effectively two dimensional. In thermal systems, fluctuations are strong enough in two dimensions to overcome truly long-ranged positional ordering [22, 23]; as macroscopic objects, the floating balls are not strictly thermal but we can expect reminiscent behaviour emerging from any fluctuation source e.g. water waves.

Now that we have given an overview of the firmly established bulk phase behaviour of hard spheres, we can turn to address the questions which remain unresolved. So far we have only discussed the *equilibrium* properties of hard spheres which are well-described by theory. In equilibrium, a great deal is even known about the *inhomogeneous* liquid, e.g. in confinement [24], thanks to advances in density functional theory [25, 26]. By contrast, there are still much debate surrounding the nature of the *metastable* liquid phase in hard spheres, especially concerning its dynamical properties. The metastable phase is the continuation of the liquid phase above the melting point, shown by a dashed line in Fig. 1.3. We refer to this branch as the *supercooled liquid* in analogy to the metastable phase of real liquids which are formed by cooling below their freezing temperature; in this sense we think of increasing density as equivalent to lowering temperature.

The supercooled liquid is not strictly a phase in the sense of being the free energy minimum, as it will eventually crystallise, however it has many features in common with equilibrium phases. In particular, the supercooled liquid is sufficiently long-lived to eventually reach a steady state with well-defined thermodynamic observables. In simple terms, supercooled liquids are thermodynamically indistinguishable from that of an equilibrium phase *until* they spontaneously crystallise. While supercooled liquids are not markedly different from ordinary liquids immediately above freezing, at higher densities their *dynamical* properties profoundly depart and are the least understood aspects of simple liquids.

As we see it, the two central topics regarding the metastable liquid are:

1. *Fate of the liquid branch*: if crystallisation could (somehow) be circumvented, what is the ultimate fate of the supercooled liquid as one increases density? Related to this is the nature of the out-of-equilibrium

Figure 1.5: Hard spheres in a ball bit are (approximately) randomly close packed, occurring at a volume fraction $\eta_{\text{RCP}} \sim 0.64$. These disordered packings are minimally rigid until perturbed, by e.g. a child jumping in, whereupon many particles are collectively displaced in *avalanches*; disorder in ball pits is thus essential to their function. Image by Peter Ong.

state: the *glass*.

2. *Nucleation*: given that the crystal is the ground state above the freezing density, can we describe the kinetic pathway by which the liquid crystallises?

Each question is complicated by a remarkable change in the timescales involved, requiring new ideas to approach them. Regarding nucleation, the rates predicted by theory and experiments differ by some ∼12 orders of magnitude, which is claimed to be the second worst disagreement[8] between theory and experiment in all of physics [28].

In the supercooled liquid the time to reach the steady state, or 'equilibrium', dramatically increases with density until it becomes effectively infinite above a glass transition[9] where it forms a glass. If the hard sphere glass is rapidly compressed to higher densities the pressure will diverge, which is related to *jamming* in granular materials like sand; the density at jamming is highly dependent on the protocol. Empirically, rapid compression of a low density liquid leads to jamming at *random close packing* (Fig. 1.5) around $\eta_{\text{RCP}} \sim 0.64$ [29]. Our focus will be on the 'equilibrium' supercooled liquid, although the nature of the glass and jammed states provide important context for our programme, which we will return to in chapter 3. The central question of this field asks if the relaxation timescale, or viscosity, truly diverges at finite pressure; an equivalent question asks whether there is a thermodynamic transition to an *ideal glass* phase which drives the dynamical slowdown.

The goal of this thesis is to advance the methods for treating liquids at high densities, so we aim make a small contribution to addressing both topics above; in chapters 4, 5 and 6 we will develop methods to assess changes in the supercooled hard sphere liquid, while in chapter 7 we will model nucleation kinetics in drying aerosols.

In chapter 2 we will present an overview of liquid state theory, with a special emphasis on correlation functions and geometric methods as these will play a central role in later chapters. In the following chapter 3 we discuss the supercooled liquid in more detail to provide proper context for

[8] With the first being the *vacuum catastrophe*, the difference of ∼120 orders of magnitude between predicted vacuum energy density and observations of astronomers [27]. In this context, nucleation predictions become remarkably accurate.

[9] This is typically taken to occur around $\eta_g \in [0.58, 0.60]$, although the exact point where the system falls out of equilibrium will depend on many factors including the size of the particles in case of colloidal experiments, the specific dynamical rules of a simulation algorithm, and the patience of the observer.

the first topic outlined above, which is our central motivation.

In chapters 4 and 5 we develop our approach to the supercooled liquid: we use the framework of many-body correlation functions to predict the concentrations of local structures in the bulk liquid. A bulk system with 10^{23} particles has too many degrees of freedom to treat effectively, so our approach is to select a subset which remain dynamically relevant. We will justify this procedure using existing theories of the supercooled liquid discussed in chapter 2. We find that many-body correlations provide the natural framework for this task, and we develop specific theories for treating correlations in the hard sphere liquid in chapter 4. Then in chapter 5 we develop this into a predictive framework for concentrations of local structural motifs, and dynamical barriers, within the bulk liquid. Central to these chapters is the *morphometric approach*, an approximation scheme emerging as a synthesis of liquid state theory and geometry, which we will introduce gradually over the course of chapters 2 and 4. As the final stage in this sequence of connected results, we rederive the morphometric approach in chapter 6 from first principles within liquid state theory to further justify the approach and provide insight into how the approximation may be improved.

The problem that we solve is actually quite general: given an interaction potential, we want to know what kinds of structures will form in the bulk liquid. To the best of our knowledge, this has never been done for *any* system. Admittedly, we repeatedly exploit the simplicity of the hard sphere interaction potential to do this, limiting the applicability to real systems, but it is still a non-trivial problem. Were this to be generalised to more complex systems, we could imagine the methods being used to facilitate design of new chemical synthesis, tailoring the self-assembly of colloidal particles, or for predicting how proteins fold in aqueous solution. Although hard spheres will be our focus, we will indicate possible routes to extending the results throughout, and we will explicitly extend the approach to arbitrary mixtures of hard convex particles in chapter 6.

Second, our problem is intimately connected to sphere packing problems which are important for the study of granular materials and in computer science where they are essential for coding signals for transmission over noisy channels and potentially for encryption[10]. Determining the densest possible packing of spheres is a notoriously difficult problems in general [30, 31]; the close packing of three-dimensional spheres already discussed was conjectured by Johannes Kepler in 1611, but it took nearly 400 years and a *tour de force* of combined mathematical and computational arguments to actually prove it [32]. Related questions concern determining the number and nature of rigid packings [31, 33, 34], the results of which we use extensively. Our approach thus provides a connection between sphere packing problems and properties of liquids.

[10] Notably, encryption using spherical lattices is one potential candidate for post-quantum cryptography [30].

Finally, in chapter 7 we will change subject to address the nucleation kinetics in drying aerosols. This project emerged from an opportunity to collaborate with the Bristol Aerosol Research Centre, so it was driven by experimental conditions which are not adequately captured by a purely hard sphere model. The nucleation theory we employ is identical to that used to describe hard sphere crystallisation, so the questions posed in this applied context are fundamental. We intended to keep this chapter self-contained,

so we save full discussion of nucleation until chapter 7.

Chapter 2

Geometry and the liquid state

> It tells me that the Creator used the wrong kind of circles.
>
> Terry Pratchett, *Pyramids* (1989).

In this chapter we provide a self-contained account of the foundational frameworks underlying the two themes of this thesis: *integral geometry* and *liquid state theory*. I expect the reader to have a background in statistical physics, so my account of liquid state theory is not intended to be exhaustive; for more in-depth treatments see the references herein. By contrast, I do *not* expect much familiarity with integral geometry. Understanding the underlying mathematical detail of this field is not essential to follow the rest of the thesis, so I will focus on the key concepts and notation rather than detailed derivation.

This chapter was assembled from my notes on liquid state theory over the previous few years, which I wanted to organise in one place mostly for my own benefit. As such, this chapter is a little long so I anticipate the expert reader will skim over it; to facilitate this I have placed the important results in boxes as a guide to the most relevant parts.

As many-body correlation functions are a central theme of the results chapters, I have emphasised correlation functions in section 2.2.2 on liquid structure to the point where I have somewhat belaboured giving the explicit forms and normalisations of the various correlation functions. Even though we will only use one particular hierarchy of correlation functions in the results chapters, I personally found it helpful to have these formulas in one place. I have found myself frequently revisiting the transformations between the various hierarchies of correlation functions, so I include them in anticipation that someone repeating or extending this work may profit from having a kind of "cheat sheet".

2.1 Integral geometry

Or "How long is a piece of string?"

2.1.1 Towards a geometric interpretation of extensivity

Geometry has been a recurring theme in physical theories, appealing because of its intuitive nature. There are many ways that geometric ideas can be incorporated, but our focus will be on expansions of thermodynamic quantities in terms of *sizes*. The usefulness of this particular focus is directly connected to the familiar concept of *extensivity* in statistical mechanics, which we will use to guide the following discussion. Thermodynamic potentials must be extensive to remain well-defined in the thermodynamic limit, so by focusing on extensive quantities we ensure a thermodynamically consistent description in this limit.

As an example, extensive quantities include the *potential energy* of a large system which can be expressed in terms of system volume as

$$\lim_{V\to\infty} U = uV$$

where u would be an energy density which is *intensive*, meaning it does not change with system volume. Another example is the surface free energy, defined in the absence of entropic effects as the excess quantity $U_{\text{ex}} = U - uV$ In the macroscopic limit this yields the extensive quantity

$$\lim_{V\to\infty} U_{\text{ex}} = \gamma A$$

where γ is the intensive surface tension and A is the extensive surface area i.e. another size measure. More refined notions define a variable as extensive if it is a *first-order homogeneous function* of any linearly independent set of (different) extensive variables characterising the system size [35]. That is, a variable ϕ is extensive if

$$\phi(\lambda Y_1, \cdots, \lambda Y_n) = \lambda\phi(Y_1, \cdots, Y_n) \tag{2.1}$$

where $\{Y_1, \cdots, Y_n\}$ are a complete (linearly independent) set of extensive variables describing the system size. We will explore what other reasonable notions of 'size' there may be, in effect finding a complete set of extensive variables, in the hope that we arrive at ideas which prove useful in developing new theories.

We introduced the area above as a size descriptor for a surface. Borrowing ideas from differential geometry, we can also characterise the surface's shape through *curvature*. A surface is a two-dimensional manifold so its local shape is described by two basis vectors. Supposing the surface is parameterised by coordinates (x_1, x_2), then the basis vectors at a point on the surface $\mathbf{r}$ are

$$\mathbf{e}_\alpha := \frac{\partial \mathbf{r}}{\partial x_\alpha} \qquad \alpha \in \{1, 2\}. \tag{2.2}$$

Then, the shape of the surface is characterised by changes in the basis vectors leading to the curvature tensor

$$\kappa_{\alpha\beta} := \frac{\partial \mathbf{e}_\beta}{\partial x_\alpha} \qquad \alpha, \beta \in \{1, 2\}. \tag{2.3}$$

The values of the curvature tensor will depend on the choice of coordinate system (x_1, x_2), so it is usual to consider the *curvature invariants*, i.e. the trace and determinant[11], leading to the the *mean* and *Gaussian curvatures*

$$H := \frac{\operatorname{Tr}\kappa}{2}, \tag{2.4a}$$

$$G := \det\kappa. \tag{2.4b}$$

As an example of how curvature can be a useful concept in statistical mechanics, we put forward the Young-Laplace equation which writes the pressure difference between two fluids as

$$\Delta p = 2\gamma H,$$

with applications to e.g. phase coexistence [36, 37] or frost damage to porous solids [38]. Extensive curvature measures are obtained by integrating the curvature invariants over the surface, leading to the integrated mean and Gaussian curvatures C and X.

Together, the extensive geometric variables we have introduced so far can be written as[12]

$$V = \int_V d\mathbf{r}, \tag{2.5a}$$

$$A = \int_{\partial V} d\mathbf{r}, \tag{2.5b}$$

$$C = \int_{\partial V} H(\mathbf{r})\, d\mathbf{r}, \tag{2.5c}$$

$$X = \int_{\partial V} G(\mathbf{r})\, d\mathbf{r}. \tag{2.5d}$$

The latter three quantities are *expressed* here as the surface integrals, but we shall see that they are really size measures on the volume V. These clearly form a linearly independent set[13], but less obvious is the fact that these are the *only* reasonable notions of size in three-dimensions. This is a central finding of *integral geometry*, which we will expand on in subsequent sections. A consequence of this is that together $\{V, A, C, X\}$ form a complete basis for system size in three dimensions, so we could redefine an extensive quantity as one which can be written

$$\phi = a_3 V + a_2 A + a_1 C + a_0 X, \tag{2.6}$$

which, as a linear relation, clearly obeys (2.1) during the transformation[14] $\{V, A, C, X\} \to \{\lambda V, \lambda A, \lambda C, \lambda X\}$.

Integral geometry provides elegant and unified description of sizes, and was crucial in the development of modern theories of hard spheres [25, 39], including the main ideas underlying chapters 4, 5 and 6. This framework thus provides the route to generalising geometrical theories such as the Asakura-Oosawa model for depletion forces [40, 41], and more generally any free volume theory which expresses an energy in terms of a volume in space. As integral geometry is generally unfamiliar to people with a background in physics, we will place emphasis on the concepts and intuition rather than rigour and proofs. We work mainly from standard texts Refs. [42–45].

[11] This argument is readily generalised to $(d-1)$-dimensional surfaces in $\mathbb{R}^d$, where we would find $d-1$ invariants of the curvature tensor.

[12] We use the usual physicist abuse of notation where V refers to both a region in space $V \subset \mathbb{R}^3$, and also the physical volume of this space.

[13] This can be quickly determined by considering their units, i.e. $V : [\mathrm{m}^3]$, $A : [\mathrm{m}^2]$, $C : [\mathrm{m}^1]$, $X : [\mathrm{m}^0]$.

[14] Note: the rescaling of λV here refers to rescaling the volume measure (2.5a), *not* the object $V \subset \mathbb{R}^3$; in the latter case we would obtain the (non-extensive) transformation $\{V, A, C, X\} \to \{\lambda V, \lambda^{2/3} A, \lambda^{1/3} C, X\}$.

2.1.2 What do we even mean by size?

In order to proceed we must define 'size', and specify precisely which objects this definition applies to. We put forward the following qualities of the measures V, A, C and X which make them intuitive notions of size:

1. They are invariant with respect to translations and rotations, so that an object's size is independent of the observer.

2. They increase additively, i.e. they transform under combination of subsystems via the inclusion/exclusion relation e.g. for two objects K_1 and K_2[15]

$$V[K_1 \cup K_2] = V[K_1] + V[K_2] - V[K_1 \cap K_2], \tag{2.7}$$

   and similar expressions for A, C, and X. As corollaries, this property contains the idea that the size of nothing is zero, e.g. $V[\varnothing] = 0$, and leads to the homogeneity property of extensive variables (2.1) through (2.6).

3. They are continuous[16]. Loosely speaking, this means that the size measures converge as the object is approximated by increasingly finely meshed polyhedra excluding fractal geometries. As a simple intuitive example, the measurement of a length will converge continuously to some number as one uses rulers with progressively finer distance markings.

[15] We use the square brace notation $V[\cdot]$ to indicate that the size measures are generalised functions, or *functionals*, of their arguments.

[16] Specifically, in integral geometry this continuity property is with respect to the *Hausdorff metric*. Details on this can be found in standard texts, e.g. Refs. [42–45].

The final property specifically excludes geometries for which we do not expect there to be any reasonable measurement of size. These properties are the defining characteristics of more general size measures in integral geometry [42, 45].

Naively, we might attempt to evaluate the size measures on all subsets $V \subset \mathbb{R}^3$, however this turns out to be too broad a definition. In particular, this leads to the *Banach-Tarski paradox* in which an object can be broken into two, then recomposed through rigid transformations into two objects identical to the original one [46]; by (2.7), a paradox ensues where the original volume is equal to twice itself. A better definition is the restriction to *polyconvex sets*[17]: objects formed by countable union of *compact* and *convex* objects. By compact, we mean objects which are

1. *bounded*, so they must be finite in scope, as no meaningful size can be defined for a body spanning an infinite region of space, and

2. *closed*, so they contain their boundary.

[17] The set of polyconvex objects is also sometimes called the *convex ring*.

We write the collection of objects in d-dimensions which are compact and convex as $\mathcal{K}^d$. This class of objects covers most physically relevant geometries, excluding geometries where size measures may be pathological such as those with fractal structures.

As a way of justifying the above claims, and as a segue into other topics, we introduce a (seemingly) new measure: the *Euler characteristic* χ which

simply counts the number of disjoint objects in a set[18]. More precisely, for a compact and convex object $K \in \mathcal{K}^d$ we define the measure such that

$$\chi[K] := \begin{cases} 1 & \text{if } K \neq \varnothing \\ 0 & \text{if } K = \varnothing \end{cases} \tag{2.8}$$

then for it to behave additively (2.7) for a disjoint collection of objects $K_1, \cdots, K_N \in \mathcal{K}^d$ with $K_i \cap K_j = \varnothing$ for $i \neq j$ we find

$$\chi[K_1 \cup \cdots \cup K_N] = N,$$

so it is a counting measure. Some modification of its definition as a counting measure is needed in case of overlaps, however for now we focus on the fact that this measure is rigid-motion invariant, additive and continuous; as such, it would seem to be an independent measure. However, the *Gauss-Bonnet theorem* from differential geometry equates it with the Gaussian curvature through

$$X[K] = 2\pi\chi[\partial K], \tag{2.9}$$

so it is really a manifestation of a size measure we have already seen. It is worth emphasising the Euler characteristic in its own right however, as it is a very important *topological invariant* meaning it does not change with continuous geometric deformations. We state some important properties of the Euler characteristic below.

Compact objects include their boundary, so using the additivity property we can decompose the Euler characteristic on $K \in \mathcal{K}^d$ into surface and interior terms

$$\chi[K] = \chi[\partial K] + \chi[\text{int}(K)] = 1.$$

Arguing by induction, we find[19]

$$\chi[\partial K] = 1 + (-1)^d \tag{2.10a}$$

$$\chi[\text{int}(K)] = (-1)^{d+1} \tag{2.10b}$$

Thus the Gauss-Bonnet theorem (2.9), valid in $d = 3$, gives $X = 4\pi$ for convex objects i.e. a constant. By similar arguments, it can be shown that the Euler characteristic is increased by the number of *cavities* in K, and decreased by the number of *holes* in K [45]. More generally, the Euler characteristic is modified by $(-1)^{\nu+1}$ times the number of ν-dimensional *voids*.

Having defined what we mean by 'size', we can start to introduce some useful results from integral geometry. This will start with generalisations of the size measures, and their completeness as a vector space for an extensive property (2.1). Then, we will introduce formulae which are useful in evaluating partition functions for hard particle systems.

2.1.3 Intrinsic volumes as generalised size measures

It will sometimes be helpful to use a dimension independent formalism[20], so it is convenient to introduce generalisations of the geometric parameters $\{V, A, C, X\}$: the *intrinsic volumes* $\{V_d, V_{d-1}, \cdots, V_0\}$. To introduce the intuition behind these generalised volumes we start from the observation that the quantities $\{V, A, C, X\}$ can be imagined as the size of projections onto k-dimensional subspaces in $\mathbb{R}^3$; for a compact body $K \in \mathcal{K}^3$ we have:

[18] As an intuitive illustration of why this is a size measure, I like to imagine that the *size* of a pirate's treasure is the *number* of gold coins in their possession, which is the Euler characteristic of their hoard.

[19] Briefly, the only compact, convex object in $d = 1$ is a line segment, with ∂K formed by two disjoint points giving $\chi[\partial K] = 2$. Then, in arbitrary dimensions one considers cutting the object in two, leading to an iteration formula which gives the stated result. Full details can be found in Ref. [45].

[20] Specifically, in chapter 6 we will derive a theory for the liquid state. In order to obtain results for all physical dimensions $d \leq 3$, we will work in arbitrary d and substitute $d \in \{1, 2, 3\}$ at the end of our derivation.

k	ω_k	$V_k[\mathcal{B}_1]$	$V_k[\mathcal{B}_2]$	$V_k[\mathcal{B}_3]$
0	1	1	1	1
1	2	2	π	4
2	π		π	2π
3	$\frac{4\pi}{3}$			$\frac{4\pi}{3}$

Table 2.1: Intrinsic volumes of the d-dimensional unit ball $\mathcal{B}_d$ in physical dimensions $d \leq 3$.

1. $V[K]$ is trivially the volume of the intersection of K with the 3-dimensional subspace i.e. all of Euclidean space.

2. $A[K]$ can be thought of as the typical size of two-dimensional images formed by projections onto planes.

3. $C[K]$ is related to the projections onto one-dimensional subspaces i.e. lines. This curvature measure is normally thought of as a surface property, but this definition suggests an equivalence (up to a different normalisation) with the *mean width* $L[K]$ of the body.

4. $X[K]$ is obtained from projections onto a single point, corroborating the equivalence with the Euler characteristic $\chi[K]$ articulated by the Gauss-Bonnet theorem (2.9).

Generalising the above intuition to d-dimensions, we see that in general we can imagine $d+1$ projections and so expect $d+1$ corresponding volumes. We define the kth intrinsic volume as the average size of the projections onto k-dimensional linear subspaces of $\mathbb{R}^d$, i.e. [42, 45]

$$V_k[K] = C_{k,d-k} \int \chi[K \cap E_{d-k}]\, dE_{d-k} \tag{2.11}$$

where the integral is taken over all affine transformations of the plane E_{d-k} in $\mathbb{R}^d$, and flag coefficient is

$$C_{k,d-k} := \frac{d!}{k!(d-k)!} \frac{\omega_d}{\omega_k \omega_{d-k}}, \tag{2.12}$$

where the volume of the d-dimensional ball with unit radius $\mathcal{B}_d$ is

$$\omega_d := V_d[\mathcal{B}_d] = \frac{\pi^{d/2}}{\Gamma(\frac{d}{2}+1)}. \tag{2.13}$$

The flag coefficients $C_{k,d-k}$ have a similar structure to binomial coefficients, and play a similar *combinatorial* role in the combination of geometric objects (section 2.1.4). By convention, the normalisation of the measure dE_{d-k} in (2.11) is chosen to give the intrinsic volumes for the unit ball as

$$V_k[\mathcal{B}_d] = \binom{d}{k} \frac{\omega_d}{\omega_{d-k}}, \tag{2.14}$$

with values in physical dimensions $d \leq 3$ given in Table 2.1. A set of common geometrical quantities and their reduction to the intrinsic volumes in $d \leq 3$ is given in Table 2.2.

Geometric quantity		
Name	Symbol	Functional
$d = 1$		
Euler characteristic	χ	V_0
Length	L	V_1
$d = 2$		
Euler characteristic	χ	V_0
Perimeter	L	$2V_1$
Area	A	V_2
$d = 3$		
Euler characteristic	χ	V_0
Mean width	L	$\frac{1}{2}V_1$
Mean radius	R	$\frac{1}{4}V_1$
Surface area	A	$2V_2$
Volume	V	V_3
Integrated Gaussian curvature	X	$4\pi V_0$
Integrated mean curvature	C	πV_1

Table 2.2: Common geometrical quantities and their representation in terms of the intrinsic volumes $\{V_k\}$. The intrinsic volumes are morphological measures describing the size of a body. The common geometric interpretations of V_k for $k < d$ typically involves integrations over the boundary ∂K rather than K itself, leading to the curvature measures $\{C, X\}$ in $d = 3$ giving an equivalent description as one involving Euler characteristic and the typical width $\{\chi, L\}$. However, the intrinsic volumes are more general as they can be evaluated for shapes where curvatures are not locally defined, e.g. at lines and vertices.

Hadwiger's characterisation theorem

A classic theorem of integral geometry due to Hadwiger [47] states that the intrinsic volumes are the *only* class of functionals with the size properties described in section 2.1.2: rigid-motion invariance, additivity and continuity.

A corollary of this theorem is that the intrinsic volumes must form a linear vector space for any functional which also possesses these properties, thus providing the d-dimensional generalisation of an extensive variable (2.6) as one which adopts the form

$$\phi = \sum_{k=0}^{d} a_k V_k. \tag{2.15}$$

Exploiting this theorem, we will use the intrinsic volumes to construct theories of the hard sphere liquid in section 2.3.4 and subsequent chapters. In the next section we will state some useful results for doing calculations in statistical mechanics with the intrinsic volumes.

2.1.4 Kinematic formulae

Here we introduce the *kinematic formulae* which calculate the probabilities that uniformly distributed objects collide. This problem is applicable to the evaluation of partition functions in statistical mechanics, of which we will see specific examples in section 2.3.4 and chapter 6.

Two compact and convex objects $K_1, K_2 \in \mathcal{K}^d$ overlap if their intersection is non-empty $K_1 \cap K_2 \neq \varnothing$. The intersection of convex objects is also

convex, so from the definition of the Euler characteristic (2.8) we can write

$$\chi[K_1 \cap K_2] = \begin{cases} 1 & \text{if } K_1 \cap K_2 \neq \varnothing \\ 0 & \text{if } K_1 \cap K_2 = \varnothing \end{cases}$$

then the probability that the two objects collide is

$$\text{Prob}\,[\text{collision}] = \frac{1}{V}\int_V \chi[K_1 \cap K_2(\mathbf{r})]\, d\mathbf{r}$$

where K_2 is uniformly distributed and K_1 acts as a fixed target. Here, K_2 is *translated* over the accessible volume, however in general these objects will be non-spherical so we should also consider the *rotations*. Integral geometry more naturally deals with integrations over relative positions *and* orientations, at the small cost of additional notation. Writing the relative orientation as the Euler angle tuple $\boldsymbol{\theta}$, we consider the generalisation

$$\int_{\mathbb{R}^d} d\mathbf{r} \to \int_{\mathbb{R}^d \times \mathrm{SO}(d)} d\mathbf{r} d\boldsymbol{\theta} := \int_{G_d} dg,$$

with the normalisation in the angular measure such that $\int d\boldsymbol{\theta} = 1$. In the right-most equality we introduced the rigid-motion operation acting on a body $K \in \mathcal{K}^d$ as

$$gK := \{\mathcal{R}_\theta\, \mathbf{k} + \mathbf{r} \,|\, \mathbf{k} \in K\},$$

a member of the rigid-motion group $g \in G_d := \mathbb{R}^d \times \mathrm{SO}(d)$, and where $\mathcal{R}_\theta \in \mathrm{SO}(d)$[21] is the rotation matrix parameterised by $\boldsymbol{\theta}$. Then the generalised measure for particle collisions becomes

$$\int_{G_d} \chi[K_1 \cap gK_2]\, dg$$

if they occupy all of Euclidean space. We will see integrals like this emerge from liquid state theory in sections 2.2.4 and 2.3.4, and later in chapter 6.

[21] $\mathrm{SO}(d)$ is the *special orthogonal group*, i.e. the group of all orthogonal matrices with unit determinant.

Principal kinematic formula

A central result of integral geometry is the principal kinematic formula of Blaschke and Santaló [48–50] which gives the explicit form of these collisional integrals as [42, 45]

$$\int_{G_d} \chi[K_1 \cap gK_2]\, dg = \sum_{k=0}^{d} (C_{k,d-k})^{-1} V_k[K_1] V_{d-k}[K_2] \tag{2.16}$$

We see the flag coefficients (2.12) play an analogous role here in conjugating the intrinsic volumes as binomial coefficients do in algebraic expansions[22]. More general formulae exist for integrals over $V_k[K_1 \cap K_2]$ for all k [45], however these do not have an interpretation in terms of evaluating partition functions so we will not be using them.

[22] For this reason Klain and Rota argue that integral geometry should be called *continuous combinatorics* [45], because it generalises combinatorial results to continuous spaces

The principal kinematic formula (2.16) can be iterated for the intersections of many bodies $\{K_1, \cdots, K_n\}$ giving [42, 51]

$$\begin{aligned} &\int_{G_d^n} \chi[K_1 \cap g_2 K_2 \cap \cdots \cap g_n K_n]\, dg_2 \cdots dg_n \\ &= \sum_{\substack{i_1,\cdots,i_n=0 \\ i_1+\cdots+i_n=nd}}^{d} (C_{i_1,\cdots,i_n})^{-1} V_{i_1}[K_1] \prod_{j=2}^{n} V_{i_j}[K_j], \end{aligned} \tag{2.17a}$$

$$\text{with} \qquad C_{i_1,\cdots,i_n} := \frac{1}{i_1! \omega_{i_1}} \prod_{j=2}^{n} \left(\frac{d!}{i_j!} \frac{\omega_d}{\omega_{i_j}} \right), \tag{2.17b}$$

where $\int_{G_d^n} dg^n = \int_{G_d} dg_1 \cdots \int_{G_d} dg_n$. Here $C_{i_1,\cdots,i_n}$ would be the multinomial generalisation of the flag coefficients (2.12). We will use this iterated formula in chapter 6 to resum a piece of the virial series (to be introduced in the upcoming section 2.2.4).

2.2 Statistical physics of fluids

2.2.1 Statistical mechanics

In this section we *briefly* introduce the statistical ensembles used throughout the rest of the thesis. These emerge by considering typical fluctuations of thermodynamic quantities for a subsystem within a macroscopic system called the *ensemble*; the properties of this larger system define average quantities of the subsystem [52]. Alternatively, the same formalism can be interpreted from a Bayesian perspective to emerge from maximisation of the entropy[23] subject to the constraint of average energy and (optionally) the average particle number [53, 54].

[23] The entropy represents a thermodynamic quantity in the former picture, whereas it represents our own *uncertainty* about the system in the latter.

A d-dimensional system of N particles consists of $\mathbf{r}^N = \{\mathbf{r}_1, \cdots, \mathbf{r}_N\} \in \mathbb{R}^{dN}$ coordinates and $\mathbf{p}^N = \{\mathbf{p}_1, \cdots, \mathbf{p}_N\} \in \mathbb{R}^{dN}$ momenta. The classical Hamiltonian can be decomposed into kinetic and potential terms as in

$$\mathcal{H}_N(\mathbf{r}^N, \mathbf{p}^N) = K_N(\mathbf{p}^N) + U_N(\mathbf{r}^N) \tag{2.18}$$

in the absence of an external field. Further, we constrain the coordinates inside the volume V. The *canonical* ensemble describes an equilibrium system at constant temperature T with probability measure[24]

$$f^{(N)}(\mathbf{r}^N, \mathbf{p}^N) \propto e^{-\beta \mathcal{H}_N}. \tag{2.19}$$

[24] As a reminder for the reader, in the previous chapter we introduced $\beta = (k_B T)^{-1}$, with Boltzmann constant k_B and temperature T.

The proportionality constant ensures the probability distribution is properly normalised, leading to the canonical partition function

$$Q_N = \int_{\mathbb{R}^{dN}} \int_{V^N} e^{-\beta \mathcal{H}_N} d\mathbf{r}^N d\mathbf{p}^N. \tag{2.20}$$

Classically, the kinetic energy is simply

$$K_N(\mathbf{p}^N) = \sum_{i=1}^{N} \frac{|\mathbf{p}_i|^2}{2m_i}$$

which can be integrated leaving

$$Q_N = \frac{Z_N}{\Lambda^{dN} N!} \tag{2.21}$$

where Λ is the thermal de Broglie wavelength, and the configurational integral is given by

$$Z_N = \int_{V^N} e^{-\beta U_N} d\mathbf{r}^N. \tag{2.22}$$

Averaged quantities with N fixed are obtained through

$$\langle \cdots \rangle_N = \frac{1}{Z_N} \int_{V^N} (\cdots)\, e^{-\beta U_N} d\mathbf{r}^N,$$

and the Helmholtz free energy is given by

$$\beta F = -\ln Z_N.$$

We will work almost exclusively in the *grand canonical ensemble*, where particle number varies according to a chemical potential μ, which is convenient for liquid state descriptions[25]. The corresponding partition function features summation over N, as in

$$\Xi = \sum_{N=0}^{\infty} \frac{z^N}{N!} Z_N = \sum_{N=0}^{\infty} \frac{z^N}{N!} \int_{V^N} e^{-\beta U_N} d\mathbf{r}^N, \tag{2.23}$$

where the activity is $z = \exp(\beta\mu)/\Lambda^d$. Accordingly, average quantities are found via

$$\langle \cdots \rangle = \frac{1}{\Xi} \sum_{N=0}^{\infty} \frac{z^N}{N!} \int_{V^N} (\cdots)\, e^{-\beta U_N} d\mathbf{r}^N, \tag{2.24}$$

and the corresponding free energy (or *grand potential*) is obtained via

$$\beta\Omega = -\ln \Xi.$$

For a homogeneous system this reduces to the standard result

$$\Omega_{\text{hom}} = -pV. \tag{2.25}$$

Thermodynamic quantities are easily calculated for the ideal gas, e.g.

$$\beta\Omega = -\frac{e^{\beta\mu^{\text{id}}}}{\Lambda^d} V.$$

Comparing the homogeneous result (2.25) with the ideal gas law $\beta p = \rho$ gives the chemical potential of an ideal gas as

$$\beta\mu^{\text{id}} = \ln(\Lambda^d \rho). \tag{2.26}$$

From the Legendre transform of the grand potential

$$\Omega = F - \mu N \tag{2.27}$$

we obtain the free energy density of an ideal gas as

$$\frac{\beta F^{\text{id}}}{V} = \rho(\ln(\Lambda^d \rho) - 1). \tag{2.28}$$

Finally, for interacting systems the chemical potential and free energy are typically separated into *ideal* and *excess* parts, as in

$$\beta\mu = \beta\mu^{\text{id}} + \beta\mu^{\text{ex}},$$
$$\beta F = \beta F^{\text{id}} + \beta F^{\text{ex}},$$

with the ideal contributions as expressed above.

[25] Notably the free energy is extensive without invoking Stirling's approximation for $N!$, making the thermodynamics properly self-consistent even with small system sizes.

2.2.2 Liquid structure

Interparticle interactions induce spatial structure in the liquid which are characterised by several (equivalent) hierarchies of correlation functions. The most natural description of structure starts from the *n-particle density*

$$\text{Prob}\,[\textit{any } n \text{ particles in volume } d\mathbf{r}^n] := \rho^{(n)}(\mathbf{r}^n)\, d\mathbf{r}^n, \tag{2.29}$$

where $\mathbf{r}^n := \{\mathbf{r}_1, \cdots, \mathbf{r}_n\}$ are the particle positions. This is formally obtained by integrating the full (configurational) probability distribution over the remaining degrees of freedom. For the single-component system this yields [12]

$$\rho^{(n)}(\mathbf{r}^n) = \frac{1}{\Xi} \sum_{N=n}^{\infty} \frac{z^N}{(N-n)!} \int_{V^N} e^{-\beta U_N}\, d\mathbf{r}^{(N-n)}. \tag{2.30}$$

The n-particle density is an intuitive descriptor for liquid structure because it generalises the probability density function for a closed system, i.e.

$$\text{Prob}\,[N \text{ particles in volume } d\mathbf{r}^n] := \frac{e^{-\beta U_N}}{Z_N}\, d\mathbf{r}^N,$$

to a subset of particles within an open system. $\rho^{(n)}$ thus provides the correct procedure for coarse-graining onto selected degrees of freedom within a bulk system. The analogy with the canonical ensemble is imperfect in that $\rho^{(n)}$ is unnormalised so it is not strictly a probability density function; integrating (2.30) over the remaining degrees of freedom yields[26]

$$\frac{1}{n!} \int_{V^n} \rho^{(n)}(\mathbf{r}^n)\, d\mathbf{r}^n = \left\langle \frac{N!}{n!(N-n)!} \right\rangle$$

i.e. the average binomial coefficient. The n-particle density scales proportionally to ρ^n so it is usual to remove this by defining the *n-particle distribution function* as

$$g^{(n)}(\mathbf{r}^n) := \frac{\rho^{(n)}(\mathbf{r}^n)}{\prod_{i=1}^{n} \rho^{(1)}(\mathbf{r}_i)}, \tag{2.31}$$

which provides our first (and primary) hierarchy of correlation functions.

Physically, particles become decorrelated when they are separated by macroscopic distances[27]. This property manifests in the distribution functions via a *product property* where [55]

$$g^{(n)}(\mathbf{r}^n) \simeq g^{(s)}(\mathbf{r}^s)\, g^{(n-s)}(\mathbf{r}^{n-s})$$

in the limit where the s particles become macroscopically separated from the remaining $(n-s)$ particles. This property causes the distribution functions to decay to their ideal gas value $g^{(n)}(\mathbf{r}^n) \to 1$ in the limit of infinite separations between all particles. Moreover, the product property suggests that there is a great deal of redundancy inside the distribution functions; in certain applications it is convenient to introduce an additional hierarchy of correlation functions which only capture the excess correlations. If we imagine the normalisation of the distribution functions $g^{(n)}$ as *moments* of an unspecified probability distribution, then we can formally imagine a dual

[26] In keeping with the analogy to canonical ensemble we treat this integral as a partition function, and so account for indistinguishability of the n particles by dividing through by $n!$.

[27] This limit behaviour is only valid for 'normal' liquid behaviour far from the critical point where the correlation length diverges.

set of correlation functions $h^{(n)}$ which generate the *cumulants*. Formally, this relationship is expressed [13]

$$1+\sum_{n=1}^{\infty}\frac{\epsilon^n}{n!}\int_{V^n}g^{(n)}(\mathbf{r}^n)\,d\mathbf{r}^n=\exp\left(\sum_{n=1}^{\infty}\frac{\epsilon^n}{n!}\int_{V^n}h^{(n)}(\mathbf{r}^n)\,d\mathbf{r}^n\right),$$

with ϵ as a formal expansion parameter of the moment generating function. In addition, we require that these new functions share the same symmetries as $g^{(n)}$ e.g. permutation invariance in the arguments. These conditions specify a new hierarchy: the *cluster correlation functions*[28] where the first few terms are given by [55]

$$h^{(1)}(\mathbf{r})=g^{(1)}(\mathbf{r})=1, \tag{2.32a}$$

$$h^{(2)}(\mathbf{r}_1,\mathbf{r}_2)=g^{(2)}(\mathbf{r}_1,\mathbf{r}_2)-g^{(1)}(\mathbf{r}_1)g^{(1)}(\mathbf{r}_2), \tag{2.32b}$$

$$\begin{aligned}h^{(3)}(\mathbf{r}_1,\mathbf{r}_2,\mathbf{r}_3)=&g^{(3)}(\mathbf{r}_1,\mathbf{r}_2,\mathbf{r}_3)-\{3\}g^{(2)}(\mathbf{r}_1,\mathbf{r}_2)g^{(1)}(\mathbf{r}_3)\\&+g^{(1)}(\mathbf{r}_1)g^{(1)}(\mathbf{r}_2)g^{(1)}(\mathbf{r}_3),\end{aligned} \tag{2.32c}$$

where $\{\cdot\}$ indicates the number of similar terms which differ only by permutation of indices which we omit for brevity. The pair cluster correlation function[29] $h^{(2)}(\mathbf{r}_1,\mathbf{r}_2)=g^{(2)}(\mathbf{r}_1,\mathbf{r}_2)-1$ is the main function we will use from this hierarchy.

[28] These are so-named because they possess a *cluster property* where they decay to zero in the limit where any particles become macroscopically separated [55]. This feature directly emerges from, and is dual to, the product property for $g^{(n)}$.

[29] This is often called simply the *total correlation function*, especially in the context of integral equation theories (cf. section 2.3.3).

We can define two further hierarchies of correlation functions from the moments and fluctuations in the density. Writing the instantaneous density as

$$\widehat{\rho}(\mathbf{r})=\sum_{i=1}^{N}\delta(\mathbf{r}-\mathbf{r}_i)$$

where $\delta(\cdot)$ is the Dirac delta function, then the various *density moments* are determined as

$$\langle\widehat{\rho}(\mathbf{r})\rangle=\rho^{(1)}(\mathbf{r}), \tag{2.33a}$$

$$\left\langle\widehat{\rho}(\mathbf{r}_1)\widehat{\rho}(\mathbf{r}_2)\right\rangle=\rho^{(2)}(\mathbf{r}_1,\mathbf{r}_2)+\rho^{(1)}(\mathbf{r}_1)\delta(\mathbf{r}_1-\mathbf{r}_2), \tag{2.33b}$$

$$\begin{aligned}\left\langle\widehat{\rho}(\mathbf{r}_1)\widehat{\rho}(\mathbf{r}_2)\widehat{\rho}(\mathbf{r}_3)\right\rangle=&\rho^{(3)}(\mathbf{r}_1,\mathbf{r}_2,\mathbf{r}_3)+\{3\}\rho^{(2)}(\mathbf{r}_1,\mathbf{r}_2)\delta(\mathbf{r}_1-\mathbf{r}_3)\\&+\rho^{(1)}(\mathbf{r}_1)\delta(\mathbf{r}_1-\mathbf{r}_2)\delta(\mathbf{r}_1-\mathbf{r}_3).\end{aligned} \tag{2.33c}$$

Importantly, (2.33a) shows that the single-particle density is simply the equilibrium density profile. The normalisation of these functions gives the moments of particle number N, i.e.

$$\int_{V^n}\left\langle\prod_{i=1}^{n}\widehat{\rho}(\mathbf{r}_i)\right\rangle d\mathbf{r}^n=\langle N^n\rangle\,. \tag{2.34}$$

We can define a dual hierarchy of *density-density correlation functions* $H^{(n)}$ by the same procedure used to generate $h^{(n)}$ from $g^{(n)}$, i.e. through a cumulant generating function. The first few functions in this hierarchy are

$$H^{(1)}(\mathbf{r})=\rho^{(1)}(\mathbf{r}), \tag{2.35a}$$

$$H^{(2)}(\mathbf{r}_1,\mathbf{r}_2)=\left\langle\widehat{\rho}(\mathbf{r}_1)\widehat{\rho}(\mathbf{r}_2)\right\rangle-\rho^{(1)}(\mathbf{r}_1)\rho^{(1)}(\mathbf{r}_2), \tag{2.35b}$$

$$\begin{aligned}H^{(3)}(\mathbf{r}_1,\mathbf{r}_2,\mathbf{r}_3)=&\left\langle\widehat{\rho}(\mathbf{r}_1)\widehat{\rho}(\mathbf{r}_2)\widehat{\rho}(\mathbf{r}_3)\right\rangle-\{3\}\left\langle\widehat{\rho}(\mathbf{r}_1)\widehat{\rho}(\mathbf{r}_2)\right\rangle\rho^{(1)}(\mathbf{r}_3)\\&+\rho^{(1)}(\mathbf{r}_1)\rho^{(1)}(\mathbf{r}_2)\rho^{(1)}(\mathbf{r}_3),\end{aligned} \tag{2.35c}$$

or more generally [12]

$$H^{(n)}(\mathbf{r}^n) = \left\langle \prod_{i=1}^{n} \left[\widehat{\rho}(\mathbf{r}_i) - \rho^{(1)}(\mathbf{r}_i) \right] \right\rangle \qquad \forall\, n \geq 2. \tag{2.36}$$

The normalisations of $H^{(n)}$ give the cumulants in N i.e.

$$\int_{V^n} H^{(n)}(\mathbf{r}^n)\, d\mathbf{r}^n = \frac{d^n}{d\epsilon^n} \left[\log \left(1 + \sum_{m=1}^{\infty} \frac{\epsilon^m}{m!} \langle N^m \rangle \right) \right]_{\epsilon=0}$$

or explicitly for the first few functions

$$\int_V H^{(1)}(\mathbf{r})\, d\mathbf{r} = \langle N \rangle, \tag{2.37a}$$

$$\int_{V^2} H^{(2)}(\mathbf{r}_1, \mathbf{r}_2)\, d\mathbf{r}_1 d\mathbf{r}_2 = \langle N^2 \rangle - \langle N \rangle^2, \tag{2.37b}$$

$$\int_{V^3} H^{(3)}(\mathbf{r}_1, \mathbf{r}_2, \mathbf{r}_3)\, d\mathbf{r}_1 d\mathbf{r}_2 d\mathbf{r}_3 = \langle N^3 \rangle - 3\langle N^2 \rangle \langle N \rangle + 2\langle N \rangle^3. \tag{2.37c}$$

This class of correlation functions thus describes the fluctuations in density, which can play an important thermodynamic role; we will give a specific example of how these functions connect to thermodynamic response functions below.

An important response function for liquid structure is the isothermal compressibility

$$\kappa_T := \frac{1}{\rho} \left(\frac{\partial \rho}{\partial p} \right)_{V,T}.$$

Using standard thermodynamic manipulations we can obtain the equivalent expression

$$\kappa_T = \frac{1}{\rho^2} \left(\frac{\partial \rho}{\partial \mu} \right)_{V,T}$$

or defining the dimensionless *isothermal susceptibility* as

$$\chi_T := \rho k_B T \kappa_T = \frac{1}{\rho} \left(\frac{\partial \rho}{\partial (\beta\mu)} \right)_{V,T}.$$

It is straightforward to evaluate this through the grand canonical average (2.24) of density $\rho = \langle N \rangle / V$, obtaining[30]

$$\chi_T = \frac{\langle N^2 \rangle - \langle N \rangle^2}{\langle N \rangle}. \tag{2.38}$$

[30] The thermodynamic definitions of κ_T and χ_T above apply to a bulk homogeneous liquid, whereas the definition of χ_T in (2.38) allows generalisation to an inhomogeneous liquid.

From the normalisation of $H^{(2)}$ (2.37b) as the second cumulant in N, we find

$$\begin{aligned} \chi_T &= \frac{1}{\langle N \rangle} \int_{V^2} H^{(2)}(\mathbf{r}_1, \mathbf{r}_2)\, d\mathbf{r}_1 d\mathbf{r}_2 \\ &= 1 + \rho \int_V h^{(2)}(\mathbf{r})\, d\mathbf{r} \end{aligned} \tag{2.39}$$

where the latter step is valid for the homogeneous liquid where $g^{(2)}(\mathbf{r}_1, \mathbf{r}_2) = g^{(2)}(\mathbf{r}_2 - \mathbf{r}_1)$ and we used the pair cluster correlation function (2.32b).

The various correlation functions introduced are all structural descriptors in real space, but we can imagine equivalent descriptors in Fourier space. The most important Fourier space correlation are the static structure factors $S^{(n)}$, of which the pair structure factor $S^{(2)}$ is particularly important for scattering experiments. We define this from the Fourier transform of the pair distribution function in the case of the uniform liquid as

$$\begin{aligned} S^{(2)}(\mathbf{k}) :=& \frac{\left\langle \widetilde{\rho}(\mathbf{k})\widetilde{\rho}(-\mathbf{k})\right\rangle}{\langle N\rangle} = 1 + \rho\widetilde{g}^{(2)}(\mathbf{k}) \\ =& 1 + \rho\widetilde{h}^{(2)}(\mathbf{k}) + \rho\delta(\mathbf{k}) \end{aligned} \tag{2.40}$$

where the tilde over a function denotes its Fourier transform. In terms of the structure factor (2.39) is written succinctly as[31]

$$\chi_T = \lim_{\mathbf{k}\to 0} S^{(2)}(\mathbf{k}). \tag{2.41}$$

[31] The Dirac delta function at the origin in $S^{(2)}(\mathbf{k})$ is often omitted to regularise the function, in which case the right-hand side can be written more simply as $S^{(2)}(0)$.

2.2.3 Thermodynamic routes to the free energy

Often the main objective of a statistical physicist is to determine the phase diagram of a system, which can be deduced from the free energy if known. Liquid state theory contains several routes to calculate the free energy, of which we will describe two below. Often, the end result of these approaches is an equation of state for the pressure $p = p(\rho)$, giving the free energy implicitly through the thermodynamic relation

$$p = -\left(\frac{\partial\Omega}{\partial V}\right)_{\mu,T}, \tag{2.42}$$

although a state equation for any other thermodynamic observable would suffice.

The first option for determining the free energy is through the compressibility, from the thermodynamic relation

$$\frac{1}{\chi_T} = \left(\frac{\partial\beta p}{\partial\rho}\right)_{V,T}. \tag{2.43}$$

Integrating this relation over the density and making use of the isothermal compressibility identity for a uniform system (2.39) gives

$$\beta p = \int_0^\rho \frac{1}{\chi_T} d\rho' = \int_0^\rho \lim_{\mathbf{k}\to 0} \frac{1}{S^{(2)}(\mathbf{k})} d\rho', \tag{2.44}$$

i.e. the *compressibility route* to the pressure.

Another option evaluates the pressure directly (2.42) from the partition function. In terms of partition functions this becomes

$$\beta p = \left(\frac{\partial(\ln\Xi)}{\partial V}\right)_{\mu,T} = \frac{1}{\Xi}\sum_{N=0}^{\infty}\frac{z^N}{N!}\left(\frac{\partial Z_N}{\partial V}\right)_{N,T}. \tag{2.45}$$

We consider what happens during a volume change $V \to \alpha^d V$ emerging from the affine rescaling $\mathbf{r} \to \alpha\mathbf{r}$, so that the configurational integral (2.22) becomes

$$Z_N(\alpha^d V) = \int_{\alpha V^N} e^{-\beta U_N(\mathbf{r}^N)} d\mathbf{r}^N = \alpha^{dN}\int_{V^N} e^{-\beta U_N(\alpha\mathbf{r}^N)} d\mathbf{r}^N$$

Using the identity

$$\frac{\partial f(xy)}{\partial y} = \frac{x}{y}\frac{\partial f(xy)}{\partial x},$$

we can write

$$\frac{\partial(Z_N(\alpha^d V))}{\partial V} = \frac{\alpha}{dV}\frac{\partial(Z_N(\alpha^d V))}{\partial \alpha}. \tag{2.46}$$

This trick allows the derivatives appearing on the right-hand side of the pressure relation (2.45) to be re-expressed as

$$\left(\frac{\partial Z_N}{\partial V}\right)_{N,T} = \frac{1}{dV}\left.\frac{\partial(Z_N(\alpha^d V))}{\partial \alpha}\right|_{\alpha=1}.$$

The derivative of $Z_N(\alpha^d V)$ with respect to α can be calculated explicitly as

$$\begin{aligned}\frac{\partial Z_N(\alpha^d V)}{\partial \alpha} &= \frac{dN}{\alpha} Z_N + \alpha^{dN}\int_{V^N}\frac{\partial}{\partial \alpha}\left(e^{-\beta U_N(\alpha \mathbf{r}^N)}\right) d\mathbf{r}^N \\ &= \frac{dN}{\alpha} Z_N - \alpha^{dN}\int_{V^N}\frac{\partial \beta U_N(\alpha \mathbf{r}^N)}{\partial \alpha} e^{-\beta U_N} d\mathbf{r}^N,\end{aligned}$$

which combined with (2.46) yields

$$\left(\frac{\partial Z_N}{\partial V}\right)_{N,T} = \rho Z_N - \frac{1}{dV}\int_{V^N}\left.\frac{\partial \beta U_N(\alpha \mathbf{r}^N)}{\partial \alpha}\right|_{\alpha=1} e^{-\beta U_N} d\mathbf{r}^N.$$

Inserting this back into (2.45) gives the final result

$$\frac{\beta p}{\rho} = 1 - \frac{1}{\rho dV}\left\langle \left.\frac{\partial \beta U_N(\alpha \mathbf{r}^N)}{\partial \alpha}\right|_{\alpha=1}\right\rangle, \tag{2.47}$$

which is known as the *virial route*[32] to the pressure.

There are other routes involving different observables (e.g. through the potential energy or the chemical potential [13]) to obtain the equation of state from the correlation functions; however, we will not discuss them as we will only use the virial route in the results chapters. The degree of self-consistency between different routes can act as a proxy for the accuracy of an approximate theory.

[32] This is so-named because historically it was derived through the virial theorem. Despite the similar name, this approach has no relation to the virial series which will be introduced in section 2.2.4.

Contact theorem for hard spheres

For a single-component system interacting through a spherically symmetric pair potential $u(r)$, the virial route (2.47) yields

$$\frac{\beta p}{\rho} = 1 - \frac{\rho}{2d}\int_V r g^{(2)}(r)\frac{d\beta u}{dr}\,d\mathbf{r}, \tag{2.48}$$

using the definition of the 2-particle distribution function (2.31) as the average over the remaining degrees of freedom. In the case of hard spheres $u'(r)$ is not well-defined because the pair potential (1.1) is singular, however the cavity function

$$y^{(2)}(r) = g^{(2)}(r)e^{\beta u(r)}$$

is continuous (see e.g. Refs. [12, 13]) even in cases where the pair potential is not. In terms of the cavity function, the virial route (2.48) becomes

$$\frac{\beta p}{\rho} = 1 + \frac{\rho}{2d}\int_V r y^{(2)}(r)\frac{d}{dr}\left(e^{-\beta u(r)}\right)d\mathbf{r},$$

which for d-dimensional hard spheres of diameter σ yields

$$\frac{\beta p}{\rho} = 1 + \frac{\eta(2\sigma)^d}{2}y^{(2)}(\sigma^+), \tag{2.49}$$

the *contact theorem*, so-named because only the value at contact $y^{(2)}(\sigma^+) = \lim_{r\to\sigma} y^{(2)}(r)$ (approached from $r > \sigma$) remains.

The pair distribution function $g^{(2)}$ appeared in the virial route because the specified system interacts via a pair potential; we could reasonably expect the generalisation to an n-body interaction potential to give the equation of state in terms of the n-body distribution function $g^{(n)}$.

2.2.4 Virial series

The virial series provides a properly rigorous approach to evaluating the partition function, and thus the free energy, from first principles [12, 13, 56–58]. We introduce it here as it will be used in chapter 6 to place the fundamental approximation, the morphometric approach, underlying chapters 4 and 5 on firmer ground. This approach can also be used to derive free energy functionals for application to (classical) density functional theory (section 2.3): cf. Refs. [51, 59, 60]. The series derived below is only valid for systems interacting via a pair potential $u(\mathbf{r})$.

The partition function Ξ, defined in (2.23), is an expansion in *fugacity* featuring intractable integrals; the trick to make calculations more tractable is to transform Ξ into a *density* expansion. The final series involves an infinite number of individually more tractable integrals. Traditionally, the

virial series for the equation of the state is written

$$\frac{\beta p}{\rho} = 1 + \sum_{n=2}^{\infty} B_n \rho^{n-1} \tag{2.50}$$

where $\{B_n\}$ are the *virial coefficients* to be determined. As a self-consistency check, observe that the ideal gas law is recovered in the low density limit $\rho \to 0$. Alternatively, the virial series can be expressed for the (excess) free energy density, defined through

$$\beta f^{\text{ex}} := \frac{\beta F^{\text{ex}}}{V} = \rho \int_0^{\rho} \left(\frac{\beta p}{\rho'} - 1 \right) \frac{d\rho'}{\rho'}. \tag{2.51}$$

Inserting the virial expression (2.50) gives

$$\beta f^{\text{ex}} = \sum_{n=2}^{\infty} \frac{1}{n-1} B_n \rho^n \tag{2.52}$$

which is more useful for connecting with density functional theory approaches (section 2.3).

To determine the coefficients in the virial series, we start by writing the Boltzmann factor for a pairwise interacting system as the product

$$e^{-\beta U_N(\mathbf{r}^N)} = \prod_{1 \le i < j \le N} (1 + f_{ij}) \tag{2.53}$$

where we introduced the *Mayer function*

$$f_{ij} := e^{-\beta u(\mathbf{r}_i, \mathbf{r}_j)} - 1. \tag{2.54}$$

Expanding out terms in the n-particle configurational integral leads to expressions like

$$\begin{aligned} Z_3 =& \frac{z^3}{3!} \int (1 + f_{12})(1 + f_{23})(1 + f_{31})\, d\mathbf{r}_1 d\mathbf{r}_2 d\mathbf{r}_3 \\ =& \frac{z^3}{3!} \int_{V^3} (1 + \{3\} f_{12} + \{3\} f_{12} f_{23} + f_{12} f_{23} f_{31})\, d\mathbf{r}_1 d\mathbf{r}_2 d\mathbf{r}_3 \end{aligned}$$

which is the term for $n = 3$. In the above expression we used the $\{\cdot\}$ notation which we introduced to indicate different permutations in the various standard correlation functions[33] e.g. (2.32). Expressions involving Mayer functions can become unwieldy so it is usual practice to express them as diagrams: graphs with n vertices connected by edges representing each f_{ij}. For example, the integrand in the above expression would be written

[33] The notational similarity is not merely superficial: the integrand, the Boltzmann weight, is really another correlation function.

$$1 \quad + \{3\} \; f_{12} \quad + \{3\} \; f_{12} f_{23} \quad + f_{12} f_{23} f_{31} \tag{2.55}$$

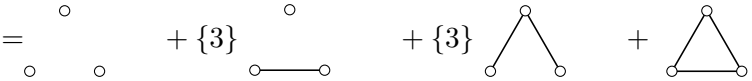

$$= \quad + \{3\} \quad + \{3\} \quad + \quad . \tag{2.56}$$

Integrations over the positions of each particle are represented by blackening the integrating vertices, so that the previous integral becomes

$$\begin{aligned} Z_3 =& \int_{V^3} (1 + \{3\} f_{12} + \{3\} f_{12} f_{23} + f_{12} f_{23} f_{31})\, d\mathbf{r}_1 d\mathbf{r}_2 d\mathbf{r}_3 \\ =& \end{aligned}$$

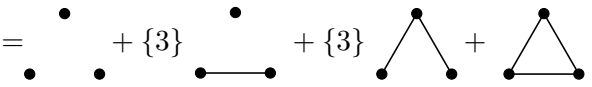

$$+ \{3\} \quad + \{3\} \quad + \quad .$$

To make calculations more tractable we have to reduce the total number of diagrams.

Firstly, we will use the same trick as we used to construct dual correlation functions (cf. discussion around (2.32)): we treat the grand canonical partition function as a moment generating function, with fugacity as the control parameter, and consider its the dual cumulant generating function $\ln \Xi = -\beta\Omega$. It follows that

$$1 + \sum_{n=1} \frac{z^n}{n!} Z_n = \exp\left(\sum_{n=1}^{\infty} \frac{z^n}{n!} \int_{V^n} W^{(n)}(\mathbf{r}^n)\, d\mathbf{r}^n \right),$$

which defines a new hierarchy of *cluster functions*[34] $W^{(n)}$. The transformation to cluster functions eliminates all disconnected diagrams, e.g. the first few are defined as [13]

[34] These are sometimes called *Ursell functions*.

$$W^{(1)}(\mathbf{r}) = 1, \tag{2.57a}$$

$W^{(2)}(\mathbf{r}_1, \mathbf{r}_2) =$  , (2.57b)

$W^{(3)}(\mathbf{r}_1, \mathbf{r}_2, \mathbf{r}_3) = \{3\}$ 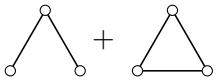 . (2.57c)

The normalisations of these new functions are the so-called *cluster integrals* defined as

$$b_n := \frac{1}{n! V} \int_{V^n} W^{(n)}(\mathbf{r}^n)\, d\mathbf{r}^n, \tag{2.58}$$

so that

$$\ln \Xi = V \sum_{n=1}^{\infty} b_n z^n.$$

We pulled out a volume factor in front of the definition of b_n so that the cluster integral is an intensive quantity; translation invariance in a homogeneous liquid means that only the relative distances matter in $W^{(n)}$, so we obtain a volume term from integration of the first particle.

Secondly, we transform from an expansion in fugacity to one in density, obtaining the virial coefficients B_n as seen in the pressure (2.50) and free energy (2.52) expansions. From the explicit form of the partition function (2.23) we can write the density as

$$\rho = \frac{z}{V} \frac{\partial(\ln \Xi)}{\partial z},$$

or using the cluster expansion for $\ln \Xi$ stated above we obtain

$$\rho = \sum_{n=1}^{\infty} n b_n z^n.$$

This expression, connecting density and fugacity, can be used to transform the expansion in fugacity to one in density, giving the first few virial coefficients

$$\begin{aligned} B_2 &= -b_2, \\ B_3 &= 4b_2^2 - 2b_3, \\ B_4 &= -20b_2^3 + 18 b_2 b_3 - 3 b_4. \end{aligned}$$

The virial coefficients

Further cancellations occur after inserting the explicit expressions for the cluster integrals (2.58) into the previous coefficients. This remaining terms consist only of the *stars*[35]: those diagrams which cannot be disconnected by deleting a single vertex. We obtain the first few virial coefficients as

$$B_2 = -\frac{1}{2}$$ 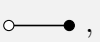 , (2.60a)

$$B_3 = -\frac{2}{3!}$$  , (2.60b)

$$B_4 = -\frac{3}{4!}\left(3\right.$$  $+ 6$  $+$  $\left.\right)$. (2.60c)

and more generally [12, 13]

$$B_n = -\frac{n-1}{n!V}\int_{V^n}\sum\left(\text{all } \textit{stars} \text{ with } n \text{ vertices}\right) d\mathbf{r}^n \tag{2.61}$$

[35] These are also called the *irreducible diagrams* because they cannot be expressed as products of other diagrams. In graph theoretic terms, these diagrams would be described as *2-vertex connected*.

In the above derivation we only considered a single-component system, however the generalisation to mixtures is straightforward. Considering an m-component mixture we label each species with index $s \in \{1, \cdots, m\}$. The virial coefficients generalise to [13]

$$B_n = \sum_{s_1=1}^{m} \cdots \sum_{s_n=1}^{m} B_{s_1,\cdots,s_n} \prod_{i=1}^{n} x_{s_i} \tag{2.62}$$

where x_i is the mole fraction of species i such that $x_i > 0$ and $\sum_{i=1}^{m} x_i = 1$. $B_{s_1,\cdots,s_n}$ are the composition independent virial coefficients describing the contribution from interactions between n particles of species $\{s_1, \cdots, s_n\}$. In the next section we will discuss important restrictions obtained by requiring self-consistency in the limit of continuous mixtures $m \to \infty$.

2.2.5 Truncatability of the free energy: a requirement for self-consistency

Thermodynamic consistency of the (osmotic) pressure requires

$$\beta p = \rho - \beta f^{\text{ex}} + \rho\left(\frac{\partial \beta f^{\text{ex}}}{\partial \rho}\right)_{V,T}, \tag{2.63a}$$

$$= \rho - \beta f^{\text{ex}} + \rho\sum_{i=1}^{m} x_i\left(\frac{\partial \beta f^{\text{ex}}}{\partial x_i}\right)_{V,T}. \tag{2.63b}$$

The latter line, valid in the case of discrete mixtures, becomes poorly defined in the *polydisperse* limit $m \to \infty$ with $x_i \to 0$. A general requirement to remain well-defined in this limit is thus that composition dependence should enter only through a (finite) set of *weighted densities* [61–64], e.g. a set $\{\xi_1, \cdots, \xi_M\}$ so that

$$\beta p = \rho - \beta f^{\text{ex}} + \rho\sum_{k=1}^{M} \xi_k\left(\frac{\partial \beta f^{\text{ex}}}{\partial \xi_k}\right)_{V,T}, \tag{2.64}$$

with weighted densities adopting the form

$$\xi_k = \rho \sum_i x_i f_k(\sigma_i),$$

where $f_k(\cdot)$ is the probability measure describing the size distribution. In the limit of continuous distributions the weighted densities become integrals

$$\xi_k = \rho \int f_k(\sigma) d\mu(\sigma) \tag{2.65}$$

introducing the probability measure $\mu(\sigma)$ for the molarities of particle species such that $\int d\mu(\sigma) = 1$. (2.64) remains well-defined in this limit so long as there are a finite set of weighted densities.

This concludes our summary of liquid state theory for homogeneous systems. In subsequent sections we will review its extensions to inhomogeneous systems, with the purpose of introducing the main framework we will use for our treatment of correlations inside the homogeneous liquid in chapters 4, 5 and 6.

2.3 Classical density functional theory

Classical density functional theory is a general framework for describing inhomogeneous systems. Although our primary focus will be the homogeneous liquid, many useful results can be obtained from an inhomogeneous description. We will work primarily from the classic texts Refs. [65–67], although we found Refs. [12, 68] to be helpful supplementary texts.

Our intention in this section is to provide more exposition on the various correlation functions which are important for liquid state physics, as well as historical context for the *morphometric approach* which will be the focus of chapters 4, 5 and 6. For the latter goal we will introduce its historical antecedent, fundamental measure theory, in section 2.3.4. The morphometric approach will be fully described in subsequent chapters, so we will introduce it here only to provide further context.

2.3.1 Inhomogeneous generalisations of the thermodynamic potentials

In this section we introduce the inhomogeneous generalisations of the thermodynamic potentials introduced in section 2.2.1. These generalisations will provide a route to a fully inhomogeneous theory of fluids, with many useful applications to correlations within the homogeneous fluid.

For inhomogeneous systems the Legendre transform of Ω (2.27) generalises to

$$\Omega = F - \int \rho^{(1)}(\mathbf{r}) \mu \, d\mathbf{r}. \tag{2.66}$$

Subtracting external potential contributions from the Helmholtz free energy defines an *intrinsic free energy* containing contributions arising solely from the internal interactions, i.e.

$$\mathcal{F} = F - \int \rho^{(1)}(\mathbf{r}) \phi_{\text{ext}}(\mathbf{r}) \, d\mathbf{r} \tag{2.67}$$

so that the grand potential becomes

$$\begin{aligned}\Omega &= \mathcal{F} - \int \rho^{(1)}(\mathbf{r})(\mu - \phi_{\text{ext}}(\mathbf{r}))\, d\mathbf{r} \\ &= \mathcal{F} - \int \rho^{(1)}(\mathbf{r})\psi(\mathbf{r})\, d\mathbf{r}\end{aligned} \tag{2.68}$$

where we defined the *intrinsic chemical potential* $\psi(\mathbf{r}) = \mu - \phi_{\text{ext}}(\mathbf{r})$ in the final step.

Furthermore, the intrinsic free energy can be decomposed into an *ideal* and *excess* part as in

$$\mathcal{F} = \mathcal{F}^{\text{id}} + \mathcal{F}^{\text{ex}}. \tag{2.69}$$

The excess component emerges as from the interactions between particles and in general it is intractably hard to determine this exactly except in special limits (e.g. in the one-dimensional limit). As such, approximate forms for $\mathcal{F}^{\text{ex}}$ must be used in general which constrains the success of applications of DFT to the accuracy of this contribution. By contrast, the ideal component can be computed explicitly. For an ideal gas, the absence of particle interactions leads to

$$U_N = \sum_{i=1}^{N} \phi_{\text{ex}}(\mathbf{r}_i)$$

and the partition function is easily calculated giving

$$\Xi^{\text{id}} = \sum_{N=0}^{\infty} \frac{(zZ_1)^N}{N!} = \exp\left(\frac{Z_1 e^{\beta\mu}}{\Lambda^d}\right), \tag{2.70}$$

with single-particle partition function

$$Z_1 = \int e^{-\beta\phi_{\text{ext}}(\mathbf{r}')}\, d\mathbf{r}'.$$

Then, following Ref. [68], we write the equilibrium single-particle density as

$$\begin{aligned}\rho^{(1)}(\mathbf{r}) &= \left\langle \sum_{i=1}^{N} \delta(\mathbf{r} - \mathbf{r}_i) \right\rangle \\ &= \frac{1}{\Xi} \sum_{N=0}^{\infty} \frac{z^N}{N!} \int_{V^N} \sum_{i=1}^{N} \Big(\delta(\mathbf{r} - \mathbf{r}_i)\Big) e^{-\beta U_N}\, d\mathbf{r}^N, \\ &= \frac{1}{\Xi} \sum_{N=0}^{\infty} \frac{z^N}{N!} N e^{-\beta\phi_{\text{ext}}(\mathbf{r})} Z_1^{N-1}\end{aligned}$$

using the definition of the thermal average (2.24) in the second line. Comparison with (2.70) above yields the simplified form

$$\rho^{(1)}(\mathbf{r}) = \frac{\langle N \rangle e^{-\beta\phi_{\text{ext}}(\mathbf{r})}}{\int e^{-\beta\phi_{\text{ext}}(\mathbf{r}')}\, d\mathbf{r}'} = \frac{e^{-\beta(\phi_{\text{ext}}(\mathbf{r}) - \mu)}}{\Lambda^d}. \tag{2.71}$$

We can express the grand potential for the non-interacting system as a functional of the external potential from the partition function (2.70) as

$$\beta\Omega^{\text{id}} = -\ln \Xi^{\text{id}} = -\int \frac{e^{-\beta(\phi_{\text{ext}}(\mathbf{r}) - \mu)}}{\Lambda^d} d\mathbf{r}$$

or in its dual form as a functional of density (2.68) as

$$\beta\Omega^{\mathrm{id}} = \beta\mathcal{F}^{\mathrm{id}} - \int \rho^{(1)}(\mathbf{r})\beta\psi(\mathbf{r})\, d\mathbf{r}.$$

Equating these two forms and rearranging we find the ideal part of the Helmholtz free energy as

$$\begin{aligned}\beta\mathcal{F}^{\mathrm{id}} &= -\int \left(\rho^{(1)}(\mathbf{r})\beta(\phi_{\mathrm{ext}}(\mathbf{r}) - \mu) + \frac{e^{-\beta(\phi_{\mathrm{ext}}(\mathbf{r})-\mu)}}{\Lambda^d}\right) d\mathbf{r} \\ &= \int \rho^{(1)}(\mathbf{r}) \left(\ln\left(\Lambda^d \rho^{(1)}(\mathbf{r})\right) - 1\right) d\mathbf{r} \end{aligned} \tag{2.72}$$

using the ideal density (2.71) in the final step. The inhomogeneous ideal gas free energy density is thus identical to the homogeneous case (2.28) after replacing the global density with a local one.

Armed with functional generalisations of the thermodynamic potentials we can begin to describe the inhomogeneous liquid. Our focus will be on correlations within the equilibrium liquid, so in the next section we will directly connect the thermodynamic functionals to the correlations functions.

2.3.2 Thermodynamic potentials as generating functionals

Having defined thermodynamic potentials for an inhomogeneous system as functionals, we can make a connection to liquid structure through the various correlation functions. In sections 2.2.2 and 2.2.4 we saw how the homogeneous correlation functions could be obtained from various generating functions. In the inhomogeneous liquid, correlation functions are obtained in a similar way using *generating functionals*.

The fundamental thermodynamic relation describing an infinitesimal change in the Helmholtz free energy, i.e.

$$dF = -SdT - pdV + \mu dN,$$

generalises to an inhomogeneous system as

$$\delta F = -S\delta T + \int \rho^{(1)}(\mathbf{r})\delta\phi_{\mathrm{ext}}(\mathbf{r})\, d\mathbf{r} + \int \mu\delta\rho^{(1)}(\mathbf{r})\, d\mathbf{r}$$

The change in the intrinsic free energy is then

$$\begin{aligned}\delta\mathcal{F} &= \delta F - \int \delta\rho^{(1)}(\mathbf{r})\phi_{\mathrm{ext}}(\mathbf{r})\, d\mathbf{r} - \int \rho^{(1)}(\mathbf{r})\delta\phi_{\mathrm{ext}}(\mathbf{r})\, d\mathbf{r} \\ &= -S\delta T + \int \delta\rho^{(1)}(\mathbf{r})\psi(\mathbf{r})\, d\mathbf{r}. \end{aligned} \tag{2.73}$$

By similar steps, or using the Legendre transform of the grand potential (2.27), it follows that

$$\delta\Omega = -S\delta T - \int \rho^{(1)}(\mathbf{r})\delta\psi(\mathbf{r})\, d\mathbf{r} \tag{2.74}$$

Hence, from functional differentiation of (2.73) and (2.74) it follows that

$$\frac{\delta \mathcal{F}}{\delta \rho^{(1)}(\mathbf{r})} = \psi(\mathbf{r}), \tag{2.75}$$

$$\frac{\delta \Omega}{\delta \psi(\mathbf{r})} = -\rho^{(1)}(\mathbf{r}), \tag{2.76}$$

i.e. the intrinsic free energy and grand potentials act as *generating functionals* for the intrinsic chemical potential and density respectively.

Repeated functional differentiation of the thermodynamic potentials produces a whole hierarchy of correlation functions. The hierarchy obtained from the grand potential gives the density-density correlations which we already introduced in (2.36); these are generated by the grand potential as [12]

$$H^{(n)}(\mathbf{r}^n) = -\frac{\delta^n \beta \Omega}{\delta\beta\psi(\mathbf{r}_1)\cdots\delta\beta\psi(\mathbf{r}_n)} = \frac{\delta^{n-1}\rho^{(1)}(\mathbf{r}_1)}{\delta\beta\psi(\mathbf{r}_2)\cdots\delta\beta\psi(\mathbf{r}_n)}. \tag{2.77}$$

The intrinsic free energy also generates a new hierarchy of correlation functions, however the contribution from the ideal part is not especially interesting. We thus define the *direct correlation functions* as the hierarchy generated from the excess part as

$$c^{(n)}(\mathbf{r}^n) = -\frac{\delta^n \beta \mathcal{F}^{\mathrm{ex}}}{\delta\rho^{(1)}(\mathbf{r}_1)\cdots\delta\rho^{(1)}(\mathbf{r}_n)}. \tag{2.78}$$

These correlation functions form the basis of integral equation theories which we will outline in the next section.

2.3.3 Equilibrium conditions

In the preceding sections we defined the thermodynamic potentials for an inhomogeneous system in equilibrium with density profile $\rho(\mathbf{r}) = \rho^{(1)}(\mathbf{r})$. However, we can imagine the generalisation where the equilibrium profile $\rho^{(1)}(\mathbf{r})$ is replaced by an arbitrary $\rho(\mathbf{r})$ so

$$\begin{aligned}\Omega &\to \Omega[\rho(\mathbf{r})],\\ \mathcal{F}^{\mathrm{id}} &\to \mathcal{F}^{\mathrm{id}}[\rho(\mathbf{r})],\\ \mathcal{F}^{\mathrm{ex}} &\to \mathcal{F}^{\mathrm{ex}}[\rho(\mathbf{r})].\end{aligned}$$

These generalised functionals are not strictly the same as the thermodynamic potentials, which only concern equilibrium properties, but there is an important correspondence between them. Focusing on the grand potential, the following two properties are provable[36]:

1. It is bounded from below by the grand potential, i.e.

$$\Omega[\rho(\mathbf{r})] \geq \Omega.$$

2. Equality with the grand potential occurs *only* in the case of the equilibrium density profile, i.e.

$$\Omega[\rho^{(1)}(\mathbf{r})] = \Omega.$$

[36] Full accounts of the classical arguments can be found in Refs. [65, 69], and a more compact argument has recently been formulated in Ref. [70].

These two properties can be elegantly captured by the *variational principle*

$$\left.\frac{\delta\Omega}{\delta\rho^{(1)}(\mathbf{r})}\right|_{\rho(\mathbf{r})=\rho^{(1)}(\mathbf{r})} = 0, \tag{2.79}$$

which provides the route to numerical applications of DFT; minimisation of the grand potential with respect to density is sufficient to determine the equilibrium density profile and its corresponding free energy.

To bring the variational principle to more practical use we can insert the functional form of Ω deduced in section 2.3.1 into (2.79) giving

$$\frac{\delta\mathcal{F}}{\delta\rho^{(1)}(\mathbf{r})} - \psi(\mathbf{r}) = \int \rho^{(1)}(\mathbf{r}')\frac{\delta\psi(\mathbf{r}')}{\delta\rho^{(1)}(\mathbf{r})}\,d\mathbf{r}'.$$

The separate condition (2.75) causes the first two terms to cancel, leading to the two equilibrium conditions

$$\frac{\delta\mathcal{F}^{\mathrm{id}}[\rho(\mathbf{r})]}{\delta\rho(\mathbf{r}')} + \frac{\delta\mathcal{F}^{\mathrm{ex}}[\rho(\mathbf{r})]}{\delta\rho(\mathbf{r}')} = \psi(\mathbf{r}'), \tag{2.80a}$$

$$\int \rho^{(1)}(\mathbf{r})\frac{\delta\psi(\mathbf{r})}{\delta\rho^{(1)}(\mathbf{r}')}\,d\mathbf{r} = 0, \tag{2.80b}$$

of which the first is most useful. The first functional derivative of the ideal intrinsic free energy (2.72) yields

$$\frac{\delta\beta\mathcal{F}^{\mathrm{id}}}{\delta\rho^{(1)}(\mathbf{r})} = \ln\left(\Lambda^d\rho^{(1)}(\mathbf{r})\right),$$

and using (2.78) we obtain

$$\ln\left(\Lambda^d\rho^{(1)}(\mathbf{r})\right) - c^{(1)}(\mathbf{r}) = \psi(\mathbf{r})$$

or rearranged for the density

$$\rho^{(1)}(\mathbf{r}) = \frac{\exp\left(\beta\psi(\mathbf{r}) + c^{(1)}(\mathbf{r})\right)}{\Lambda^d}. \tag{2.81}$$

This equation provides the basis for iterative schemes to solve (2.79) (see e.g. [26]). Importantly, this process incorporates an arbitrary external potential inside $\psi(\mathbf{r})$ which could represent e.g. a test-particle inserted into the liquid so that the grand potential represents a chemical potential. This example provides a potential way of using an inhomogeneous framework to approach the homogeneous liquid, illustrating the usefulness of the DFT formalism.

Further functional derivatives of the equilibrium condition provides a whole hierarchy of equivalent equilibrium criteria. Of particular note is the next equation in the hierarchy, the Ornstein-Zernike equation, which forms the basis for integral theories of the liquid state[37]. This connects the density-density and direct correlation functions through the chain rule of functional calculus, i.e.

$$\delta(\mathbf{r}_1 - \mathbf{r}_2) = \int \frac{\delta\rho^{(1)}(\mathbf{r}_1)}{\delta\beta\psi(\mathbf{r}')}\frac{\delta\beta\psi(\mathbf{r}')}{\delta\rho^{(1)}(\mathbf{r}_2)}\,d\mathbf{r}'. \tag{2.82}$$

[37] Conventionally this class of theories is presented in its own right rather than as a special case of density functional theory; we opted for this more modern presentation to be marginally more economical with chapter length.

The first term appearing in the integrand is simply the pair density-density correlation function $H^{(2)}$ via (2.77), so we will require an explicit expression for the second term to proceed.

We require the functional derivative of $\psi(\mathbf{r})$ corresponding to the second functional derivatives of the intrinsic free energy through (2.80a). To obtain the higher order functional derivatives of the ideal term, it is helpful to write it as an integral with a delta function

$$\frac{\delta\beta\mathcal{F}^{\mathrm{id}}}{\delta\rho^{(1)}(\mathbf{r})} = \int \delta(\mathbf{r}' - \mathbf{r}) \ln\left(\Lambda^d \rho^{(1)}(\mathbf{r}')\right) d\mathbf{r}',$$

so we can obtain the second derivative as

$$\frac{\delta^2\beta\mathcal{F}^{\mathrm{id}}}{\delta\rho^{(1)}(\mathbf{r})\delta\rho^{(1)}(\mathbf{r}')} = \frac{\delta(\mathbf{r}' - \mathbf{r})}{\rho^{(1)}(\mathbf{r})}.$$

Functional differentiation of (2.80a) then yields

$$\frac{\delta\beta\psi(\mathbf{r})}{\delta\rho^{(1)}(\mathbf{r}')} = \frac{\delta(\mathbf{r} - \mathbf{r}')}{\rho^{(1)}(\mathbf{r}')} - c^{(2)}(\mathbf{r}, \mathbf{r}').$$

using the definition of the direct correlation function (2.78) in the latter step. Inserting this expression into (2.82) gives

$$\delta(\mathbf{r}_1 - \mathbf{r}_2) = \int H^{(2)}(\mathbf{r}_1, \mathbf{r}') \left(\frac{\delta(\mathbf{r}' - \mathbf{r}_2)}{\rho^{(1)}(\mathbf{r}')} - c^{(2)}(\mathbf{r}', \mathbf{r}_2) \right) d\mathbf{r}'$$

which upon inserting the definition of $H^{(2)}$ from (2.35b) rearranges to give the Ornstein-Zernike equation

$$h^{(2)}(\mathbf{r}_1, \mathbf{r}_2) = c^{(2)}(\mathbf{r}_1, \mathbf{r}_2) + \int \rho^{(1)}(\mathbf{r}') h^{(2)}(\mathbf{r}_1, \mathbf{r}') c^{(2)}(\mathbf{r}', \mathbf{r}_2)\, d\mathbf{r}', \tag{2.83}$$

which is a classic result of liquid state theory (cf. Refs. [12, 65, 71]).

Ornstein-Zernike equation for a uniform simple liquid

For a uniform liquid interacting through a spherically symmetric pair potential the Ornstein-Zernike equation becomes

$$\begin{aligned} h^{(2)}(r) &= c^{(2)}(r) + \rho \int h^{(2)}(r') c^{(2)}(|\mathbf{r}' - \mathbf{r}|)\, d\mathbf{r}' \\ &= c^{(2)}(r) + \rho \left(h^{(2)} * c^{(2)}\right)(r), \end{aligned} \tag{2.84}$$

where $r = |\mathbf{r}_2 - \mathbf{r}_1|$ and $(f * g)(\mathbf{r})$ denotes a convolution between functions f and g. In Fourier space the convolution becomes

$$\widetilde{h}^{(2)}(\mathbf{k}) = \widetilde{c}^{(2)}(\mathbf{k}) + \rho\, \widetilde{h}^{(2)}(\mathbf{k}) \widetilde{c}^{(2)}(\mathbf{k})$$

where a tilde over a function denotes its Fourier transform. This rearranges to give

$$\widetilde{h}^{(2)}(\mathbf{k}) = \frac{\widetilde{c}^{(2)}(\mathbf{k})}{1 - \rho\widetilde{c}^{(2)}(\mathbf{k})}$$

which gives the static structure factor (2.40) as

$$S^{(2)}(\mathbf{k}) = \rho\delta(\mathbf{k}) + \frac{1}{1 - \rho\widetilde{c}^{(2)}(\mathbf{k})}.$$

If the pair direct correlation function is known, it is thus straightforward to obtain the equation of state through the compressibility route (2.44)

$$\frac{\beta p}{\rho} = 1 - \frac{1}{\rho}\int_0^\rho \widetilde{c}^{(2)}(0)\rho' d\rho'.$$

The main task in an integral equation approach is to find an approximate closure for $c^{(2)}$ in order to solve the Ornstein-Zernike equation. The process of determining the direct correlation functions is equivalent (at least formally) to finding its generating functional $\mathcal{F}^{\text{ex}}$.

2.3.4 Fundamental measure theory

DFT provides an elegant framework for treating the inhomogeneous liquid, however as we have shown any application is limited by the accuracy of the (excess) intrinsic free energy. It is generally difficult to derive accurate approximations to $\mathcal{F}^{\text{ex}}$; however, for hard spheres[38] it is possible to exploit ideas from integral geometry (section 2.1) and derive a highly accurate class of free energy functionals. In this section we describe fundamental measure theory (FMT), which provides the most successful theory for inhomogeneous hard particle systems. We mainly follow Refs. [26, 79], but we mention also the review [80] which has more of a focus on crystallisation.

[38] We concentrate on hard spheres here, however we note that generalisations exist for hard particle systems of more general shapes [72–78]. The more recent works are accurate enough to capture isotropic–nematic transitions in the fluid.

To introduce this topic we will first consider the free energy of the homogeneous system, and then generalise to the inhomogeneous one. Noting that the free energy is determined from the free energy density through

$$\beta\mathcal{F}^{\text{ex}} = \int_V \beta f^{\text{ex}}\, d\mathbf{r},$$

we can draw a correspondence with the virial series expression for the free energy density (2.52). Using the virial coefficients for an m-component mixture (6.3), the free energy density in the dilute limit becomes[39]

$$\beta f^{\text{ex}} = -\frac{\rho^2}{2}\sum_{i=1}^m\sum_{j=1}^m x_i x_j \int_V f_{ij}(\mathbf{r})\, d\mathbf{r} + \mathcal{O}(\rho^3).$$

[39] In this step we are implicitly focusing on systems interacting through pair potentials, where the virial coefficients introduced in section 2.2.4 are valid.

We consider mixtures of hard spheres of radii R_i, so the Mayer function f_{ij} must depend on R_i and R_j. The Mayer function for the hard sphere interaction (1.1) is purely geometric in nature, i.e.

$$-f_{ij}(\mathbf{r}) = \Theta(R_i + R_j - |\mathbf{r}|)$$

where $\Theta(\cdot)$ is the Heaviside theta function. This can be recast into the revealing form

$$\begin{aligned} -f_{ij} &= \begin{cases} 0 & \text{if } \mathcal{B}_i \cap \mathcal{B}_j = \varnothing \\ 1 & \text{if } \mathcal{B}_i \cap \mathcal{B}_j \neq \varnothing \end{cases} \\ &= \chi[\mathcal{B}_i \cap \mathcal{B}_j] \end{aligned}$$

i.e. the Euler characteristic of their intersection. This allows us to write the free energy density in the dilute limit for a homogeneous system as

$$\beta f^{\text{ex}} = \frac{\rho^2}{2}\sum_{i=1}^m\sum_{j=1}^m x_i x_j \int_V \chi[\mathcal{B}_i \cap \mathcal{B}_j(\mathbf{r})]\, d\mathbf{r} + \mathcal{O}(\rho^3),$$

or in the notation introduced in section 2.1

$$\beta f^{\text{ex}} = \frac{\rho^2}{2} \sum_{i=1}^{m} \sum_{j=1}^{m} x_i x_j \int_{G_d} \chi[\mathcal{B}_i \cap g\mathcal{B}_j]\, dg + \mathcal{O}(\rho^3)$$

which can be evaluated using the principal kinematic formula (2.16). Each integral results in $d+1$ terms featuring the intrinsic volumes of the respective particles; we can expect a similar decomposition in the inhomogeneous case.

It is straightforward to generalise the virial series to inhomogeneous systems by localising the the density terms, i.e. making the replacement $\rho^n \to \rho(\mathbf{r}_1) \cdots \rho(\mathbf{r}_n)$, and bringing them inside the cluster integrals [81, 82]. The low density free energy then adopts the form

$$\beta \mathcal{F}^{\text{ex}}[\{\rho_i\}] = -\frac{1}{2} \sum_{i=1}^{m} \sum_{j=1}^{m} \int_{V^2} \rho_i(\mathbf{r}) \rho_j(\mathbf{r}') f_{ij}(\mathbf{r} - \mathbf{r}')\, d\mathbf{r} d\mathbf{r}' + \mathcal{O}(\rho^3). \quad (2.85)$$

Inspired by the intrinsic volumes and the principal kinematic formula, Rosenfeld observed that Mayer function in $d = 3$ could be *exactly* decomposed into variants of the intrinsic volumes[40] [25]

$$\begin{aligned} -f_{ij}(\mathbf{r}) = \quad & \omega_i^{(0)} \otimes \omega_j^{(3)} + \omega_i^{(1)} \otimes \omega_j^{(2)} + \omega_i^{(2)} \otimes \omega_j^{(1)} + \omega_i^{(3)} \otimes \omega_j^{(0)} \\ & - \boldsymbol{\omega}_i^{(1)} \otimes \boldsymbol{\omega}_j^{(2)} - \boldsymbol{\omega}_i^{(2)} \otimes \boldsymbol{\omega}_j^{(1)} \end{aligned}$$

[40] Rosenfeld called these *fundamental measures* giving the theory its name.

introducing the weight functions

$$\omega_3^i(\mathbf{r}) = \Theta(R_i - r), \quad (2.86a)$$

$$\omega_2^i(\mathbf{r}) = \delta(R_i - r), \quad (2.86b)$$

$$\omega_1^i(\mathbf{r}) = \frac{\omega_2^i(\mathbf{r})}{4\pi R_i}, \quad (2.86c)$$

$$\omega_0^i(\mathbf{r}) = \frac{\omega_2^i(\mathbf{r})}{4\pi R_i^2}, \quad (2.86d)$$

$$\boldsymbol{\omega}_2^i(\mathbf{r}) = \frac{\mathbf{r}}{r} \delta(R_i - r), \quad (2.86e)$$

$$\boldsymbol{\omega}_1^i(\mathbf{r}) = \frac{\boldsymbol{\omega}_1^i(\mathbf{r})}{4\pi R_i}. \quad (2.86f)$$

The appearance of the weight functions inside the free energy (2.85) through the Mayer function naturally leads to convolutions with the density. This gives rise to a set of *weighted densities* defined as [25, 83]

$$n_\alpha(\mathbf{r}) = \sum_{i=1}^{m} \int_V \rho_i(\mathbf{r}')\, \omega_\alpha^i(\mathbf{r} - \mathbf{r}')\, d\mathbf{r}' \quad (2.87)$$

where we use shorthand such that α indexes both the scalar and vector weight functions. The low density excess free energy becomes a local function of the (nonlocal) weighted densities, as in

$$\beta \mathcal{F}^{\text{ex}}[\{\rho_i\}] = \int_V \Big(n_0(\mathbf{r}) n_3(\mathbf{r}) + n_1(\mathbf{r}) n_2(\mathbf{r}) - \mathbf{n}_1(\mathbf{r}) \cdot \mathbf{n}_2(\mathbf{r}) \Big) d\mathbf{r} + \mathcal{O}(\rho^2).$$

Fortuitously, all of the molarity information has been absorbed into the definition of the weighted densities, so the final form contains no explicit

mixture dependence; this is an example of a truncatable free energy (section 2.2.5).

To generalise the exact dilute limit result to arbitrary densities, we postulate that the free energy remains a functional of density *only* through the weighted densities $\{n_\alpha\}$: this is the central assumption of FMT. This assumption can be expressed as the *ansatz*

$$\beta\mathcal{F}^{\text{ex}}[\{\rho_i\}] = \beta\mathcal{F}^{\text{ex}}[\{n_\alpha\}] = \int_V \beta f^{\text{ex}}(\{n_\alpha\})\, d\mathbf{r}, \tag{2.88}$$

which is postulated to be exact for all densities. To determine approximate functionals of the above form, we start by writing the chemical potential of species i as

$$\beta\mu_i^{\text{ex}} = \left(\frac{\partial\beta f^{\text{ex}}}{\partial\rho_i}\right)_{V,T}. \tag{2.89}$$

In the large particle limit the chemical potential is simply the work required to create a cavity large enough to contain the particle[41], i.e. [84, 85]

$$\lim_{V_i\to\infty} \frac{\beta\mu_i^{\text{ex}}}{V_i} = \beta p. \tag{2.90}$$

[41] We will formally derive this property in the context of many-body correlations in section 4.2.

For concentration dependence which enters only through a finite set of weight functions we have

$$\frac{\partial}{\partial\rho_i} = \sum_\alpha \frac{\partial n_\alpha}{\partial\rho_i}\frac{\partial}{\partial n_\alpha},$$

of which the explicit differentials give

$$\frac{\partial n_3}{\partial\rho_i} = \frac{4\pi R_i^3}{3}, \tag{2.91a}$$

$$\frac{\partial n_2}{\partial\rho_i} = 4\pi R_i^2, \tag{2.91b}$$

$$\frac{\partial n_1}{\partial\rho_i} = R_i, \tag{2.91c}$$

$$\frac{\partial n_0}{\partial\rho_i} = 1, \tag{2.91d}$$

and similar expressions for the vectorial terms. In the large volume limit the n_3 term dominates leading to

$$\lim_{V_i\to\infty} \frac{\partial}{\partial\rho_i} = V_i\frac{\partial}{\partial n_3}$$

so it follows from (2.89) and (2.90) that

$$\beta p = \frac{\partial\beta f^{\text{ex}}}{\partial n_3}. \tag{2.92}$$

Secondly, we find the derivative with respect to density reduces to

$$\frac{\partial}{\partial\rho} = \sum_i \frac{\partial\rho_i}{\partial\rho}\frac{\partial}{\partial\rho_i} = \frac{1}{\rho}\sum_\alpha n_\alpha\frac{\partial}{\partial n_\alpha}.$$

Combining these two expressions leads to the scaled particle[42] differential equation [25]

$$(1-n_3)\frac{\partial f^{\text{ex}}}{\partial n_3} = n_0 - f^{\text{ex}} + \sum_{\alpha=0}^{2} n_\alpha \frac{\partial f^{\text{ex}}}{\partial n_\alpha} \tag{2.93}$$

In Refs. [79, 86] it was shown that the solution to (2.93) which correctly recovers the low density behaviour and maximises self-consistency for mixtures must have the generic form

$$\beta f^{\text{ex}}(\Psi) = \beta f_1^{\text{ex}} + \beta f_2^{\text{ex}} + \beta f_3^{\text{ex}} + \beta f_2^{\text{ex}} \Psi\left(\frac{2f_3^{\text{ex}}}{f_2^{\text{ex}}}\right), \tag{2.94}$$

with

$$\beta f_1^{\text{ex}} = -n_0 \ln(1-n_3), \tag{2.95a}$$

$$\beta f_2^{\text{ex}} = \frac{n_1 n_2 - \mathbf{n}_1 \cdot \mathbf{n}_2}{1-n_3}, \tag{2.95b}$$

$$\beta f_3^{\text{ex}} = \frac{n_2^3 - 3n_2\, \mathbf{n}_2 \cdot \mathbf{n}_2}{24\pi(1-n_3)^2}. \tag{2.95c}$$

This defines a whole class of self-consistent free energy functionals which differ only by the choice of function Ψ which corresponds to fixing the free energy density of the bulk liquid. The simplest functional in this class is the Rosenfeld (RF) functional which takes $\Psi_{\text{RF}}(\cdot) = 0$. Written explicitly the resulting free energy density is then [25]

$$\beta f_{\text{RF}}^{\text{ex}} = -n_0 \ln(1-n_3) + \frac{n_1 n_2 - \mathbf{n}_1 \cdot \mathbf{n}_2}{1-n_3} + \frac{n_2^3 - 3n_2 \mathbf{n}_2 \cdot \mathbf{n}_2}{24\pi(1-n_3)^2}. \tag{2.96}$$

From their definition as functional derivatives of the excess free energy (2.78), we find that direct correlation functions for FMT functionals must generically adopt the form of [25]

$$c^{(n)}(\mathbf{r}^n; f^{\text{ex}}) = -\sum_{\alpha_1,\cdots,\alpha_n} \int d\mathbf{r}' \prod_{i=1}^{n} \Big(\omega_{\alpha_i}(\mathbf{r}' - \mathbf{r}_i)\Big) \partial^n_{\alpha_1,\cdots,\alpha_n} \beta f^{\text{ex}}(\mathbf{r}') \tag{2.97}$$

where we use the shorthand

$$\partial^n_{\alpha_1,\cdots,\alpha_n} \beta f^{\text{ex}}(\mathbf{r}) = \left.\frac{\partial^n \beta f^{\text{ex}}}{\partial n_{\alpha_1} \cdots \partial n_{\alpha_n}}\right|_{\{n_\alpha\}=\{n_\alpha(\mathbf{r})\}}.$$

At uniform density $\partial^n_{\alpha_1,\cdots,\alpha_n} \beta f^{\text{ex}}$ is position independent. We define

$$\chi_{\alpha_1,\cdots,\alpha_n}(f^{\text{ex}}) = \left.\frac{\partial^n \beta f^{\text{ex}}}{\partial n_{\alpha_1} \cdots \partial n_{\alpha_n}}\right|_{\{n_\alpha(\mathbf{r})\}=\{\xi_\alpha\}} \tag{2.98}$$

where their values in the bulk, the so-called the *scaled particle variables*[43],

[42] We will leave discussion of scaled particle theory until chapter 4 where we describe it in detail.

[43] Again, we sidestep discussion of this naming convention here as we will discuss scaled particle theory in detail in chapter 4.

can be obtained from (2.91) as [87]

$$\xi_3 = \rho \sum_{i=1}^{m} x_i \, \frac{4\pi R_i^3}{3}, \tag{2.99a}$$

$$\xi_2 = \rho \sum_{i=1}^{m} x_i \, 4\pi R_i^2, \tag{2.99b}$$

$$\xi_1 = \rho \sum_{i=1}^{m} x_i \, R_i, \tag{2.99c}$$

$$\xi_0 = \rho. \tag{2.99d}$$

Each of the scaled particle variables correspond to moments of the size distribution, so this is an example of a truncatable theory which remains physically well-posed in the limit of continuous mixtures (see section 2.2.5). The direct correlation functions (2.97) in the uniform liquid become [88]

$$\begin{aligned} c^{(n)}(\mathbf{r}^n; f^{\text{ex}}) &= - \sum_{\alpha_1,\cdots,\alpha_n} \chi_{\alpha_1,\cdots,\alpha_n}(f^{\text{ex}}) \int d\mathbf{r}' \prod_{i=1}^{n} \Big(\omega_{\alpha_i}(\mathbf{r}' - \mathbf{r}_i) \Big) \\ &= - \sum_{\alpha_1,\cdots,\alpha_n} \chi_{\alpha_1,\cdots,\alpha_n}(f^{\text{ex}}) \, (\omega_{\alpha_1} \otimes \cdots \otimes \omega_{\alpha_n})(\mathbf{r}^n). \end{aligned} \tag{2.100}$$

Percus-Yevick theory in hard spheres

Inserting the Rosenfeld free energy density (2.96) into (2.88) yields the functional $\beta\mathcal{F}^{\text{ex}}_{\text{RF}}$. Taking the second functional derivative of this using (2.100) for the single-component system $R_i + R_j = 2R = \sigma$ yields the Percus-Yevick direct correlation function [89, 90]

$$\begin{aligned} c^{(2)}_{\text{PY}}(r) = -\frac{\delta^2 \beta \mathcal{F}^{\text{ex}}_{\text{RF}}}{\delta\rho(\mathbf{r})\delta\rho(\mathbf{r}')} = &- \chi_{3,3}(f^{\text{ex}}_{\text{RF}})\Delta V(r) - \chi_{3,2}(f^{\text{ex}}_{\text{RF}})\Delta A(r) \\ &- \chi_{3,1}(f^{\text{ex}}_{\text{RF}})\Delta L(r) \end{aligned} \tag{2.101}$$

where $r = |\mathbf{r} - \mathbf{r}'|$ and $\Delta V, \Delta A, \Delta L$ are the intrinsic volumes for the region where the two spheres overlap. With an exact form of the direct correlation function it is straightforward to determine the pair distribution function $g^{(2)}(r)$ from solving the Ornstein-Zernike equation (2.84). The equation of state can then be determined through the virial route (2.47) giving

$$\frac{\beta p^{\text{PY-V}}}{\rho} = \frac{1 + \eta + \eta^2 - 3\eta^3}{(1-\eta)^3}, \tag{2.102}$$

or through the compressibility route (2.44) giving

$$\frac{\beta p^{\text{PY-C}}}{\rho} = \frac{1 + \eta + \eta^2}{(1-\eta)^3}. \tag{2.103}$$

The latter route is more accurate and also consistent with the pressure of the Rosenfeld functional (2.96) through (2.92) and the scaled particle differential equation[44] (2.93).

[44] In chapter 4 we will refer to this as the scaled particle theory/Percus-Yevick (SPT/PY) equation of state because of this correspondence.

Curiously, an empirical interpolation between the two solutions of the Percus-Yevick theory yields the highly accurate Carnahan-Starling (CS) equation of state [15]

$$\begin{aligned}\frac{\beta p^{\mathrm{CS}}}{\rho} &= \frac{1}{3}\frac{\beta p^{\mathrm{PY-V}}}{\rho} + \frac{2}{3}\frac{\beta p^{\mathrm{PY-C}}}{\rho} \\ &= \frac{1+\eta+\eta^2-\eta^3}{(1-\eta)^3}.\end{aligned} \tag{2.104}$$

We will assume this equation of state to construct an accurate theory for correlations in the hard sphere liquid in chapter 4. However, this equation of state as it predicts a finite pressure until $\eta \to 1$, so given that close packing occurs at $\eta \simeq 0.74$ it *must* fail at high densities.

Crucially, in addition to describing the equilibrium liquid well, the CS equation has been demonstrated to be accurate at very high densities in the supercooled regime [91]. The liquid is metastable above the melting transition, so high density simulations require the introduction of polydispersity to prevent crystallisation; to determine its accuracy the CS equation has to be extended to mixtures. Entering the single-component equation of state (2.104) as an input into the generic FMT solution (2.94) yields a more accurate free energy functional with [79]

$$\Psi_{\mathrm{CS}}(y) = \frac{4}{3} + \frac{y}{3} - \frac{\ln(1+y)}{3y}. \tag{2.105}$$

The resulting free energy functional $f_{\mathrm{CS}}^{\mathrm{ex}}$ then predicts the following equation of state for hard sphere mixtures [79]

$$\beta p^{\mathrm{CS}} = \frac{\xi_0}{1-\xi_3} + \frac{4\xi_1\xi_2}{3(1-\xi_3)^2} + \frac{\xi_2^3}{18\pi(1-\xi_3)^3} - \frac{4\pi\xi_1^2\xi_2}{(\xi_2^2+12\pi\xi_1(1-\xi_3))(1-\xi_3)}, \tag{2.106}$$

with scaled particle variables $\{\xi_i\}$ defined in (2.99). Other extensions of the CS equation of state to mixtures exist[45], however the above equation represents the state of the art [79].

[45] The most popular of which is the Boublik-Mansoori-Carnahan-Starling-Leland equation of state [92, 93], which corresponds to a different FMT functional derived in Refs. [84, 94].

The pressures predicted by (2.106) compare favourably against novel Monte-Carlo simulations of a highly polydipserse hard sphere system [91] at very high densities in Fig. 2.1. To apply the CS equation of state (2.106) for a polydisperse system we must use the generalisations of $\{\xi_i\}$ for continuous mixtures outlined in section 2.2.5. For Fig. 2.1 we had to select the size distribution measure $d\mu(\sigma)$ entering (2.65) to correspond to the system used in Ref. [91]. Specifically, this corresponds to

$$d\mu(\sigma) \propto \begin{cases} \frac{1}{\sigma^3}d\sigma & \sigma \in [0.4492, 1] \\ 0 & \text{otherwise} \end{cases} \tag{2.107}$$

with a proportionality constant to ensure normalisation.

Finally, we introduce the central approximation of chapters 4, 5 and 6 as a limit case of FMT. The chemical potential of a new sphere s can be determined as the free energy of a mixture where the limit where the new

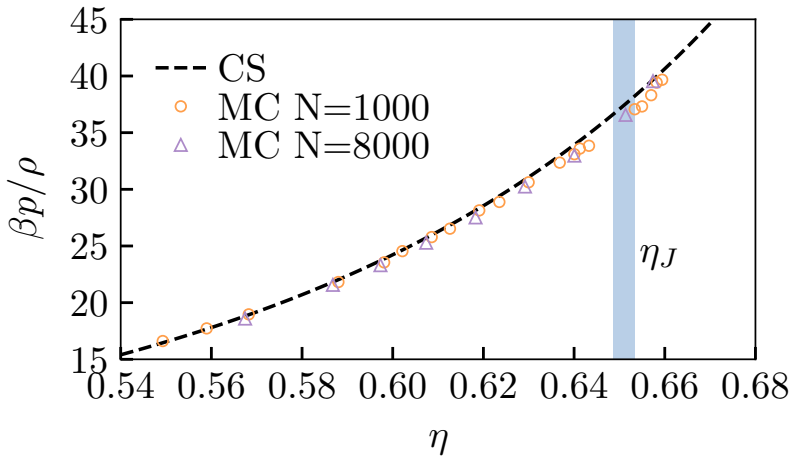

Figure 2.1: Accuracy of empirical Carnahan-Starling (CS) equation of state (2.106) in the supercooled regime from comparison with novel Monte-Carlo (MC) simulations for a system with 23% polydispersity. The size distribution of this system is described by (2.107). The range of jamming volume fractions η_J from non-equilibrium compression protocols with this system are indicated by the blue region. Simulation data and jamming densities reproduced from Ref. [91].

species is infinitely dilute, as in

$$\begin{aligned}\mu_s &= \lim_{\rho_s\to 0}\frac{\partial f^{\text{ex}}}{\partial \rho_s} = \lim_{\rho_s\to 0}\sum_\alpha \frac{\partial n_\alpha}{\partial \rho_s}\frac{\partial f^{\text{ex}}}{\partial n_\alpha},\\ &= \frac{\partial f^{\text{ex}}}{\partial \xi_3}\frac{4\pi R_s^3}{3} + \frac{\partial f^{\text{ex}}}{\partial \xi_2}4\pi R_s^2 + \frac{\partial f^{\text{ex}}}{\partial \xi_1}R_s + \frac{\partial f^{\text{ex}}}{\partial \xi_0}\end{aligned} \tag{2.108}$$

using the explicit derivatives (2.91) in the second line. Noting that the partial derivatives of f^{ex} are constants of the bulk liquid and the other contributions are normalisations of the intrinsic volumes (cf. Table 2.2), the central conjecture of the morphometric approach is that this generalises to arbitrary shapes; that is, the chemical potential can be written [39, 95]

$$\mu_s = pV_s + a_2A_s + a_1R_s + a_0 \tag{2.109}$$

with thermodynamic coefficients $\{p, a_2, a_1, a_0\}$ independent of the geometry. We leave detailed discussion of this approximation until chapter 4, but for reference we will give the explicit coefficients for the already introduced FMT functionals below.

The thermodynamic coefficients in (2.109) can be determined for an FMT functional using the special case of spherical solutes (2.108). For the Rosenfeld functional (2.96) we obtain the thermodynamic coefficients for the single-component hard sphere liquid

$$\beta a_0^{\text{RF}} = -\ln(1-\eta), \tag{2.110a}$$

$$\beta a_1^{\text{RF}} = \frac{6\eta}{\sigma(1-\eta)}, \tag{2.110b}$$

$$\beta a_2^{\text{RF}} = \frac{6\eta+3\eta^2}{2\pi\sigma^2(1-\eta)^2}, \tag{2.110c}$$

$$\frac{\beta p^{\text{RF}}}{\rho} = \frac{1+\eta+\eta^2}{(1-\eta)^3}. \tag{2.110d}$$

Dual hierarchies	
Correlation function	Dual function
Distribution $g^{(n)}$ (2.31)	Cluster $h^{(n)}$ (2.32)
Density moments $\langle \widehat{\rho}_1 \cdots \widehat{\rho}_n \rangle$ (2.33)	Density-density $H^{(n)}$ (2.36)
Boltzmann weight $e^{-\beta U_n}$	Ursell $W^{(n)}$ (2.57)
Other correlation functions	
n-particle density $\rho^{(n)}$ (2.30)	
Static structure factor $S^{(n)}$ (2.40)	
Direct $c^{(n)}$ (2.78)	

Table 2.3: Summary of the various correlation functions in liquid state theory.

and for the CS functional (2.94) with (2.105) we find

$$\beta a_0^{\text{WBII}} = -\ln(1-\eta), \tag{2.111a}$$

$$\beta a_1^{\text{WBII}} = \frac{2}{\sigma}\left(\frac{5\eta+\eta^2}{1-\eta} + 2\ln(1-\eta)\right), \tag{2.111b}$$

$$\beta a_2^{\text{WBII}} = \frac{1}{\pi\sigma^2}\left(\frac{\eta(2+3\eta-2\eta^2)}{(1-\eta)^2} - \ln(1-\eta)\right), \tag{2.111c}$$

$$\frac{\beta p^{\text{WBII}}}{\rho} = \frac{1+\eta+\eta^2-\eta^3}{(1-\eta)^3}, \tag{2.111d}$$

We label these as the White Bear II (WBII) coefficients because they were first derived from the WBII free energy functional[46] [96, 97] which is similar in form and construction to the CS functional described, although it is (marginally) less self-consistent.

[46] These are not exactly as stated in Ref. [96] because we use a different definition of surface. The conversions between the different surfaces are stated in chapter 4: see the discussions around (4.9).

2.4 Summary

We have seen that integral geometry provides the formalism for describing sizes, and thus defines an *ansatz* for strictly extensive variables. Specifically, such variables must be a linear combination of the $(d+1)$ intrinsic volumes, which are the only meaningful size measures in d-dimensions in the sense of rigid-motion invariance, additivity and continuity. We expect in general that thermodynamic potentials are extensive in the thermodynamic limit, so this formalism provides a good starting point for their description. However, it is worth noting that extensive quantities could contain subleading terms which disappear in the thermodynamic limit; these would not be captured by an integral geometric *ansatz*.

We introduced liquid state theory, with a particular focus on the various correlation functions which are summarised in Table 2.3. A key result for hard spheres was the highly accurate Carnahan-Starling equation of state (2.104), which we will use throughout to treat the hard sphere liquid. We saw how the intrinsic volumes could be applied to liquid state theory to construct accurate free energy functionals for hard particle systems. We obtained the morphometric approach, an expansion of the chemical potential with the properties of sizes outlined above, as a special case of this theory. In chapters 4 and 6 we will provide additional justifications of this

approach, and we will apply it to predict the concentrations of local structures in chapter 5.

In the next chapter we will discuss the phenomenology of supercooled liquids and the glass transition, which will provide the key context for the treatment of the high density hard sphere liquid in subsequent chapters.

Chapter 3

Supercooled liquids and glasses

> Truly, he thought, the way of enlightenment is like unto half a mile of broken glass.
>
> Terry Pratchett, *Mort*, (1987).

In the introduction we established the supercooled liquid in hard spheres as the extension of the stable liquid above the freezing density, where it is metastable to the crystal phase. To provide proper context we will discuss supercooled liquids more generally here, including thermal systems where temperature is the more natural control parameter. As such, we will be considering the effect of decreasing temperature on the supercooled liquid.

3.1 Properties of the supercooled liquid

We will start by exploring the ways in which supercooled liquids are the *same* as regular liquids, expanding in more detail on ideas discussed in the introduction. Then we will move onto the ways in which they *differ* from ordinary liquids, notably in their dynamical properties and their structure at the many-body level.

Thermodynamically, supercooled liquids are not meaningfully different from their ordinary counterparts. Operationally, a supercooled liquid is equilibrated in the sense that all observables are time independent and the thermodynamics is self-consistent[47]. Formally speaking, the system is sometimes said to be in *local equilibrium*, where it samples all the liquid microstates ergodically; or that it obeys *detailed balance*, where the dynamics is microscopically reversible. As a consequence, the liquid loses any memory of its preparation and all observables become time independent. That is, for some observable A we can write

$$\langle A(t) \rangle = \langle A \rangle.$$

This includes the static correlation functions, introduced in section 2.2.2, which remain well-defined in the supercooled regime. Furthermore, the pair

[47] Different routes to measuring thermodynamic quantities, e.g. the pressure, may give different values in an out-of-equilibrium system. This is not the case in supercooled liquids, even though they are not strictly in equilibrium.

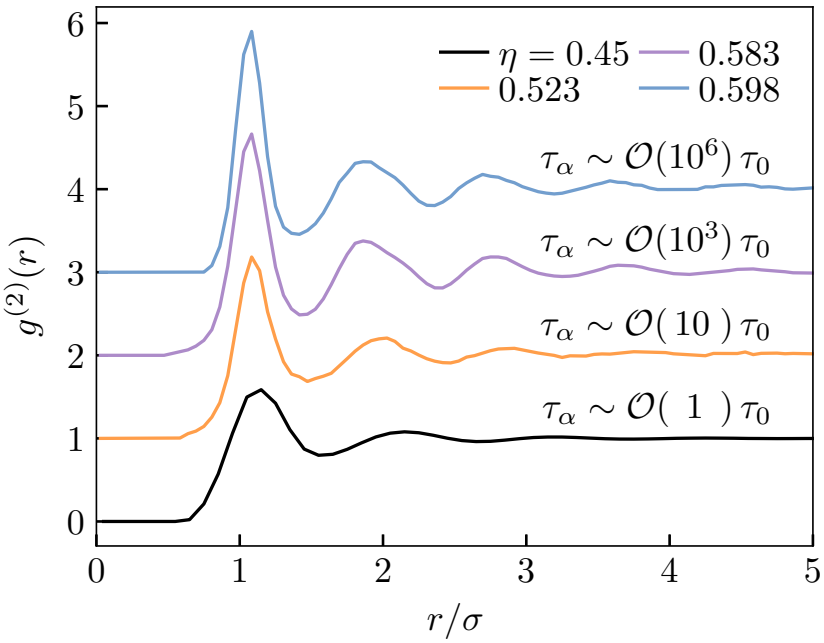

Figure 3.1: Change occurring in pairwise structure of hard spheres as density is increased above the melting point, as measured by the pair distribution function (2.31). Each state-point is offset for clarity. Results for $\eta = 0.45$ were obtained for a 7-component equimolar mixture with 16% polydispersity using the DynamO software package [98], whereas the data in the metastable regime is from colloidal experiments kindly provided by the authors of Ref. [99]. The α-relaxation times (described in text) in terms of a microscopic time τ_0 are indicated for each state-point, with the last two state-points displaying a large dynamical change with minimal accompanying change in pairwise structure.

distribution function $g^{(2)}(r)$ changes very little as the density (or temperature) is increased (decreased) from the normal liquid; as an example, we show this for hard spheres in Fig. 3.1. As pair correlations are the main measure of structure in simple liquids, this *seems* to suggest that minimal structural change occurs in the high density liquid. As a corollary, time correlation functions become *time-translation invariant* meaning they depend only on time differences i.e.

$$\langle A(t)A(t')\rangle = \langle A(0)A(t-t')\rangle.$$

A more sophisticated way in which supercooled liquids can be thought of as equilibrium systems involves the response functions. In an equilibrium system, the response of a system to a small perturbation is directly related to the microscopic source of fluctuations[48]. The *fluctuation-dissipation relation* for an observable A expresses the system's susceptibility to a perturbation at time t' as [35]

$$\chi_A(t,t') = -\beta\Theta(t-t')\frac{d}{dt}\big\langle \delta A(0)\delta A(t-t')\big\rangle$$

where $\delta A(\cdot)$ is the spontaneous and instantaneous fluctuation in A, and the Heaviside theta function imposes causality. These relations are obeyed in supercooled liquids, even though they are not a proper equilibrium state.

In spite of these similarities, supercooled liquids are markedly different from normal liquids in their *dynamics*. Typically, this is discussed in the context of two (related) quantities: the *viscosity* and the *relaxation time*[49]. Viscosity measures how resistant the system is to flow, while relaxation time measures the typical microscopic time for the density profile to relax i.e. for liquid-like behaviour caused by particle diffusion. A defining feature of supercooled liquids is that these numbers become so large that the precise details of the measurement used do not matter. We will discuss this

[48] Temperature, in the case of liquids.

[49] In Maxwell's viscoelasticity theory, these are linearly related with constant of proportionality G_∞, the high frequency shear modulus. As such, these can be thought of as equivalent quantities.

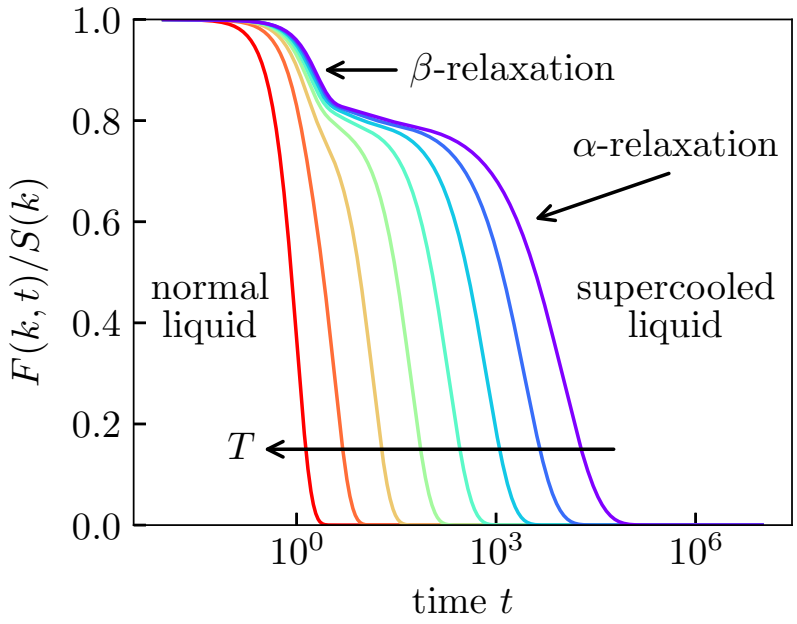

Figure 3.2: Typical intermediate scattering functions in a supercooled liquid, for values of $k \sim 2\pi/\sigma$ where σ is the interaction lengthscale. In the ordinary liquid decay is purely exponential, but as a liquid is supercooled we observe a timescale separation between short-time vibrational (β-) and longer time liquid-like (α-) relaxation processes.

dynamical slowdown further on, but for now we introduce a specific time correlation function in order to frame the discussion. A popular measurement is the intermediate scattering function, defined by [100]

$$F(k,t) = \frac{\langle \widetilde{\rho}(\mathbf{k},t)\widetilde{\rho}(-\mathbf{k},0)\rangle}{\langle N\rangle} \tag{3.1}$$

which reduces to the static structure factor (2.40) at zero elapsed time $F(k,t=0) = S^{(2)}(k)$. An example $F(k,t)$ is shown in Fig. 3.2, displaying features which distinguish the supercooled liquid from a regular liquid. In particular, there is a timescale separation between distinct dynamical processes. For short times there is a ballistic regime, where particles are essentially free to move unencumbered. At intermediate times, highly correlated interactions with neighbours inhibit motion and $F(k,t)$ plateaus; this plateau is absent in regular liquids. Finally, in the long time limit particles are able to diffuse so that $F(k,t)$ completely relaxes to zero. The latter two processes are called β- and α-relaxation respectively. The timescale of the longer α-relaxation τ_α is more central to our discussion as it corresponds to the timescale of liquid-like behaviour.

A helpful framework to guide discussion of dynamical processes is *transition state theory*. In this approach a dynamical process, e.g. a chemical reaction, is imagined to occur through a dynamical bottleneck (Fig. 3.3). We imagine evaluating a thermodynamic potential[50] Φ at every point along the reaction path. The process will then be limited by the rate of thermal fluctuations of size $\Delta\Phi$, i.e. those able to reach the transition state. In equilibrium, the timescale for the process will then scale by the Boltzmann weight

$$\tau \sim e^{\beta\Delta\Phi}. \tag{3.2}$$

There will be additional kinetic prefactors out in front, however for large barriers we expect the thermodynamic contribution to dominate because of

[50] Which thermodynamic potential this corresponds to will depend on the ensemble.

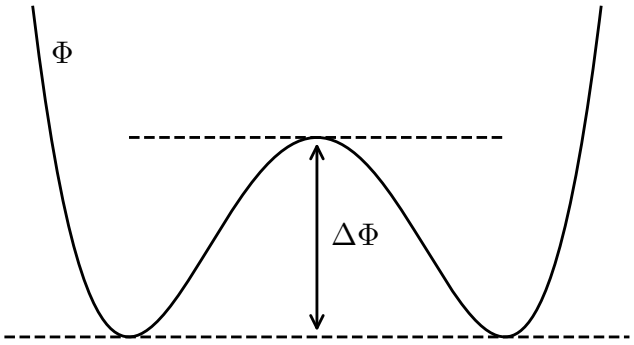

Figure 3.3: A double-well potential featuring a barrier $\Delta\Phi$, representing the minimum energy required for the system to pass between the two *basins*. The x-axis is the *reaction coordinate*, representing a one-dimensional projection of the complete degrees of freedom.

its exponential weighting. This framework can be more rigorously justified through e.g. an *instanton* approach [101]. The main limitation of transition state theory is the assumption that dynamical processes occur through effectively one-dimensional reaction paths; later, we will introduce a more sophisticated form of this framework which considers the high dimensional *energy landscape*.

As an example of how useful transition state theory can be, we very briefly consider *classical nucleation theory* which we will return to in more detail in chapter 7. Imagining crystallisation to occur by the spontaneous formation of the new phase inside of the liquid, then the timescale for this process will scale as

$$\tau_{\text{crys}} \sim e^{\beta\Delta\Phi_{\text{crys}}}.$$

Then, assuming a temperature-independent barrier $\Delta\Phi_{\text{crys}}$, the timescale for nucleation will increase exponentially as temperature is lowered allowing for the supercooled liquid to become long-lived[51] [102]. This argument is highly system dependent, as systems with small barriers to crystallisation will not be long-lived enough for the metastable liquid to be observed. Single-component hard spheres are particularly prone to crystallise at very high densities, so polydispersity is typically introduced to frustrate the crystal structure and extend the lifetime of the supercooled liquid[52]

Applying transition-state theory (3.2) to relaxation time in the liquid, we may expect the α-relaxation time to scale as

$$\tau_\alpha \sim e^{\beta\Delta\Phi_\alpha} \tag{3.3}$$

where $\Delta\Phi_\alpha$ is the barrier to relaxation. Naively, we might expect the barrier to remain constant with temperature, corresponding to e.g. the cost of breaking a bond, then we arrive at the Arrhenius law

$$\ln\tau_\alpha \propto \frac{1}{T}. \tag{3.4}$$

This argument captures the high temperature behaviour very well and, outside of soft matter, it applies reasonably well to many molecular glassformers e.g. silica-based materials[53], where relaxation essentially depends on the timescale to break a chemical bond. Experimental data for SiO_2 [105] confirms that $\ln\tau_\alpha$ scales linearly with β (Fig. 3.4). By convention, systems which scale in an Arrhenius fashion are called *strong*[54] glassformers.

[51] Note: the time for crystallisation also scales inversely with system size, so in the thermodynamic limit nucleation occurs instantaneously unless it is strictly forbidden.

[52] This process is imperfect, as even highly polydisperse systems have been found to crystallise without careful fine tuning of the size distribution [91, 103, 104]. However, crystallisation of polydisperse systems occurs through *fractionation* rather than nucleation.

[53] That is, the material which the average person would mean when they say "glass".

[54] This baffling naming convention has nothing to do with the mechanical properties.

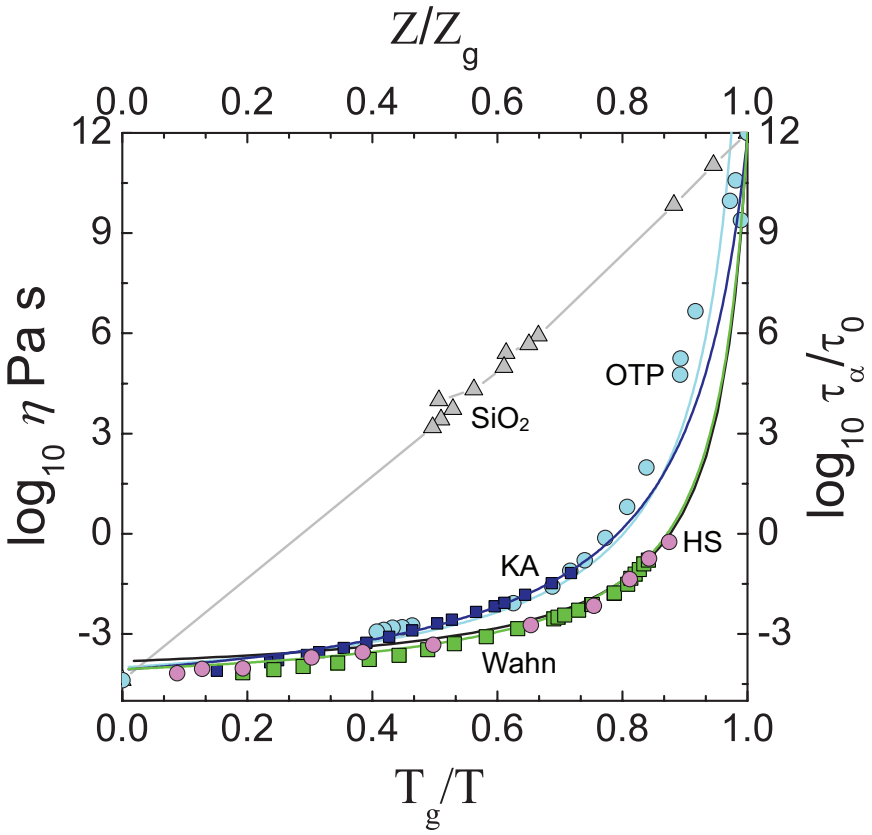

Figure 3.4: *Angell* plot [106] for molecular and model glassformers showing the temperature/pressure dependence of viscosity (labelled here as η) or equivalently relaxation time τ_α. The molecular systems SiO_2 and orthoterphenyl (OTP) respectively display the *strong* and *fragile* behaviours described in text, with data obtained from Refs. [105, 107]. Kob-Anderson (KA) and Wahnstrom (Wahn) are binary mixtures of Lennard-Jones atoms designed to exhibit fragility. The compressibility factor $Z = \beta p/\rho$ is argued to be equivalent to inverse temperature for hard spheres (HS) [107], with data taken from Ref. [108]. Reproduced from Ref. [109].

Our focus is on soft matter, with hard spheres as the prototypical model, where the interactions (typically van der Waals attractions) are much weaker than in molecular systems (and absent in hard spheres). Consequently, there is less of a case for an Arrhenius relationship (3.4), and empirically we find striking deviations from it. Many systems show *super-Arrhenius* scaling with temperature (Fig. 3.4), including mixtures of Lennard-Jones atoms and molecular systems such as orthoterphenyl. Correspondingly, systems where τ_α increases more rapidly than exponential are labelled as *fragile*. A super-Arrhenius scaling of τ_α implies that the thermodynamic barrier to relaxation $\Delta\Phi_\alpha$ increases with supercooling. This means that the dynamics fundamentally changes at high densities (or low temperatures), which must be caused by the onset of *collective* (or *cooperative*) effects; given the weakness of bonds in soft matter, we can conclude that many particles must contribute to create a large barrier. We will discuss this more in the next section.

Some modification is required for hard particle systems, where temperature is not a natural control parameter. As we argued in the introduction, pressure[55] is the only meaningful state variable. The authors of Ref. [107] argue that pressure plays a role equivalent to inverse temperature in athermal systems, because of similarities in their limit behaviour. Alternatively, we could make a free volume argument, where we expect a relaxation event to involve fluctuations of volume ΔV. In equilibrium, volume fluctuations are created by reversible work $p\Delta V$ so to leading order[56] we then expect

$$\tau_\alpha \sim e^{\beta p \Delta V}.$$

[55] Equivalent to density, with the connection made through the equation of state $p = p(\rho)$.

[56] The leading order behaviour can be given more justification by invoking the morphometric approach (2.109), or from more general arguments which we will introduce in section 4.2.2.

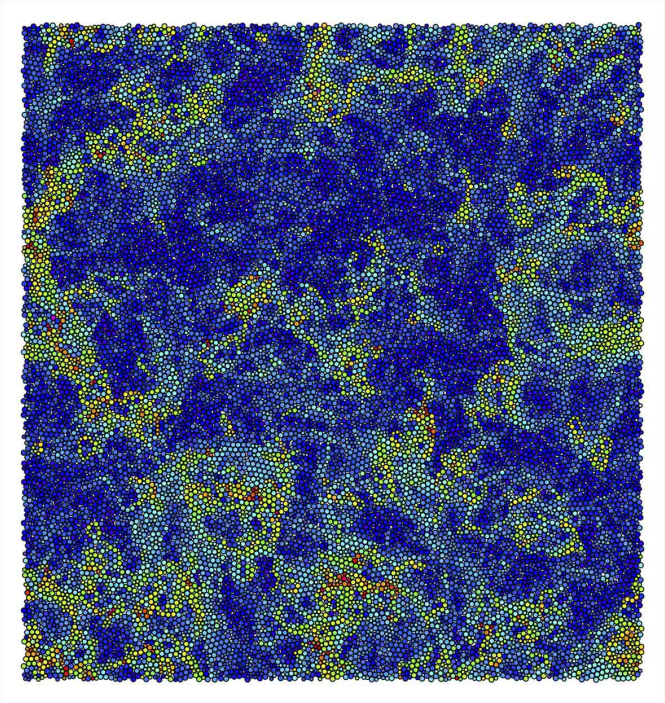

Figure 3.5: Dynamical heterogeneities in a binary hard disc system with a size ratio of 1 : 1.4. Particles are coloured according to distance moved over a relaxation time τ_α, with blue having moved the least and red the most. Reproduced from Ref. [109].

Taking ΔV as the equivalent of an energy barrier, we find the conjugate variable βp does indeed play the role of inverse temperature. It is usual to work with the dimensionless *compressibility factor*, defined by

$$Z = \frac{\beta p}{\rho}, \tag{3.5}$$

in terms of which hard spheres show the same phenomenology as thermal systems (Fig. 3.4); we find that hard spheres are comparable in fragility to various binary Lennard-Jones mixtures. Relaxation barriers in hard spheres are entropic in nature, so perhaps it is easier to see the need for collective effects. Moreover, the geometrical interpretation in terms of volume fluctuations ΔV provides an intuitive picture for collective motion: at high densities more particles have to move out of the way to create space for motion.

Given the rapid increase in dynamical timescales with supercooling, there comes a point where the relaxation time exceeds the observation time so it is impossible to equilibrate the system. This is the *experimental glass transition*, operationally set as the point where $\tau_\alpha(T = T_g \text{ or } \eta = \eta_g) = 100\,\text{s}$. In some sense, this threshold defines a subjective limit of a human observer's patience, and so the point T_g (or η_g) is not strictly a transition. However, in practice τ_α is increasing so rapidly by this point that the location of T_g (or η_g) is insensitive to the choice of observation time [102].

As the final piece of the phenomenology we introduce two more important dynamical features which differentiates the supercooled liquid from normal liquids. First, the Stokes-Einstein equation, relating diffusion, temperature and viscosity, holds at high temperatures (low densities) but significant deviations are observed at supercooling to low temperatures (high densities) [110]. This finding possibly suggests the existence of multiple competing relaxation mechanisms in the supercooled liquid, which are probed differently

by the two measures [111]. Second, the dynamics becomes highly spatially heterogeneous with increased supercooling (Fig. 3.5). Furthermore, simulation studies have revealed that the initial configuration strongly correlates with the locations of mobile events [112]. This shows that the sites of mobility are encoded in the static configuration, which could be interpreted structurally. Dynamical heterogeneities are now seen as quintessential features of the glass transition [110, 113], so the origin of the growing dynamical length would be a necessary component for any theory to be accepted.

The main point of contention is over what causes the dynamical slowdown: whether it is driven by an underlying phase transition in the thermodynamic viewpoint, or if it is purely a kinetic effect. The former viewpoint includes the related *mode-coupling* and *random first-order transition* theories, which are connected in the mean-field picture of glasses. By contrast, the kinetic viewpoint *dynamical facilitation* is based entirely around study of fluctuations. Having introduced the phenomenology of supercooled liquids we can now proceed to discuss these theories in turn. We will emphasise the thermodynamic theories because in recent years there has been a substantial shift towards them because of the success of mean-field theories. Furthermore, our approach focuses on static many-body correlation functions and local structure, which lends itself more towards a thermodynamic viewpoint.

3.2 Mode-coupling theory

The central tenet of mode-coupling theory (MCT) is to separate the liquid's degrees of freedoms into *slow* and *fast* variables. Fast variables are those that thermalise very quickly, e.g. the solvent in a colloidal liquid, so that they can be integrated out leaving only slowly evolving variables of interest. We advocate essentially the same philosophy, of coarse-graining onto a few dynamically relevant degrees of freedom, in developing a theory for many-body correlations in chapters 4 and 5. The difference between the two approaches is that MCT explicitly treats *dynamical* processes whereas we focus on *static* correlations. We will discuss our own approach more in section 3.5.

As an example of separation into fast and slow variables, consider classical Langevin equation of motion. Newton's equation for a particle in an external field becomes

$$m\ddot{\mathbf{r}} = \boldsymbol{\nabla}\phi_{\text{ext}}(\mathbf{r}) - \lambda\dot{\mathbf{r}} + \mathbf{f}(t) \tag{3.6}$$

where m is the particle mass, λ is a coefficient of damping and $\mathbf{f}$ is the *fluctuating force* from the fast variables, normally approximated as a Gaussian random field

$$\langle f_i(t) f_j(t') \rangle = 2D\delta_{i,j}\delta(t - t'),$$

with diffusion constant D. Here, the position $\mathbf{r}$ represents the slowly evolving variable of interest, whereas the remaining degrees of freedom (e.g. small solvent particles) are imagined to equilibrate rapidly leaving only the force field $\mathbf{f}$.

Mode-coupling theory starts from a formally *exact* Langevin equation, which generalises the classical result (3.6) above. Defining the instantaneous

state of the liquid as

$$\mathbf{X}(t) := \begin{pmatrix} \hat{\rho}(\mathbf{r},t) \\ \hat{\mathbf{j}}(\mathbf{r},t) \end{pmatrix}$$

with instantaneous current $\hat{\mathbf{j}}(\mathbf{r},t) := \partial\hat{\rho}(\mathbf{r},t)/\partial t$, the generalised Langevin equation then reads [100, 114]

$$\frac{d\widetilde{\mathbf{X}}(\mathbf{k},t)}{dt} = i\boldsymbol{\Omega}\cdot\widetilde{\mathbf{X}}(\mathbf{k},t) - \int_0^t \mathbf{K}(t')\cdot\widetilde{\mathbf{X}}(\mathbf{k},t-t')\,dt' + \mathbf{f}(t) \tag{3.7}$$

where $\mathbf{f}$ is (again) the fluctuating force obtained by integrating out the fast degrees of freedom, $\mathbf{K}(t')$ is a time-dependent *memory function* containing the history of $\mathbf{f}$ as an autocorrelation function [114] and $\boldsymbol{\Omega}$ is the *frequency matrix* containing the forces internal to the slow variables [100]. Each of these terms has an allegory in the classical Langevin equation (3.6) above. Similar equations to (3.7) can be constructed for observables such as the correlation functions; the goal of MCT is to construct (and solve) an equation for $F(\mathbf{k},t)$ (3.1) obtaining the dynamical behaviour of the liquid at long times. The central challenge of this approach is finding suitable approximations for the memory function $\mathbf{K}$.

In the standard MCT approach, the fluctuating force is assumed to be dominated by the pair correlations so that K becomes a four-point correlation function. Then, through a second approximation where K is factorised into a product of two two-point correlation functions, it is possible to construct an evolution equation for the intermediate scattering function (3.1) as [114]

$$\frac{d^2F(k,t)}{dt^2} + \frac{k^2}{\beta m S^{(2)}(k)}F(k,t) + \int_0^t K_{\mathrm{MCT}}(k,t')\frac{dF(k,t-t')}{dt}\,dt' = 0 \tag{3.8}$$

with[57]

$$K_{\mathrm{MCT}} = \frac{\rho}{16\pi^3\beta m}\int |V_{\mathbf{q},\mathbf{k}-\mathbf{q}}|^2 F(q,t)F(|\mathbf{k}-\mathbf{q}|,t)\,d\mathbf{q}, \tag{3.9a}$$

$$V_{\mathbf{q},\mathbf{k}-\mathbf{q}} = \frac{\mathbf{k}\cdot\mathbf{q}\,c^{(2)}(q) + \mathbf{k}\cdot(\mathbf{k}-\mathbf{q})\,c^{(2)}(|\mathbf{k}-\mathbf{q}|)}{k}. \tag{3.9b}$$

[57] As a reminder to the reader, the $c^{(2)}$ appearing here is the two-body direct correlation function defined through (2.78).

The latter function $V_{\mathbf{q},\mathbf{k}-\mathbf{q}}$ is the so-called *vertex*, which takes the pair direct correlation, and the initial condition for (3.8) is $F(k,t=0) = S^{(2)}(k)$; as such, standard MCT takes only pair correlation functions as input. This method requires knowledge of the structure factor, which implicitly depends the state point. Together (3.8) and (3.9) form a non-linear coupled set of integro-differential equations that can be numerically solved, providing a reasonable description of the first few decades of dynamical slowdown, with deviations only becoming noticeable at deep supercooling [115, 116].

Crucially, MCT predicts a diverging timescale at $\eta \sim 0.52$ in hard spheres, where the dynamics would become completely arrested, and numerical fits to colloidal experimental data with the same power behaviour law predicted by MCT move this point up to $\eta \sim 0.58$ [117]. However, this predicted transition has long been known to be spurious as the theory does not allow for activated dynamical events. Moreover, recent experiments have managed to equilibrate colloidal hard sphere liquids up to $\eta \lesssim 0.60$

[99, 116] and to even higher densities in simulations [91]. Despite this failing of MCT, it remains the only properly first-principles theory for treating liquid dynamics in physical dimensions[58].

[58] In higher dimensions, very similar theories emerge from mean-field theory [118, 119].

Extensions incorporating fluctuations can be found in Refs. [119, 120], and more recently a generalised MCT has been developed which avoids the uncontrolled factorisation of the pair densities [100, 121]. Importantly, the latter approach incorporates closures of the many-body correlation functions, which will be a central theme of later chapters; by doing this the authors were able to move the diverging timescale to higher densities, bringing the theory into better agreement with available data from simulations and experiments.

3.3 Mean-field theories

We introduced MCT as an explicitly dynamical theory which attempts to model dynamical arrest in supercooled liquids by directly describing the decay of time correlation functions like $F(k,t)$. Thermodynamics only entered implicitly into MCT through the structural input of the static structure factor $S^{(2)}(k)$. By contrast, *mean-field theories* of glass take a primarily thermodynamic approach, though they are broadly compatible with the dynamical descriptions of MCT. The mean-field picture has been rapidly gaining traction in recent years since exact solutions have been developed for hard spheres [122–126]. To describe mean-field theory we will invoke the concept of an *energy landscape*, the natural generalisation of transition state theory introduced in section 3.1 and summarised by (3.2). While this conceptual framework is not unique to mean-field theories, it is most closely associated with them.

In an energy landscape description, the thermodynamic potential is interpreted *geometrically* as a mapping from every point in configuration space to a 'height' representing energy e.g. $\Phi : \mathbb{R}^{dN} \mapsto \mathbb{R}$ for an N particle system. The appeal of this approach is that physical processes can be understood *topographically*: the system will spend more time at the bottom of 'valleys' (minima of Φ), especially at lower temperatures, and dynamics will occur primarily through low-lying 'mountain passes' (saddles of Φ) [127]. The timescales of transitions over saddles are expected to scale via the usual Boltzmann weight (3.2), just as in ordinary transition state theory, however this refined picture emphasises the importance of landscape *connectivity*: the number, separation and relative weights of the various dynamical paths could drive the glass transition.

The energy landscape is particularly relevant in mean-field, formally corresponding to the high dimensional limit[59] $d \to \infty$, because its *exact* properties can be determined. In mean-field, hard spheres undergo a *clustering* (or *dynamical*) transition at a volume fraction η_c where the landscape splits into disconnected regions [122, 123, 128], and the dynamics are described by an almost identical theory to MCT [118, 128]. As configuration space becomes disconnected at η_c, the system is frozen into a single region and so the relaxation time diverges; contemporaneously, the memory function analogous to K_{MCT} in mean-field develops a plateau reflecting the fact that the density profile can no longer completely relax [129]. In this light,

[59] To understand why, consider the typical number of particle neighbours increases with dimensionality. Then, formally in the limit $d \to \infty$ a particle is able to achieve a macroscopic number of neighbours, equivalent to an interaction with an average field representing the rest of the system.

the diverging relaxation time predicted by standard MCT is not necessarily a failure of the theory, but is indicative of this genuine mean-field transition.

Although the dynamics is singular at the dynamical transition, the thermodynamic observables are continuous as the system is compressed beyond η_c [122]. We can imagine what happens to the system under further compression if it could continue to sample these disconnected regions in equilibrium, i.e. with Boltzmann weighted measure. The free energy, normally expressed as a sum over all microstates[60] Γ, can be re-expressed as a sum over a collection of *mesostates* $\Gamma = \{\alpha_1, \cdots, \alpha_M\}$ giving

$$\Phi = \sum_{i \in \Gamma} p_i \left(\epsilon_i - k_B T \ln p_i\right) = \overline{\Phi} - T\Sigma \tag{3.10}$$

where ϵ_i is the energy of microstate i and p_i its probability measure. In the latter step we defined[61]

$$\overline{\Phi} = \sum_\alpha p_\alpha \underbrace{\sum_{i \in \alpha} \frac{p_i}{p_\alpha} \left(\epsilon_i - k_B T \ln \frac{p_i}{p_\alpha}\right)}_{\text{free energy of mesostate } \alpha}, \tag{3.11a}$$

$$\Sigma = -k_B \sum_\alpha p_\alpha \ln p_\alpha. \tag{3.11b}$$

The *complexity* Σ is an extensive quantity characterising the multiplicity of mesostates; at the dynamical transition this becomes a positive non-zero number $\Sigma(\eta = \eta_c) > 0$ corresponding to the clustering in configuration space. As the system is compressed further Σ decreases [122, 130, 131] corresponding to the rarefaction of clustered regions. At a volume fraction $\eta_K > \eta_c$ an *entropy crisis* occurs: Σ vanishes, leading to the system being frozen into a single, unique region in configuration space called an *ideal glass* phase [110, 122, 130–133].

If an equilibrium glass state in the regime $\eta \in [\eta_c, \eta_K]$ is compressed out-of-equilibrium without sampling the other clusters, a further phase transition occurs to a so-called *Gardner phase* [124–126]. Each cluster splits further into fractal sub-regions arranged hierarchically. Whereas the clustered regions formed at η_c are geometrically dissimilar[62], these regions are close in configuration space to one another. This phase has deep connections with the jamming transition seen at diverging pressure, providing a unified description of glass and jamming conjectured since the landmark paper of Ref. [134]. Remarkably, this mean-field theory is able to predict anomalous d-independent critical scaling coefficients, matching those known around jamming [135–137]. The existence of the Gardner phase provides context for the importance of mean-field theory, but it cannot be directly connected to our approach in subsequent chapters so we will not discuss it further. For more information on the mean-field Gardner phase see the reviews of Refs. [129, 138].

The mean-field picture introduces complexity as the important quantity of interest, relating the number of metastable regions in configuration space. The relevance of mean-field descriptions in physical dimensions requires a finite-dimensional description of the supercooled liquid and its energy landscape.

[60] Which microstates this includes depends on the ensemble.

[61] This expression is obtained by writing the probability of the system being in mesostate α as $p_\alpha = \sum_{i \in \alpha} p_i$, then p_i/p_α is the probability of microstate i given that the system is in this mesostate.

[62] As measured by e.g. the intermediate scattering function.

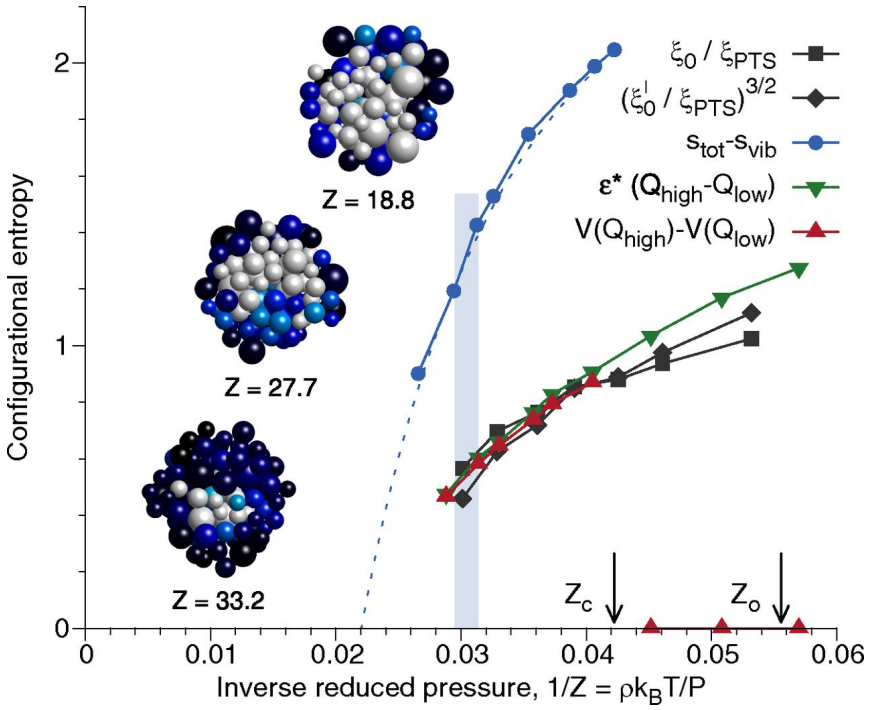

Figure 3.6: Configurational entropy in hard spheres from novel Monte-Carlo (MC) simulations for a system with 23% polydispersity. $Z_0 \approx 18$ ($\eta_0 \approx 0.56$) marks the onset pressure, above which the intermediate scattering function $F(k,t)$ decays non-exponentially, and $Z_c \approx 23.5$ ($\eta_c \approx 0.598$) is the location of the dynamical transition predicted by fitting mode-coupling theory's power-law scaling to the lower density behaviour. The various methods used (described in Ref. [139]) all broadly agree that this quantity is trending to zero at a finite pressure, suggesting the existence of a thermodynamic glass transition. The equation of state for this system is given in Fig. 2.1. Reproduced from Ref. [139].

3.4 Finite-dimensional theories

The relevance of mean-field ideas in physical dimensions can be seen by an interpretation of Refs. [130, 131, 133], with antecedent ideas found in [132, 140]. This *random first-order transition* (RFOT) scenario acknowledges that the clustering of states appearing at the dynamical transition in mean-field will not be strictly metastable over finite lengthscales in finite d [141, 142]. As such, the complexity is not well-defined because the metastable states will not be strictly separated with infinite barriers, though they may be arbitrarily long-lived; the dynamical transition of mean-field thus becomes a cross-over. In finite dimensions, the *configurational entropy* S_{conf} is introduced as the closest equivalent to the complexity; this does not have a generally agreed upon meaning, but a common definition invokes the timescale separation between vibrational (β–) and liquid-like (α–) dynamics. The configurational entropy then describes the entropy of the latter process, obtained as the residual entropy after removing vibrations

$$S_{\text{conf}} := S - S_{\text{vib}} \tag{3.12}$$

with S_{vib} as the *vibrational entropy*, though some refinement is required for polydisperse systems [143, 144] and where additional non-vibrational processes exist that do not relax the density profile [145]. The exact definition of S_{conf} thus depends on how one defines S_{vib}, which can be defined in multiple distinct, though broadly equivalent, ways. For example, a common convention is to define the vibrations as all those excitations around an energy minimum [146]; we will use this convention in chapter 5.

The RFOT scenario imagines the mean-field dynamical transition as a crossover to an *energy landscape dominated* dynamics. Specifically, the number of unique (non-vibrational) states possible in a subregion of size ξ will scale $\propto \exp\left(s_{\text{conf}}\xi^d/k_B\right)$, where $s_{\text{conf}} = S_{\text{conf}}/V$ is the configurational

entropy density. A dynamical event which changes a state is expected to pay an energy penalty $\gamma_{\text{eff}}\xi^\theta$ where $\theta \leq d$ from inducing a mismatch with the surrounding fluid. The thermodynamic potential for this subregion is then expected to adopt the form

$$\Phi(\xi) \sim \gamma_{\text{eff}}\xi^\theta - Ts_{\text{conf}}\,\xi^d. \tag{3.13}$$

The maximum of Φ occurs at the *point-to-set* length

$$\xi_{\text{PS}} := \arg\max_\xi \left(\Phi(\xi)\right) \sim \left(\frac{\theta\gamma_{\text{eff}}}{dTs_{\text{conf}}}\right)^{\frac{1}{d-\theta}}, \tag{3.14}$$

after which Φ grows infinitely negative, so the metastable states are unstable to activated dynamics for $\xi \gtrsim \xi_{\text{PS}}$. The RFOT interpretation thus predicts the formation of a *mosaic* of droplets of typical lengthscale ξ_{PS} [130, 131, 133, 141]. The nature of the entropic droplets forming the mosaic state and the processes by which they relax is an active area of study [141, 147–152]. Notably, a lot of attention has been devoted to the treatment of the subleading term $\gamma_{\text{eff}}\xi^\theta$.

This thermodynamic argument above concerns whether a region of the liquid *will* relax eventually, but an even more direct connection with relaxation timescale was proven in Ref. [142]. Briefly, dynamical barriers must remain finite within a finite subregion, so they scale Arrheniusly via (3.2); any Arrhenius process will eventually overwhelm the super-Arrhenius scaling of τ_α at deep supercooling. Fragile behaviour then suggests a reduction in S_{conf} to limit the number of possible Arrhenius processes. Moreover, the authors of Ref. [142] then show that the relaxation time is rigorously bounded from above by S_{conf}, proving that any diverging relaxation time *must* coincide with an entropy crisis where S_{conf} becomes sub-extensive. Measurements of the configurational entropy from simulations of hard spheres suggest a vanishing S_{conf} at finite pressure in $d = 3$ (Fig. 3.6), pointing to a mean-field/RFOT scenario in hard spheres. This necessarily relies on extrapolation as the point where S_{conf} vanishes cannot be reached in finite time because of the argument above. Recent numerical evidence suggests that S_{conf} only vanishes at $T = 0\,\text{K}$ for a model glassformer in $d = 2$ [153], suggesting a lower critical dimension for mean-field/RFOT scenario of at least $d_L \geq 2$. However, while a vanishing S_{conf} would necessarily coincide with a phase transition, it was argued in Ref. [154] that this cannot explain the observed dynamical arrest around the operational glass transition; see also Ref. [138] for interesting discussion of this argument.

A different scenario in physical dimensions focuses on the role of geometry. This picture starts from the observation that crystal structures (e.g. the face-centred cubic introduced for hard spheres at close packing) are generally not the optimal energetic arrangement for small clusters of particles, even though they must be for bulk systems. For example, 13 isolated Lennard-Jones atoms will preferentially arrange as vertices of a fivefold symmetric *icosahedron* [155] (Fig. 3.7b). As fivefold symmetric structures cannot tessellate Euclidean space, Sir Charles Frank conjectured that glassformers suppress crystallisation through formation of icosahedra (or similar structures) [155].

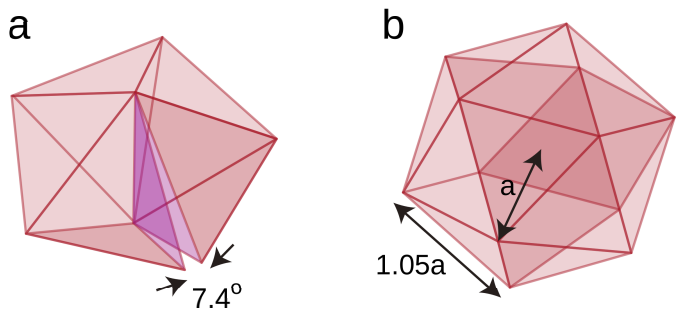

Figure 3.7: Structures formed by combining tetrahedra. (a) The pentagonal bipyramid constructed from five regular tetrahedra must leave a small gap of 7.4°. (b) The icosahedron formed by vertices a distance a from the centroid must have edge length $\sim 1.05a$, so if hard spheres of diameter a were placed on the vertices they would not be in contact. Reproduced from Ref. [109].

The above viewpoint has been developed into the more complete theory called *geometric frustration* [156, 157]. This approach characterises the liquid by its *locally favoured structures* (LFS), i.e. those structures which are energetically favoured at small length scales. A system could have a single LFS, or a whole collection; recently, it has been shown through numerical simulations that *competition* between different LFS enhances the propensity for glassformation [158]. This competition is an example of *frustration* where continual growth of domains of LFS is hindered by geometric constraints. Frustration can also emerge from a single LFS if it cannot tile space, as is the case of fivefold symmetric structures like icosahedra. Incorporating frustration into a theory modelling the energy of LFS-rich domains leads to a similar scaling relation as in RFOT (3.13). The key difference from RFOT is that the theory predicts an avoided phase transition, the proximity to which causes dynamical arrest. Static lengthscales[63] emerging from this theory ξ_{LFS} are interpreted as the size of the domains. Details can be found in the review of Ref. [157].

[63] There are multiple ways of extracting lengthscales from the LFS, see e.g. Refs. [99, 159, 160].

The prototypical model for geometric frustration is the Wahnstrom mixture, whose icosahedral LFS can form a crystal in curved space; flattening space induces frustration suppressing the crystal structure [109, 159]. In a recent work, Turci et al. [161] varied the curvature of space to effectively treat frustration as a control parameter. They found that the collective dynamical behaviour was dominated by the LFS for small frustration, as expected, but that increasingly the static and dynamical lengthscales decouple with strong frustration [161]. This decoupling signals the appearance of additional relaxation mechanisms beyond the geometric frustration picture. In Euclidean space, model systems are typically too strongly frustrated for this scenario to apply verbatim.

Even though the full geometric frustration scenario now seems implausible for most systems, there is room for geometric ideas play a role in a more complete theory. Notably, the formation of LFS has been found to strongly correlate with dynamically slow regions in gels [162], binary Lennard-Jones mixtures [163, 164] and colloidal hard spheres [165]. Unfortunately, this correlation seems to be highly system dependent [166], so it may only be one piece in the puzzle. A more complete review of the phenomenology of LFS can be found in [109]. Finally, a viewpoint emphasising the role of local structure is broadly compatible with the mean-field picture: the propensity for a system to form certain structures can be interpreted as a manifestation (or a driving force) of a reduced S_{conf}. In this picture repeating patches in

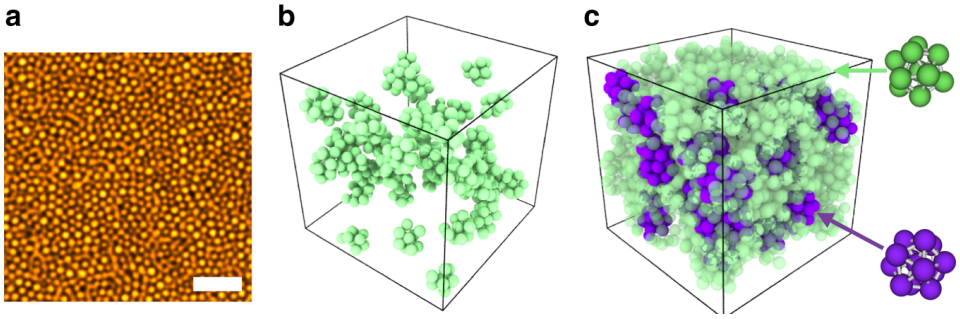

Figure 3.8: Growth of icosahedral domains in a colloidal hard sphere liquid with supercooling, i.e. increased volume fraction η, over a density change which coincides with minimal structural change at the pair level (Fig. 3.1). (a) STED nanoscopy image for $\eta = 0.598$, with scale bar 3 µm. (b), (c) Rendered coordinates of partial icosahedra (green, top right structure) and full icosahedra (purple, bottom right structure) for volume fractions (b) $\eta = 0.523$ and (c) $\eta = 0.598$. Reproduced from Ref. [99].

the liquid would be interpreted as indicative of a growing amorphous order [167].

In hard spheres, the dominant LFS are found to be icosahedral motifs in accordance with Frank's original conjecture. Icosahedral motifs cannot be formed by regular tetrahedra (Fig. 3.7) and do not tile space, so these are highly frustrated. In Fig. 3.8 we see the growth of large domains of icosahedra in the supercooled liquid, over a range in densities where τ_α changes by a factor of $\mathcal{O}(10^5)$ (Fig. 3.1) [99]. This fact demonstrates that significant structural change occurs alongside dynamical arrest, even though minimal changes are seen at the pair level. This does not prove that structural change *causes* the slowdown, but it does suggest the idea is worth investigating.

The main opposition theory to the thermodynamic scenarios outlined above is *dynamical facilitation*, which focuses on the role of kinetic constraints. This theory was motivated by *kinetically constrained models*, which share many of the same phenomenology as supercooled liquids but possess trivial thermodynamics ruling out the thermodynamic theories outlined above. Instead, dynamics is inhibited through kinetic constraints which must be overcome by a series of subsequent localised events [168], rather than single collective events predicted by e.g. the mean-field/RFOT scenario. Inspired by this, dynamical facilitation posits that relaxation in supercooled liquids occurs through a series of connected elementary excitations [168, 169]. Dynamical heterogeneity and its associated lengthscale are the fundamental features of glass in this picture, and no thermodynamic phase transition occurs so the relaxation time remains finite until $T = 0\,\mathrm{K}$. The dynamical lengthscale corresponds to the distance between dynamical defects in this theory, which could have a structural interpretation although the nature of the defects are usually considered incidental to the theory. Notably, the agreement of dynamical facilitation with available structural relaxation time data is comparable with the mean-field/RFOT scenario up to the experimental glass transition [169]. However, dynamical facilitation fails to explain other observables such as the reduction in S_{conf} seen in Fig. 3.6.

3.5 Perspective: usefulness of many-body correlations

In subsequent chapters we will heavily focus on the treatment of static many-body correlation functions in the bulk liquid. Here, we motivate their study for the treatment of the supercooled liquid. In section 2.2.3 we saw how the compressibility and virial routes lead to expressions of the free energy in terms of pair correlations. This is emblematic of conventional routes to the free energy, so in some sense all of the thermodynamically relevant information is contained in the two body correlation functions. It is thus natural to wonder what new information can be obtained from the many-body correlation functions that is not already present at the pair level.

Firstly, while it is true that thermodynamic quantities like the pressure can certainly be inferred from the pair correlations, there is no such simple relationship for dynamical quantities. In the absence of a thermodynamic phase transition, we would not expect the pair correlation function alone to reveal much about the nature of dynamical arrest, beyond the lack of a transition. Even supposing the existence of a transition, the precision required to detect such a signal in $g^{(2)}(r)$ may be arbitrarily subtle. It is straightforward to show that [13]

$$\chi_T \rho \left(\frac{\partial \rho^{(n)}}{\partial \rho} \right)_{V,T} = (n - \rho V)\rho^{(n)}(\mathbf{r}^n) + \int \rho^{(n+1)}(\mathbf{r}^{n+1})\, d\mathbf{r}_{n+1}. \qquad (3.15)$$

The important feature to take away from this expression is the presence of $\rho^{(n+1)}$; we see the emergence of higher-order correlation functions in the derivatives. As such, any changes in the pair correlations approaching a transition *must* be magnified at the many-body level.

We have emphasised the structural components of theories of the glass transition such as the amorphous ordering in RFOT, the LFS in geometrical viewpoints and even the static structure factors which are input into MCT. Notably, incorporating many-body generalisations of structural measures has been found to significantly improve MCT [100, 121]. The many-body correlation functions have potential to place the entropic droplet scenario of (3.13) on more rigorous footing, by providing a means to calculate the subleading penalty term $\gamma_{\text{eff}}\xi^\theta$. Alternatively, local mechanisms based on LFS should show strong signatures at the many-body level. The usefulness of many-body correlation functions is less obvious in kinetic theories such as facilitation, which do not posit a thermodynamic or explicitly structural mechanism. In this case, the *absence* of a thermodynamic signal would potentially support kinetic theories. Moreover, the correlation function $g^{(n)}$ explores a liquid lengthscale set by n, so in a trivial sense these functions must be able to explore facilitation in the limit of large n where bulk behaviour is recovered.

Secondly, even at the thermodynamic level the many-body correlations have advantages. To illustrate this we borrow an argument originally made by Evans [170]. Pair correlations yield thermodynamic quantities which are *derivatives* of the free energy at an instantaneous state point, so to infer the free energy multiple state points must be sampled. Equivalently, we could consider the derivatives of the pair correlation function. Considering (3.15),

we could in principle use highly accurate measurements of the many-body correlation functions to infer $g^{(2)}$ at other statepoints, and thus measure the free energy at a *single* state point. This is essentially the spirit of the *entropy route*, which writes [171]

$$S = \sum_{n=1}^{\infty} S_n \tag{3.16}$$

with entropic terms S_n containing contributions from n-particle correlations. The first few terms are given by [171]

$$\frac{S_1}{V} = k_B \rho \left(1 + \frac{d}{2} - \ln \rho \Lambda^d\right), \tag{3.17a}$$

$$\frac{S_2}{V} = \frac{\rho^2}{2T} \int g^{(2)}(\mathbf{r}) \ln g^{(2)}(\mathbf{r})\, d\mathbf{r}, \tag{3.17b}$$

$$\frac{S_3}{V} = \frac{\rho^3}{6T} \int g^{(3)}(\mathbf{r}, \mathbf{r}') \ln \left(\frac{g^{(3)}(\mathbf{r}, \mathbf{r}')}{g^{(2)}(\mathbf{r}) g^{(2)}(\mathbf{r}') g^{(2)}(\mathbf{r} - \mathbf{r}')} \right) d\mathbf{r} d\mathbf{r}'. \tag{3.17c}$$

Then, for a pair-interacting system the excess free energy is obtained as

$$\begin{aligned} \frac{\beta F^{\text{ex}}}{V} = \quad & \frac{\rho^2}{2} \int g^{(2)}(\mathbf{r}) \left(\beta u(\mathbf{r}) - \ln g^{(2)}(\mathbf{r})\right) d\mathbf{r} \\ & + \frac{\rho^3}{6} \int g^{(3)}(\mathbf{r}, \mathbf{r}') \ln \left(\frac{g^{(3)}(\mathbf{r}, \mathbf{r}')}{g^{(2)}(\mathbf{r}) g^{(2)}(\mathbf{r}') g^{(2)}(\mathbf{r} - \mathbf{r}')} \right) d\mathbf{r} d\mathbf{r}' \\ & + \mathcal{O}\left(\rho^4 g^{(4)}(\mathbf{r}, \mathbf{r}', \mathbf{r}'')\right), \end{aligned}$$

so the free energy can be directly obtained from accurate determination of the correlation functions.

3.6 Summary

We introduced the basic phenomenology of dynamical arrest as supercooled liquids undergo a glass transition. The liquid undergoes a dramatic slowdown, accompanied by changes in the relaxation mechanisms. Most notably, the autocorrelation functions feature a timescale separation between short-time vibrational and longer-time liquid-like processes signifying collective effects, and the dynamics become highly spatially heterogeneous. Structurally, minimal change is seen at the pair level, but more subtle measures of structure which are explicitly many-body do show marked change.

In the mean-field/RFOT scenario, an underlying amorphous order caused by a reduction in configurational entropy is proposed as the mechanism for dynamical arrest. Broadly compatible geometric viewpoints interpret the growth of amorphous order geometrically, as the size of domains of locally favoured structures. We argued that any subtle structural changes in these thermodynamic approaches should be detectable by examining the many-body correlation functions. Furthermore, the connectivity of the energy landscape for local arrangements of particles inside the fluid could in principle place the formalism of RFOT on more precise footing. By contrast, the dynamical facilitation picture does not require static ordering, in which case

structural signs of arrest should be absent from the many-body correlation functions.

This concludes the relevant background in supercooled liquids and glasses. In subsequent chapters we will develop a framework for treating the many-body correlation functions, with the hope that it can address some of the questions outlined here. By setting the number of particles in the correlation function we effectively fix the liquid lengthscale.

Chapter 4

Many-body correlations from integral geometry

> Ninety percent of everything is crap.
>
> Theodore Sturgeon, *Galaxy* (1956).

This chapter covers the theory for using morphological thermodynamics to treat many-body correlations inside the hard sphere liquid. We introduced the morphometric approach in section 2.3.4 as a special case of fundamental measure theory, which is the traditional way it has been derived. In this chapter we present the morphometric approach in a new context as a generalisation of scaled particle theory, and derive several morphometric theories for hard spheres of fundamental and practical interest. Our central result will be a new theory which is particularly suited to the treatment of many-body correlation functions in the hard sphere liquid, which we demonstrate by numerical tests against simulation. We leave applications of this framework to the next chapter.

Part of the work in this chapter is published in Ref. [1], and the remaining parts will appear in a forthcoming paper [3].

4.1 Introduction

[64] By "modern" theories we mean those which provide a statistical mechanical description of the liquid based on correlation functions.

Since the beginnings of modern liquid state theory[64] [172], the hard sphere liquid has remained the archetypal model for atomic systems and soft matter. The dynamics of the system at high density in the metastable regime above the freezing transition are hotly debated, despite relentless study. Proposed mechanisms for dynamical phenomena all loosely fall under the broad umbrella of many-body correlations; nucleation occurs via crystal seed formation [173], and to explain dynamical arrest approaching the glass transition thermodynamic theories invoke cooperatively rearranging regions [174] or elastic soft modes [175] while kinetic theories posit the existence of dynamical defects [169]. Here we propose a framework for treating many-body correlations, which in the next chapter we will develop into an operational scheme for predicting the populations and dynamics of local structural

motifs within a uniform liquid. Central to this is the use of the *morphometric approach*.

The morphometric approach provides an efficient means of treating the thermodynamics of a bulk liquid without fully determining its equilibrium density profile [1, 39, 95, 176]. Detailed investigations have shown that it is highly accurate in the hard sphere liquid regime [177–182], so we can expect an accurate treatment where the bulk system provides background depletion interactions while its detailed microstates remain unimportant. This feature makes it ideally suited for many-body correlations if we can identify relevant dynamical degrees of freedom. While existing morphometric theories have been proven accurate in the liquid regime, we require a theory which works in the supercooled regime. Here we derive such a theory using scaled particle theory (SPT).

SPT determines bulk properties from consideration of a spherical solute of varying radius. It remains one of most enduring theories of simple liquids; though 60 years old as of this year [183], aspects of this approach remain in modern theories. This is particularly true for hard spheres where SPT has been unified with the Percus-Yevick integral equation solution (2.103) [90], another old theory, in the form of fundamental measure theory (FMT) [25] which we introduced in section 2.3.4. Though originally a theory of single-component hard spheres [183], SPT has been extended to other potentials [85, 184, 185] and shapes [186, 187], mixtures [87], dimers [188, 189] and discs [190–192]. Morphological thermodynamics can be seen as a modern generalisation of SPT for a wide class of physically relevant geometries. Its basis in integral geometry replaces the semi-empirical approach of classical SPT with clearly defined postulates. In this chapter we present the morphometric approach in the context of SPT and derive three theories for the single-component hard sphere liquid: the classical SPT coefficients, the White Bear II morphometric coefficients[65] and a new theory suitable for high densities above freezing.

[65] These are given in (2.111), which we obtained through their classical derivation as part of FMT. In this chapter we will derive them through a new, self-contained route.

In section 4.2 we show how one can map the problem of treating many-body correlations onto a solvent-solute problem. We spend the rest of the chapter discussing the solvation problem through the lens of SPT. We argue for the morphometric approach as a useful generalisation of SPT in section 4.3. Then, through scaled particle arguments for hard spheres, we derive the classical SPT theory, the White Bear II morphometric theory [96] and a new set of coefficients well-suited for treating many-body correlations. In section 4.5 we numerically test these theories' two– and three–body correlation functions to demonstrate their effectiveness in treating correlation functions.

4.2 Solvation expression for many-body correlations

4.2.1 Correlations in terms of the insertion cost

We will show that correlations of n particles at positions $\mathbf{r}^n := \{\mathbf{r}_1, \cdots, \mathbf{r}_n\}$ can be expressed in terms of the free energy cost of inserting them at $\mathbf{r}^n$, by generalising the *potential distribution theorem* [193, 194] to many particles. The classical approach, also known as *Widom's insertion method*, expresses

the (excess) chemical potential μ^{ex} of a single-component system as the free energy cost of inserting an additional particle. See Ref. [195] and references therein for a detailed review of this classical approach. Our generalisation results in a *potential of mean force* for interactions between the n particles, which is formally identical to the chemical potential of a solute; this latter form is particularly suitable for geometric approximation schemes.

We consider a bulk liquid (the solvent) of N particles with interaction potential energy U_N surrounding the n particles (the solute). To coarse-grain onto the $n \ll N$ degrees of freedom we must perform an average over all arrangements of this solvent. Specifically, we will describe many-body correlations with the n-particle density defined in (2.29); the specific form for grand-canonical ensemble is given already in (2.30) but we restate it here for ease of reference:

$$\rho^{(n)}(\mathbf{r}^n) = \frac{1}{\Xi} \sum_{N=n}^{\infty} \frac{z^N}{(N-n)!} \int e^{-\beta U_N} \, d\mathbf{r}^{(N-n)}.$$

Changing the summation limits $N \to N+n$ we obtain

$$\begin{aligned} \rho^{(n)}(\mathbf{r}^n) &= \frac{z^n}{\Xi} \sum_{N=0}^{\infty} \frac{z^N}{N!} \int e^{-\beta U_{N+n}} \, d\mathbf{r}^N \\ &= z^n e^{-\beta U_n} \left\langle e^{-\beta U_{n \leftrightarrow N}} \right\rangle \end{aligned} \tag{4.1}$$

where in the latter step we decomposed the total potential U_{N+n} into purely local and solvent terms, i.e. $U_{N+n} = U_n + U_N + U_{n \leftrightarrow N}$, where U_α for $\alpha \in \{n, N\}$ indicates the internal interactions between particles in component α. The "interspecies" interactions are contained within $U_{n \leftrightarrow N}$ which acts as an external field for the solvent. Thus, (4.1) becomes

$$\rho^{(n)}(\mathbf{r}^n) = z^n e^{-\beta(U_n + \Omega_n - \Omega_{\text{hom}})}.$$

where Ω_n is the grand potential of the solvent in the presence of the n-particle inhomogeneity. Splitting the chemical potential into its ideal and excess parts so that $\beta\mu = \ln \Lambda^d \rho + \beta\mu^{\text{ex}}$ gives

$$\rho^{(n)}(\mathbf{r}^n) = \rho^n e^{-\beta(U_n + \Omega_n - \Omega_{\text{hom}} - n\mu^{\text{ex}})}.$$

The n-particle distribution functions are then determined from (2.31)

$$g^{(n)}(\mathbf{r}^n) := \frac{\rho^{(n)}(\mathbf{r}^n)}{\rho^n} = e^{-\beta(U_n + \Delta\Omega - n\mu^{\text{ex}})} \tag{4.2}$$

where $\Delta\Omega := \Omega_n - \Omega_{\text{hom}}$ is the reversible (free energy) cost of inserting the particles at fixed position $\mathbf{r}^n$, or equivalently describes the average depletion interactions between mobile particles. For $n = 1$ we have $\Delta\Omega = \mu^{\text{ex}}$ and this is identical to the potential distribution theorem of Widom [193, 194]. The distribution functions are written in terms of the potential

$$\begin{aligned} \phi^{(n)}(\mathbf{r}^n) &:= -k_B T \ln g^{(n)}(\mathbf{r}^n) \\ &= U_n + \Delta\Omega - n\mu^{\text{ex}}, \end{aligned} \tag{4.3}$$

which we call the *generalised potential of mean force*. For the case $n = 2$ this reduces to the usual potential of mean force in the liquid state literature [12].

This completes our proof that the correlations can be transformed to a potential, and we can proceed with a geometrical construction for $\Delta\Omega$.

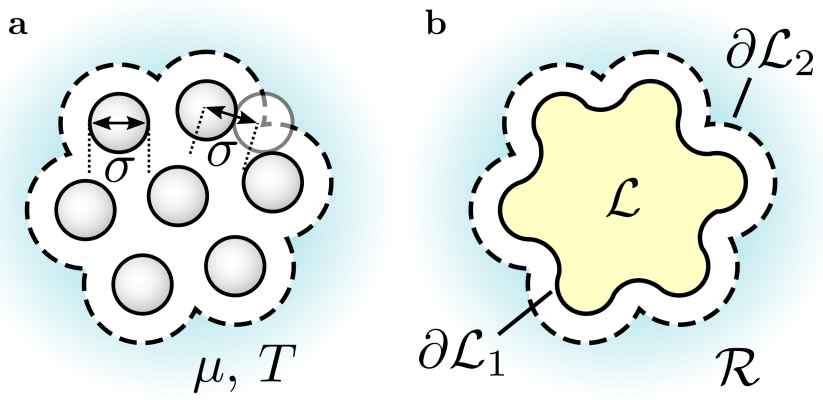

Figure 4.1: The system considered for many-body correlations showing (a) the local particles surrounded by the remaining liquid acting as a thermal reservoir at fixed chemical potential and temperature, and (b) possible partitions of space into the local $\mathcal{L}$ and remaining $\mathcal{R}$ components for two choices of dividing surface: $\partial\mathcal{L}_1$ is the molecular surface while $\partial\mathcal{L}_2$ is the solvent accessible surface (see discussion around Eq. (4.9)).

4.2.2 Representing the insertion cost as a solvation problem

For systems with excluded volume interactions, we can divide the space into a local component $\mathcal{L} \subset \mathbb{R}^d$ of volume $V_\mathcal{L}$ inaccessible to solvent degrees of freedom and the remaining space $\mathcal{R} = \mathbb{R}^d \setminus \mathcal{L}$ of volume $V_\mathcal{R}$ filled by the rest of the liquid (Fig. 4.1). The total volume is $V = V_\mathcal{L} + V_\mathcal{R}$ so the homogeneous grand potential is

$$\Omega_{\text{hom}} = -pV.$$

After inserting the inhomogeneity the total volume accessible to the rest of the liquid will be reduced by $V_\mathcal{L}$, so the grand potential becomes

$$\Omega_n = -pV_\mathcal{R} + \Omega_{\text{ex}}[\partial\mathcal{L}],$$

where Ω_{ex} is an excess term brought about by the introduction of a dividing surface $\partial\mathcal{L}$ between the two liquid components. Subtracting these two expressions gives

$$\Delta\Omega := \Omega_n - \Omega_{\text{hom}} = pV_\mathcal{L} + \Omega_{\text{ex}}[\partial\mathcal{L}].$$

This dividing surface has area $A_{\partial\mathcal{L}}$, creating a surface tension γ so we can write the excess term as

$$\Omega_{\text{ex}}[\partial\mathcal{L}] = \gamma[\partial\mathcal{L}]A_{\partial\mathcal{L}}$$

which is a formal definition of surface tension and depends on the choice of dividing surface (see two examples in Fig. 4.1(b)). We know from density functional theory [65] that the excess free energy is a functional of the density profile, which will in turn depend on the shape of the boundary; we write $\gamma = \gamma[\partial\mathcal{L}]$ to indicate this functional dependence on the surface shape. The *solvation form* of the inhomogeneous grand potential term in (4.3) is then

$$\Delta\Omega[\mathcal{L}] = pV_\mathcal{L} + \gamma[\partial\mathcal{L}]A_{\partial\mathcal{L}}. \tag{4.4}$$

The problem of determining the n-particle distributions has been reduced to a solvation problem: we must find the surface tension between a solute (the specific local arrangement) and a solvent (the rest of the liquid). We will use the solute–solvent terminology, but one could also think of local–bulk nomenclature.

4.3 Scaled particle ansatz

In every formulation of scaled particle theory one considers a hard *spherical* solute of radius R. In most approaches, the cost $\Delta\Omega$ is assumed to have an analytic expansion in powers of the radius; in classical approaches this was simply postulated, however we will be able provide proper justification below through geometric arguments. Recognising that terms scaling faster than R^3 must be zero for it to remain well-defined in the limit of large solutes leads to the third order polynomial [183]

$$\Delta\Omega(R) = p\,\frac{4\pi R^3}{3} + a_2\,4\pi R^2 + a_1\,4\pi R + a_0\,4\pi, \tag{4.5}$$

where we identified the largest power with the work term pV from comparison with (4.4), and $\{a_0, a_1, a_2\}$ are thermodynamic coefficients describing the subleading corrections. We have chosen to introduce factors of 4π in front of subleading terms to suggest how we will generalise beyond spherical geometries; these are normalisations of the intrinsic volumes, as can be seen by comparison with Table 2.2. Specifically, these terms can be identified with the volume, surface area, and integrated mean and Gaussian curvatures. For a general solute $K \subset \mathbb{R}^3$ we then write the morphometric insertion cost as[66]

$$\Delta\Omega[K] = pV[K] + a_2 A[K] + a_1 C[K] + a_0 X[K]. \tag{4.6}$$

All of these functionals act on K but the latter three can also be *expressed* as surface integrals, as given by (2.5). For a spherical solute these reduce to the values given in (4.5), so this represents a proper generalisation of SPT for more general geometries.

We now give a brief justification of the above *ansatzes*, in particular why there are only four terms in the expansion. Radius is the only natural parameter for a sphere, however for more general geometries there might be arbitrarily many parameters so one may wonder if they should be included in a general geometric expansion. Nevertheless, we can make compelling arguments using integral geometry, introduced in section 2.1, to only retain the terms listed. Most notably, the terms included are the *only* physically meaningful size measures (cf. section 2.1.2), and so $\Delta\Omega$ is strictly extensive if it is a linear combination of these measures[67]. This argument was first applied to hard sphere solvation in Ref. [39].

The central assertion of the morphometric approach is that the insertion cost $\Delta\Omega$ *exactly* possesses the properties above, providing the connection between geometry and thermodynamics [39]. The morphometric form (4.6) then follows. In addition to providing a more general *ansatz* than SPT, this approach lays out its underlying assumptions explicitly eschewing the *ad hoc* way in which the original SPT *ansatz* (4.5) was obtained. Moreover, classical SPT assumes hard spheres from the outset while our generalisation based on integral geometry is more flexible, allowing for generalisations to mixtures, more realistic pair potentials and non-spherical particles without compromising its assumptions.

The morphometric approach is certainly an approximation, as the insertion cost will not rigorously possess the properties of size measures in

[66] This *ansatz* is identical to the result we obtained as a limit of FMT in (2.109), up to different normalisations of the intrinsic volumes. We will not emphasise this point, as our intent is to develop the ideas independent of FMT with the goal of arriving at a more flexible theory which can be specialised to the correlation functions.

[67] See discussion on extensivity and references cited around equations (2.1) and (2.6), as well as Hadwiger's theorem (2.15).

reality. This approximation must break down approaching a critical point if the interaction potential features attractions, because a diverging bulk correlation length would violate the additivity assumption. Similarly, attractions would lead to surface phase transitions involving the formation of wetting or drying films [196, 197], which cannot be captured by this analytic theory. Even for hard spheres we expect to see singularities which cannot be captured by the morphometric *ansatz* (4.6). Notably, in SPT $\Delta\Omega$ is known to contain singularities in its high order derivatives with solute radius[68]; these non-analytic terms result from violations of the additivity assumption. Nevertheless, the approximation has been found to be numerically accurate in hard spheres when compared with simulations [177–182] so these violations should be small[69].

[68] We review the original argument for this from Ref. [183] in Appendix A. This argument is quite general, demonstrating that *any* analytic form of $\Delta\Omega$ in terms of geometric quantities cannot be exact.

[69] Below the freezing density at least, where these numerical tests were performed.

4.4 Obtaining thermodynamic coefficients

We will consider a single-component hard sphere fluid, for particles of diameter σ and bulk volume fraction η. We will take the morphometric *ansatz* (4.6) and obtain coefficients for this system using scaled particle arguments. However, unlike the classical arguments this *ansatz* is more general in its scope; we will exploit this feature of the morphometric approach to construct new theories suitable for the treatment of many-body correlations with high accuracy. Before we obtain new coefficients we will rederive the classical SPT and the White Bear II coefficients. The latter set of coefficients was originally obtained as a limiting case of FMT [96]; here we obtain them through purely scaled particle arguments, which lays the groundwork for construction of the new coefficients.

All coefficients we give are for the molecular geometry bounded by the *molecular surface* ($\partial\mathcal{L}_1$ in Fig. 4.1b), the surface where interactions occur between the solute and a test particle representing the remaining liquid. However, it is usually more convenient to do calculations with the excluded geometry: the space inaccessible to the *centre* of a test particle bounded by the *solvent accessible surface* ($\partial\mathcal{L}_2$ in Fig. 4.1b). The original definitions of these surfaces can be found in Refs. [198, 199]. Note that there is also an infinite family of well-defined parallel surfaces between these two extremes, but they are not widely used in practice so we will not consider them [177]. The choice of dividing surface will change the surface tension, and thus requires new coefficients $\{a_0', a_1', a_2'\}$ i.e.

$$\Delta\Omega[K] = pV_+[K] + a_2'A_+[K] + a_1'C_+[K] + a_0'X_+[K], \tag{4.7}$$

where the excluded geometry terms transform via the canonical relations [42, 45, 96, 177]

$$X_+[K] = X[K], \tag{4.8a}$$

$$C_+[K] = C[K] + \frac{\sigma}{2}X[K], \tag{4.8b}$$

$$A_+[K] = A[K] + \sigma C[K] + \frac{\sigma^2}{4}X[K], \tag{4.8c}$$

$$V_+[K] = V[K] + \frac{\sigma}{2}A[K] + \frac{\sigma^2}{4}C[K] + \frac{\sigma^3}{24}X[K]. \tag{4.8d}$$

It is straightforward to transform between these two conventions via [96, 177]

$$a_0' = a_0 - \frac{\sigma}{2}a_1 + \frac{\sigma^2}{4}a_2 - \frac{\sigma^3}{24}p, \tag{4.9a}$$

$$a_1' = a_1 - \sigma a_2 + \frac{\sigma^2}{4}p, \tag{4.9b}$$

$$a_2' = a_2 - \frac{\sigma}{2}p. \tag{4.9c}$$

The resulting $\Delta\Omega$ will be identical whichever surface is chosen, except when there is a topological change in the molecular surface marking the breakdown of the theory; this is discussed in detail in Ref. [177].

A crucial component of scaled particle approaches is thermodynamic consistency of the (osmotic) pressure (2.63a) which we restate here as[70]

$$\beta p = \rho - \beta f^{\text{ex}} + \rho \left(\frac{\partial \beta f^{\text{ex}}}{\partial \rho} \right)_{V,T}. \tag{4.10}$$

[70] We remind the reader that $f^{\text{ex}} = F^{\text{ex}}/V$ is the (excess) free energy density.

The form most useful for a single-component system comes from taking the derivative with respect to density, and noting the definition of the excess chemical potential

$$\beta\mu^{\text{ex}} = \left(\frac{\beta f^{\text{ex}}}{\partial \rho} \right)_{V,T},$$

giving

$$\left(\frac{\partial \beta p}{\partial \rho} \right)_{V,T} = \rho \left(\frac{\partial \beta \mu}{\partial \rho} \right)_{V,T} = 1 + \rho \left(\frac{\partial \beta \mu^{\text{ex}}}{\partial \rho} \right)_{V,T}. \tag{4.11}$$

Note that the consistency relation (4.10) provides the route to generalising all of our arguments to arbitrary mixtures [25, 64, 79]. As we discussed in 2.2.5, the free energy remains well-defined for polydisperse mixtures if the composition dependence enters only through a set of weighted moments of the density $\{\xi_k\}$. Then (4.10) becomes

$$\beta p = \rho - \beta f^{\text{ex}} + \sum_k \xi_k \left(\frac{\partial \beta f^{\text{ex}}}{\partial \xi_k} \right)_{V,T}. \tag{4.12}$$

For weighted densities consistent with an SPT (or FMT) approach, it has been shown in Ref. [79] that the thermodynamic coefficients for mixtures are determined once an equation of state for the single-component system is known.

4.4.1 Classical scaled particle relations

The key advantage of a geometric expansion of the free energy is that the role of thermodynamics and geometry are kept separate. Thermodynamics only enters through the coefficients $\{p, a_2, a_1, a_0\}$, so they can be determined in simple geometries to obtain a general theory. After determining these coefficients all the complexity of computing $\Delta\Omega$ is reduced to measuring the geometric quantities $\{V, A, C, X\}$ of the specific solute.

Following the protocol of scaled particle theories, we consider the insertion of a hard spherical solute of radius R into the liquid. Assuming the

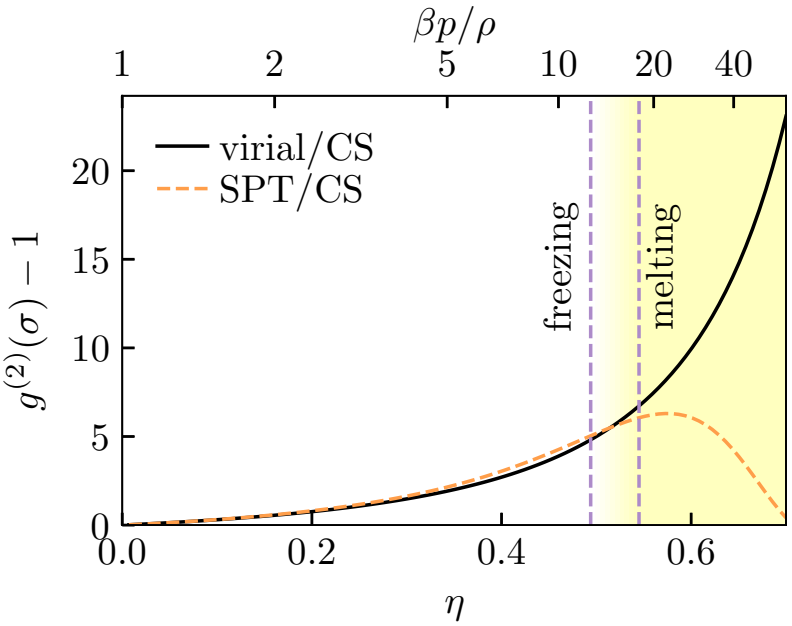

Figure 4.2: Contact values of the radial distribution function against volume fraction η and reduced pressure for the hard sphere liquid using (4.19) with (4.2) and (4.6) for the explicit form of $g^{(2)}$, assuming the Carnahan-Starling (CS) equation of state. Contact values are determined with two sets of morphometric coefficients: SPT/CS (section 4.4.2, specifically (4.23), or equivalently the White Bear II bulk coefficients (2.111) of Ref. [96]) which performs poorly in the supercooled regime (shaded area), and coefficients derived in this chapter (section 4.4.3) using the virial theorem which is exact by construction. The hard sphere freezing and melting volume fractions are indicated by purple dashed lines to show the onset of the supercooled regime.

morphometric form for the insertion cost returns us to the *ansatz* (4.5). The approximate theory is linear so we need *only* 4 equations to set the thermodynamic coefficients. With many thermodynamic relations to choose from the theory is overconstrained in general. We must use physical intuition to choose suitable equations, after which the accuracy of the resulting coefficients can be assessed. Below we give the exact thermodynamic relations for hard spheres which produce the classical SPT coefficients.

It is possible to consider the insertion of a solute with a *negative* radius: the hard core interaction between the two particles only occurs when the solute is 'inside' a solvent particle. In this limit the insertion cost can be determined exactly as [183]

$$\beta\Delta\Omega = -\ln\left(1 - \frac{4\pi\left(R + \frac{\sigma}{2}\right)^3}{3}\rho\right) \tag{4.13}$$

for $-\frac{\sigma}{2} \leq R \leq 0$. It may appear concerning that this result does not possess the morphometric form (4.6); however, this does not discount the validity of the morphometric approach as the nonphysical geometry violates the continuity assumption (section 4.3) because it cannot be approximated by polyhedra. This places the result for $R < 0$ outside the theory's stated regime of validity, however $\Delta\Omega$ is continuous up to its second derivative across $R = 0$ with a discontinuity in its third derivative [183]. In the limit $R \to 0$ the expression above corresponds to the cost of inserting a hard

point giving

$$\beta\Delta\Omega(R=0) = -\ln(1-\eta), \tag{4.14a}$$

$$\beta\left(\frac{\partial\Delta\Omega}{\partial R}\right)_{\mu,V,T}\bigg|_{R=0} = \frac{6\eta}{\sigma(1-\eta)}, \tag{4.14b}$$

$$\beta\left(\frac{\partial^2\Delta\Omega}{\partial R^2}\right)_{\mu,V,T}\bigg|_{R=0} = \frac{12\eta^2+24\eta}{\sigma^2(1-\eta)^2}. \tag{4.14c}$$

Note that (4.14a) can also be justified by considering that the probability of a randomly selected position in space being empty is simply the free volume $1-\eta$.

Together applying (4.14) to (4.5) fixes the coefficients $\{a_0, a_1, a_2\}$, so the theory requires an additional thermodynamic relation to determine the pressure. When $R = \frac{\sigma}{2}$ the solute is equivalent to the solvent particles themselves and we recover $\Delta\Omega = \mu^{\text{ex}}$, so from (4.5) we have

$$\Delta\Omega\left(R=\frac{\sigma}{2}\right) = \frac{\pi\sigma^3}{6}p + \pi\sigma^2\, a_2 + 2\pi\sigma\, a_1 + 4\pi\, a_0 = \mu^{\text{ex}}. \tag{4.15}$$

Combining this expression with the thermodynamic relation (4.11) gives a differential equation for βp whose solution gives the classical SPT coefficients for hard spheres as [87, 183]

$$\beta a_0^{\text{SPT/PY}} = -\frac{\ln(1-\eta)}{4\pi}, \tag{4.16a}$$

$$\beta a_1^{\text{SPT/PY}} = \frac{3\eta}{2\pi\sigma(1-\eta)}, \tag{4.16b}$$

$$\beta a_2^{\text{SPT/PY}} = \frac{6\eta+3\eta^2}{2\pi\sigma^2(1-\eta)^2}, \tag{4.16c}$$

$$\frac{\beta p^{\text{SPT/PY}}}{\rho} = \frac{1+\eta+\eta^2}{(1-\eta)^3}. \tag{4.16d}$$

The equation of state (4.16d) is equivalent to the one obtained through the solution of the Percus-Yevick (PY) integral equation[71]; these two routes have been unified within FMT as the Rosenfeld functional (2.96) [25] which we have already seen produces *identical* coefficients in the bulk limit (2.110).

[71] See section 2.3.4 and Ref. [90].

Before we move on to generalisations of SPT, we will review one more thermodynamic relation which is satisfied by the classical solution (4.16). This emphasises the remarkable degree of self-consistency of SPT, and the additional relation will be used to construct new theories in subsequent sections.

We can relate the radial derivative of $\Delta\Omega(R)$ to the solvent density at contact; by connecting this to the virial theorem we can obtain a new thermodynamic relation. Following Ref. [200] we take the normal derivative of Ω with respect to R, and noting that $\Delta\Omega(R) = \Omega(R) - \Omega_{\text{hom}}$ and the R dependence only enters through the external potential gives

$$\left(\frac{\partial\Delta\Omega}{\partial R}\right)_{\mu,V,T} = \left(\frac{\partial\Omega}{\partial R}\right)_{\mu,V,T} = \int \rho^{(1)}(\mathbf{r})\left(\frac{\partial\phi_{\text{ext}}(\mathbf{r};R)}{\partial R}\right)_{\mu,V,T} d\mathbf{r}, \tag{4.17}$$

where ϕ_{ext} is the external potential (i.e. the potential of the solute). As a reminder, we defined $\rho^{(1)}$ as the equilibrium density profile in (2.33a). As the solute is hard, the external potential and its derivative are zero everywhere except at a distance $\frac{\sigma}{2}$ from the surface where both $\rho^{(1)}$ and ϕ_{ext} are discontinuous. We consider its Boltzmann weight, i.e.

$$e^{-\beta\phi_{\text{ext}}(\mathbf{r})} = \Theta\left(|\mathbf{r}| - R - \frac{\sigma}{2}\right).$$

Taking the (distributional) derivative of both sides gives

$$\beta\left(\frac{\partial\phi_{\text{ext}}(\mathbf{r})}{\partial R}\right)_{\mu,V,T} = \delta\left(|\mathbf{r}| - R - \frac{\sigma}{2}\right) e^{\beta\phi_{\text{ext}}(\mathbf{r})}.$$

Inserting this expression into (4.17) and using the fact that $\rho^{(1)}(\mathbf{r})e^{\beta\phi_{\text{ext}}(\mathbf{r})}$ is a continuous function (cf. Ref. [12]) gives the contact theorem

$$\beta\left(\frac{\partial\Omega}{\partial R}\right)_{\mu,V,T} = 4\pi\left(R + \frac{\sigma}{2}\right)^2 \rho^{(1)}\left(R + \frac{\sigma}{2}\right)$$

and the contact density in this inhomogeneous system is $\rho^{(1)}(\sigma;\phi_{\text{ext}}) := \rho^{(2)}(\sigma)/\rho = \rho\, g^{(2)}(\sigma)$ recalling the definition of $\rho^{(n)}$ for the homogeneous system[72] (2.29), so we have

$$\begin{aligned}\beta\left(\frac{\partial\Delta\Omega}{\partial R}\right)_{\mu,V,T}\bigg|_{R=\frac{\sigma}{2}} &= \beta\left(\frac{\partial\Omega}{\partial R}\right)_{\mu,V,T}\bigg|_{R=\frac{\sigma}{2}} \\ &= 4\pi\sigma^2\rho\, g^{(2)}(\sigma).\end{aligned}$$

So inserting the SPT *ansatz* (4.5) gives

$$\pi\sigma^2\, p + 4\pi\sigma\, a_2 + 4\pi\, a_1 = \frac{4\pi\sigma^2\rho}{\beta}\, g^{(2)}(\sigma). \tag{4.18}$$

The virial theorem (2.49) in $d = 3$ gives the value of $g^{(2)}(r)$ at contact as

$$g^{(2)}(\sigma) = \frac{3}{2\pi\sigma^3\rho}\left(\frac{\beta p}{\rho} - 1\right), \tag{4.19}$$

which we insert into the right-hand side of (4.18) to obtain the final expression:

$$\pi\sigma^2\, p + 4\pi\sigma\, a_2 + 4\pi\, a_1 = \frac{6}{\beta\sigma}\left(\frac{\beta p}{\rho} - 1\right). \tag{4.20}$$

This relation is satisfied by the coefficients (4.16), which is surprising given that it was obtained from a completely different thermodynamic route and the *ansatz* (4.5) is inexact. Nonetheless, this self-consistency is a testament to the effectiveness of SPT and related approaches.

[72] This argument, due to Percus [201], is ordinarily used to construct integral equation theories based around the Ornstein-Zernike equation (2.84) (cf. Ch. 4 of Ref. [12]).

4.4.2 First generalisation: SPT with an empirical equation of state

In the classical SPT approach described in the previous section, the SPT/PY equation of state emerges as an *output* of the theory. Taking inspiration

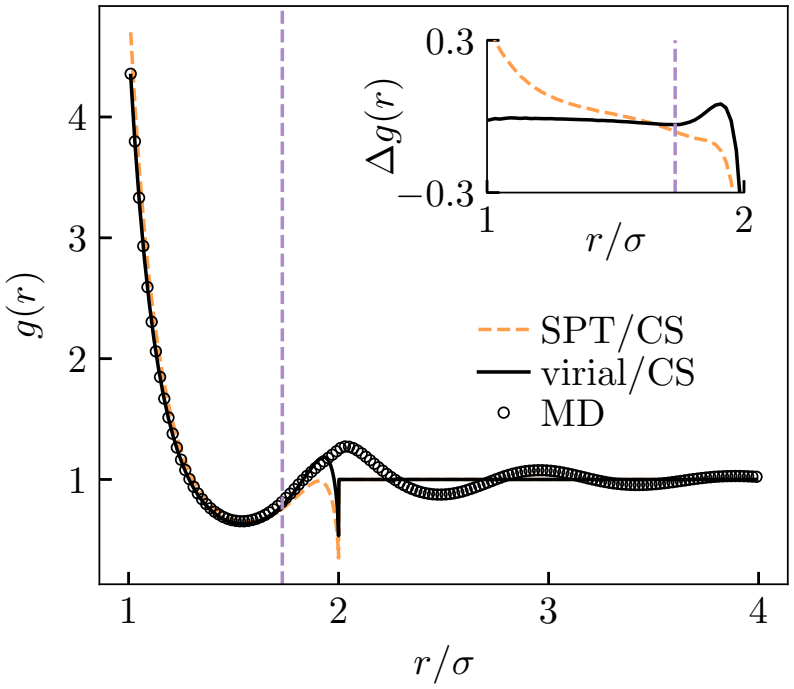

Figure 4.3: Comparing radial distribution functions of the morphometric theories with coefficients of (4.23) (SPT/CS), equivalent to the White Bear II in the bulk limit [96]; and (4.27) with the Carnahan-Starling equation of state (2.104) (virial/CS), against results of molecular dynamics (MD) simulations at volume fraction $\eta = 0.45$. The inset shows the difference between the two theoretical distribution functions and the molecular dynamics. The purple dashed line indicates where the molecular surface self-intersects at $r = \sqrt{3}\sigma$, marking the end of the theory's regime of validity.

from the White Bear free energy functional [84], we reformulate the SPT argument so that the equation of state is an *input* to the theory. In so doing we aim to construct a theory from a more accurate equation of state, with the trade-off being that we must sacrifice some self-consistency. The main equation of state we will impose is the empirical Carnahan-Starling (CS) relation (2.104) known to be accurate across the whole stable liquid regime [15], and even at the high density limits accessible to simulation in the supercooled regime [91] (Fig. 2.1). Since the pressure is now a known input, the excess chemical potential can be determined by integrating (4.11) i.e.

$$\beta\mu^{\text{ex}}[p] = \left(\frac{\beta p}{\rho} - 1\right) + \int_0^\eta \left(\frac{\beta p}{\rho} - 1\right) \frac{d\eta'}{\eta'}. \tag{4.21}$$

To keep the expressions simple we will not evaluate the chemical potential until the very end, but it should be recognised as a known variable wherever it appears.

With the pressure fixed we have three free parameters in the theory $\{a_0, a_1, a_2\}$; we must thus choose three out of the five available thermodynamic relations in (4.14), (4.15) and (4.20) to satisfy[73]. Therefore, we must lose consistency with two of these relations to obtain a more accurate theory for practical applications.

To set the correct energy scale we choose to fix $\Delta\Omega(R = 0)$ and $\Delta\Omega(R = \sigma/2)$ through equations (4.14a) and (4.15) using the chemical potential determined above in (4.21). This in turn imposes the consistency of the osmotic pressure (4.10). For the final equation we choose to set the contact value of $g^{(2)}$ through (4.20) which better represents solutes of interest than the two relations for point geometries at $R = 0$. Solving these three equa-

[73] Attempting to satisfy *all* relations would necessarily require the previously obtained pressure (4.16d).

tions gives the generalised SPT coefficients

$$\beta a_0^{\mathrm{SPT}} = -\frac{\ln(1-\eta)}{4\pi}, \tag{4.22a}$$

$$\beta a_1^{\mathrm{SPT}} = \frac{1}{2\pi\sigma}\left((\eta-3)\frac{\beta p}{\rho} + 2\beta\mu^{\mathrm{ex}}[p] + 2\ln(1-\eta) + 3\right), \tag{4.22b}$$

$$\beta a_2^{\mathrm{SPT}} = -\frac{1}{\pi\sigma^2}\left((2\eta-3)\frac{\beta p}{\rho} + \beta\mu^{\mathrm{ex}}[p] + \ln(1-\eta) + 3\right). \tag{4.22c}$$

It can be verified that inserting the Percus-Yevick equation of state (4.16d) into these expressions yields the previously obtained coefficients (4.16), as expected. For the CS equation of state we obtain

$$\beta a_0^{\mathrm{SPT/CS}} = -\frac{\ln(1-\eta)}{4\pi}, \tag{4.23a}$$

$$\beta a_1^{\mathrm{SPT/CS}} = \frac{1}{2\pi\sigma}\left(\frac{5\eta+\eta^2}{1-\eta} + 2\ln(1-\eta)\right), \tag{4.23b}$$

$$\beta a_2^{\mathrm{SPT/CS}} = \frac{1}{\pi\sigma^2}\left(\frac{\eta(2+3\eta-2\eta^2)}{(1-\eta)^2} - \ln(1-\eta)\right), \tag{4.23c}$$

$$\frac{\beta p^{\mathrm{SPT/CS}}}{\rho} = \frac{1+\eta+\eta^2-\eta^3}{(1-\eta)^3}, \tag{4.23d}$$

which are *identical* to the coefficients derived from the White Bear II (WBII) free energy functional[74]. The exact form of these coefficients differs from that stated in Ref. [96] due to a different definition of the surface, so the equivalence only becomes clear after transforming to the excluded geometry through the canonical relations (4.9). Remarkably, we have obtained these coefficients through a route completely different from their original derivation.

[74] We use a different normalisation of the intrinsic volumes in this chapter, so a_1 and a_0 must be multiplied through by 4π to recover (2.111).

In Ref. [96] the coefficients were determined within FMT by taking the limit of a binary mixture where one component is infinitely dilute. Here we completely avoided FMT, in favour of geometrical arguments similar to the classical SPT approach outlined in the previous section. This suggests that this generalised scaled particle argument is built into the structure of the WBII functional of Ref. [96]; this is not an obvious fact as the derivation of this functional did not explicitly involve these arguments. Rather, the WBII functional was constructed based on a novel extension of the CS equation to mixtures by requiring self-consistency of the pressure in (4.12) [97]. We imposed this relation by setting the chemical potential in (4.15) using the chemical potential obtained via (4.11). It is unclear to us how our final choice of using (4.15) instead of one of the two relations at the origin, i.e. (4.14b) or (4.14c), is built into the WBII functional.

Finally, note that the resulting $g^{(2)}$ obtained from direct evaluation of the potential of mean force (4.3) with the SPT/CS coefficients performs poorly in the supercooled regime compared with the "exact" result from the virial theorem i.e. equation (4.19). To demonstrate this we plot the contact value in Fig. 4.2 for this set of coefficients, finding that it is reasonably accurate until around the freezing density where contact correlations spuriously decay. The next section will detail how to modify this argument to produce coefficients which describe more accurate correlation functions at high densities.

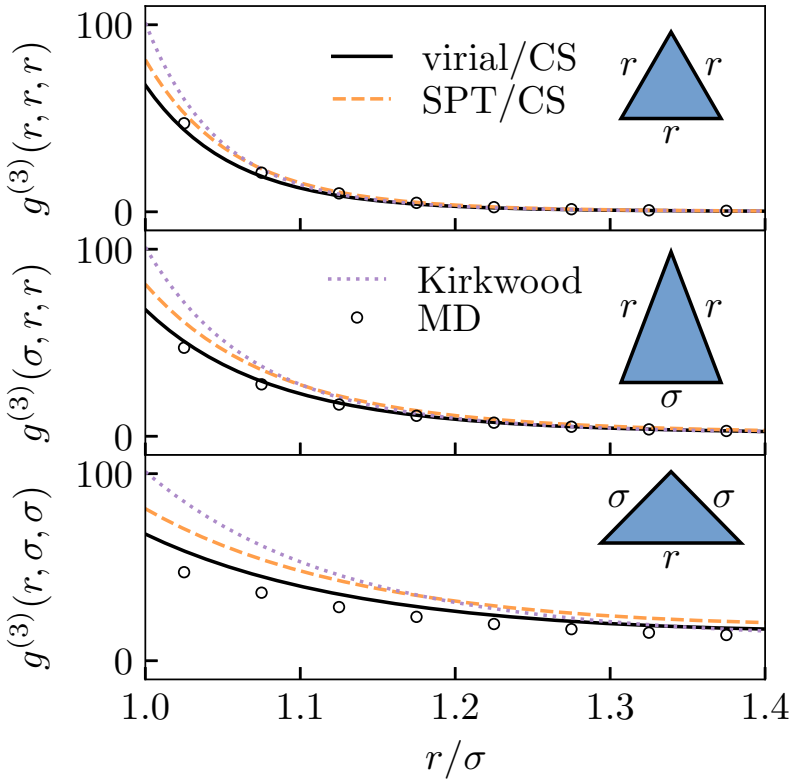

Figure 4.4: Comparison of predicted correlations for triangular geometries against molecular dynamics simulations at volume fraction $\eta = 0.45$.

4.4.3 Second generalisation: self-consistency of the contact value of $g^{(2)}(r)$ with the virial theorem

Our goal is to develop a morphometric theory which produces accurate correlation functions $g^{(n)}$. As described at the end of the last section, the correlation functions produced by an SPT approach are inaccurate at high densities. We will correct the spurious decay of the contact value of the pair distribution function $g^{(2)}(r)$ at high densities by building this into the theory explicitly, with the aim of producing more accurate correlation functions.

The potential of mean force (4.3) for non-overlapping spheres with the morphometric *ansatz* (4.6) is written

$$\begin{aligned}\phi^{(2)}(r) :=& -k_B T \ln g^{(2)}(r) \\ =& pV_3(r) + a_2 A(r) + a_1 C(r) + a_0 X(r) - 2\mu^{\text{ex}}[p]\end{aligned} \tag{4.24}$$

so we need the size measures for the two particle solute resembling a "dumbbell". It is easier to calculate the excluded volume geometry, after which we can obtain the molecular volumes using the canonical relations given in e.g. Ref. [177]. The excluded volume consists of the union of two balls of radius σ separated by a distance r. The geometric properties at contact are

then [177]

$$
\begin{aligned}
X_+(\sigma) &= 4\pi \\
C_+(\sigma) &= \left(6 - \frac{\pi}{2\sqrt{3}}\right)\pi\sigma, \\
A_+(\sigma) &= 6\pi\sigma^2, \\
V_+(\sigma) &= \frac{9\pi\sigma^3}{4}.
\end{aligned}
$$

Transforming to the parallel molecular surface using the inverse transformation of (4.8) gives the solute parameters as

$$C(\sigma) = \left(4 - \frac{\pi}{2\sqrt{3}}\right)\pi\sigma, \tag{4.25a}$$

$$A(\sigma) = \left(1 + \frac{\pi}{2\sqrt{3}}\right)\pi\sigma^2, \tag{4.25b}$$

$$V(\sigma) = \left(\frac{7}{12} - \frac{\pi}{8\sqrt{3}}\right)\pi\sigma^3. \tag{4.25c}$$

Inserting these volumes into (4.24) and applying the virial theorem (4.19) for the contact value of $g^{(2)}$ gives the final expression

$$
\begin{aligned}
&p\left(\frac{7}{12} - \frac{\pi}{8\sqrt{3}}\right)\pi\sigma^3 + a_2\left(1 + \frac{\pi}{2\sqrt{3}}\right)\pi\sigma^2 + a_1\left(4 - \frac{\pi}{2\sqrt{3}}\right)\pi\sigma + a_0\,4\pi \\
&= 2\mu^{\mathrm{ex}}[p] - \beta^{-1}\ln\frac{3}{2\pi\rho\sigma^3}\left(\frac{\beta p}{\rho} - 1\right).
\end{aligned} \tag{4.26}
$$

We will use this last expression instead of the contact theorem (4.20) in order to obtain new coefficients. Together (4.14a), (4.15) and (4.26) solve to give coefficients:

$$\beta a_0^{\mathrm{virial}} = -\frac{\ln(1-\eta)}{4\pi}, \tag{4.27a}$$

$$
\begin{aligned}
\beta a_1^{\mathrm{virial}} = \frac{1}{(\sqrt{3}\pi - 4)\pi\sigma}\Bigg[&\left(5 - \frac{5\pi}{2\sqrt{3}}\right)\eta\frac{\beta p}{\rho} - \left(2 - \frac{\pi}{\sqrt{3}}\right)\beta\mu^{\mathrm{ex}}[p] \\
&+ \frac{\pi}{\sqrt{3}}\ln(1-\eta) + 2\ln\left(\frac{\frac{\beta p}{\rho} - 1}{4\eta}\right)\Bigg],
\end{aligned} \tag{4.27b}
$$

$$
\begin{aligned}
\beta a_2^{\mathrm{virial}} = -\frac{1}{(\sqrt{3}\pi - 4)\pi\sigma^2}\Bigg[&\left(6 - \frac{2\pi}{\sqrt{3}}\right)\eta\frac{\beta p}{\rho} - \frac{\pi}{\sqrt{3}}\beta\mu^{\mathrm{ex}}[p] \\
&+ \left(4 - \frac{\pi}{\sqrt{3}}\right)\ln(1-\eta) + 4\ln\left(\frac{\frac{\beta p}{\rho} - 1}{4\eta}\right)\Bigg].
\end{aligned} \tag{4.27c}
$$

We refer to coefficients obtained this way for the CS pressure (2.104) as virial/CS, but we will not give them explicitly. Unlike the WBII coefficients above these are new. The pair correlation produced by these coefficients (black line in Fig. 4.2) is self-consistent with CS at contact by construction.

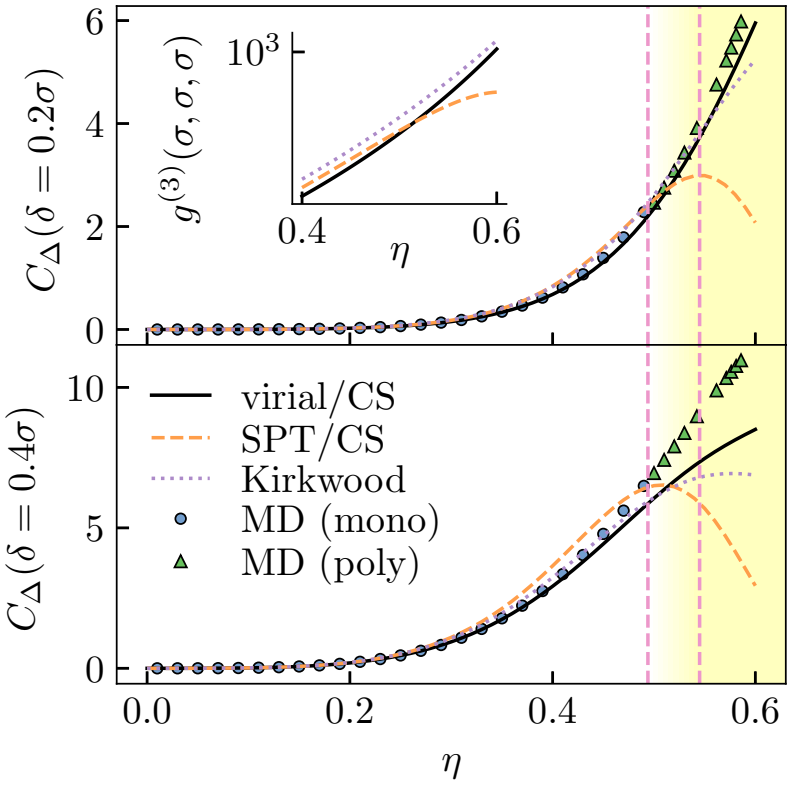

Figure 4.5: Concentration of triangles in the hard sphere liquid with side lengths $r, s, t \in [\sigma, \sigma + \delta]$ versus volume fraction. Direct measurements by molecular dynamics using a single-component system and an 8% polydisperse system, while the lines show predictions from the morphometric theories described in text. The hard sphere freezing and melting volume fractions are indicated by pink dashed lines to show the onset of the supercooled regime. Inset: contact value of $g^{(3)}$ showing how the errors in the SPT/CS theory arise from underestimation close to contact.

4.5 Numerical results

We apply the thermodynamic coefficients determined in previous sections for a system of hard spheres to obtain two– and three–body distribution functions using the generalised potential of mean force (4.3) with the morphometric approach (4.6), and compare these against molecular dynamics simulations. For the analytics we determine the input geometric quantities $\{V, A, C, X\}$ using the algorithms of Refs. [202, 203]. For the simulations we performed event-driven molecular dynamics of $N = 1372$ monodisperse hard spheres using the DynamO software package [17]. We measure the pair and triplet distribution functions $g^{(2)}$ and $g^{(3)}$ for simulations at $\eta = 0.45$. For simulations above freezing $\eta \simeq 0.494$ we used a 5-component equimolar distribution with $\sim 8\%$ polydispersity.

For $g^{(2)}$ shown in Fig. 4.3 we find the virial/CS theory outperforms the SPT/CS theory even away from contact. The agreement with the molecular dynamics simulations is excellent, until $r \gtrsim \sqrt{3}\sigma$ where the solute boundary self-intersects and outside the regime of the theory's validity (see discussion in Ref. [177]). The physical interpretation of this breakdown is that for $r > \sqrt{3}\sigma$ interactions between solvent particles can occur *through* the solute, so these correlations will not be captured by the theory. Only the contact value was fixed, so accuracy for $r > \sigma$ was not guaranteed; the accuracy is a welcome bonus. We can quantify this accuracy through the integrated value

$$z(\delta) = 4\pi \int_\sigma^{\sigma+\delta} \rho^{(2)}(r)\, r^2\, dr \tag{4.28}$$

shown in the top panel of Fig. 4.6 where we take $\delta = 0.4\sigma$.

Now we look at the three-body correlation functions. Triplet geometries are characterised by a triangle of side lengths r, s, t so $g^{(3)} = g^{(3)}(r, s, t)$. We also compare the morphometric theories against the Kirkwood approximation [172] i.e.

$$g^{(3)}(r, s, t) \approx g^{(2)}(r)g^{(2)}(s)g^{(2)}(t) \tag{4.29}$$

where we take the values of $g^{(2)}$ from the virial/CS theory because of its already demonstrated accuracy at the two body level. Comparison of the morphometric correlation functions, including with the Kirkwood closure, against molecular dynamics are shown in Fig. 4.4. The virial/CS closure most closely matches the simulations at high densities, suggesting the theory is suitable for modelling complex many-particle local structures [1]. To illustrate this we consider the concentration of triangles with side lengths $r, s, t \in [\sigma, \sigma + \delta]$ in the bulk liquid, from (2.29) we find this as[75]

$$C_\Delta(\delta) = 8\pi^2 \int_\sigma^{\sigma+\delta} \int_\sigma^{\sigma+\delta} \int_\sigma^{\sigma+\delta} \rho^{(3)}(r, s, t)\, rst\, drdsdt. \tag{4.30}$$

Comparison of this quantity against molecular dynamics simulations shows similar levels of accuracy for small δ, though the performance decreases as it is increased above the first minimum of the $g^{(2)}(r)$; this is not surprising as our virial closure emphasised accuracy at contact. Notably, the Kirkwood approximation performs surprisingly well at the three-body level in both of these tests.

Next we compare the theories' predicted surface tension against simulation data. The surface tension at a planar wall is simply a_2 because it conjugates with the area. In Ref. [205] a highly accurate a_2 was measured for hard spheres through extensive simulation, which was parameterised by the following expression

$$\beta a_2 = \frac{1}{\pi\sigma^2} \left(\frac{\eta(2 + 3\eta - \frac{9}{5}\eta^2 - \frac{4}{5}\eta^3 - (5 \times 10^4)\eta^{20})}{(1 - \eta)^2} - \ln(1 - \eta) \right). \tag{4.31}$$

Comparing this highly accurate expression against the values predicted from the morphometric coefficients, we find the virial/CS surface tension is less accurate than the SPT/CS prediction (Fig. 4.6) despite its superior correlation functions at high densities. One of the great strengths of the SPT/CS theory is its accuracy in the planar limit [96], so this suggests that the virial/CS theory sacrifices asymptotic accuracy for more self-consistency in the correlation functions. For this reason, SPT/CS coefficients may give more accurate grand potentials (and thus correlations) for large solutes where the surface becomes approximately planar.

[75] We state the measure here without proof, though we present a general method to obtain this (at least numerically) for arbitrary n in the next chapter. The analytic form $rst\, drdsdt$ for the specific three-body case is presented in e.g. Ref. [204].

4.6 Conclusions

We have presented the morphometric approach as a generalisation of SPT, thus placing the scaled particle *ansatz* on more precise and physically motivated assumptions i.e. those underlying the theorems of integral geometry. Using the scaled particle approach we have systematically derived several

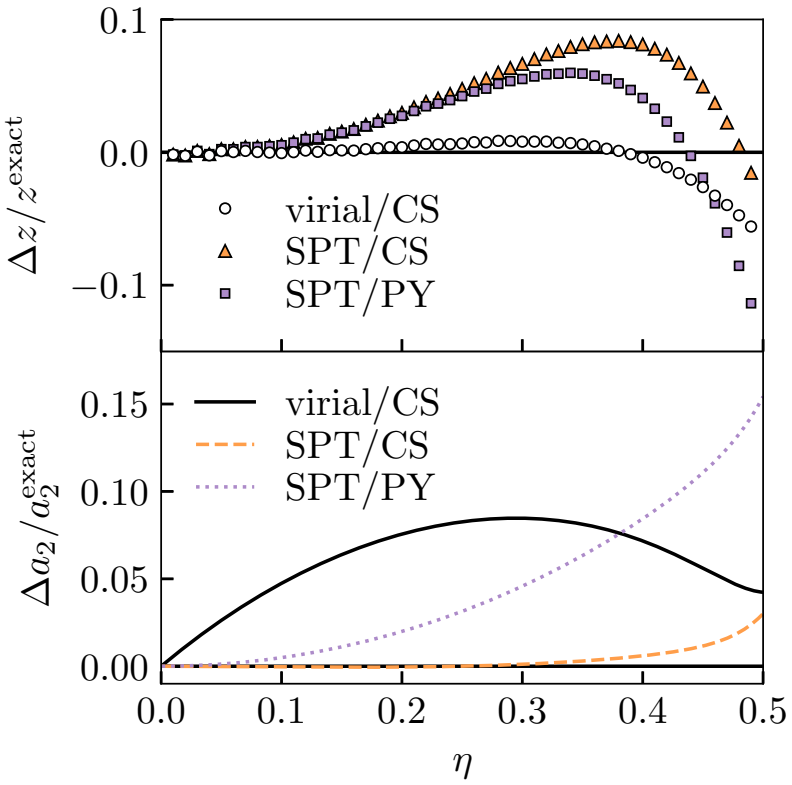

Figure 4.6: Errors in different morphometric theories for hard spheres. Top panel: error in the coordination defined in (4.28), giving the average number of neighbours in the shell $r < 1.4\sigma$ around a particle. Bottom panel: planar surface tensions against volume fraction, using the highly accurate result (6.34) from Ref. [205] valid until $\eta \sim 0.5$. The theories compared are virial/CS, new coefficients given in (4.27); SPT/CS, equivalent to the White Bear II [96] given in (4.23); and SPT/PY, the classical scaled particle theory [183] given in (4.16).

theories for the hard sphere liquid. This included the classical SPT solution and the morphometric theory obtained in the bulk limit of free energy functionals based on the CS equation of state[76], although our method of deriving the latter theory is new. The third theory we derived is particularly suited for treating many-body correlations, which we used to accurately treat local structures in the hard sphere liquid in Ref. [1].

[76] See the discussion around (2.111) in section 2.3.4 for details of the original derivation.

In principle this approach could be extended to simple liquids where the interaction potential can be approximated as a perturbation around a hard core. However, as we exploited features of the hard sphere interaction potential to achieve closed form expressions, more realistic interaction potentials would likely require numerical expressions. Additionally, attractions can introduce non-analytic behaviour through surface phase transitions not present in our theory [196, 197]. In chapter 6 we provide a generalisation to arbitrary mixtures of hard (convex) particles in arbitrary dimensions.

By making the underlying assumptions explicit we can better understand the limits of the theory: any deviation from the morphometric/SPT *ansatz* must be due to a violation of translation/rotation invariance, additivity or continuity. The fact that these theories are very accurate for hard spheres suggests that the assumptions are only weakly violated for this system. While translational/rotational invariance and continuity are physically plausible conditions on $\Delta\Omega$, additivity is a very strong assumption. In particular, we expect significant deviations from additivity where the liquid develops a static length scale exceeding the size of the solute [39]. As such, we expect the validity of the morphometric approach to require

the solute to be larger than the point-to-set length [142], which acts as an upper bound for all structural length scales [206]. The morphometric *ansatz* must break down approaching a critical point, so it cannot be used to obtain asymptotics in the event of a thermodynamic glass transition.

Finally, we remark that while it is tempting to call the treatment of bulk degrees of freedom with the morphometric approach mean-field, this is not a completely accurate characterisation. Mean-field theories typically become formally exact in the limit of infinite spatial dimensions, where the thermodynamic role of fluctuations disappears. By contrast, the morphometric approach (and related theories like SPT and FMT) become formally exact in the one-dimensional limit of hard rods[77]. Though this theory does not explicitly describe fluctuations, they are built into the choice of thermodynamic coefficients entering the theory. In this sense it is more accurate to describe the morphometric approach (and related theories) as an *excluded volume* theory, or as a *free volume* theory because the thermodynamics only shows divergent behaviour as $\eta \to 1$.

[77] We will discuss this limit in more detail in chapter 6.

Chapter 5

Local structure in the hard sphere liquid

hardball 1.1 *informal*
Uncompromising and ruthless methods or dealings.

Oxford English Dictionary (2019).

This chapter applies the theory developed in the previous chapter to the treatment of local structures in the hard sphere liquid. Using the framework of many-body correlations and the morphometric approach, we calculate absolute free energies of local geometric motifs. We find these to be in excellent quantitative agreement with molecular dynamics simulations across the liquid and supercooled liquid regimes. We find a bimodality in the density library of states where fivefold symmetric structures appear lower in free energy than fourfold symmetric structures, and from a single reaction path predict an Arrhenius-like scaling of local relaxation dynamics. The method provides a new route to assess changes in the free energy landscape at volume fractions dynamically inaccessible to conventional techniques.

The majority of this chapter consists of work published as Ref. [1]. Towards the end of this chapter we introduce a new unpublished method for analytical calculations. This has the potential to improve the efficiency of evaluating hard sphere free energies, as well as treat the saddles of the hard sphere energy landscape to make a connection with dynamics. The details are somewhat technical however, so we have relegated them to Appendix C.

5.1 Introduction

While mean-field theories provide insight into complex phenomena, physical accuracy is ensured only by a proper treatment of correlations. For example, the simplest case of two-body correlations is at the foundation of predictive theories of the liquid state (section 2.2), colloids, and complex plasmas [207, 208]. In particular, the thermodynamics of simple liquids with solely pairwise interactions can be exactly expressed in terms of two-body correlations

(section 2.2.3). However, to resolve these integrated quantities *spatially* into structural motifs, and *temporally* into specific dynamical events, one needs to calculate many-body correlations. While such a many-body approach may often be neglected in normal liquids, long-standing challenges such as the dramatic dynamical changes occurring in supercooled liquids approaching their glass transition [109, 110] and phase transitions such as crystal nucleation [209] call for a many-body description.

In the case of supercooled liquids, theories based on pair correlations such as the standard mode-coupling framework [210] fail to account for activated events thus predicting a spurious ergodicity breaking transition [99, 116]. Activated dynamics are often rationalised through collective (i.e. many-body) effects within contrasting thermodynamic and purely kinetic scenarios [119–121, 157, 169, 174]. These include exact mean-field results in high dimensions [122, 129] whose relevance to the dynamics of finite-dimensional systems is hotly debated [154]. A finite-dimensional theoretical description of many-body effects is therefore much needed. We discussed the various theories mentioned above in more detail in chapter 3.

However, many-body correlations are challenging to compute and typically combine both energetic and entropic contributions. Physical insight can be gleaned by exploring the potential energy landscape of isolated clusters [146, 211], but such methods are only exhaustive for small system sizes. This limitation has been partly addressed by embedding clusters in a mean-field approximation of the surrounding liquid [212, 213]. Nonetheless, this approach neglects by construction the intra-cluster entropic contributions that may dominate in the supercooled regime of interest. Furthermore, computer simulations, which naturally deliver full many-body correlations are limited in the range of dynamics they can access, hampering an approach to the glass transition, except for recent developments with certain models [91].

In this chapter we place theoretical predictions of many-body local structure on a fundamentally more rigorous footing using inhomogeneous liquid state theory [65], which we reviewed in section 2.3 and advanced in chapter 4. Using the morphometric approach to treat the many-body interactions between a local subsystem and the remaining liquid, we can directly access the many-body *free* energy of local arrangements of particles. This allows us to predict the populations of specific local structures[78] in the bulk system across the entire liquid phase, and beyond the dynamically accessible supercooled regime.

[78] We have actually already seen two simple examples of this in section 4.5: the concentrations of the dimer ($n = 2$) and triangle ($n = 3$) structures in (4.28) and (4.30). The aim of this chapter is to generalise to arbitrary n.

5.2 Free energy of local structures

From the definition of the n-particle density (2.29) as a probability density function, the total number of a local structure in a system volume V is

$$\mathcal{N} = \frac{1}{n!} \int_{\mathcal{Q}} \rho^n g^{(n)}(\mathbf{r}^n)\, d\mathbf{r}^n, \tag{5.1}$$

where $\mathcal{Q}$ is the domain *defining* the particular local structure. In terms of the potential of mean force $\phi^{(n)}$ defined in (4.3) this would be written

equivalently as

$$\mathcal{N} = \frac{1}{n!}\int_{\mathcal{Q}} \rho^n \exp\left(-\beta\phi^{(n)}(\mathbf{r}^n)\right) d\mathbf{r}^n,$$

which has a similar structure as the canonical partition function (2.22) so we can think of structure population $\mathcal{N}$ as being the equivalent partition function in our ensemble[79]. From the latter observation we could define a free energy for the local structure from $-k_BT\ln\mathcal{N}$, but we will find it more useful to define the free energy as an excess quantity. Specifically, we exploit translational invariance of $\phi^{(n)}$ in the uniform liquid to integrate the centre of mass over the system volume, as in

$$\mathcal{N} = \frac{\rho^n V}{n!}\int_{\mathcal{D}} g^{(n)}(\mathbf{r}^{n-1})\, d\mathbf{r}^{n-1}, \tag{5.2}$$

defining the internal structure space $\mathcal{D}$ through $\mathcal{Q} = \mathcal{D}\times V^d$. The prefactor $\rho^n V$ is the trivial scaling of the ideal gas, so we define the free energy of the structure through the excess quantity[80]

$$e^{-\beta F} = \frac{\mathcal{N}}{\sigma^{d(n-1)}\rho^n V},$$

with powers of particle diameter σ introduced to make the right-hand side dimensionless. Note that $\mathcal{N}/V$ is the *concentration* of the structure, so the right-hand side could be thought of as an excess concentration. Written explicitly, the free energy of the local structure is

$$\begin{aligned}\beta F &= -\ln\left(\frac{1}{\sigma^{d(n-1)}n!}\int_{\mathcal{D}} g^{(n)}(\mathbf{r}^{n-1})\, d\mathbf{r}^{n-1}\right),\\ &= -\ln\left(\frac{1}{\sigma^{d(n-1)}n!}\int_{\mathcal{D}} \exp\left(-\beta\phi^{(n)}(\mathbf{r}^{n-1})\right) d\mathbf{r}^{n-1}\right).\end{aligned} \tag{5.3}$$

Evaluating this free energy thus requires a closure for $\phi^{(n)}$, a definition of the structure to set integration limits through $\mathcal{D}$, and a method of actually doing the integration.

We calculate $\phi^{(n)}$ from its definition (4.3) and using the morphometric *ansatz* (4.6) as a closure for $\Delta\Omega$. Our focus is on $d = 3$, so we use the virial route coefficients (4.27) with the Carnahan-Starling equation of state (2.104) because the resulting correlation functions are highly accurate (cf. section 4.5). We have already seen how this equation of state is accurate at high densities (Fig. 2.1), though it is worth emphasising that it must fail at some point setting limits on our approach. We calculate the morphological quantities $\{V, A, C, X\}$ using an algorithm described in Ref. [203], which we have extended to calculate curvature measures (see details in Appendix B).

In conventional energy landscape approaches, a structure[81] would be defined by the region, or *basin*, surrounding an energy minimum called the *inherent state* [127, 146, 214]. Defining the location of the inherent state as

$$\mathbf{y}^* := \underset{\mathbf{y}\in\mathcal{D}}{\arg\min}\left(\phi^{(n)}(\mathbf{y})\right),$$

[79] Formally, this is the *semi-grand canonical ensemble* because there is a chemical potential μ for the bulk component, but also a fixed number of particles for the local component n.

[80] In previous chapters we used the symbol F to refer to the Helmholtz free energy; here it will *only* refer to the free energy of a local structure.

[81] Energy landscape approaches are actually more general than just pertaining to local structures, as they could in principle refer to the landscape of a macroscopic system as they do in e.g. mean field approaches (cf. section 3.3). It is only in this context of small system sizes that they refer to local structures.

with $\mathbf{y}$ as shorthand for $\mathbf{r}^{n-1}$. The partition function would then be evaluated via a perturbation theory around the inherent state, i.e. from the Taylor expansion [146]

$$\phi^{(n)}(\mathbf{y}) = \phi^{(n)}(\mathbf{y}^*) + \frac{1}{2}(\mathbf{y}-\mathbf{y}^*)\cdot\nabla\nabla\phi^{(n)}(\mathbf{y}^*)\cdot(\mathbf{y}-\mathbf{y}^*) + \mathcal{O}(\mathbf{y}^3)$$

which is valid in the case of *smooth* potentials where $\nabla\phi^{(n)}(\mathbf{y}^*) = 0$. Then, [146]

$$\begin{aligned}\int_{\mathcal{D}} e^{-\beta\phi^{(n)}(\mathbf{y})}d\mathbf{y} &\simeq e^{-\beta\phi^{(n)}(\mathbf{y}^*)}\int_{\mathcal{D}}\exp\left(-\frac{\Delta\mathbf{y}\cdot\mathbf{H}\cdot\Delta\mathbf{y}}{2}\right)d\mathbf{y} \\ &\approx \sqrt{\frac{(2\pi)^{d(n-1)}}{\det\mathbf{H}}}e^{-\beta\phi^{(n)}(\mathbf{y}^*)}\end{aligned} \tag{5.4}$$

where $\mathbf{H} = \nabla\nabla\beta\phi^{(n)}(\mathbf{y}^*)$ is the (positive-definite) Hessian matrix and $\Delta\mathbf{y} = \mathbf{y}-\mathbf{y}^*$, and in the latter line the integral is taken over all of space (as an approximation) using the multivariate Gaussian integral[82]. This method is variously referred to as the *saddlepoint approximation*, *Laplace's method* or the *harmonic approximation* in different communities. This approach fails in hard particle systems because the pair potential is pathological: $\nabla\phi^{(n)}(\mathbf{y}^*) \neq 0$, the Hessian generally has negative eigenvalues and the integral cannot be approximated over all of space.

[82] As a simplification in this step we ignored rigid rotations, which cannot be treated perturbatively in general. We give the correct treatment of rotations in section 5.3.

As the hard sphere pair potential is singular, we require non-perturbative methods to evaluate the free energy which we will introduce in sections 5.4 and 5.5. We will begin by proposing an operational definition for the structures so that we have a domain of integration.

5.3 How do we define a local structure?

An ideal definition of local structures would exactly partition the phase space of possible states within the liquid, so that the free energy and configurational entropy with varying lengthscale (through n) could be determined. This would allow direct comparison with the mean-field of glass (sections 3.3 and 3.4), particularly with equations (3.13) and (3.14). In an attempt to work towards this ideal, we develop an approximate coarse-graining scheme borrowing intuition from traditional energy landscape approaches.

Towards the end of the previous section we indicated an approach which treats structures as perturbations from inherent states. This approach has been highly successful in advancing the understanding of colloidal and molecular clusters [215, 216], liquids [214, 217, 218], glasses [127, 219] and proteins [146]. To remain as close as possible to the spirit of this approach, we choose to define structures starting from energy minima. The minima of $\phi^{(n)}$ occur around contact in hard spheres. To justify this, consider that the dominant term in the morphometric approach (4.6) is the volume term pV, which is minimised when particles are as compact as possible i.e. at contact; we cannot prove this rigorously, but we have yet to find a counter example.

A complete list of rigid packings of hard spheres for $n \leq 14$ particles has been diligently determined in Refs. [33, 34, 211, 220], which we use as

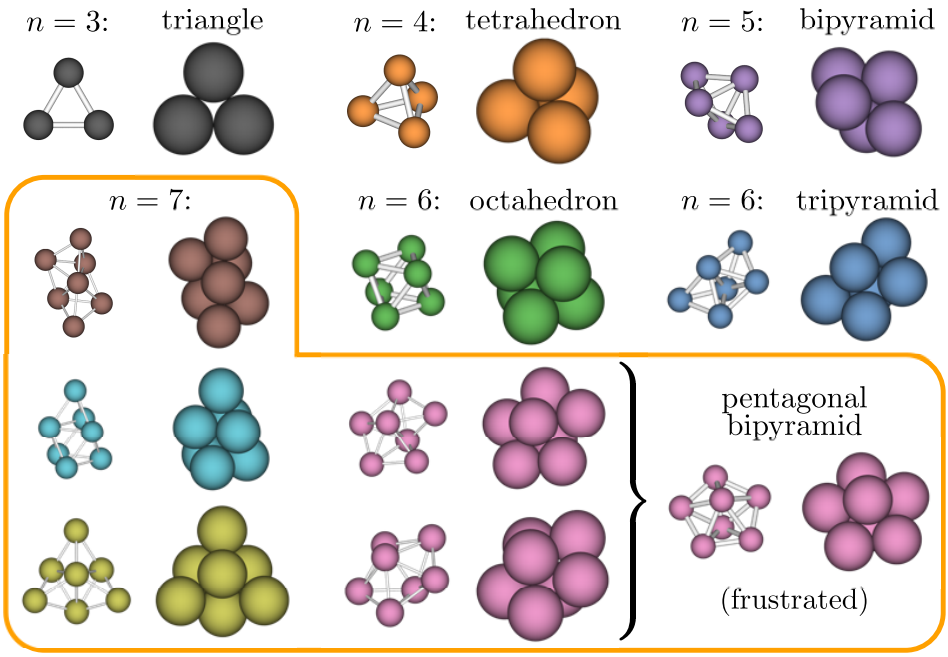

Figure 5.1: Rigid sphere packings for $3 \leq n \leq 7$ particles, as determined in Refs. [33, 211]. For each packing we show their bond network with particles at half radius (left) and with full size particles (right). There are 5 possible rigid packings for $n = 7$, of which two correspond to variants of the frustrated pentagonal bipyramid introduced in Fig. 3.7(a). The first 3 structures for $n = 7$ (left column) do not have standard names so we leave them unlabelled.

inherent states for local structures in hard sphere. The first few packings for $3 \leq n \leq 7$ are shown in Fig. 5.1. As these states are exhaustive, they represent a complete *local library of states*, of fundamental interest to random first-order transition theory [174] with the potential to significantly improve upon previous extensions of mean-field theory into finite-dimensions [130, 131, 133, 141, 147–152].

Some explanation of what is meant by 'rigid' is warranted. A structure is rigid if the only degrees of freedom are rigid-body motions i.e. translations and rotations, but this is hard to test so stronger criteria are required in general [33, 34, 221]. Some of the oldest ideas surrounding rigidity originate to Maxwell [222] and focus on the number of contacts. These ideas are based on a linear analysis: each particle coordinate is a degree of freedom and each contact is a constraint. Matching the number of freedoms and constraints yields the *Maxwell criterion*, where the number of contacts is exactly [222]

$$m_{\text{Maxwell}} = dn - \frac{d(d+1)}{2}, \tag{5.5}$$

with the right-most term a correction for the number of rigid-body modes ($= 6$ in $d = 3$). In the thermodynamic limit $n \to \infty$ we obtain the *isostatic* condition where the *coordination number*, the average number of neighbours per particle, converges to

$$z_{\text{iso}} = \lim_{n\to\infty} \frac{2m_{\text{Maxwell}}}{n} = 2d.$$

These ideas have been refined in Ref. [223], but they are still fundamentally based on a linear analysis. By contrast, rigidity is a non-linear notion for $d > 1$ and so these ideas are not rigorous[83]. Curiously, the overwhelming majority of rigid structures appear to satisfy the Maxwell criterion (5.5) [33, 34], even though the linear theories are inexact. Furthermore, jammed states are empirically found to be isostatic, a result also predicted by mean-field calculations [125, 126].

[83] In $d = 3$ rigid structures exist which violate the Maxwell criterion (5.5); examples exist of both *hyperstatic* structures like the face-centred cubic unit cell with $m > m_{\text{Maxwell}}$ and *hypostatic* structures with $m < m_{\text{Maxwell}}$ [33, 34]. Finally, note that hypostatic structures are the dominant packings for non-spherical particles [224].

Geometries with at least d contacts for each particle and exactly $m = m_{\text{Maxwell}}$ overall contacts are termed *minimally rigid* [211], but this is neither a necessary nor sufficient criterion for rigidity [34]. Three sufficient criteria for rigidity are: [34, 221]

1. *First-order rigidity*: the natural extension of the Maxwell criterion ensuring the constraints are linearly independent, based on a first-order expansion of the forces about contact. This is also called *Calladine's extension* [223].

2. *Second-order rigidity*: based on an expansion of the forces to second-order. This is hard to test numerically [34].

3. *Prestress stability*: the structure would be stable for an effective (harmonic) energy function [221]. This is a stronger criterion than second-order rigidity, but can be tested more efficiently. It is a non-linear criterion and is satisfied by all of the packings determined in Refs. [33, 211].

All of our calculations are valid for first-order rigid structures, though recently methods have been developed to do free energy calculations with prestress stable structures [225]. It would be interesting to extend the current work to these other structures to explore a more complete library of possible states.

As we cannot use perturbation theory (5.4), we must *choose* a definition for the basin surrounding each energy minimum occurring at contact. For simplicity, we define a particular local structure by its bond topology i.e. the m contacts at the reference point. We write the set of contacts as

$$\mathcal{M} = \{(a_1, b_1), \cdots, (a_m, b_m)\} \tag{5.6}$$

where $a_i, b_i \in \{1, \cdots, n\}$ are the indices of touching particles. Following [226] we introduce the *bond distance* as the size of the gap between particles

$$h_{a_k b_k} = |\mathbf{r}_{a_k} - \mathbf{r}_{b_k}| - \sigma, \tag{5.7}$$

clearly contact occurs where $h_{a_k b_k} = 0$ for all $k \in \{1, \cdots, m\}$. We introduce a pairwise cutoff δ such that the gaps between these particles are bounded in the range $h_{a_k b_k} \in [0, \delta]$, with the lower limit set by the hard particle constraint. All the results we present use a cutoff of $\delta = 0.2\sigma$, but we have tested that our findings are not significantly affected by a choice of $\delta = 0.4\sigma$ indicating their robustness.

As an aside, it was demonstrated in [227] that for hard sphere glasses approaching isostaticity, every pair of contacting particles $i, j \in \mathcal{M}$ interacts through the effective potential

$$\beta u_{\text{eff}}(\overline{h_{ij}}) = -\ln(\overline{h_{ij}}),$$

where $\bar{\cdot}$ indicates averaging over all spacings $\{h_{ij}\}_{\mathcal{M}}$. This form describes an effective force between *average positions* rather than the average of instantaneous forces described by the potential of mean force $\phi^{(n)}$; as such, the above form is not valid for our approach and we must explicitly evaluate the free energy through integrals over $\mathcal{D}$. In addition, it is unclear

whether the fundamental assumptions of the morphometric approach are valid approaching jamming. In that regime, we expect strong deviations from the Carnahan-Starling equation of state input to the morphometric theory (2.104), so our approach is limited to the non-isostatic liquid.

The definition of structure in terms of bond-distances (5.7) naturally leads to calculations in *bond-distance space* as introduced in Ref. [226] in the context of sticky spheres. The bond-distances are unaffected by rigid rotations so we must integrate them out, and for simplicity we now specialise to $d = 3$. We define[84] $\mathcal{Q} = \mathcal{D}' \times G_3$ with $\mathcal{D}'$ as the space of the structure's internal degrees of freedom i.e. the thermal vibrations. We separate rigid body from internal motion by applying the following transformation to each particle coordinate

$$\mathbf{r} = \mathbf{t} + \mathbf{R}(\boldsymbol{\theta})\,\mathbf{f}(\mathbf{x}),$$

where $\mathbf{t}$ is the translation vector, $\mathbf{R}$ the rotation matrix for Euler angles $\boldsymbol{\theta}$, and $\mathbf{f}(\cdot)$ is a mapping from the structure's internal coordinates $\mathbf{x} \in \mathbb{R}^{3n-6}$ to real-space. For a minimally constrained geometry $\mathbf{x}$ could simply correspond to the bond distances $\mathbf{y}$; we can take advantage of this simple analytical calculations (Appendix C). We need to compute the metric of the above transformation $G_{ij} = \mathbf{G}_i \mathbf{G}_i^T$ where the (generally curvilinear) basis vectors are $\mathbf{G}_i = \partial_i \mathbf{r}$, and indices i, j summing over all of $\{\mathbf{t}, \boldsymbol{\theta}, \mathbf{x}\}$. To do this we loosely follow the method outlined in the Supplementary Information of Ref. [226].

To simplify calculation we choose $\mathbf{f}(\mathbf{x})$ to always be in the centre-of-mass frame and orthogonal to rotations such that G_{ij} reduces to block-diagonal form. If the rotation matrix is expressed in Euler-angle representation as $\mathbf{R}(\boldsymbol{\theta}) = \mathbf{R}_3(\theta_3)\mathbf{R}_2(\theta_2)\mathbf{R}_1(\theta_1)$ then we have

$$\mathbf{G}(\boldsymbol{\theta}, \mathbf{x}) = \begin{pmatrix} n\mathbf{E} & 0 & 0 \\ 0 & \mathbf{U}^T(\boldsymbol{\theta})\mathbf{I}(\mathbf{x})\mathbf{U}(\boldsymbol{\theta}) & 0 \\ 0 & 0 & \overline{\mathbf{G}}(\mathbf{x}) \end{pmatrix}, \tag{5.8}$$

where $\mathbf{E}$ is the identity matrix, $\overline{\mathbf{G}}$ is the metric for internal motion, $\mathbf{I}$ is the moment of inertia tensor, and we have defined the matrix $\mathbf{U}$ as

$$\mathbf{U}(\boldsymbol{\theta}) = \begin{pmatrix} 1 & 0 & -\sin\theta_2 \\ 0 & \cos\theta_1 & \cos\theta_2 \sin\theta_1 \\ 0 & -\sin\theta_1 & \cos\theta_2 \cos\theta_1 \end{pmatrix} \qquad \begin{aligned} &\theta_1 \in [0, 2\pi] \\ &\theta_2 \in \left[-\frac{\pi}{2}, \frac{\pi}{2}\right] \\ &\theta_3 \in [0, 2\pi]. \end{aligned} \tag{5.9}$$

Importantly, $\det \mathbf{U} = \cos\theta_2$ is independent of $\mathbf{x}$, so the angular dependence can be integrated out. The volume element in the new coordinates is

$$d\mathbf{r}^n = \frac{\sqrt{\det G_{ij}(\mathbf{x})}}{\nu}\, d^3\mathbf{t}\, d^3\boldsymbol{\theta}\, d^{3n-6}\mathbf{x}, \tag{5.10}$$

where ν is the symmetry number (discussed below) and

$$\sqrt{\det G_{ij}(\mathbf{x})} = \cos\theta_2 \sqrt{\det \mathbf{I}(\mathbf{x})} \sqrt{n^3 \det \overline{G_{ij}}(\mathbf{x})}. \tag{5.11}$$

The symmetry number emerges because the choice of internal coordinates typically fixes the particle labels breaking permutation symmetry; we have

[84] Here we have reintroduced the notation from section 2.1.4 where the rigid-motion group $G_d := \mathbb{R}^d \times \mathrm{SO}(d)$ is the space of translations and rotations.

to multiply by the $n!$ possible labellings, which introduces double counting if the structure possesses rotational symmetry so we have to divide by the correcting factor ν. This is explained in detail in Ref. [228]. Thus (5.1) reduces to[85]

$$\frac{\mathcal{N}}{\rho^n V} = \frac{8\pi^2\sqrt{n^3}}{\nu} \int_{D'} g^{(n)}(\mathbf{x}) \sqrt{\det \overline{G_{ij}}(\mathbf{x}) \det \mathbf{I}(\mathbf{x})}\, d^{3n-6}\mathbf{x}. \tag{5.12}$$

[85] This form is not valid in the limit of linear molecules, i.e. where all particles fall on a line, where there is one less rotation mode.

This is essentially the classical equivalent of the molecular partition function.

In general, the integrand in (5.12) is only exactly solvable for the simplest geometries due to the high dimensionality of $\mathbf{x}$. This is further complicated by the fact that the basis vectors for $\overline{G_{ij}}$ are curvilinear, and must be evaluated perturbatively in general; we will do this in section 5.5.1. We have now defined our structures and presented the general formalism for calculating their free energies. In the next section we introduce numerical methods to evaluate the partition functions. We will return to analytical calculations in 5.5 for the reaction paths.

5.4 The local library of states

With a definition of the structures we can now evaluate the free energies using thermodynamic integration techniques. From the fundamental theorem of calculus, the free energy change from the ideal gas can be *exactly* expressed as [229]

$$\beta F(\eta) - \beta F^{\mathrm{id}} = \int_0^\eta \frac{\partial \beta F(\eta')}{\partial \eta'}\, d\eta' = \int_0^\eta \left\langle \frac{\partial \beta \phi^{(n)}(\mathbf{r}^{n-1}; \eta')}{\partial \eta'} \right\rangle_{\mathcal{D}} d\eta', \tag{5.13}$$

where the latter step used the definition of free energy (5.3) and $\langle\cdot\rangle_{\mathcal{D}}$ indicates the thermal average over the structure space $\mathcal{D}$. The integrand can be measured within a Monte-Carlo simulation, which equilibrate rapidly for small n so it is straightforward to perform this integration. More complicated is the evaluation of the ideal gas term, i.e.

$$\beta F^{\mathrm{id}} := \beta F(\eta = 0) = -\ln\left(\frac{1}{\sigma^{d(n-1)} n!} \int_{\mathcal{D}} d\mathbf{r}^{n-1}\right), \tag{5.14}$$

which still involves an integral over $\mathcal{D}$.

We will introduce approximate analytic methods to evaluate the integral in (5.14) in subsequent sections, but here we use another thermodynamic integration step using the method of Ref. [230] to obtain essentially exact results. We introduce an interaction potential which imposes the integration limits of $\mathcal{D}$, i.e.

$$e^{-\beta W(\mathbf{x})} = \mathbb{I}_{\mathcal{D}}(\mathbf{x})$$

defining the indicator function[86]

$$\mathbb{I}_{\mathcal{D}}(\mathbf{x}) = \begin{cases} 1 & \text{if } \mathbf{x} \in \mathcal{D} \\ 0 & \text{otherwise.} \end{cases}$$

[86] This is really the Euler characteristic (2.8) of the intersection $\chi[\mathcal{D} \cap \mathbf{x}]$.

We use the interaction potential $W(\mathbf{x})$ to switch to an integral over all of space, i.e. we make the replacement

$$\int_{\mathcal{D}} d\mathbf{x} = \int_{\mathbb{R}^{d(n-1)}} e^{-\beta W(\mathbf{x})} d\mathbf{x}.$$

The free energy of the W-interacting system is thus identical to F^{id}. To perform the thermodynamic integration we simulate with an intermediate interaction potential [230]

$$\widetilde{W}(\mathbf{x}, \lambda) = \lambda W(\mathbf{x}) + (1-\lambda) V_{\text{ref}}(\mathbf{x}),$$

where $\lambda \in \{0, 1\}$ is a mixing parameter that switches between the potential of interest and the reference potential V_{ref}. Over the course of a Monte-Carlo sweep, in addition to regular steps, λ is allowed to switch between these values according to the Metropolis-Hastings rule. The free energy difference from the reference system is determined from the ratio of histogram frequencies describing the probability that each potential is active, i.e.

$$F(\eta = 0) - F_{\text{ref}} = -\log\left(\frac{t_W}{t_{\text{ref}}}\right) \tag{5.15}$$

where t_i is the probability that potential i is active (as selected by λ). For the reference potential, we introduce harmonic springs between the bonded particles in the contact set (5.6) i.e.

$$V_{\text{ref}}(\mathbf{x}) = \epsilon \sum_{(i,j)\in\mathcal{M}} \left(h_{ij} - \frac{\delta}{2}\right)^2.$$

To optimise the simulations the value of ϵ should be chosen to keep the free energy difference of order $\mathcal{O}(1\, k_B T)$ [230]; we found $\epsilon = 75/\sigma^2$ to be a reasonable choice with the system sizes considered for the cutoff $\delta = 0.2\sigma$. As the reference system is exactly harmonic, we can use (5.4) to evaluate F_{ref} to within numerical precision[87]. Finally, combining this reference F_{ref} with the thermodynamic integration steps (5.15) and (5.13) gives the free energy of the structure at the target volume fraction $F(\eta)$.

To demonstrate the effectiveness of this approach we have taken structures for $3 \leq n \leq 13$ which are global minima of clusters in different simple liquids [146]. This set includes frustrated structures for $n \geq 7$ which do not correspond to rigid packings with unique energy minima; we will return to the rigid packings afterwards. We selected these structures because we can identify them in molecular dynamics simulations using the algorithm of Ref. [231]. Using this algorithm we can compare the theoretical predictions against molecular dynamics simulations of both mono- and moderately polydisperse hard spheres at all volume fractions accessed by the simulations i.e. $\eta \lesssim 0.585$. For the polydisperse simulations we used data from Ref. [108] with a 5-component equimolar distribution with $\sim 8\%$ polydispersity, to avoid freezing at high densities, and for the monodisperse simulations we used the DynamO software for event-driven molecular dynamics [98]. We determined their free energies using the thermodynamic integration steps outlined above.

[87] This integral must be performed in the bond-distance space introduced of section 5.3, i.e. we perform the multivariate Gaussian integral in the space of $\{h_{a_1 b_1}, \cdots, h_{a_m b_m}\}$ with a perturbation expansion of the rotational metric in (5.12). In addition, evaluating this Gaussian over all of space i.e. $h_{a_k b_k} \in [-\infty, \infty]$ introduces a small approximation as we have the strict lower bound $h_{a_k b_k} > -\sigma$ from (5.7).

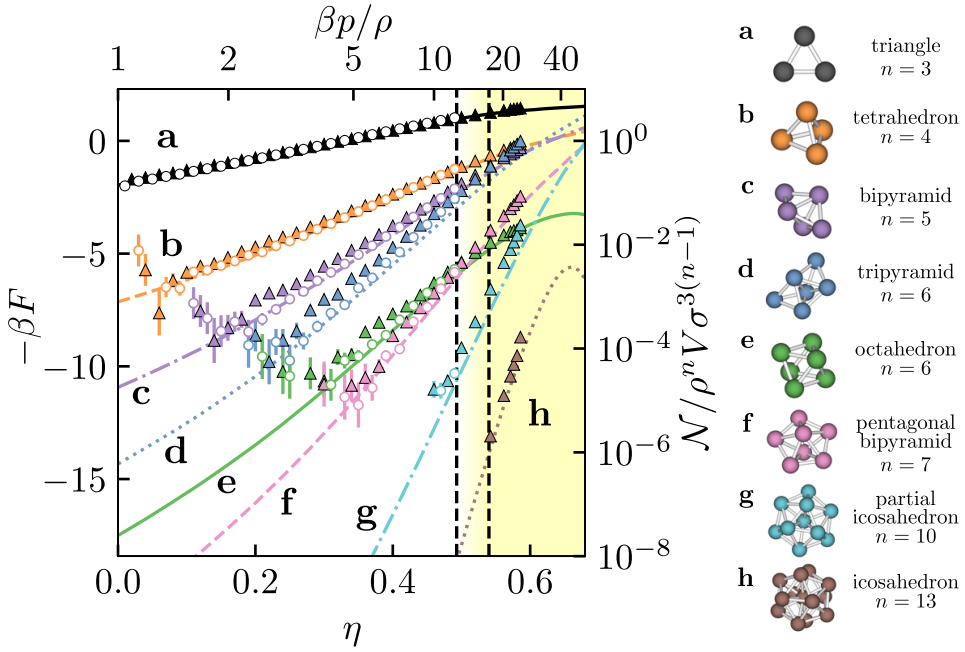

Figure 5.2: Static many-body structure in the hard sphere liquid: populations of small local structures in the hard sphere liquid determined from molecular dynamics simulations of 1372 monodisperse (open circles) and 8% polydisperse (solid triangles) hard spheres against the theoretical prediction of this chapter (lines). Variations against volume fraction η and compressibility factor $Z = \beta p/\rho$ shown. The hard sphere freezing and melting volume fractions are indicated by vertical dashed lines.

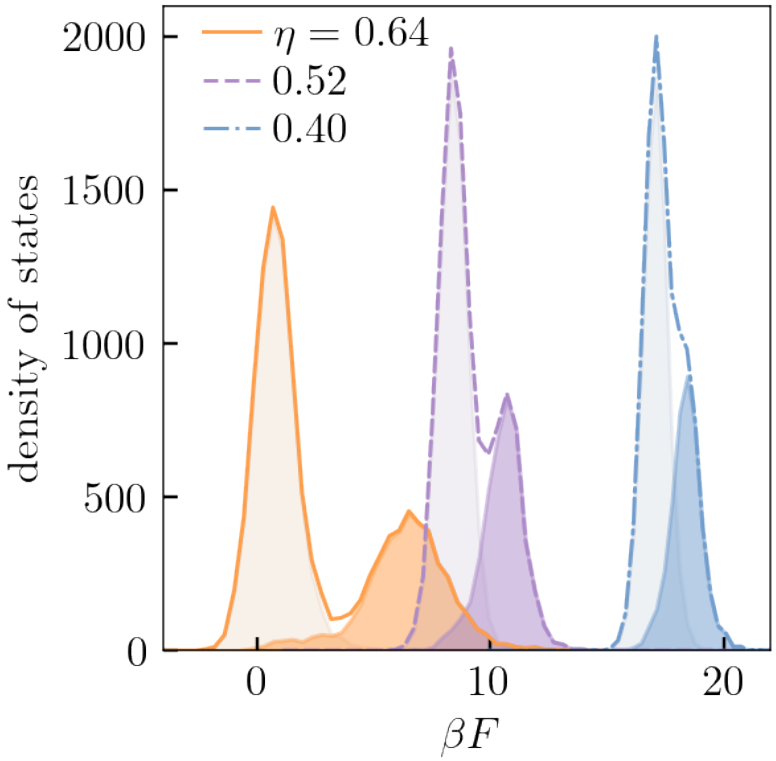

Figure 5.3: Theoretical free energy distribution for the $n = 12$ local library of states at several volume fractions. The distribution is shifted to lower energies at higher volume fractions, and develops an increasingly bimodal structure. Populations are decomposed into those structures containing pentagonal bipyramids without octahedra (light fill) and the remaining structures (dark fill).

In Fig. 5.2 we find excellent agreement between the theoretical prediction and the observed concentration of local structure seen in the simulations. Our approach is able to predict populations of local structures well beyond the regime dynamically accessible to simulation, finding nontrivial structural change deep in the glassy regime highlighted by a rescaling with respect to the trivial ρ^n density contribution. The free energy of considered structures changes approximately linearly across the entire liquid regime, with deviations from linear becoming more apparent in the supercooled regime.

All structures apart from the fourfold symmetric octahedron in Fig. 5.2 are subunits of the icosahedron, and increase in concentration more rapidly than the octahedron until high density. For $n = 6$ we consider the free energies of two structures: the tripyramid and octahedron. We find that the tripyramid occurs ~ 20 times more often than the octahedron, their free energy difference being dominated by the different point group symmetries [228, 232, 233]. We can also estimate vibrational contributions, which allow us to match not only the relative but also the absolute values of free energies obtained from simulation. In particular, we are able to capture the gradual reduction of the population of octahedral motifs in favour of the tripyramids at high volume fractions. This is related to the previously observed emergence of fivefold symmetric motifs (such as the full and partial icosahedron) [99, 109, 157, 234], which is here directly predicted from liquid state theory.

Having tested that the theory is accurate for selected geometries, we now take the exhaustive list of 11980 rigid structures for $n = 12$ determined in Ref. [33] to obtain a local density of states for a given sized inhomogeneity. We calculated the free energy of all (first-order) rigid structures using (5.3) (right panel of Fig. 5.2), finding a bimodal distribution with two main peaks separated by a free energy difference that increases with increasing volume fraction. We find the that lower energy distribution consists of structures rich in fivefold (icosahedral) symmetry in the absence of fourfold (octahedral) symmetry. This shows that the hard sphere liquid is highly frustrated, and would be interpreted as the reason hard spheres make good glassformers with respect to crystallisation in the geometric frustration picture [155]. However, this result is also compatible with other thermodynamic scenarios like random first-order transition theory (RFOT) [174].

Each of the structures correspond to unique contact topologies, but in thermal systems (i.e. with finite gaps between particles) we expect many of them to be indistinguishable as found in Ref. [235]. As such, we have likely overestimated the height of the each peak, and especially the lower energy peak which contains more frustrated structures; we will find evidence of this in the next section. Nevertheless, because this set of packings is exhaustive they represent a complete local density of states in the liquid, which is of fundamental interest to RFOT [174]. The distribution of energy levels is a key quantity, but to really examine the connection with dynamics we also need to know the *connectivity* of the different energy states. For this we need their reaction paths.

We used thermodynamic integration with Monte-Carlo methods to evaluate the free energies in this section, which cannot be straightforwardly applied along reaction paths. Along reaction paths the geometries are saddles

of the potential $\phi^{(n)}$, so the unstable direction must be excluded from integration. In the next section we introduce analytical methods for evaluating the free energy to address this problem.

5.5 Free energies along reaction paths

While the thermodynamic integration techniques of the previous section are exact in principle, it is desirable to develop analytic approaches for evaluating the free energy. Analytic approaches are typically faster which is desirable for dealing with larger n, as the number of possible packings appears to grow super-exponentially with particle number [33]. Moreover, analytic approaches are more readily able to calculate free energies along saddles, which are needed to obtain dynamical information in the vein of energy landscape approaches [146].

Evaluating the free energy of hard sphere local structures is challenging, because the singular nature of the pair potential requires a non-perturbative treatment. This effectively corresponds to having non-trivial integration limits. However, the smoothly varying parts of the integrands can and will be treated perturbatively.

5.5.1 Formalism for structure integrals

The integrals in (5.12) are generically of the form

$$\mathcal{I} = \int_{D'} g^{(n)}(\mathbf{x}) R(\mathbf{x})\, d^l\mathbf{x}, \tag{5.16}$$

where $l = 3n-6$ and $R(\mathbf{x}) = \sqrt{\det \overline{G_{ij}}(\mathbf{x}) \det \mathbf{I}(\mathbf{x})}$ is the rotational metric. The rotational metric is a complicated function as the internal coordinates are curvilinear in general, however we found it to be slowly varying in all of our numerical tests so we can treat it perturbatively. Treating the combined effect of the distribution function $g^{(n)}$, including the hard sphere interactions, and integration limits of $\mathcal{D}'$ as a probability distribution $\mathcal{P}$ acting over *all* of space, we can formally write

$$\mathcal{I} = Z \int_{\mathbb{R}^l} p(\mathbf{x}) R(\mathbf{x})\, d^l\mathbf{x}, \tag{5.17a}$$

$$Z = \int_{\mathcal{D}'} g^{(n)}(\mathbf{x})\, d^l\mathbf{x}, \tag{5.17b}$$

$$1 = \int_{\mathbb{R}^l} p(\mathbf{x})\, d^l\mathbf{x}, \tag{5.17c}$$

where $p(\mathbf{x}) \sim \mathcal{P}$ and Z is the normalisation of the integral in the absence of the metric.

Taylor expanding the metric about the contact point $\mathbf{x}^*$, i.e.

$$R(\mathbf{x}) = R(\mathbf{x}^*) + \nabla R(\mathbf{x}^*) \cdot \Delta\mathbf{x} + \frac{1}{2}\Delta\mathbf{x} \cdot \nabla\nabla R(\mathbf{x}^*) \cdot \Delta\mathbf{x} + \mathcal{O}(\Delta\mathbf{x}^3),$$

where $\Delta\mathbf{x} = \mathbf{x} - \mathbf{x}^*$ leads to the formula

$$\frac{\mathcal{I}}{Z} = R(\mathbf{x}^*) + \nabla R(\mathbf{x}^*) \cdot \langle \Delta\mathbf{x} \rangle_{\mathcal{P}} + \frac{1}{2}\nabla\nabla R(\mathbf{x}^*) : \langle \Delta\mathbf{x} \otimes \Delta\mathbf{x} \rangle_{\mathcal{P}} + \mathcal{O}(\langle \Delta\mathbf{x}^3 \rangle_{\mathcal{P}}), \tag{5.18}$$

with $\langle\cdot\rangle_{\mathcal{P}} = \int_{\mathbb{R}^l}(\cdot)p(\mathbf{x})\,d^l\mathbf{x}$ as the average over the distribution $\mathcal{P}$. With this series expansion in mind, we will concentrate on methods which determine Z and the moments of $\mathcal{P}$ to avoid explicitly considering the nonlinear role of the metric $R(\mathbf{x})$. This formalism shifts all the complexity into determining approximation schemes for $p(\mathbf{x})$.

Formally, the probability distribution is written

$$p(\mathbf{x}) = \frac{g^{(n)}(\mathbf{x})\mathbb{I}_{\mathcal{D}'}(\mathbf{x})}{Z}, \tag{5.19}$$

which contains singularities from both the hard sphere interactions in $g^{(n)}$ and from the integration limits of $\mathcal{D}'$ through $\mathbb{I}_{\mathcal{D}'}$. Separated into smooth and singular contributions, we can write

$$p(\mathbf{x}) = \underbrace{\frac{y^{(n)}(\mathbf{x})}{Z}}_{\text{smooth}}\ \underbrace{\mathbb{I}_{\mathcal{D}'}(\mathbf{x})\prod_{\substack{i<j\\(i,j)\notin\mathcal{M}}}\Theta\Big(|\mathbf{r}_i-\mathbf{r}_j|-\sigma\Big)}_{\text{singular terms}},$$

where we did not include the particles in $\mathcal{M}$ in the final product because their effect is already by the definition of structure $\mathbb{I}_{\mathcal{D}'}$, and where we defined the n-particle cavity distribution as

$$y^{(n)}(\mathbf{x}) := e^{\beta U_n}g^{(n)}(\mathbf{x}) = e^{-\beta(\Delta\Omega(\mathbf{x})-n\mu^{\text{ex}})},$$

using (4.2) in the latter step. The cavity distribution is known to be a continuous function [12], so we can perform a perturbation expansion; we will do this to leading order i.e.

$$y^{(n)}(\mathbf{x}) = y^{(n)}(\mathbf{x}^*)e^{-\mathbf{A}\cdot\Delta\mathbf{x}} + \mathcal{O}(\Delta\mathbf{x}^2) \tag{5.20}$$

where $\mathbf{A} = \nabla\beta\Omega(\mathbf{x}^*) \neq 0$. By contrast, the singular terms require a non-perturbative treatment.

The singular terms can be expressed in terms of one-dimensional indicator functions; specifically, our choice of structure laid out in 5.3 is a restriction of to the space $h_{ij} \in [0,\delta]$ for particles in contact at the reference point $\mathbf{x}^*$, and the full space $[0,\infty]$ for the remaining particle pairs. We write this as

$$\mathbb{I}_{\mathcal{D}'}(\mathbf{x}) = \prod_{k=1}^{m}\Theta(h_{a_kb_k})\Theta(\delta-h_{a_kb_k}) = \prod_{(i,j)\in\mathcal{M}}\mathbb{I}_{[0,\delta]}(h_{ij}) \tag{5.21a}$$

$$\prod_{\substack{i<j\\(i,j)\notin\mathcal{M}}}\Theta\Big(|\mathbf{r}_i-\mathbf{r}_j|-\sigma\Big) = \prod_{\substack{i<j\\(i,j)\notin\mathcal{M}}}\mathbb{I}_{[0,\infty]}(h_{ij}). \tag{5.21b}$$

So together with (5.20), the probability distribution becomes

$$p(\mathbf{x}) \simeq \frac{y^{(n)}(\mathbf{x}^*)e^{-\mathbf{A}\cdot\Delta\mathbf{x}}}{Z}\prod_{(i,j)\in\mathcal{M}}\mathbb{I}_{[0,\delta]}(h_{ij})\prod_{\substack{i<j\\(i,j)\notin\mathcal{M}}}\mathbb{I}_{[0,\infty]}(h_{ij}). \tag{5.22}$$

In the special case of minimally constrained geometries i.e. $m = l$, then the integration limits are equivalent to a hypercube. The resulting integral

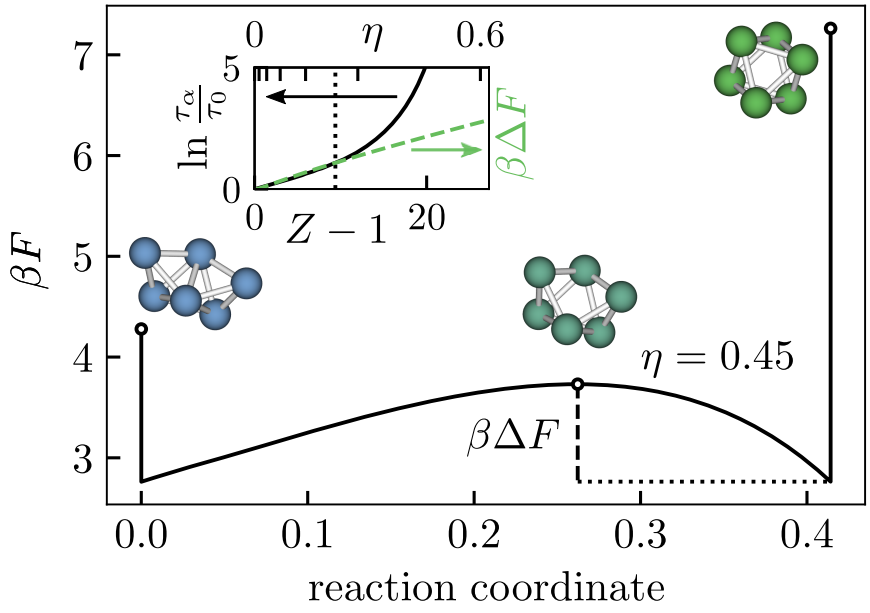

Figure 5.4: Reaction for transition between tripyramid and octahedron $n = 6$ structures. Stationary points are indicated by markers: there is a discontinuity in free energy at the end points due to the additional integration over the reaction coordinate, and symmetry in the case of the octahedron. Inset: variation of activation barrier with volume fraction η and compressibility factor $Z = \beta p/\rho$ from this theoretical reaction path (dashed line) and measured α-relaxation times in bulk molecular dynamics simulations (solid line), where $\eta = 0.45$ is indicated with a vertical dotted line.

can be evaluated analytically if the additional hard sphere interactions are ignored (Appendix C).

More generally, we employ two approximations (full details in Appendix C):

1. *Polyhedral approximation*: we approximate the integration domain as a high dimensional polyhedron by expanding the generally curvilinear bond-distances to leading order i.e.

$$h_{ij}(\mathbf{x}) \simeq h_{ij}(\mathbf{x}^*) + \nabla h_{ij}(\mathbf{x}^*) \cdot \Delta\mathbf{x} + \mathcal{O}(\Delta\mathbf{x}^2).$$

2. *Expectation propagation*: inspired by the harmonic approximation (5.4), we approximate $p(\mathbf{x})$ by a Gaussian distribution with parameters obtained using this technique from Bayesian inference described in Refs. [236–239]. This method yields an approximate Z, and the Gaussian parameters immediately give the first and second moments of $p(\mathbf{x})$; the perturbative effects of the rotation metric can thus be included through application of (5.18).

In the next section we apply this approximate technique to the calculation of free energies along reaction paths.

5.5.2 Integration along reaction paths

We are now able to make a connection with dynamical properties of the supercooled liquid by calculating the free energy along reaction paths between (geometrically similar) structures. We obtain a reaction path by breaking a contact, which creates an unstable direction that can be explored using the technique suggested in the Supplementary Material of Ref. [33]. Along this reaction path we obtain the free energies by integrating over all but the coordinate parameterising the unstable direction s. We therefore obtain

from (5.12)

$$\beta F = -\ln\left(\frac{8\pi^2\sqrt{n^3}}{\nu}\int_{D'\setminus s} g^{(n)}(\mathbf{z};s)R(\mathbf{z};s)\; d^{l-1}\mathbf{z}\right), \tag{5.23}$$

where $\mathbf{z} \in \mathbb{R}^{(3n-7)}$ does not include the reaction coordinate s. Importantly, ν is the new symmetry number along this reaction path, which is different in general from the symmetry numbers of the terminating minima [146]. This integral has the same form as (5.16), which we evaluate using the methods outlined in the previous section and described in full in Appendix C.

In Fig. 5.1 we see that for $n < 6$ only a single rigid packing of hard spheres exists, but for $n = 6$ we see two distinct packings making it the first interesting landscape. The two structures are connected by a single unstable reaction path, making the entire landscape simple enough to explore. Comparing this dynamical barrier to the structural relaxation for (α-) relaxation timescale τ_α extracted from simulations relative to a microscopic time τ_0 (inset of Fig. 5.4), we find this single reaction path barrier agrees with the low density scaling of τ_α (linear in the compressibility factor $\beta p/\rho$ [107]). However, activated dynamics are not expected in this regime so this agreement may be coincidental.

Secondly, we consider the reaction path separating the two variants of the frustrated pentagonal bipyramid with $n = 7$ in Fig. 5.5. We find that the energy increases monotonically along the path without an activation barrier; this means that these two distinct packings are really just thermal fluctuation of the same structure. This further justifies the use of the frustrated structures in Fig. 5.2, even though they do not strictly correspond to unique energy minimum. On the flip side, it shows that our operational definition of structures needs refining, as we cannot meaningfully distinguish the different energy minima after thermalisation. This suggests that we have likely overcounted the number of structures in the density of states 5.3. This calculation relied on expectation propagation [236–239] (and Appendix C) to handle the hard sphere interactions, which opens the way to assess the connectivity of the energy landscape for local structures in hard spheres.

It is possible to extend our methodology for larger rearrangements, which may be sufficient to access (α-) relaxation *at very deep supercooling* for equilibrium systems. However, the rapid growth in the number of possible states presents a considerable numerical challenge requiring new methods and approximations, so we leave this exciting avenue for future study.

5.6 Conclusions

We have presented a formalism for treating local structure in simple liquids using the framework of many-body correlations. Using the morphometric approach of the previous chapter, we developed this formalism into an accurate and computationally efficient parameter-free theory for hard spheres relying solely on the equation of state as input.

We applied the framework to a selection of local structures, therefore predicting nontrivial changes in the energy landscape with supercooling.

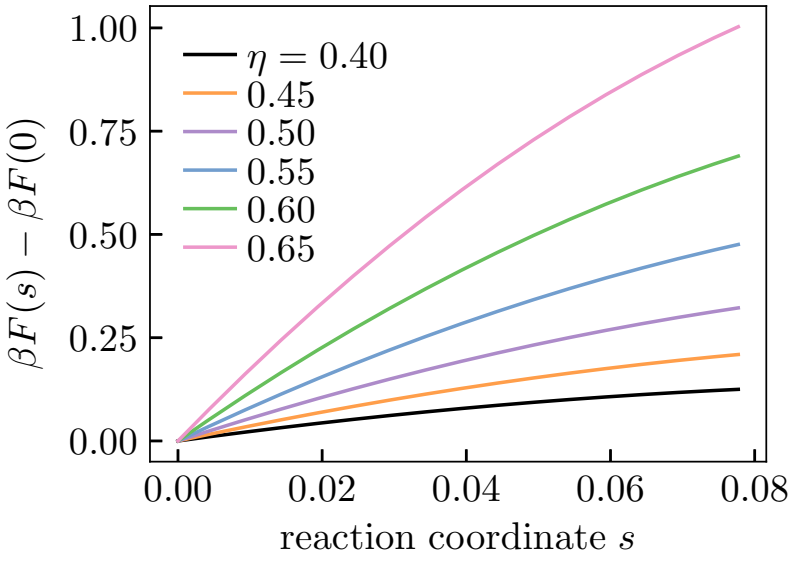

Figure 5.5: Reaction for transition between the two $n = 7$ pentagonal bipyramids variant structures, from the variant with a broken spindle (bottom variant in Fig. 5.1) to the variant with broken fivefold symmetry (top variant). The free energy increases monotonically along this reaction path, so there is no barrier separating these two structures.

This placed previous empirical observations on more solid ground. In particular, our analysis provides evidence for the existence of two populations of structures with distinct symmetries and free energies which causes the local density of states to become increasingly bimodal at high densities; this observation supports structural interpretations of dynamical arrest. Examining the reaction pathways we found there was no activation barrier separating two structures with fivefold symmetry, suggesting we have overestimated the number of structures in the lower energy peak. However, this latter limitation does not challenge the existence of the bimodality caused by an energy separation.

We note that we have treated densities corresponding to a degree of supercooling only accessible using novel swap Monte Carlo techniques [91]; however, these simulations introduce large polydispersity, changing the local structure [240] and thus limiting direct comparison with our calculations for the single-component liquid.

Our framework can be easily adapted to more complex liquids such as systems with soft repulsive interactions and polydisperse mixtures [241]. Calculations may even become easier with softer interactions, as perturbation techniques (5.4) could be used in place of thermodynamic integration, or the bespoke analytic techniques presented in this chapter. However, extending the approach to softer interactions would require new morphometric coefficients as input to the theory. This suggests a route for predicting static properties of equilibrium liquids, with direct applications to self-assembly, nucleation and protein structure.

The morphometric approach can extend straightforwardly to hard particles of more complex shapes where the interaction potential is still geometric in nature; in the next chapter we will derive a morphometric theory for arbitrary mixtures of hard convex particles. The downside of this extension is that this introduces rotational degrees of freedom for each particle, and more complex interactions, so evaluating free energies is likely to become

substantially more complicated. This extension includes the generalisation to arbitrary dimensions d, which may provide a route to connect with the mean-field theory of glasses (section 3.3) which is formally exact in the limit $d \to \infty$

Chapter 6

Morphological thermodynamics for hard bodies from a controlled expansion

> He said that the geometry of the dream-place he saw was abnormal, non-Euclidean, and loathsomely redolent of spheres and dimensions apart from ours.
>
> H. P. Lovecraft, *The Call of Cthulhu* (1926).

This is the final chapter on the morphometric approach, but has a different focus from the previous two. Here we derive the morphometric approach from first-principles in the case of hard particle systems, to place it on more rigorous footing and potentially indicate how the approximation may be improved. We intend to publish part of this work at a later time as Ref. [4].

6.1 Introduction

The standard theoretical framework for treating inhomogeneous liquids is classical density functional theory (DFT), which we introduced in section 2.3. Central to this theory is the result that the free energy can be *exactly* expressed as a functional of the density $\Omega = \Omega[\rho(\mathbf{r})]$ [65], though approximate functionals must be used in general. For example, fundamental measure theory (FMT) [25] provides a class of highly accurate functionals for the hard sphere liquid (cf. section 2.3.4). A common practical application of DFT is to its *dual* problem: determining the free energy $\Omega = \Omega[\phi_{\text{ext}}(\mathbf{r})]$ for a fixed external potential $\phi_{\text{ext}}(\mathbf{r})$. Approaching this through DFT requires minimisation of Ω to obtain the equilibrium density profile, a tractable but expensive procedure. In situations where many function evaluations are required, e.g. when integrating over many different realisations of ϕ_{ext}, this minimisation operation can become prohibitively expensive. It is worth-

while to investigate more direct routes to approximating $\Omega[\phi_{\text{ext}}(\mathbf{r})]$, especially where accuracy may be less important than fast calculation.

Unsurprisingly, we advocate the morphometric approach of previous chapters as a promising alternative to the dual problem outlined above, which has the potential to enable fast and accurate calculations in hard spheres [1, 95, 176]. The morphometric approach concerns sharply repulsive external potentials where ϕ_{ext} acts as a container for the fluid or as an exclusion volume for e.g. a solute. In this limit, the density profile is negligible over a volume V and the free energy is expanded in terms involving V and its boundary ∂V. We have hitherto focused on the morphometric approach in three dimensions[88], but in this chapter we will examine its fundamental basis and we will find it useful to consider the d-dimensional generalisation. Motivated by integral geometry, we approximate the free energy change due to the inhomogeneous potential $\Delta\Omega := \Omega[\phi_{\text{ext}}] - \Omega_{\text{hom}}$ as the *strictly extensive* quantity

$$\Delta\Omega = \sum_{k=0}^{d} a_k V_k, \tag{6.1}$$

with V_k as the intrinsic volumes of the region defined by ϕ_{ext}. This form of the grand potential is motivated by Hadwiger's characterisation theorem (2.15).

[88] See (2.108) for the morphometric approach as a limit of FMT, or (4.6) as a generalisation of scaled particle theory.

Despite its accuracy in hard spheres, the morphometric expansion (6.1) is still an approximation as has been demonstrated in numerous detailed investigations [177–182]. Fundamental questions remain over *why* it is accurate and how one might improve the approximation. Inaccuracies become significant in hard spheres at very high densities approaching the glass transition, as we have seen in previous chapters, so an approximation scheme including additional terms could be desirable. In this chapter we will attempt to start the path towards supplementing the morphometric approach (6.1) with higher-order terms, by deriving the known terms as the leading contribution in the only properly rigorous free energy expansion: the *virial series* introduced in section 2.2.4. This route suggests a properly controlled way of including successive corrections to the approach. The virial series is dimension-independent so this approach could potentially connect with calculations in high dimensions [59, 122]; though we work in physical dimensions $d \leq 3$ it would be straightforward to extend to $d > 3$.

Traditionally, expansions of $\Delta\Omega$ have been obtained in an *ad hoc* way rather than as part of a controlled expansion. To illustrate this we consider what happens if one attempts to extend (6.1) by including higher moments of curvature. A prototypical example of this is the *Helfrich expansion* for elastic membranes [242], which is often argued to be the most general expansion for the surface tension [180]. In this expansion, the next leading order correction to (6.1) would be[89]

$$\int_{\partial V} H(\mathbf{r})^2 d\mathbf{r},$$

which is not well-defined for general surfaces, in particular for surfaces containing vertices and/or arcs as occurs in e.g. polyhedra. To demonstrate this we consider the line where two planes intersect with dihedral angle $\Delta\theta$.

[89] We remind the reader that $H(\mathbf{r})$ is the mean curvature along the surface, in the notation we used to introduce the key geometric quantities of integral geometry in $d = 3$ in (2.5).

This can be considered as a cylindrical sector in the limit of vanishing radius r, giving the contribution per unit length

$$\int H^2 r d\theta = \frac{\Delta\theta}{r}$$

diverging as $1/r$ in the limit where the sector becomes an arc $r \to 0$. By contrast, the geometric terms already present in the morphometric approach remain well defined even where a curvature tensor is not locally definable, at e.g. a cusp. Thus, the coefficients of any higher-order moments of curvature must necessarily be zero within a controlled expansion. The inclusion of higher-order curvatures was originally motivated by continuum elasticity [242], so it is not surprising that features on small lengthscales are pathological.

More generally, we find that *any* analytic geometric expansion of $\Delta\Omega$ cannot be exact. It was shown in the original papers on scaled particle theory [85, 183] that $\Delta\Omega$ contains singularities, which cannot be captured by simple geometric expansions; we recount this argument in Appendix A. The virial series is in principle exact[90] , so any singularities should be captured by resumming its terms which could suggest forms for new approximation schemes.

[90] This is true within the radius of convergence of the series, which is not known for $d > 1$. The weak convergence of this series has been a major obstacle in being used to predict e.g. bulk phase behaviour.

In sections 6.2.2 and 6.2.1 we will present the limiting cases where the insertion cost rigorously takes the morphometric form, i.e. the low density limit and for one-dimensional hard rods. In section 6.3 we resum the terms contributing in these exact limits to obtain a piece of the solvation energy which *exactly* obeys the morphometric form, and we are able to calculate the thermodynamic coefficients explicitly. Our main result is valid for hard interactions where the solute and solvent particles are compact and convex. Though applicable to arbitrary mixtures of particle geometries, the resulting form is equivalent to the standard morphometric approach (6.1). The methods we use are identical to those used in analysis of inhomogeneous FMT, reflecting the deep underlying connections between FMT and the morphometric approach [51, 59, 60].

6.2 Exact morphometric limits

6.2.1 One-dimensional hard rods

The one-dimensional analogue of a hard sphere is a hard rod[91]. The cost of inserting a new rod of length L exactly fits the morphometric form independent of density.

[91] In fact, rods are the only convex shape possible in 1d (as line segments) so they are really the one-dimensional analogue of *any* convex object.

Imagine a hard rod fluid occupying all of space. If we insert a single fixed hard point at the origin, this splits the fluid into two half spaces on either side of the origin, i.e. $x < 0$ (left) and $x > 0$ (right). Because the interactions are hard the two half spaces will be completely decorrelated; thus, growing the point to become a rod of finite size L will simply correspond to translating one of the spaces a distance L requiring work pL. In the limit $L \to 0$ where the rod becomes a point there will be a fixed insertion cost

$$\beta\Delta\Omega(L = 0) = -\ln(1 - \eta)$$

coming from the fact that the probability that a randomly chosen position is unoccupied is simply the free volume $1-\eta$ [183]. Combining these two terms gives the total cost of inserting a finite sized rod as

$$\beta\Delta\Omega(L) = \beta pL - \ln(1-\eta) \tag{6.2}$$

which is exactly of morphometric form (cf. (2.15)). The pressure can be determined as [243]

$$\frac{\beta p}{\rho} = \frac{1}{1-\eta}. \tag{6.3}$$

The morphometric form is violated when multiple rods are inserted at such a distance apart that a liquid is confined between them. In this case long-range correlation effects form between the rods which are not captured by the geometric expansion.

6.2.2 Low densities in arbitrary dimensions

We will now obtain the low density asymptotics of the chemical potential, and show that this exactly follows the morphometric form for convex bodies. This argument is very similar to the one we used in the introduction of FMT in section 2.3.4, and an argument from Ref. [244].

Hard particles feature purely geometric interactions, a property that allows us to make progress. In particular, the interaction potential between two compact and convex hard bodies $A, B \in \mathcal{K}^d$ is normally written

$$u(A,B) = \begin{cases} 0 & \text{if } A \cap B = \varnothing \\ \infty & \text{if } A \cap B \neq \varnothing \end{cases}$$

from which the Mayer function (2.54) can be written in the revealing form

$$-f_{AB} = 1 - e^{-\beta u(A,B)} = \begin{cases} 0 & \text{if } A \cap B = \varnothing \\ 1 & \text{if } A \cap B \neq \varnothing \end{cases}$$

The latter form is identical in form to the Euler characteristic, introduced in (2.8), of their intersection i.e.

$$\chi[A \cap B] = \begin{cases} 0 & \text{if } A \cap B = \varnothing \\ 1 & \text{if } A \cap B \neq \varnothing \end{cases}$$

valid for convex bodies. Comparing this expression with (6.2.2) we can rewrite the thermodynamic quantity as the purely geometrical measure

$$1 - e^{-\beta u(A,B)} = \chi[A \cap B] = -f_{AB}. \tag{6.4}$$

Rewriting the interactions in terms of the Euler characteristic allows us to exploit theorems from integral geometry to evaluate thermodynamic quantities.

Including their relative orientations, the cost of inserting a solute A into a liquid of B particles in the low density limit $\rho \to 0$ is determined from the leading contribution to the virial series using [12, 13]

$$\begin{aligned} \beta\Delta\Omega &= \frac{\rho}{2} \; \text{ 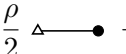 } \; + \mathcal{O}(\rho^2) \\ &= \frac{\rho}{2} \int_{G_d} \chi[A \cap gB] \, dg + \mathcal{O}(\rho^2) \end{aligned} \tag{6.5}$$

where we indicate the A particle with a triangle and the B particle by a circle in the diagram, and we made the replacement (6.4) in the second line. The integrand in the latter line of (6.5) can be directly evaluated using the principal kinematic formula (2.16) giving the morphometric form (6.1) with coefficients

$$a_k = \frac{V_{d-k}[B]}{C_{k,d-k}},$$

with coefficients $C_{k,d-k}$ defined in (2.12). Thus the morphometric approach is exact in the low density limit. This leads to elegant formulae e.g. for $d = 3$ we obtain

$$\frac{\beta\Delta\Omega}{2\pi\rho} = V[A]X[B] + A[A]C[B] + C[A]A[B] + X[A]V[B]$$

for $\rho \ll 1$, where we have used normalisations of intrinsic volumes as surface measures given in (2.5) and Table 2.2. The low density result is a classic application of integral geometry to the liquid state, first obtained by Isihara [245].

6.3 Extension to finite densities in arbitrary dimensions

We can identify the insertion cost of a solute particle with the chemical potential of a new species of particle (a single solute) in the infinitely dilute limit [96, 182, 183]. Interestingly, taking this limit for a bulk hard sphere system modelled with fundamental measure theory (FMT) gives the morphometric approach (cf. section 2.3.4 and Ref. [96]); this is due to the approximation underlying FMT, i.e. that the free energy density can be represented in terms of weighted densities which are deeply connected to intrinsic volumes. Alternatively, the exact free energy of this system can be expressed as a virial expansion [12]. This idea was explored in Ref. [96] to show that the morphometric approach (6.1) is inexact, however here we will attempt a different strategy: we will identify a contribution in the virial expansion which guarantees an insertion cost of morphometric form. The remaining contributions are unlikely to be rigorously of this form, and their omission is an approximation.

We consider an $(m+1)$-component mixture and we label each species with index $s \in \{0, 1, \cdots, m\}$: the components labelled $\{1, \cdots, m\}$ make up those species present the bulk liquid while the additional component with index $\{0\}$ represents the solute. Furthermore, we assume each particle in this mixture is a compact and convex body $K_0, K_1, \cdots K_m \in \mathcal{K}^d$. We will shortly find the chemical potential of the solute by considering the infinitely dilute limit. For convenience, we restate the virial series for the excess free energy density (2.51) here as

$$\frac{\beta F^{\text{ex}}}{V} = \sum_{n=2}^{\infty} \frac{1}{n-1} B_n \rho^n, \tag{6.6}$$

and restating the nth virial coefficient as

$$B_n = \sum_{s_1=0}^{m} \cdots \sum_{s_n=0}^{m} B_{s_1,\cdots,s_n} \prod_{i=0}^{n} x_{s_i}, \tag{6.7}$$

where x_i is the mole fraction of species i such that $x_i > 0$ and $\sum_{i=0}^{m} x_i = 1$. $B_{s_1,\cdots,s_n}$ are the composition independent virial coefficients describing the contribution from interactions between n particles of species $\{s_0, s_1, \cdots, s_n\}$. Each contribution contains integrals over all configurations of the n particles [12, 13]. We will refer to these integrals as diagrams because they are normally represented using graph theoretic tools, such as when they were introduced in section 2.2.4.

We now identify the insertion cost for a new solute particle with its chemical potential in the dilute limit. The chemical potential of the solute species is

$$\beta\mu_0^{\text{ex}} = \frac{1}{\rho}\frac{\partial}{\partial x_0}\left(\frac{\beta F^{\text{ex}}}{V}\right)_{V,T} \tag{6.8}$$

giving in the dilute limit $x_0 \ll 1$

$$\begin{aligned}\beta\Delta\Omega &= \lim_{x_0\to 0}\sum_{n=2}^{\infty}\frac{1}{n-1}\frac{\partial B_n}{\partial x_0}\rho^{n-1} \\ &= \sum_{n=2}^{\infty}\frac{n}{n-1}B_{n-1}^{*}\rho^{n-1} = \sum_{n=1}^{\infty}\frac{n+1}{n}B_n^{*}\rho^n\end{aligned} \tag{6.9}$$

with modified virial coefficient

$$B_n^{*} = \sum_{s_1=1}^{m}\cdots\sum_{s_n=1}^{m} B_{0,s_1,\cdots,s_n}\prod_{i=1}^{n} x_{s_i} \tag{6.10}$$

which contains contributions from all diagrams containing a single member of the solute species. In a single-component system we obtain the first few terms as [13]

$B_2 = -\frac{1}{2}$, (6.11a)

$B_3 = -\frac{2}{3!}$, (6.11b)

$B_4 = -\frac{3}{4!}\Bigg($ 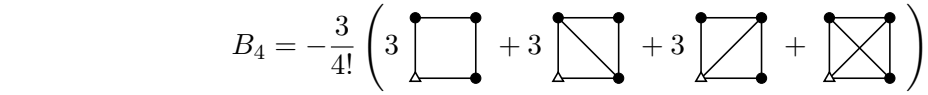 $\Bigg)$ (6.11c)

using the diagrammatic notation for the integrals introduced in section 2.2.4 with the small modification being that the solute is represented by a triangle.

We now introduce our central approximation which generically results in a morphometric form for $\beta\Delta\Omega$, for arbitrary mixtures of hard particles and in all densities and dimensions: we select only contributions to $B_{0,s_1,\cdots,s_n}$ where there is a common point of intersection between the $n+1$ particles. The intuition behind this approximation can be understood by considering again the two limits where the morphometric approach is rigorously exact. First, in the low density limit the integral (2.16) selects only those geometries where the solute and solvent particle intersect at a common point. Second, in the one-dimensional limit all of the nonzero contributions to the virial expansion occur where there is a common point of intersection [51]. This approximation scheme has been systematically explored in the more

general case of inhomogeneous systems [51, 59, 60], and can be used to derive FMT from first-principles. This approximation allows us to write (6.9) as

$$\beta\Delta\Omega = \sum_{n=1}^{\infty} c_n \rho^n \sum_{s_1=1}^{m} \cdots \sum_{s_n=1}^{m} \Lambda_{s_1,\cdots,s_n} \prod_{i=1}^{n} x_{s_i} \tag{6.12}$$

where c_n is a combinatorial prefactor independent of the interactions or dimensionality, and

$$\Lambda_{s_1,\cdots,s_n} = \int_{G_d^n} dg^n \chi[K_0 \cap g_1 K_{s_1} \cap \cdots \cap g_n K_{s_n}] \tag{6.13}$$

with $\int_{G_d^n} dg^n = \int_{G_d} dg_1 \cdots \int_{G_d} dg_n$ counts the number of microstates where there is a region of mutual overlap. This expression $\Lambda_{s_1,\cdots,s_n}$ is a real contribution in the n-particle diagrams of the full virial expansion, and the only approximation here is in neglecting additional terms; this feature makes the resulting theory part of a controlled approximation.

Formally, the terms retained in this approximation contain contributions from multiple Mayer diagrams. The diagrams contributing to $\Lambda_{s_1,\cdots,s_n}$ can be determined by introducing *Ree-Hoover diagrams* [246]. To obtain these new diagrams we can rewrite the Mayer function (2.54) as

$$1 = e_{ij} - f_{ij}$$

where $e_{ij} := \exp(-\beta u_{ij})$ is the Boltzmann weight of the pair potential. We represent this rule *graphically* as

with dashed lines indicating the Boltzmann term. By repeatedly applying this rule to the Mayer diagrams we obtain the fully connected Ree-Hoover diagrams, for example

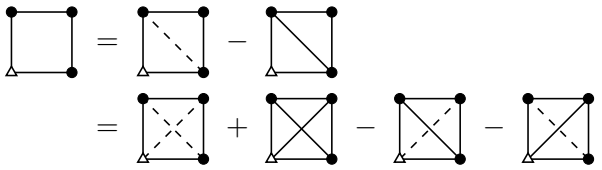

These diagrams have two distinct advantages: firstly, cancellations occur reducing the overall number of diagrams, and secondly each diagram corresponds to unique and disjoint regions of phase space reducing the redundancy of calculation [246]. This approach has been laid out in detail in Refs. [51, 60] in the context of FMT. The main result of this formalism is that the only diagrams contributing to $\Lambda_{s_1,\cdots,s_n}$ are the fully f-connected diagrams, i.e. those without any e-bonds. So as a first approximation, the free energy density is approximated by the series

$$\frac{\beta F^{\text{ex}}}{V} \approx$$ 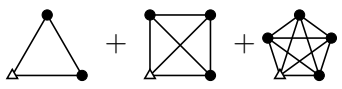 $$+ \mathcal{O}(\rho^6),$$

with prefactors $c_n\rho^n$ omitted for clarity. In a second approximation, the fully connected diagrams are approximated by n-particle intersections e.g.

[51, 60]


$$:= \int_{G_d^2} \chi[K \cap g_1 K_{s_1}]\, \chi[K \cap g_2 K_{s_2}]\, \chi[g_1 K_{s_1} \cap g_2 K_{s_2}]\, dg_1 dg_2.$$

$$\simeq \int_{G_d^2} dg^2 \chi[K_0 \cap g_1 K_{s_1} \cap g_2 K_{s_2}] = \Lambda_{s_1,s_2} :=$$ 

using a diagram with a single-vertex to represent an integral of an n-particle intersection (6.13). Making these replacements approximates the free energy density as

$$\frac{\beta F^{\text{ex}}}{V} \approx$$  $$+ \mathcal{O}(\rho^6). \tag{6.14}$$

This diagrammatic formulation provides a formal context, but is unnecessary for the derivation to follow.

The iterated kinematic formula (2.17) gives the explicit value of the intersections of many bodies $\{K_i\}$ as [42, 51]

$$\Lambda_{s_1,\cdots,s_n} = \sum_{\substack{i_0,\cdots,i_n=0 \\ i_0+\cdots+i_n=nd}}^{d} (C_{i_0,\cdots,i_n})^{-1} V_{i_0}[K_0] \prod_{j=1}^{n} V_{i_j}[K_{s_j}], \tag{6.15a}$$

$$\text{with} \qquad C_{i_0,\cdots,i_n} := \frac{1}{i_0! \omega_{i_0}} \prod_{j=1}^{n} \left(\frac{d!}{i_j!} \frac{\omega_d}{\omega_{i_j}} \right). \tag{6.15b}$$

[92] As a reminder to the reader, the ω_d terms appearing in these expressions are the volumes of the d-dimensional unit ball $\mathcal{B}_d$ defined in (2.13). Explicit values are given in Table 2.1, along with their corresponding intrinsic volumes $V_k[\mathcal{B}_d]$.

Introducing the rescaled volumes[92]

$$\widetilde{V}_k[K_s] = \frac{k! \omega_k}{d! \omega_d} V_k[K_s] \tag{6.16}$$

eliminates the combinatorial factor in (6.13) giving

$$\Lambda_{s_1,\cdots,s_n} = d! \omega_d \sum_{\substack{i_0,\cdots,i_n=0 \\ i_0+\cdots+i_n=nd}}^{d} \widetilde{V}_{i_0}[K_0] \prod_{j=1}^{n} \widetilde{V}_{i_j}[K_{s_j}]. \tag{6.17}$$

Summing this equation over all the different species in the mixture gives

$$\begin{aligned} \Lambda^* :=& \sum_{s_1,\cdots s_n=1}^{m} \Lambda_{s_1,\cdots,s_n} \prod_{i=1}^{n} x_{s_i} \\ =& d! \omega_d \sum_{\substack{i_0,\cdots,i_n=0 \\ i_0+\cdots+i_n=nd}}^{d} \widetilde{V}_{i_0}[K_0] \prod_{j=1}^{n} \xi_{i_j} \\ =& d! \omega_d \sum_{k=0}^{d} \frac{\lambda_k^{(n)}}{\rho^n} \widetilde{V}_k[K_0], \end{aligned} \tag{6.18}$$

where we simplified the final expression by reintroducing the *scaled particle variables*[93]

$$\xi_k = \rho \sum_{s=1}^{m} x_s \widetilde{V}_k[K_s] \tag{6.19a}$$

$$\lambda_k^{(n)} = \sum_{\substack{i_1,\cdots,i_n=0 \\ i_1+\cdots+i_n=nd-k}}^{d} \prod_{j=1}^{n} \xi_{i_j}. \tag{6.19b}$$

The bulk volume fraction is generically $\eta = \xi_d$, and the Euler characteristic of the particles must be unity for convex particles giving $\xi_0 = \rho/(d!\omega_d)$.

At this point we can observe that the resulting free energy is already of morphometric form, as can be seen by combining (6.12), (6.16) and (6.18) giving

$$\beta\Delta\Omega = \sum_{k=0}^{d} \beta a_k V_k[K_0] \tag{6.20a}$$

$$\text{with} \qquad \beta a_k = k!\omega_k \sum_{n=1}^{\infty} c_n \lambda_k^{(n)} \tag{6.20b}$$

which has the form of the morphometric approach (6.1). This is not surprising as the integral in (6.13) rigorously has the properties of intrinsic volumes outlined in section 2.1.2, so Hadwiger's theorem (2.15) (and Ref. [47]) states that it *must* adopt this form i.e. as a linear combination of the intrinsic volumes. To find explicit expressions for the thermodynamic coefficients a_k we have to determine the combinatorial prefactor c_n and evaluate the geometric/mixture contribution $\lambda_k^{(n)}$.

To obtain the combinatorial coefficient c_n we use a technique suggested in [51]: the coefficients are independent of dimensionality so we can compare the form of (6.20) against the exact free energy known for $d = 0$. The (quasi–) zero dimensional limit can be thought of as a small cavity which is only able to fit a single particle, as the system size approaches the particle size $V \sim \xi_d$. The exact free energy is known to be [51, 247]

$$\begin{aligned} \lim_{d\to 0} \beta F^{\text{ex}} &= (1-\rho V)\ln(1-\rho V) + \rho V \\ &= \sum_{n=2}^{\infty} \frac{(\rho V)^n}{n(n-1)} \end{aligned} \tag{6.21}$$

where $\rho V < 1$ is the average occupancy of the cavity. To make comparison with our expression for the chemical potential, we observe that the $k = d$ term in (6.20) involves the volume of the inserting particle $\widetilde{V}_d(K_0)$ so its conjugate variable must be the pressure $a_d = \beta p$ [183]. Explicit evaluation in the $d \to 0$ limit then gives

$$\lim_{d\to 0} \left(\frac{\beta p}{\rho} - 1 \right) = \sum_{n=2}^{\infty} c_n (\rho V)^{n-1}$$

where we recognised $c_1 = 1$ for consistency with the ideal gas law, from which we can obtain the excess free energy through the thermodynamic

[93] These are different normalisations of the scaled particle variables introduced in (2.99) in the context of FMT, and originally derived in Ref. [87].

relation

$$\begin{aligned}\lim_{d\to 0}\beta F^{\text{ex}} &= \rho V\int_0^\rho \lim_{d\to 0}\left(\frac{\beta p}{\rho'}-1\right)\frac{d\rho'}{\rho'}\\ &= \sum_{n=2}^{\infty}\frac{c_n}{n-1}(\rho V)^n.\end{aligned} \tag{6.22}$$

Comparing (6.21) and (6.22) allows us to read off the combinatorial term as

$$c_n = \frac{1}{n}. \tag{6.23}$$

Finally, collecting terms of the same index in (6.19b) gives the more tractable sum [51]

$$\lambda_k^{(n)} = \sum_{\substack{N_0,N_1,\cdots,N_d\geq 0\\ dN_0+(d-1)N_1+\cdots+N_{d-1}=k\\ N_0+N_1+\cdots+N_d=n}} n!\prod_{j=0}^{d}\frac{\xi_j^{N_j}}{N_j!} \tag{6.24}$$

with the factorials accounting for the different combinations of terms.

Despite the complicated form of the summation limits in (6.24), there are very few contributing terms in physical dimensions $d \leq 3$; we will work these out explicitly in the next section. Resumming the $\lambda_k^{(n)}$ terms gives the thermodynamic coefficients a_k through (6.20b) after inserting the combinatorial term (6.23) giving

$$\beta a_k = k!\omega_k\sum_{n=1}^{\infty}\frac{\lambda_k^{(n)}}{n}. \tag{6.25}$$

Notably, $a_d = p$ gives the equation of state.

6.4 Explicit morphometric contributions in the virial expansion

Here we explicitly evaluate the contributions in the virial expansion from configurations sharing a common point of intersection via (6.19b).

For $d = 1$ the index runs over $k \in \{0, 1\}$, so the criteria on the summation indices is that $N_0 = k$ and $N_1 = n - N_0$ leading to a single term for each value of k:

$$\lambda_0^{(n)} = \xi_1^n, \tag{6.26a}$$

$$\lambda_1^{(n)} = n\xi_0\xi_1^{n-1}. \tag{6.26b}$$

For $d = 2$ we have $k \in \{0, 1, 2\}$, with summation conditions $2N_0 + N_1 = k$ and $N_2 = n - N_1 - N_0$ giving:

$$\lambda_0^{(n)} = \xi_2^n, \tag{6.27a}$$

$$\lambda_1^{(n)} = n\xi_1\xi_2^{n-1}, \tag{6.27b}$$

$$\lambda_2^{(n)} = n\xi_0\xi_2^{n-1} + \frac{n(n-1)}{2}\xi_1^2\xi_2^{n-2}. \tag{6.27c}$$

Finally, for $d = 3$ we have $k \in \{0, 1, 2, 3\}$, with summation conditions $3N_0 + 2N_1 + N_2 = k$ and $N_3 = n - N_2 - N_1 - N_0$ giving:

$$\lambda_0^{(n)} = \xi_3^n, \tag{6.28a}$$

$$\lambda_1^{(n)} = n\xi_2\xi_3^{n-1}, \tag{6.28b}$$

$$\lambda_2^{(n)} = n\xi_1\xi_3^{n-1} + \frac{n(n-1)}{2}\xi_2^2\xi_3^{n-2}, \tag{6.28c}$$

$$\lambda_3^{(n)} = n\xi_0\xi_3^{n-1} + n(n-1)\xi_1\xi_2\xi_3^{n-2} + \frac{n(n-1)(n-2)}{6}\xi_2^3\xi_3^{n-3}. \tag{6.28d}$$

We will now resum $\lambda_k^{(n)}$ over n in order to determine the values of a_k for $d \leq 3$. For $d = 1$ we insert (6.26) into (6.25):

$$\beta a_0 = -\ln(1 - \xi_1), \tag{6.29a}$$

$$\beta p = \beta a_1 = \frac{2\xi_0}{1 - \xi_1}, \tag{6.29b}$$

with $\xi_0 = \rho/2$ and $\xi_1 = \eta$ giving the exact result for hard rods (6.2) and (6.3).

For $d = 2$ we insert (6.27) into (6.25):

$$\beta a_0 = -\ln(1 - \xi_2), \tag{6.30a}$$

$$\beta a_1 = \frac{2\xi_1}{1 - \xi_2}, \tag{6.30b}$$

$$\beta p = \beta a_2 = 2\pi\left(\frac{\xi_0}{1 - \xi_2} + \frac{\xi_1^2}{2(1 - \xi_2)^2}\right). \tag{6.30c}$$

For hard discs of diameter σ we obtain $V_1 = \pi\sigma/2$ so $\xi_0 = \rho/(2\pi)$, $\xi_1 = \rho\sigma/2$ and $\xi_2 = \eta$ for the single-component fluid, which produces coefficients identical to two-dimensional scaled particle theory. In this limit the chemical potential of inserting a disc of radius R becomes

$$\Delta\Omega(R) = \frac{1}{\sigma^2(1 - \eta)^2}\,\pi R^2 + \frac{4\eta}{\sigma(1 - \eta)}R - \ln(1 - \eta).$$

It is straightforward to verify by insertion that this satisfies the two-dimensional equivalents of the scaled particle conditions (4.14a), (4.14b) and (4.15), demonstrating that this is indeed the scaled particle theory solution.

Finally, for $d = 3$ we insert (6.28) into (6.25):

$$\beta a_0 = -\ln(1 - \xi_3), \tag{6.31a}$$

$$\beta a_1 = \frac{2\xi_2}{1 - \xi_3}, \tag{6.31b}$$

$$\beta a_2 = 2\pi\left(\frac{\xi_1}{1 - \xi_3} + \frac{\xi_2^2}{2(1 - \xi_3)^2}\right), \tag{6.31c}$$

$$\beta p = \beta a_3 = 8\pi\left(\frac{\xi_0}{1 - \xi_3} + \frac{\xi_1\xi_2}{(1 - \xi_3)^2} + \frac{\xi_2^3}{3(1 - \xi_3)^3}\right). \tag{6.31d}$$

For hard spheres of diameter σ we obtain $V_1 = 2\sigma$ and $V_2 = \pi\sigma^2/2$ so $\xi_0 = \rho/(8\pi)$, $\xi_1 = \rho\sigma/(2\pi)$, $\xi_2 = \rho\pi\sigma^2/8$ and $\xi_3 = \eta$ for the single-component

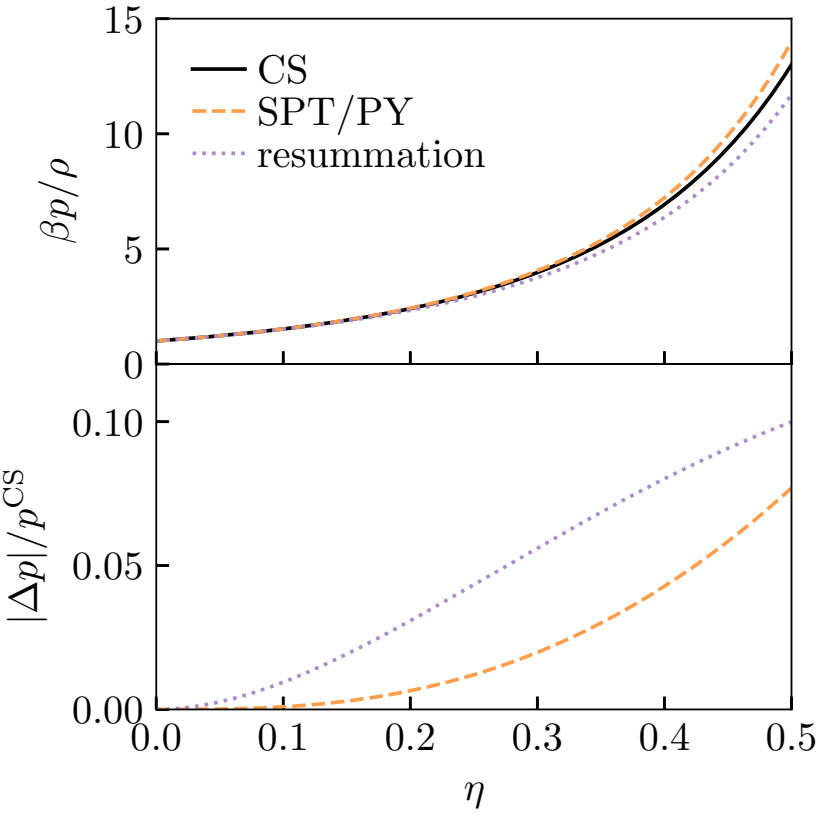

Figure 6.1: Equations of state for the single-component hard sphere liquid in $d = 3$: Carnahan-Starling (CS), scaled particle/Percus-Yevick (SPT/PY) and the equation obtained from resumming terms in the virial series where there is a common point of intersection. Top panel: pressure equations of state. Bottom panel: errors in the SPT/PY and resummation pressures are comparable across the whole liquid regime, taking the CS equation as the quasi-exact result.

fluid. This is similar but not identical to the Percus-Yevick equation of state[94] for additive mixtures, which in terms of this chapter's normalisations of the scaled particle variables reads [13]

$$\beta p^{\mathrm{PY}} = 8\pi \left(\frac{\xi_0}{1-\xi_3} + \frac{\xi_1\xi_2}{(1-\xi_3)^2} + \frac{16\xi_2^3}{3\pi^2(1-\xi_3)^3} \right), \tag{6.32}$$

which is exact up to the third virial coefficient B_3, and reduces to the SPT/PY equation (4.16d) in the case of single-component hard spheres. By contrast, the resummation approach only provides a lower bound on B_3; the omitted configurations are known in the FMT literature as "lost cases" [248]. A semi-empirical approach to obtain (6.32) could involve reweighting the final term in (6.31d) to produce the exact third virial coefficient, giving an equation of state for arbitrary mixtures of convex particles. This reweighting is implicit in scaled particle theory and the Rosenfeld FMT functional (2.96) [51, 248]. In particular, scaled particle theory in $d = 3$ is able to achieve accuracy at the B_3 level because of the additional constraint at the origin (4.14c) which is not available in $d = 2$. Such a reweighting approach is redundant because (6.32) and the Rosenfeld functional are already known, so this of fundamental rather than practical interest.

[94] Specifically via the compressibility route. See section 2.3.4 for a description of the single-component case.

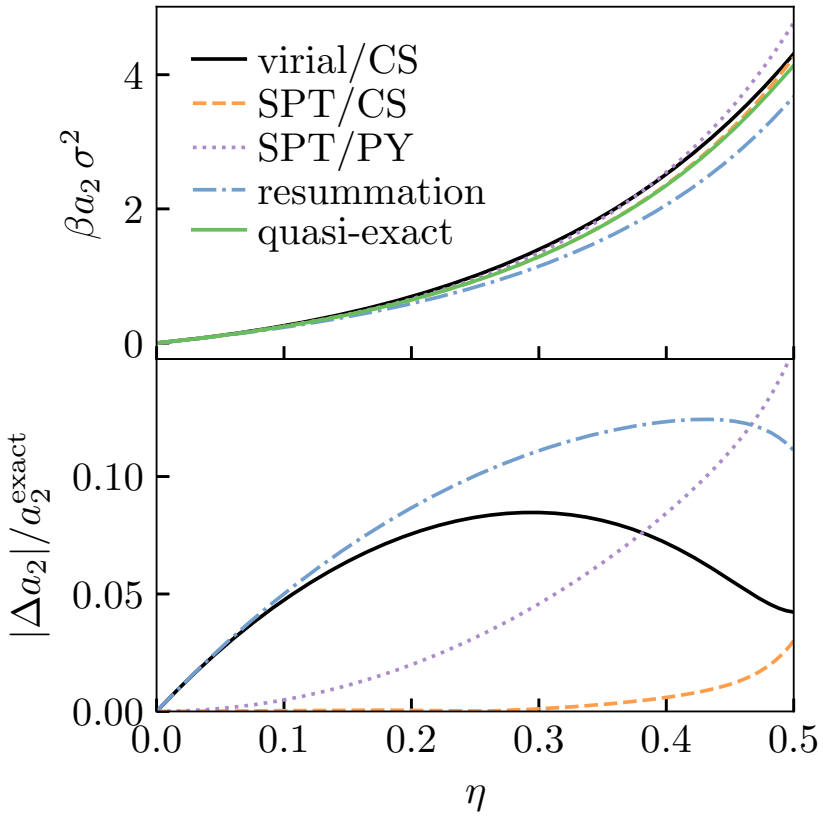

Figure 6.2: Comparison of surface tensions for different morphometric theories. using the highly accurate result (6.34) from Ref. [205] valid until $\eta \sim 0.5$.

6.5 Numerical results for single-component hard spheres

For single-component hard spheres the pressure obtained from the resummation in the previous section yields

$$\frac{\beta p}{\rho} = \begin{cases} \frac{1}{1-\eta} & d = 1 \\ \frac{1}{(1-\eta)^2} & d = 2 \\ \frac{1+\eta+(\frac{3\pi^2}{16}-2)\eta^2}{(1-\eta)^3} & d = 3. \end{cases} \tag{6.33}$$

The resulting pressures for $d \leq 2$ are identical to those obtained by scaled particle theory, where the first is actually exact (6.3). For $d = 3$ the resulting equation of state has a similar structure to the scaled particle theory solution (or equivalently the Percus-Yevick equation of state by the compressibility route) (SPT/PY) but it is slightly less accurate: at the freezing point $\eta_f \simeq 0.494$ the PY equation overestimates the pressure by $\sim 7\%$ while for the above equation this is underestimated by $\sim 11\%$, taking the Carnahan-Starling (CS) equation of state [15] as an estimate of the exact value. The three equations of state mentioned in $d = 3$ are plotted together in Fig. 6.1 across the whole liquid regime in hard spheres. While not exact, this shows that the morphometric contributions account for ∼90% of the equation of state which may suggest why morphological thermodynamics has been found to be highly accurate for descriptions of the hard sphere liquid [1, 95, 179–182]. This is discussed in more detail in the context of FMT in

[51], and is partially attributable to cancellations of terms omitted from the resummation.

We see similar accuracy in the predicted surface tension at an infinite planar wall determined by[95] a_2. To measure accuracy we restate the quasi-exact result (6.34) of Ref. [205] in terms of the normalisations used in this chapter as

$$\beta a_2 = \frac{2}{\pi\sigma^2}\left(\frac{\eta(2+3\eta-\frac{9}{5}\eta^2-\frac{4}{5}\eta^3-(5\times10^4)\eta^{20})}{(1-\eta)^2}-\ln(1-\eta)\right). \quad (6.34)$$

[95] This is true up to a normalisation constant, as a_2 conjugates with the intrinsic volume V_2 rather than the area $A = 2V_2$. The usual planar surface tension is thus obtained as $\gamma_\infty = a_2/2$.

We also compare the values of a_2 predicted by other morphometric theories of (4.23) (SPT/CS, or equivalently the coefficients (2.111) of Ref. [96]) and the coefficients derived in chapter 4 (virial/CS) given in (4.27). The surface tensions are plotted in Fig. 6.2; the accuracy of the new result is comparable to SPT/PY in the liquid regime with the maximum error reaching $\sim 12\%$. Unsurprisingly, the other morphometric theories feature more accurate surface tensions; this is likely because they were constructed to satisfy thermodynamic relations which improves their accuracy. Curiously, the error in the new theory scales almost identically to virial/CS theory at small η even though it has the opposing sign; all of the previous morphometric theories overestimate the surface tension, whereas the resummation route underestimates it.

6.6 Conclusions

We have derived an exact morphometric contribution for a general class of hard particle liquids by resumming terms in the virial series. Previous studies have primarily used FMT to develop morphometric theories, so we have successfully developed an independent justification for the morphometric approach as the leading term in a controlled expansion. The exact result applies for mixtures of hard convex particles in an isotropic phase.

In hard spheres, this exact contribution features similar accuracy as scaled particle theory, and exactly coincides with it for $d \leq 2$. Numerical comparison in $d = 3$ shows that the pressure and surface tension are comparable in accuracy to the classic SPT/PY route, so it captures the dominant contributions to the bulk free energy across a large density range; this latter fact seems to suggest why the approach has been successful. Though as noted in Ref. [51], this is partially due to a cancellation in the omitted terms of the virial expansion. The usefulness of the new route extends beyond mere accuracy; the free energy we have identified emerges *rigorously* as a contribution from the virial series.

The free energy we have identified emerges *rigorously* as a contribution from the virial series, and its accuracy indicates that the success of morphological theories reported in previous investigations [1, 95, 179–182] is enabled by this being a significant leading contribution. Moreover, the exact contribution provides a suitable starting point for including additional terms where improved accuracy is needed at e.g. high densities approaching dynamical arrest. We could write the insertion cost for a solute K as the

exact decomposition

$$\Delta\Omega[K] = \sum_{k=0}^{d} a_k V_k[K] + \Delta\Omega_{\text{extra}}[K] \tag{6.35}$$

with coefficients a_k as previously calculated, and $\Delta\Omega_{\text{extra}}$ containing the subleading corrections. Notably, the exponentially damped oscillations occurring in pair correlations at asymptotically large separations must be contained within $\Delta\Omega_{\text{extra}}$. The insertion cost is known to contain singularities [183] so it is unlikely that $\Delta\Omega_{\text{extra}}$ possesses a simple analytic form. It is possible that additional exact morphometric contributions exist, and they would be contained in $\Delta\Omega_{\text{extra}}$ also. Furthermore, the formal derivation we have followed naturally leads to explicit expressions for $\Delta\Omega_{\text{extra}}$.

The next leading contribution from the virial series would be:

$$\Delta\Omega_{\text{extra}}[K] = \frac{\rho^2}{2} \sum_{s_1=1}^{m} \sum_{s_2=1}^{m} x_{s_1} x_{s_2} \left(\Delta_{s_1,s_2} - \Lambda_{s_1,s_2}\right) + \mathcal{O}(\rho^3), \tag{6.36}$$

where Δ_{s_1,s_2} is the three-body *ring integral* given explicitly in the first line of (6.3). Ring integrals can be calculated straightforwardly in hard spheres [58], or using the Radon transform for convex geometries of arbitrary shapes [244, 249, 250]. Corrections to the morphometric approximation could be systematically included by further resummations over other classes of diagrams, with ring integrals as the leading order terms. The integral corrections are discussed in Ref. [51] in the context of free energy functionals for inhomogeneous liquids; our system is effectively homogeneous so we expect it to be easier to construct a theory with these higher-order terms. Notably, the ring integrals are argued to be the sole contributions in the mean-field infinite-dimensional limit, i.e. for a single-component system [122, 251]

$$\lim_{d\to\infty} \frac{\beta F_{ex}}{V} = \rho^2$$  $$+ \rho^3$$  $$+ \rho^4$$  $$+ \rho^5$$  $$+ \mathcal{O}(\rho^6),$$

ignoring combinatorial prefactors for clarity. The equivalent diagrams in the morphometric/FMT approaches are given in (6.14). Resumming the ring diagrams would lead to a contribution in $\Delta\Omega$ involving a double volume integral over the solute geometry, and their inclusion could possibly provide more of a connection between the morphometric approach and the results of mean-field hard sphere calculations (section 3.3).

The form of the exact contribution is instructive in how it applies to mixtures. It is argued in Ref. [241] that for an m-component mixture the appropriate morphometric form reads

$$\Delta\Omega[K] = \sum_{i=1}^{m} a_3^{(i)} V_i[K] + a_2^{(i)} A_i[K] + a_1^{(i)} C_i[K] + a_0^{(i)} X_i[K] \tag{6.37}$$

where the coefficients $a_k^{(i)}$ now depend on the specific interactions with each species and their composition, and $\{V_i, A_i, C_i, X_i\}$ are geometric measures on some composite body of the solute with solvent particles of species i, e.g. their specific excluded volume. By contrast, our exact morphometric

contribution does not involve different intrinsic volumes for the different cross-species interactions, suggesting (6.1) is a general enough *ansatz* and the extension for mixtures (6.37) proposed in Ref. [241] may be unnecessary. Moreover, as functions of the scaled particle variables $\{\xi_i\}$ the coefficients we derive remain well-defined in the polydisperse limit $m \to \infty$, discussion of which can be found in section 2.2.5 and in more detail in Refs. [61–64]. With the number of coefficients growing with m in (6.37), it is unclear how well-posed this *ansatz* is in that limit.

Chapter 7

Nucleation kinetics in simple drying aerosols

Remove the plastic.

Sears® cross-trainer manual.

In previous chapters we focused on modelling hard spheres at high densities, with a particular focus on supercooled liquids and glasses. As we mentioned in the introduction, another central topic of the high density liquid is the process of nucleation by which the liquid becomes a crystal. This chapter addresses nucleation within the context of drying aerosol droplets, with applications to climate modelling and industrial spray drying. The chemistry involved in aerosols makes this system much more complicated than can be captured with a simple hard sphere interaction, so our microscopic morphometric formalism will not work here at present. Instead, we start from the mesoscale limit where the droplet can be treated as a continuum.

This work was undertaken in collaboration with members of the Reid group in the School of Chemistry at the University of Bristol. In particular, the experiments were carried out by Flo Gregson. My contribution to this work was through theory and numerical modelling to better understand the experimental data. Consequently, while I will describe the experiments the focus of the chapter will be theoretical. Some of this work has already been published in Ref. [2], and we hope to publish the remainder as Refs. [5, 6] later this year.

Finally, for the benefit of those working in the field of supercooled liquids and glasses who are reading this and wondering what this chapter has to do with the rest of the thesis, we put forward the following additional motivation: in order to finally solve the glass transition, we must address the looming climate crisis to keep glass researchers alive long enough to actually reach a consensus[96]. As such, consider this chapter a small step in consensus building.

[96] On second thought, I suppose another option would be: "last statistical physicist alive gets to decide the nature of the glass transition".

7.1 Introduction

The impact of atmospheric aerosols on the climate remains the leading single uncertainty in climate predictions [252–255]. In particular, the radiative forcing caused by anthropogenic aerosols in clouds features large uncertainties due to the difficulty of direct measurement, and the large parameter spaces of theoretical models [254]. Thus, the importance of improving models for atmospheric aerosols to better predict climate change and inform policy cannot be overstated. In addition, atmospheric aerosols have potential applications in geoengineering [256].

Notably, radiative forcing of atmospheric aerosols is strongly influenced by their optical properties [257, 258]. The solute concentration and physical state (i.e. whether it is crystalline or amorphous) can thus have a dramatic effect on climate predictions. Central to this is the nucleation and drying kinetics of atmospheric droplets. Where aerosols are included in climate models the focus is typically on sulphates [259, 260]. However, sea salt aerosols (e.g. those containing NaCl), deposited into the atmosphere through natural processes, are more prevalent in the atmosphere than sulphates making up the second largest component of atmospheric aerosols by mass [261]; a major component of aged NaCl aerosols is sodium nitrate ($NaNO_3$) formed through reactions with nitrogen oxides [262], a significant industrial emission. Subsequent reactions form secondary organic aerosols which further impact the climate [263, 264] and are associated with adverse health effects [264]. Given their abundance and relative simplicity we focus on NaCl and $NaNO_3$ aerosol droplets.

Understanding the droplet drying and crystallisation process is also important for industrial applications, most notably in spray-drying. The goal in these applications is to control the distribution of sizes, morphology and phase of the final droplets, which are very sensitive to processing conditions such as solvent [265, 266], temperature [267–269], pH [270, 271] and additional co-excipients [272–274]. Tailoring crystallisation is particularly important because crystal and amorphous states have fundamentally different properties: crystalline droplets are typically more stable, suitable for e.g. product storage [275, 276], whereas amorphous droplets are more soluble which is desirable for e.g. drug delivery [277, 278]. Our investigation of crystal nucleation rates can be inverted to design spray-drying conditions to achieve a desired final state.

In this chapter we will investigate drying and crystal nucleation of free aerosol droplets, by combining experiments and a numerical model of free aerosol droplets. The experiments are described in section 7.2, and we report comparisons with a diffusional model of droplet evolution in section 7.3. We find that classical nucleation theory accurately predicts the crystallisation times for NaCl aerosols, but not for $NaNO_3$, in section 7.4. For $NaNO_3$ we report nucleation rates with non-monotonic behaviour with increasing solute concentration.

7.2 Experiments

The kinetics of drying NaCl and $NaNO_3$ droplets were measured using the Comparative-Kinetics Electrodynamic Balance (CK-EDB). The CK-EDB instrument has been detailed in previous work [279] so we will only describe it briefly here. Droplets of known concentration are produced by a droplet-on-demand generator (MicroFab) and injected into the CK-EDB instrument. Upon generation the droplets are charged ($< 10\,\mathrm{fC}$ through an ion imbalance) with an induction electrode such that they become trapped within the centre of the electrodynamic field, produced by the application of an AC field between two sets of concentric cylindrical electrodes. An additional DC field is applied to the lower set of electrodes to counteract gravity and drag forces acting on the droplet. A circulating current of ethylene glycol coolant across the electrodes controls the chamber temperature T_∞ in the range 273–323 K.

To determine the size and physical state of the droplet, it is illuminated with a 532 nm continuous-wave laser. The resulting elastic light scattering pattern is recorded by a CCD camera placed at 45° to the beam over an angular range of ∼24°. For isotropic droplets in a liquid or dried amorphous state the droplet radius R determines the angular separation between the fringes in the pattern $\Delta\theta$. Assuming the geometric optics approximation of Mie theory, this relationship is given by

$$R = \frac{\lambda}{\Delta\theta}\left(\cos\left(\frac{\theta}{2}\right) + \frac{n\sin\left(\frac{\theta}{2}\right)}{\sqrt{1+n^2-2n\cos\left(\frac{\theta}{2}\right)}}\right)^{-1}$$

where λ is the laser wavelength, θ is the central viewing angle and n is the droplet refractive index. This approximation scheme allows estimation of the droplet radius within an accuracy of ±100 nm. This method fails when crystallisation occurs breaking isotropy and the scattering pattern dramatically changes; this feature allows the time of crystallisation to be determined to within ∼10 ms. Nucleation and growth occur on such a short time scale that it is not possible to obtain information from the experiments on where inside the droplet nucleation occurs or how many initial nucleation sites there are; we can only determine that the droplet has nucleated crystals.

The instrument features two gas flows for humidified and dry nitrogen applied to the droplet at a rate of $0.03\,\mathrm{m\,s^{-1}}$. Controlling the ratio of these two flows through a mass-flow controller (MKS instruments) sets the relative humidity (RH) inside the CK-EDB chamber. Liquid aqueous NaCl and aqueous $NaNO_3$ droplets (20% solute concentration by weight) were evaporated into dry conditions at 20 °C. In all experiments HPLC-grade water, BioXtra ≥ 99.5% NaCl (Sigma-Aldrich) and analytic grade $NaNO_3$ (Fisher-Scientific) were used. Crystallisation of multiple NaCl droplets occurred reproducibly 1 s after droplet generation [2], whereas $NaNO_3$ droplets showed stochastic behaviour with a fraction of droplets not crystallising over the timescale of the experiment (droplets were typically trapped for 10 s). The stochastic behaviour persists when the experiment was repeated for the *same* $NaNO_3$ droplet over a cycle of repeatedly lowering and raising the RH (described in more detail elsewhere [6]), ruling out impurity-driven heterogeneous nucleation.

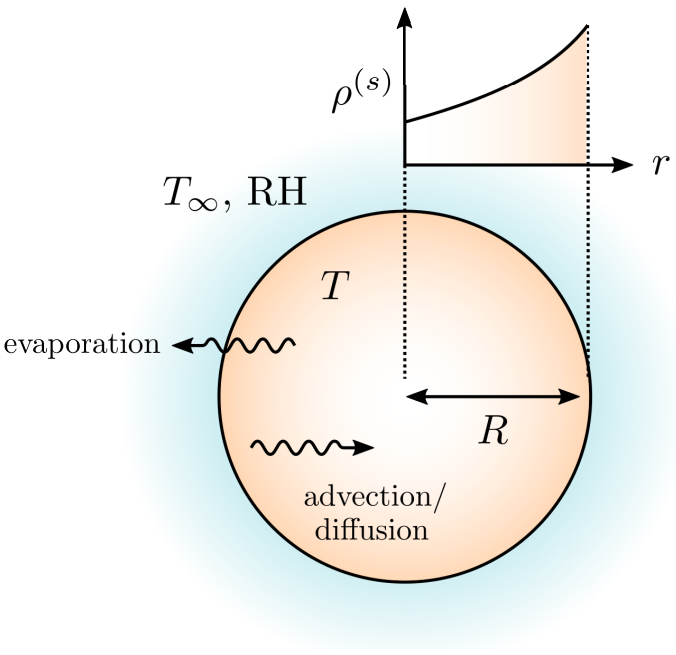

Figure 7.1: A drying droplet solution of radius $r = R(t)$ surrounded by a gas of temperature T_∞ and relative humidity RH. Evaporation of the solvent (water) causes the droplet to shrink and surface enrichment of solute concentration $\rho^{(s)}$ together with evaporative cooling $T < T_\infty$.

Follow up experiments by the Reid group placed the droplets inside a scanning electron microscope (SEM) for imaging. These found that for NaCl aerosols nucleation seems to occur at the boundary[97]. The experiments featuring slower evaporation tended to have more perfect crystals suggesting there were fewer nucleation sites, whereas the more rapidly evaporating droplets showed imperfections consistent with there being multiple nucleation sites at the boundary [6]. The SEM results for $NaNO_3$ were inconclusive, although the resulting crystals were more spherical suggesting there were multiple nucleation sites which may be less strongly distributed at the boundary.

[97] I am reversing chronology here: actually, we used our numerical model to predict this *first*, which was then was confirmed by SEM images.

7.3 Model for a drying droplet

7.3.1 Overview and notation

In order to obtain nucleation rates we require the time evolution of the droplet's concentration profile over its drying history, and a phenomenological model for nucleation rates based on concentration. To determine the concentration profile trajectory for a drying droplet we have to consider the relative motion of solute and solvent species inside the droplet, of various species in the surrounding vapour phase, as well as the evaporation of solvent across the phase boundary. Our approximations will reduce this to a moving boundary problem with solely diffusional mixing.

Prior to crystallisation a drying droplet will be approximately spherical, so we consider a phase boundary at radius $R(t)$ evolving in time t. Writing the distance from the centre of the droplet as r, the phase boundary separates the liquid phase inside $r \in [0, R(t)]$ from the vapour phase outside $r \in [R(t), \infty]$. The droplet is sketched in Fig. 7.1.

We label the solute and (ambient) gas components as s and g respectively, and the evaporating solvent component as f for *fluid* as it exists in

both the liquid and gas phases. The density is $\rho = \sum_i \rho^{(i)}$ where the (mass) concentration of each component is $\rho^{(i)}$ for $i \in (f, s)$ in the droplet and $i \in (f, g)$ in the gas. A useful auxiliary variable is the mass fraction of each component, i.e.

$$Y^{(i)} = \frac{\rho^{(i)}}{\rho}. \tag{7.1}$$

As both phases are binary mixtures[98] so we only need to solve for one component; we choose to solve for the solute mass fraction $Y^{(s)}$ in the droplet and the solvent mass fraction $Y^{(f)}$ in the surrounding vapour.

[98] This is not strictly true. The liquid phase is certainly a binary mixture of solvent and solute, however the vapour is composed of the evaporated solvent and a multicomponent ambient gas phase. However, we can treat the ambient gas as an effectively single-component system to a very good approximation.

The thermal conductivity of liquids is generally much larger than the mass diffusivity, so to leading order we can treat temperature T as homogeneous throughout the droplet. This approximation neglects potential conduction forces driven by temperature gradients. The droplet temperature will be lower than the ambient temperature T_∞ because vaporisation carries a latent heat, and we determine it self-consistently from the vaporisation rate. Later we use T in predicting nucleation rates. However, as a simplification we do not incorporate this temperature into the dynamics themselves through modified diffusion coefficients. This approximation is reasonable because the fractional temperature change is always less than 5 %.

7.3.2 Evolution of the concentration profile

In the absence of any chemical reactions the continuity equation for each species component reads

$$\frac{\partial \rho^{(i)}}{\partial t} + \boldsymbol{\nabla} \cdot (\rho^{(i)} \mathbf{v}^{(i)}) = 0 \qquad i \in \{f, s\} \tag{7.2}$$

where $\mathbf{v}^{(i)}$ is the velocity of species i, or in terms of relative flows

$$\frac{\partial \rho^{(i)}}{\partial t} + \boldsymbol{\nabla} \cdot (\rho^{(i)} \mathbf{v}) + \boldsymbol{\nabla} \cdot \mathbf{j}^{(i)} = 0 \qquad i \in \{f, s\} \tag{7.3}$$

where the mass-averaged fluid velocity is $\mathbf{v} = \sum_i Y^{(i)} \mathbf{v}^{(i)}$ and the relative mass flux is $\mathbf{j}^{(i)} = \rho^{(i)}(\mathbf{v}^{(i)} - \mathbf{v})$. Any advective/convective flows will typically be contained in $\mathbf{v}$, while diffusive effects are captured by $\mathbf{j}^{(i)}$.

Volume additivity holds to a good approximation [280], i.e. the density and concentrations are related by

$$\frac{1}{\rho} = \frac{Y^{(s)}}{\rho_0^{(s)}} + \frac{Y^{(f)}}{\rho_0^{(f)}}, \tag{7.4}$$

where $\rho_0^{(i)}$ is the liquid-phase density of the pure substance; as no stable amorphous phases of NaCl or $NaNO_3$ are known we approximate $\rho_0^{(s)}$ by the density in the crystal phase.

By considering mass conservation one obtains

$$\boldsymbol{\nabla} \cdot \mathbf{v} = \frac{1}{\rho^2} \frac{\partial \rho}{\partial Y^{(s)}} \boldsymbol{\nabla} \cdot \mathbf{j}^{(s)}$$

so assuming volume additivity (7.4) we can define the mass difference parameter as

$$\Lambda = \frac{1}{\rho^2}\frac{\partial \rho}{\partial Y^{(s)}} = \frac{1}{\rho_0^{(f)}} - \frac{1}{\rho_0^{(s)}} \tag{7.5}$$

giving $\mathbf{v} = \Lambda \mathbf{j}^{(s)}$. This simplifies the advective term in the continuity equation (7.3) leading to

$$\frac{\partial \rho^{(s)}}{\partial t} + \boldsymbol{\nabla} \cdot \left((1 + \Lambda \rho^{(s)})\, \mathbf{j}^{(s)} \right) = 0. \tag{7.6}$$

For the relative mass flux we assume Fick's law for diffusion

$$\mathbf{j}^{(i)} = -D_{\text{eff}} \rho \boldsymbol{\nabla} Y^{(i)}, \tag{7.7}$$

where D_{eff} is an effective *binary* diffusion constant for the relative motion. Inserting (7.7) into (7.6) and using the product rule gives

$$\boldsymbol{\nabla} \rho^{(s)} = \left(1 + \Lambda \rho^{(s)} \right) \rho \boldsymbol{\nabla} Y^{(s)}.$$

Finally, this gives the standard diffusion equation

$$\frac{\partial \rho^{(s)}}{\partial t} = \boldsymbol{\nabla} \cdot \left(D_{\text{eff}} \boldsymbol{\nabla} \rho^{(s)} \right), \tag{7.8}$$

where the advective forces have vanished providing a convenient form for numerical implementation. By comparison, the mass fraction is widely used in the literature (e.g. Ref. [280]) which leads to separate advection and diffusion terms i.e.

$$\rho \left(\frac{\partial Y^{(s)}}{\partial t} + \underbrace{\mathbf{v} \cdot \boldsymbol{\nabla} Y^{(s)}}_{\text{advection}} \right) - \underbrace{\boldsymbol{\nabla} \cdot (D_{\text{eff}} \rho \boldsymbol{\nabla} Y^{(s)})}_{\text{diffusion}} = 0.$$

Bulk viscosity measurements are unavailable for highly concentrated solutions because of the propensity for the salts to crystallise, so we extrapolate the available experimental data [281, 282] assuming an Arrhenius-like form

$$\log \eta = \log \left(\eta(\rho^{(s)} = 0) \right) + \alpha \rho^{(s)}, \tag{7.9}$$

where α is a fitting parameter. The fits are shown in Fig. 7.2(a). We model the diffusion constant by assuming the Stokes-Einstein form

$$D_{\text{eff}} = \frac{k_B T}{6\pi \eta a}, \tag{7.10}$$

where a is the Stokes radius and η is the dynamic viscosity. To determine a we calibrated direct measurements of diffusion from molecular dynamics simulations for NaCl [283] and experiments for $NaNO_3$ [284] against the viscosity fits. We obtain $a = 0.169\,\text{nm}$ for NaCl and $a = 0.167\,\text{nm}$ for $NaNO_3$. The resulting diffusion coefficients entering the droplet evolution equation are shown in Fig. 7.2(b).

We employ two simplifications in our calculations concerning the effects of droplet temperature. First, our volume additivity assumption (7.4) makes the density temperature independent; this neglects conduction forces caused

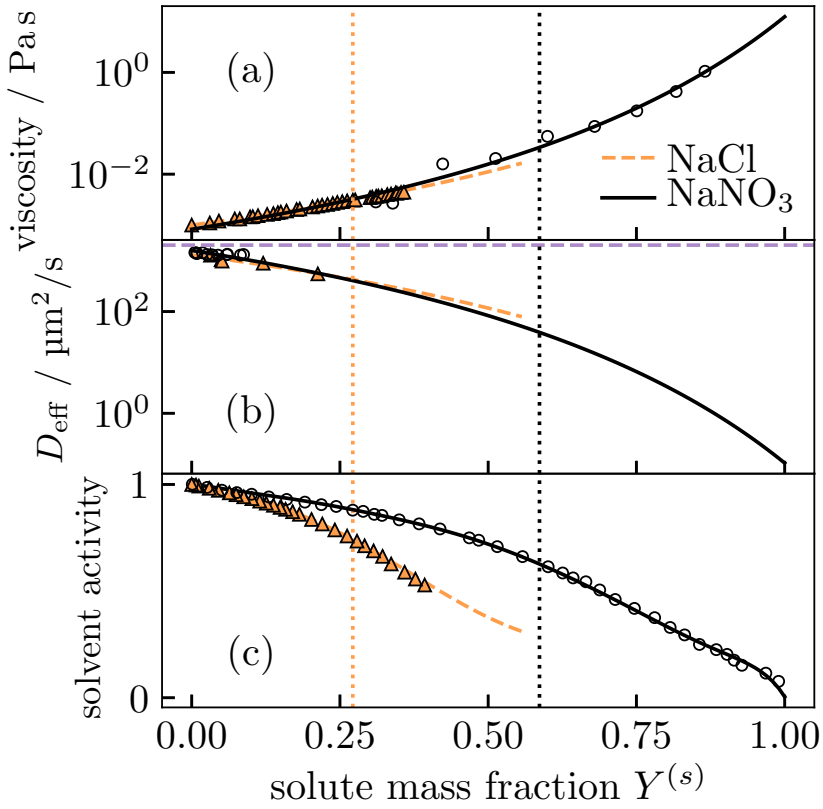

Figure 7.2: Numerical fits of binary diffusion coefficients for aqueous ionic solutions. (a) Fits of viscosity to an Arrhenius-like form (7.9) to experimental values [281, 282]. (b) Diffusion coefficient from the viscosity fits assuming a Stokes-Einstein form (7.10), where the Stokes radius is obtained by calibration with direct measurements of diffusion at 27 °C for NaCl [283] and 25 °C for $NaNO_3$ [284]. (c) Solvent activity a_f from a numerical model [285] compared with experimental data [286, 287]. The extrapolations are taken up until the maximum mass fraction explored by the numerical model. The dashed-purple horizontal line shows the diffusion constant of pure H_2O for reference, to be distinguished from the binary diffusion constants in the limit $Y^{(s)} \to 0$. The dotted lines indicate the saturation thresholds at 20 °C.

by temperature gradients and results in more heterogeneous droplets. Secondly, we approximate $T \sim T_\infty$ in the Stokes-Einstein relation (7.10). This approximation neglects evaporative cooling which would slow diffusion, so overestimates the diffusion constant and will result in more heterogeneous droplets. It is unclear *a priori* which of these opposing effects dominates. Note: later we model the droplet temperature T explicitly for treating solvent evaporation and nucleation rates, but we have not incorporated this temperature into the diffusion constant.

7.3.3 Droplet boundary conditions

Initially, the droplets are prepared as equilibrium solutions, so they are well-mixed and we can assume a uniform initial concentration profile. At $t = 0$ a droplet is produced which begins to lose solvent through evaporation due to the low RH of the CK-EDB. The evaporation rate determines the boundary conditions for the diffusion equation (7.8).

Integrating the species continuity equation (7.2) gives the total mass flow into the droplet (of each species) as

$$\frac{dm^{(i)}}{dt} = \int_{V(t)} \frac{\partial \rho^{(i)}}{\partial t}\, dV + \int_{\partial V(t)} \rho^{(i)}\, \mathbf{v}_{\partial V(t)} \cdot d\mathbf{S}, \tag{7.11}$$

where $V(t)$ is the volume of the droplet at time t and $\mathbf{v}_{\partial V(t)}$ is the velocity of the boundary, and the vectorial surface element $d\mathbf{S}$ points in the direction of the outer normal vector. We assume the solute does not leave the droplet,

so all mass flow at the boundary must be due to the solvent. Inserting the diffusion equation (7.8) into (7.11) and applying Stokes' theorem gives

$$\frac{dm^{(s)}}{dt} = \int_{\partial V(t)} \left(\rho^{(i)} \mathbf{v}_{\partial V(t)} + D_{\text{eff}} \boldsymbol{\nabla} \rho^{(s)} \right) \cdot d\mathbf{S} = 0. \tag{7.12}$$

For spherical droplets this gives the boundary condition

$$\left. \frac{\partial \rho^{(s)}}{\partial r} \right|_{r=R(t)} = -\frac{\rho^{(s)}}{D_{\text{eff}}(R)} \frac{dR}{dt}. \tag{7.13}$$

Assuming volume additivity (7.4) we can determine the radial evolution from mass conservation as

$$\frac{dR}{dt} = \frac{\dot{m}}{4\pi R^2 \rho_0^{(f)}} \tag{7.14}$$

so we need a model of the evaporation rate $\dot{m} := \frac{dm^{(f)}}{dt}$ to close this system of equations.

We now derive the classical result for quasistatic droplet vaporisation, loosely following the exposition of standard texts e.g. Refs. [288, 289]. Relaxation in the vapour phase occurs much faster than inside the liquid droplet, so we can assume that the flows in the vapour phase are quasi-steady. The time-derivative in the continuity equations (7.2) and (7.3) thus vanishes leaving

$$\boldsymbol{\nabla} \cdot (\rho \mathbf{v}) = 0 \tag{7.15a}$$

$$\boldsymbol{\nabla} \cdot (\rho^{(i)} \mathbf{v}^{(i)}) = \boldsymbol{\nabla} \cdot (\rho^{(i)} \mathbf{v} + \mathbf{j}^{(i)}) = 0 \qquad i \in \{f, g\} \tag{7.15b}$$

with the total mass continuity equation obtained by summing over both species in (7.2) and using $\sum_i \rho^{(i)} = \rho$. Assuming spherical symmetry we find that total mass conservation obeys

$$r^2 \rho v = \text{constant} = -\frac{\dot{m}}{4\pi} \tag{7.16}$$

with radial speeds $v = |\mathbf{v}|$ and $v^{(i)} = |\mathbf{v}^{(i)}|$. Similarly, for the evaporating component we obtain the ordinary differential equation

$$r^2 \rho v Y^{(f)} - r^2 \rho D_v \frac{dY^{(f)}}{dr} = -\frac{\dot{m}}{4\pi}$$

where we assumed Fickian diffusion for the relative flux term with D_v as the effective binary diffusion constant for the vapour. Using total mass conservation (7.16) we can rewrite this as

$$\frac{dQ}{dr}(Y^{(f)} - 1) - \frac{d(Y^{(f)} - 1)}{dr} = 0 \tag{7.17}$$

with

$$Q(r) = \frac{\dot{m}}{4\pi} \int_r^\infty \frac{1}{\rho D_v (r')^2} \, dr'. \tag{7.18}$$

Upon integration[99] we find

$$(Y^{(f)}(r) - 1)e^{-Q(r)} = \text{constant}.$$

or

$$\frac{1 - Y^{(f)}(R^+)}{1 - \lim_{r\to\infty} Y^{(f)}(r)} = 1 + B = e^{Q(R)}$$

where the superscript in $Y^{(f)}(R^+)$ indicates the mass fraction of the solvent component is taken on the vapour side of the boundary and we have defined the *Spalding number* as

$$B = \frac{\lim_{r\to\infty} Y^{(f)}(r) - Y^{(f)}(R^+)}{1 - \lim_{r\to\infty} Y^{(f)}(r)}. \tag{7.19}$$

Upon reinserting the definition of $Q(r)$ (7.18) and rearranging we obtain

$$\frac{dm^{(f)}}{dt} = \frac{4\pi \ln(1+B)}{\int_r^\infty \frac{1}{\rho D_v (r')^2}\, dr'}.$$

If we take $\rho = \rho_v$ and D_v as constants in the vapour phase, then we obtain the classical result for quasistatic vaporisation as [288, 289]

$$\frac{dm^{(f)}}{dt} = 4\pi\rho_v D_v R \ln(1+B). \tag{7.20}$$

For the phase boundary it is convenient to work with mole fraction instead of $Y^{(f)}(R^+)$, because it can be related to partial pressure p_f through Dalton's law for ideal gases, i.e.

$$X^{(f)}(R^+) = \frac{p_f(R^+)}{p},$$

with p as the total pressure. This can be converted back into mass fraction for use in (7.19) through

$$Y^{(f)} = \frac{M_f X^{(f)}}{M_f X^{(f)} + M_g(1 - X^{(f)})}, \tag{7.21}$$

where M_i are the molar masses of each species. We can obtain the partial pressure from the solvent concentration at the boundary from the solvent activity, defined through

$$a_f(R^-) := a_f\Big(Y^{(f)}(R^-)\Big) = \frac{p_f(R^+)}{p^*_{\text{eq}}(T)} = \frac{p\, X^{(f)}(R^+)}{p^*_{\text{eq}}(T)},$$

where p^*_{eq} is the equilibrium vapour pressure of the evaporating component. Fig. 7.2(c) shows a_f as a function of mass fraction, obtained through a numerical method that treats the non-ideality of the solution [285]. The Clausius-Clapeyron relation connects the vapour pressure at the surface to the ambient conditions via

$$p^*_{\text{eq}}(T) = p^*_{\text{eq}}(T_\infty) \exp\left(\frac{L}{R_g}\frac{T - T_\infty}{T T_\infty}\right),$$

[99] One way of doing this is to multiply through by the integrating factor $e^{-Q(r)}$.

where L is the specific latent heat of vaporisation and R_g is the molar gas constant. Combining the above expressions gives the mole fraction above the surface as

$$X^{(f)}(R^+) = \frac{a_f(R^-)\, p^*_{\mathrm{eq}}(T_\infty)}{p} \exp\left(\frac{L}{R_g}\frac{T - T_\infty}{T T_\infty}\right), \tag{7.22}$$

which requires an equation for droplet temperature T for closure. As a simplification, we ignored curvature effects on $p^*_{\mathrm{eq}}(T)$ emerging from surface tension [290].

Finally, assuming a steady state heat flux through the boundary, and neglecting the radiative heat transfer and the droplet heat capacity, gives the temperature difference between the droplet surface and the ambient temperature as [287, 291]

$$T - T_\infty = \frac{L}{4\pi R K}\frac{dm^{(f)}}{dt}, \tag{7.23}$$

where K is the thermal conductivity of the vapour phase, closing the equations at the phase boundary. Together, Eqs. (7.20), (7.19), (7.21), (7.22) and (7.23) form a complete set of equations that can be solved (numerically) to obtain the evaporation rate.

Typically the classical vaporisation rate equation (7.20) requires semi-empirical corrections to treat more complex mass and heat transport phenomena at the boundary. In order to better match the experiments, we introduce the empirical factor C to correct the vaporisation rate giving

$$\frac{dm^{(f)}}{dt} = 4\pi\, C\, \rho_v D_v R \ln(1 + B). \tag{7.24}$$

We determine C from the initial value of $\frac{dR}{dt}$ in the experiments. At constant vaporisation rate the solution to the radial evolution equation (7.14) yields

$$R(t)^2 = R(t=0)^2 + \left(2R\frac{dR}{dt}\right)_{t=0} t, \tag{7.25}$$

valid at short times. We iteratively solve Eqs. (7.14), (7.19), (7.21), (7.22), (7.23) and (7.24) with varying C until a value is obtained which produces a $\frac{dR}{dt}$ consistent with the experimental fit. We give the explicit values of C in the appendix.

7.3.4 Implementation and results

We discretise the solute concentration profile $\rho^{(s)}(r)$ onto a uniformly spaced grid over $r \in [0, R(t)]$. To handle the moving boundary it is convenient to work in the rescaled coordinate $\widetilde{r} = \frac{r}{R(t)} \in [0, 1]$. For the discretisation we define the vector $\boldsymbol{\rho} := \{\rho_0, \rho_1, \cdots, \rho_N\}$ where $\rho_i := \rho^{(s)}\left(\widetilde{r} = \frac{i}{N}\right)$. The complete history of the evolution of the droplet then involves both $\boldsymbol{\rho}$ and R variables. In addition, it is convenient to introduce $\dot{R}$ as its own variable so that the final Jacobian for the diffusion equation (7.8) has tridiagonal form. This gives us the evolving droplet state variable $\mathbf{x} = (\boldsymbol{\rho}, R, \dot{R})$.

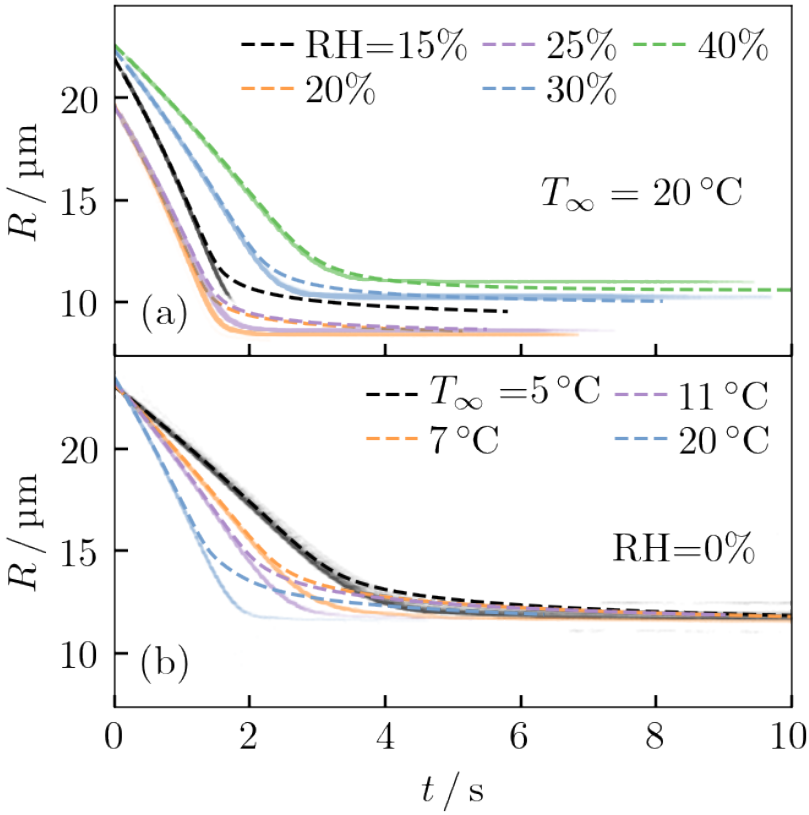

Figure 7.3: Evolution of $NaNO_3$ aerosol droplet radii from the numerical model (dashed lines) and experiments shown by points with 1% transparency, showing reasonable agreement at short times until longer times when the evaporation rate is underestimated. (a) Varying relative humidity while ambient temperature is kept fixed, for an initial solute mass fraction of $Y^{(s)} = 0.125$. (b) Varying ambient temperature while relative humidity is kept fixed, for an initial solute mass fraction of $Y^{(s)} = 0.2$.

To integrate a timestep Δt we use the Crank-Nicolson [292] method where

$$\frac{\mathbf{x}(t+\Delta t)-\mathbf{x}(t)}{\Delta t} = \frac{1}{2}\left(\left.\frac{\partial \mathbf{x}}{\partial t}\right|_{t+\Delta t} + \left.\frac{\partial \mathbf{x}}{\partial t}\right|_{t}\right) + \mathcal{O}(\Delta t^2).$$

As the evolution equations are nonlinear this must be solved iteratively to find a self-consistent solution. Introducing the kth approximation for $\mathbf{x}(t+\Delta t)$ as $\mathbf{x}^{(k)}(t+\Delta t)$, we write the next term in the sequence as $\mathbf{x}^{(k+1)} = \mathbf{x}^{(k)} + \delta\mathbf{x}^{(k)}$ and we obtain

$$\frac{\mathbf{x}_{n+1}^{(k)} + \delta\mathbf{x}_{n+1}^{(k)} - \mathbf{x}_n}{\Delta t} = \frac{1}{2}\left(\frac{\partial(\mathbf{x}_{n+1}^{(k)} + \delta\mathbf{x}_{n+1}^{(k)})}{\partial t} + \frac{\partial \mathbf{x}_n}{\partial t}\right)$$

using the subscript n as shorthand for the time. This is a matrix equation that can be inverted for $\delta\mathbf{x}^{(k)}$. Convergence is deemed to occur where $\delta\mathbf{x}^{(k)}$ falls below some threshold value. The main advantage of this scheme over more simple schemes (e.g. forward Euler method where just the initial $\frac{\partial \mathbf{x}_n}{\partial t}$ is taken) is that the error is of order Δt^2 ensuring rapid convergence with small timesteps.

We integrated initially homogeneous droplets of NaCl and $NaNO_3$ for various ambient conditions. The resulting radius is illustrated for $NaNO_3$ in Fig. 7.3; we see that at short times there is excellent agreement because of the introduction of the correcting factor C in (7.24). However, at longer times the evaporation rate is underestimated. This is likely due to limitations of the simplified evaporation model (7.24) or because the neglect of conductive forces causes the evaporation to become diffusion-limited at

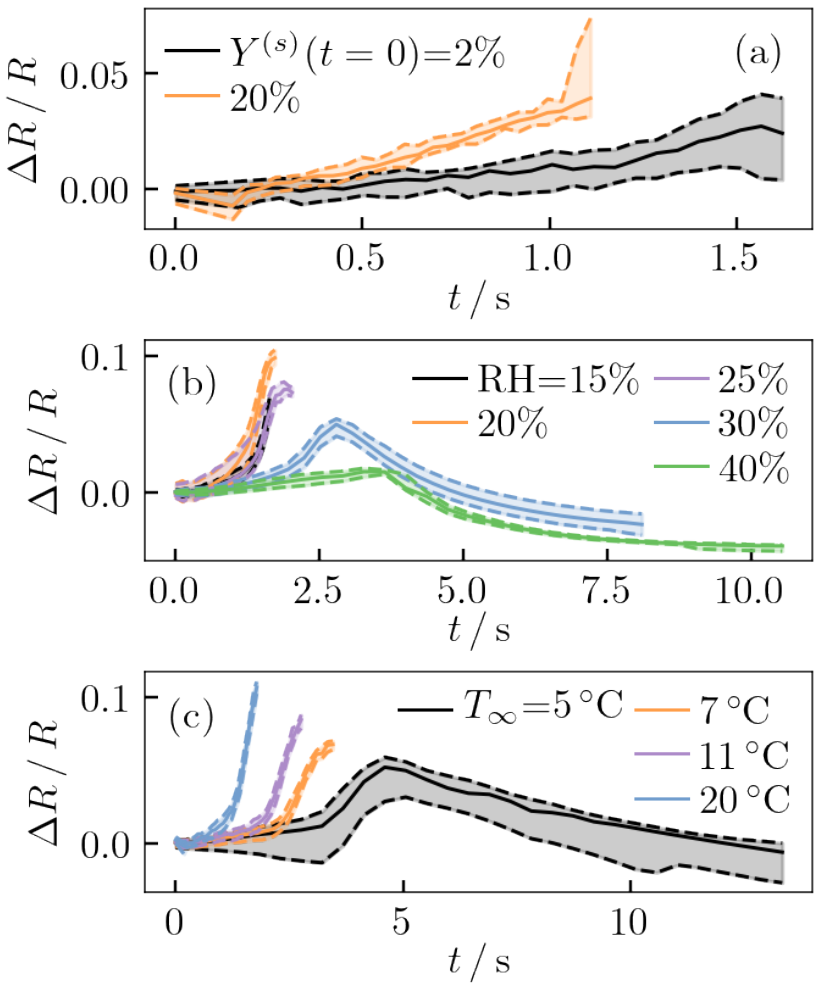

Figure 7.4: Time evolution of simulated droplet radius error by comparison with experiments. We collate data from multiple experiments at each state point; the median across the datasets (solid lines) is shown along with a shaded region indicating agreement up to the 10/90th percentiles (dashed lines). (a) NaCl solution droplets with ambient temperature $T_\infty = 20\,^\circ\mathrm{C}$ in dry conditions. (b) $NaNO_3$ solution droplets with initial solute mass fraction of $Y^{(s)} = 0.125$ and ambient temperature $T_\infty = 20\,^\circ\mathrm{C}$. (c) $NaNO_3$ solution droplets with initial solute mass fraction of $Y^{(s)} = 0.2$ in dry conditions.

long-times when the surface is highly enriched. We achieve good agreement with experiments for NaCl across their entire time evolution (Fig. 7.5(b)) because these droplets crystallise before the slowdown of the evaporation rate. To make this analysis more quantitative we show the errors in the droplet radius in Fig. 7.4; we find that the error is always within 10% in our model throughout the evolution.

7.4 Nucleation model

7.4.1 Droplet nucleation rates

Denoting the rate of solute nucleation per unit volume as J, the continuum limit nucleation rate for the entire droplet is

$$W = \int_V J dV = 4\pi \int_0^R J(r)\, r^2 dr. \tag{7.26}$$

Both the local J and total rates W contain an implicit time dependence because of their dependency on the evolving variables R, $\rho^{(s)}$ and T. For homogeneous nucleation J depends solely on the state variables $\rho^{(s)}$ and T. Nucleation rates are typically strongly concentration dependent [173,

293, 294], so we anticipate nucleation to occur at the boundary $r = R(t)$ where the solute concentration is greatest. Allowing for heterogeneous nucleation J could acquire an additional dependence on the inhomogeneities in the system; as the experiments were performed with high-purity precursor compounds to mitigate the effect of chemical impurities, we expect the main potential site for heterogeneous nucleation to be the liquid-air interface. Whichever nucleation mechanism dominates, we expect it to occur at the boundary so the total rate (7.26) reduces to

$$W \sim 4\pi R^2 J\xi, \tag{7.27}$$

where J is now evaluated at the boundary, and we introduced ξ as the thickness of the typical shell region over which nucleation occurs. We will give nucleation rates in terms of $J\xi$, assuming a value $\xi = 1\,\mu\text{m}$ to set the absolute scale of the rates predicted by theory (section 7.4.2) to most closely match the experiments.

We can relate the nucleation rates to the experimentally observed events by assuming Poisson statistics. We define the survival probability as

$$p_{\text{liq}}(t) := \text{Prob}\left[\text{no nucleation by time } t\right],$$

The mean number of nucleation events in the time interval Δt is simply $W\Delta t$, giving the probability that there is no nucleation event after a time Δt as

$$p_{\text{liq}}(t + \Delta t) = p_{\text{liq}}(t)e^{-W\Delta t}.$$

Taking the infinitesimal limit and using the fact that droplets are prepared in the liquid state giving the initial condition $p_{\text{liq}}(t = 0) = 1$ yields

$$p_{\text{liq}}(t) = \exp\left(-\int_0^t W\,dt\right). \tag{7.28}$$

As we have already determined the droplet's radius and concentration profile from the evolution equations described in section 7.3, we are left needing a model for the nucleation rate per unit volume J before we can determine p_{liq}.

7.4.2 Nucleation models

For nucleation processes with a single barrier the rate per unit volume goes as

$$J = \kappa \exp\left(-\frac{\Delta G^*}{k_B T}\right), \tag{7.29}$$

where κ is a kinetic prefactor and ΔG^* is thermodynamic barrier for the process. A widely used approximation for the kinetic prefactor is [173]:

$$\kappa = n_I j Z, \tag{7.30}$$

n_I is the number density of potential nucleation sites, j is the rate of aggregation to these sites, and Z is the Zeldovich factor. These last two quantities are typically further approximated as [173]

$$j \sim n D_{\text{eff}} R^*, \tag{7.31a}$$

$$Z \sim (N^*)^{-\frac{2}{3}}, \tag{7.31b}$$

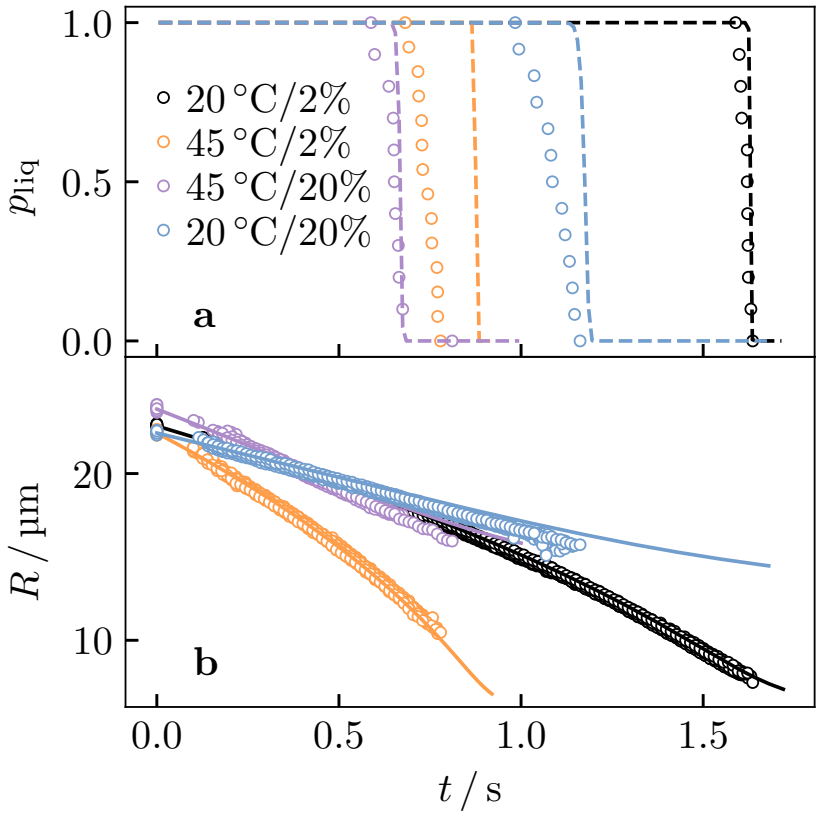

Figure 7.5: Evolution of NaCl droplets in dry air RH = 0% from experiments (points) and the numerical model (lines) for different ambient temperatures and initial solute mass fractions. (a) Probability that a droplet survives without nucleating, assuming the liquid-crystal surface tension $\gamma = 0.08\,\mathrm{N\,m^{-1}}$ [294] for the numerical model. (b) Evolution of droplet radius showing good treatment of solvent evaporation rates.

where n is the solute number density, N^* is excess number of molecules in the critical nucleus and R^* is its radius. The barrier ΔG^* depends on the specific nucleation mechanism.

For homogeneous nucleation the sites of nucleation are simply the solute molecules themselves so $n_I = n$. The driving force for the transition is the chemical potential change $\Delta\mu$ from formation of the new phase. In classical nucleation theory (CNT) the interface energy between the crystal and liquid is imagined as the main obstacle to nucleation. Combining the two contributions leads to the barrier

$$\Delta G = \gamma A - |\Delta\mu| n_c V, \tag{7.32}$$

where γ is the liquid-crystal surface tension, n_c is the crystal number density, and A, V are the surface areas and volumes of the nucleated region. The thermodynamic barrier to nucleation is then the maximum of this formula; assuming a perfectly spherical crystal seed this gives

$$\Delta G^* = \frac{4}{3}\pi (R^*)^2 \gamma, \tag{7.33}$$

$$(R^*) = \frac{2\gamma}{n_c |\Delta\mu|}. \tag{7.34}$$

The chemical potential expressed in terms of mean ionic activity is[294]

$$\frac{\Delta\mu}{k_B T} = 2 \ln\left(\frac{a_\pm}{a_{0\pm}} \frac{\rho^{(s)}}{\rho_0^{(s)}}\right), \tag{7.35}$$

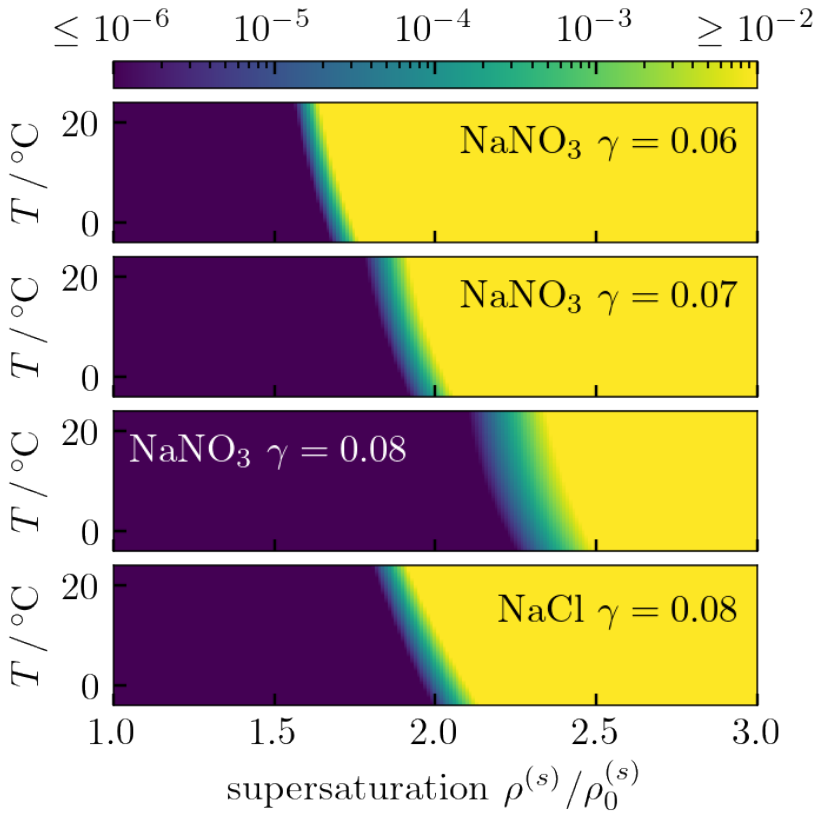

Figure 7.6: Shell nucleation rate $J\xi$ ($\mu m^{-2}\,s^{-1}$) predicted by classical nucleation theory for aqueous $NaNO_3$ and NaCl solutions at different state points. The dark purple and bright yellow regions show where nucleation is essentially impossible or instantaneous on the experimental timescale. Different values of solid-liquid surface tension γ (given in $N\,m^{-1}$) do not result in a different qualitative picture: a nucleation rate which monotonically increases with supersaturation and temperature.

where $a_\pm$ is mean ionic activity coefficient, a_0 is its value at saturation and $\rho_0^{(s)}$ is the threshold saturation concentration.

We find that CNT predicts homogeneous nucleation rates which increase monotonically in both concentration and temperature. In Fig. 7.6 we show the predicted rates for NaCl with $\gamma = 0.08\,N\,m^{-1}$ from the literature [294] and $NaNO_3$ with different trial values of surface tension to test correspondence with the experimental data; we find that the nucleation rates are essentially described by a step function of infinite magnitude over the timescale of the experiments. This is consistent with observations for NaCl, so we are able to accurately predict the time of nucleation in the experiments shown in Fig. 7.5(a). By contrast, the experiments show that the final survival probability for $NaNO_3$ droplets is often in the range $0 < p_{\text{liq}} < 1$ which is not consistent with nucleation rates being characterised by a step function, which we will make more quantitative in the next section.

7.4.3 Inferring nucleation rates from experiments

We can try to determine the nucleation rates directly from experiments by observing the stochastic nucleation behaviour over repeat trajectories and comparing these against the numerical model. The experiments give us the true survival probabilities p_{liq} of which we can determine the droplet nucleation rate W exactly by numerical differentiation. Combined with the numerical model, which gives us the precise state of the droplet, we can infer $J\xi$ from inversion of the rate formula (7.27) under the assumption that nucleation is boundary-dominated.

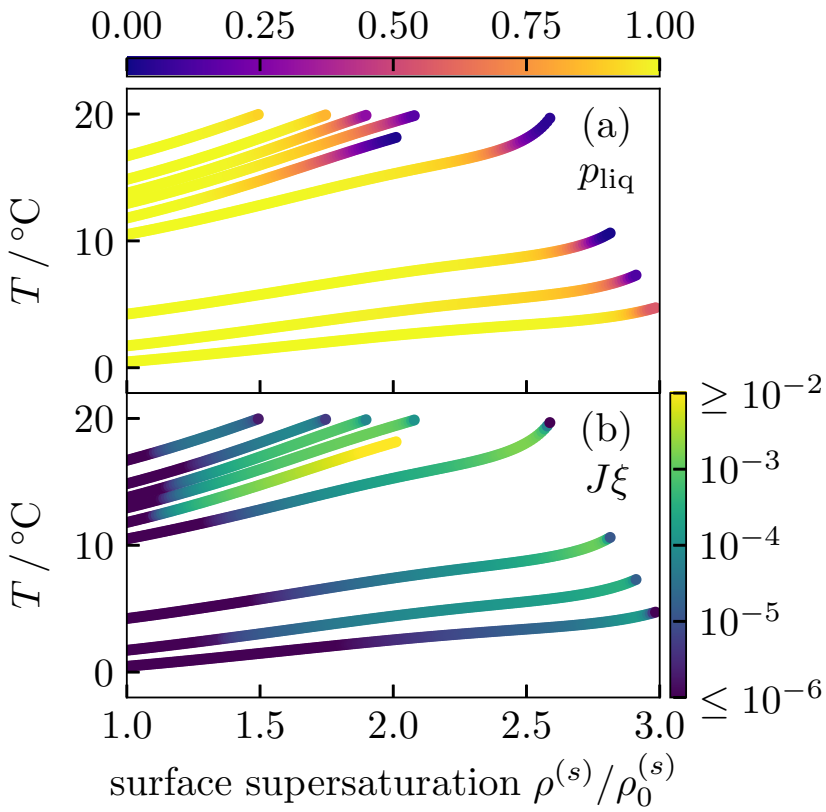

Figure 7.7: State points explored by experiments with drying $NaNO_3$–H_2O aerosol droplets as determined from our numerical model for 9 datasets for droplet evaporation under different initial conditions. (a) Survival probability in the experimental trajectories (i.e. the probability that a droplet has not crystallised), with state-point inferred from the model. (b) Shell nucleation rates $J\xi$ ($\mu m^{-2}\,s^{-1}$) inferred from trajectories assuming boundary-dominated nucleation (7.27), showing non-monotonic behaviour in increased concentration and temperature in contrast with the predictions of classical nucleation theory in Fig. 7.6.

Differentiation of the survival probability (7.28) yields

$$\dot{p}_{\mathrm{liq}} = -W p_{\mathrm{liq}}, \tag{7.36}$$

upon combining this with our assumption that nucleation occurs near the boundary (7.27) allows to write the nucleation rate as

$$J\xi = -\frac{1}{4\pi R^2}\frac{\dot{p}_{\mathrm{liq}}}{p_{\mathrm{liq}}}, \tag{7.37}$$

which we can determine from the experimentally observed p_{liq} trajectory. The derivative of p_{liq} can be obtained through fitting. The survival probabilities decay monotonically as a generalised step function, so we fit the experimental trajectories with the Fermi-Dirac form

$$p_{\mathrm{liq}}(t) - \lim_{t\to\infty} p_{\mathrm{liq}}(t) = \frac{1 - \lim_{t\to\infty} p_{\mathrm{liq}}(t)}{\exp\left[\epsilon(t - t_s)\right] + 1}, \tag{7.38}$$

where t_s is the time at which saturation is reached $\rho^{(s)}(R) = \rho_0^{(s)}$, and introducing the fitting function

$$\epsilon(t) = \begin{cases} at + bt^2 - c/t & t > 0 \\ -\infty & t < 0 \end{cases}$$

subject to the constraint that the fitting parameters $a, b, c \in [0, \infty]$ to ensure that p_{liq} decreases monotonically from $p_{\mathrm{liq}}(t = 0) = 1$.

In Fig. 7.7(a) we show the survival probabilities for the experiments with $NaNO_3$ droplets, and we perform the inversion procedure described above to infer bulk nucleation rates in Fig. 7.7(b). The resulting nucleation rates show non-mononic behaviour, increasing to a maximum before decreasing to essentially zero over the duration of the experiment. This results in a finite final survival probability $p_{\text{liq}} > 0$, and starkly contrasts with the picture captured by CNT and realised in NaCl droplets (Fig. 7.5(a)) where p_{liq} would remain close to unity for most of the experiment before sharply dropping to zero as all the droplets crystallise reproducibly. Fig. 7.6 and Fig. 7.7(b) are shown with identical ranges to highlight this contrasting behaviour.

Clearly the nucleation kinetics in drying $NaNO_3$ aerosols are more complicated than the simple homogeneous nucleation scenario we assumed in section 7.4.2. One kinetic effect we have poorly estimated is the slowing down of diffusion occurring at very high concentrations. We have assumed the Stokes-Einstein relation holds in this highly saturated regime, which may not be a valid assumption; however, more accurate knowledge of the diffusion constant would only shift the nucleation rates by an order of magnitude, which is insignificant compared to the dramatic (and monotonic) kinetic changes emerging from CNT as seen in Fig. 7.6. For this reason nucleation in drying $NaNO_3$ aerosols must occur through a qualitatively different kinetics. More exotic nucleation processes involve e.g. more sophisticated core geometries or pathways featuring multiple steps [173]. Such processes may involve multiple reaction coordinates, whereas classical nucleation theory has a single one.

7.5 Conclusions

We have developed a numerical model based on a diffusion equation with an extrapolation of the diffusion constant to high concentrations assuming the Stokes-Einstein relation. As input the model takes only the initial droplet state, and the resulting evolution conforms well to the experimental trajectories. Assuming boundary dominated nucleation we are able to predict nucleation rates inside the droplet from CNT, and by inverting this process we can infer the actual observed nucleation rates at varying state points. The nucleation rates are highly dependent on the rate of droplet drying, as this determines the state points which are ultimately explored.

We found that CNT works well for predicting crystal nucleation in NaCl but not $NaNO_3$ aerosols. In both cases CNT predicts nucleation essentially after a threshold surface saturation is reached, whereas experiments show nucleation in $NaNO_3$ has stochastic behaviour. This emerges from the fact that nucleation rates predicted by CNT monotonically increase in concentration and temperature. In particular, the change in nucleation rate from increased concentration is so dramatic that the behaviour of CNT is essentially unchanged by small adjustments to the model parameters.

CNT is a model for homogeneous nucleation, so it is possible that it fails because crystallisation occurs for $NaNO_3$ through heterogeneous nucleation. The same stochastic phenomena are observed when repeating the experiments with the same droplet on a cycle of decreasing and increasing

the RH to dry and then re-condense the droplet; this rules out heterogeneous nucleation through impurities, as the chemical makeup is the same in each cycle yet the phenomenon persists. This leaves the gas-liquid phase boundary itself as a site for hetereogeneous nucleation.

It is highly likely that the model overestimates the surface enrichment because at long times the simulated evaporation rates become limited by solute diffusion at the boundary. The diffusion limit would persist even if more sophisticated transport phenomena were introduced to the evaporation model. Surface enrichment is overestimated because we have neglected the effect of temperature gradients inside the droplet, and because we have used an extrapolation of low concentration diffusion data which likely underestimates diffusion at high concentrations. Temperature gradients create inward convection currents reducing surface enrichment. Our extrapolation of the diffusion constant assumed the Stokes-Einstein relation holds across the whole state space, however this relation can be violated at high viscosities [110]. The rapid increase of viscosity with salt concentration in our model leads to a feedback loop where diffusion becomes increasingly difficult as the surface is enriched. Correcting for these effects, we expect the surface concentrations explored by the experiments to increase to a maximum before decreasing which could explain non-monoticity. However, this can only partially explain the observed behaviour because CNT is extremely sensitive to concentration. Fundamentally, we require a deeper understanding of the nucleation kinetics at ultrahigh supersaturations in order to correctly model the crystallisation of droplet drying.

This work is important in showing that the nucleation rate of nitrate aerosol is not only influenced by the level of supersaturation, but also by the drying kinetics itself because of an interplay between the inhomogeneity of the concentration profile and droplet temperature. This is important for climate predictions where an understanding of the phase of atmospheric aerosol is crucial, and also valuable for spray-drying models where control over the resulting phase could be enabled by tuning the various drying parameters.

Chapter 8

Conclusion

> We demand rigidly defined areas of doubt and uncertainty!
>
> Douglas Adams, *The Hitchhiker's Guide to the Galaxy*, (1979).

At high densities, the dynamical properties of supercooled liquids show marked complexity distinguishing them from their ordinary counterparts at lower densities. We have attempted to develop methods to better understand the nature of dynamical arrest and the glass transition, and nucleation of crystals within the metastable liquid. Most of this work has focused on the first question, so we will emphasise that topic here and return to nucleation towards the end.

Liquids approaching their glass transition display a dramatic slowdown in their relaxation behaviour, while showing no obvious structural change at the level of pair correlations. In chapter 3 we summarised the various scenarios posited to explain this phenomenon, highlighting the potential role of amorphous order in mean-field theories and structural order in geometric theories. These thermodynamic scenarios in particular posit solely static mechanisms for dynamical arrest, which we argued could be detected through the many-body correlation functions. Developing from this observation, in chapter 4 we showed that the correlation functions could be expressed in terms of a potential of mean force, itself dependent on the interaction potential and a chemical potential term. The key approximation we employed was the *morphometric approach*, where the chemical potential is expressed as an expansion in size measures: the volume, surface area and integrated curvature measures. Using the many-body correlation functions we attempted to explore the energy landscape of local structures in chapter 5, to look for features which could be connected with dynamical arrest.

We have presented three justifications of the morphometric approach for hard particle systems. First, we derived it in the usual way as a limit of fundamental measure theory (section 2.3.4). Second, we argued for the morphometric *ansatz* as the natural generalisation of scaled particle theory (chapter 4); furthermore, we used integral geometry to argue that this *ansatz* generalises the form of an extensive quantity (section 2.1.3). And last, we derived the morphometric form for the chemical potential by resumming a

component of the virial series (chapter 6).

The latter two justifications are in principle new arguments, though we suspect neither will be of any surprise to the liquid state community; in some sense, these routes are all equivalent because they fundamentally reduce to integral geometric arguments. The primary advancements of this work have thus been technological, rather than fundamental, in nature. In particular, we introduced the trick of imposing self-consistency of the virial theorem to derive a new set of morphometric coefficients in hard spheres (chapter 4). These coefficients yield a theory for chemical potentials capable of producing highly accurate correlation functions, even at high densities. Although we have made some modest contributions to treating local structure in chapter 5 (described below), fundamentally the accuracy of all subsequent results depended on application of this trick.

In chapter 5 we introduced methods to extend the formalism of energy landscapes, normally applied to soft potentials, to local structures of hard spheres; many adaptations were required to handle the singularity of the hard sphere interaction potential. We explored a method of predicting the concentrations of structural motifs within the liquid, and developed a route to do similar calculations along saddles for connecting with dynamics. Notably, we found a bimodality in the distribution of energy states corresponding to distinct structural symmetries, of potential importance to structural viewpoints of dynamical arrest. This work lays the groundwork for a quantitative assessment of the landscape properties of local regions within the liquid, which could explore the validity of random first-order transition and related theories.

There are two factors limiting the accuracy of the morphometric approach: the thermodynamic coefficients entering the theory, and the limitations of the *ansatz* itself. We found that improving the coefficients was enough to obtain accurate results in chapters 4 and 5, though the theory was not exact and so there is room for improvement particularly at the highest densities. We attempted to provide some insight into the theory behind the morphometric approach in chapter 6, with a view to potentially supplementing the *ansatz* with additional terms. There, we found a contribution to the chemical potential which is rigorously of morphometric form, the thermodynamic coefficients of which capture most of the bulk free energy in hard spheres up to moderate densities; this observation potentially explains why the approach works well in the first place. Furthermore, the resulting theory applies to arbitrary mixtures of hard convex particles without modification of the morphometric *ansatz*, suggesting that extensions to other hard particle systems are possible.

In Refs. [295, 296] Glotzer and coworkers showed that hard polyhedra have all the richness in phase behaviour of the periodic table. For example, the propensity for glassformation can be increased by inducing competition between polyhedra of different symmetries, which form competing domains of incompatible crystal structures [158]. Subsequent developments have introduced methods for tailoring assembly into target crystal structures [297–299], many of which have been observed in simulation and experiment [300–302]. Polyhedral particles are intended as representatives of anisotropic particles (e.g. nanoparticles and colloids), in the same way that hard spheres are the starting point in simple liquids. In current theories [297] effective

entropic forces are imagined between parallel faces of adjacent polyhedra, which becomes exact at asymptotically high pressures. The morphometric approach thus has potential to significantly improve descriptions of these interactions, and become a quantitatively predictive theory for nanoparticle and colloidal self-assembly.

For an *isotropic* phase the current morphometric approach should readily extend to arbitrary mixtures of convex polyhedra; the form of the Carnahan-Starling equation for mixtures (2.106) should even give a reasonable description of the liquid pressure. However, in practice the computational geometry required to actually extend morphometric calculations to non-spherical particles would present a considerable challenge. For *anisotropic* phases (e.g. liquid crystal phases which form for highly elongated polyhedra) further theoretical developments would be required. Fundamental measure theory has been extended to anisotropic phases [74–78], so it is likely that a similar programme could be achieved for the simpler morphometric approach.

Continuing on the theme of self-assembly, a fundamental development of interest would be to the kinetics of protein folding. The entropy of the surrounding water is argued to be a major thermodynamic contribution for aqueous proteins [303–305]. The morphometric approach would thus be desirable to avoid explicit solvent modelling, and it has been used with some success [95, 241, 306]. Most of the literature on the morphometric approach concerns hard particles so, while it seems to accurately treat depletion/exclusion interactions, it is less clear how well it would perform for softer and attractive interaction potentials which better represent real systems. Notably, the presence of attractions can induce non-analytic contributions through surface phase transitions [196, 197], which cannot be captured by the morphometric *ansatz*. Moreover, with a soft potential it is not clear *a priori* how to define the surface geometry. Despite these concerns, the potential computational benefit of the morphometric approach makes this area worth exploring.

Finally, we studied the nucleation of salt crystals inside atmospheric aerosols in chapter 7. The chemistry involved was too complex to treat the nucleation kinetics with a hard sphere model, so we used a continuum diffusion model to understand experimental data. We found that classical nucleation theory had mixed success for the systems studied, suggesting more complex nucleation pathways than a simple one-dimensional model.

Were the morphometric approach to be extended to more realistic potentials, we could imagine bridging the gap between the microscopic models of the hard sphere chapters and the continuum models of the final chapter. Crystal nucleation occurs by spontaneous formation of a crystal domain inside the bulk liquid, so the free energy calculations of chapter 5 could be used for crystal geometries to assess the thermodynamic driving forces of nucleation. The morphometric approach would offer a route to access nucleation pathways of much greater complexity than the simple one-dimensional projection normally considered in classical nucleation theory. This would be another possible avenue of the morphometric approach, of interest even for hard spheres.

Appendices

Appendix A

Existence of singularities in the chemical potential

This appendix is intended to supplement chapters 4 and 6 by emphasising the fundamental limitations of the theories we advocate there. In those chapters we advanced the *morphometric approach*, an approximate theory for solvation in hard particle systems. This approximation scheme expresses a chemical potential as an expansion in terms of geometric properties. This expansion is found in any one of equations (2.6), (2.15), (2.109), (4.6), or (6.20). This approach is numerically very accurate, within its regime of validity, however there are fundamental limitations which prevent it from being readily extended. Here we revisit old arguments made by Reiss and coworkers [85, 183] which demonstrate that the cost of inserting a solute is not generally analytic in geometric measures. This argument demonstrates that *any* regular expansion of $\Delta\Omega$ in terms of geometrical measures like curvature must necessarily be approximate.

We consider a single-component hard sphere liquid with particles of diameter σ, and we imagine inserting a hard spherical solute of radius R. A sphere of radius $R + \sigma/2$ around the solute is then excluded to the centres of solvent particles. We write this excluded volume as V_{ex}, which is clearly the minimum size of cavity required to contain the solute. The insertion cost is simply the probability that a randomly chosen position for insertion contains such a cavity, i.e.

$$\Delta\Omega(R) = -k_B T \ln p_0(R) \tag{A.1}$$

where p_0 is the probability that the excluded region is empty. This can be determined as [183]

$$p_0(R) = 1 + \sum_{n=1}^{\infty} (-1)^n F^{(n)}(R) \tag{A.2}$$

where $F^{(n)}(R)$ is the average number of n-tuples of solvent particles contained in the excluded region, as in

$$F^{(n)}(R) = \frac{\rho^n}{n!} \int_{V_{\text{ex}}^n} g^{(n)}(\mathbf{r}^n)\, d\mathbf{r}^n. \tag{A.3}$$

Clearly $F^{(n)}(R) = 0$ for $R < R_n$, the minimum radius capable of containing n hard spheres. At any given state point $g^{(n)}$ will be bounded from above

[100] Typically, we would expect this to occur where the maximum number of particles are in contact, however that is not a necessary assumption for this argument.

by some finite number, so we can write the inequality[100]

$$\begin{aligned} F^{(n)}(R) &\leq \frac{\rho^n}{n!} \max_{\mathbb{R}^{dn}} \left(g^{(n)} \right) \int_{V_{\text{ex}}} d\mathbf{r}^n \\ &= \frac{\rho^n}{n!} \max_{\mathbb{R}^{dn}} \left(g^{(n)} \right) (V_{\text{ex}})^n, \end{aligned} \tag{A.4}$$

but because of the hard core interaction there will be heavy restrictions on allowable values of n for any R. Defining R_n as the smallest R such that n particles can be accommodated, we expect

$$F^{(n)}(R) = \begin{cases} 0 & R < R_n \\ \mathcal{O}\left((V_{\text{ex}})^n\right) & R > R_n \end{cases} \tag{A.5}$$

where the latter polynomial is motivated by the same argument as used in (A.4). Noting that $V_{\text{ex}} \propto R^d$ this can be expressed alternatively as a polynomial in R.

$$F^{(n)}(R) = \begin{cases} 0 & R < R_n \\ \mathcal{O}\left(R^{dn}\right) & R > R_n \end{cases}$$

Applying this bound to (A.2) gives bounds on the scaling of p_0 as

$$p_0(R) = \mathcal{O}\left(R^{dn}\right) \quad R_n < R < R_{n+1}. \tag{A.6}$$

From (A.6) we expect to see singular behaviour at the points $\{R_n\}$. To look at this in more detail we define

$$p_0^{(n)}(R) := 1 + \sum_{m=1}^{n} (-1)^m F^{(m)}(R)$$

such that $p_0 = p_0^{(n)}$ for $R \leq R_{n+1}$. Approaching the singular point R_n we find the deviation from the solution for $R < R_n$ is thus

$$\begin{aligned} \Delta p_0(R) &:= p_0(R) - p_0^{(n-1)}(R) \\ &= (-1)^n F^{(n)}(R) \qquad R < R_{n+1} \end{aligned}$$

i.e. the singular behaviour is entirely contained in $F^{(n)}$. Noting that polynomials of degree n have vanishing $(n+1)$th derivatives, and $V_{\text{ex}} \propto R^d$, we thus expect a discontinuity in the dnth derivative of p_0 about $R = R_n$; from (A.1) we find $\Delta\Omega$ will similarly feature a discontinuity in its dnth derivative at $R = R_n$. A summary of the first few singularities in three-dimensions is given in Table A.1.

Again, these singularities have long been known since the first papers on scaled particle theory [85, 183]. They are worth reiterating because any geometric expansion in simple powers of R will not capture these singularities; the morphometric approach is an example of such an expansion, albeit generalised beyond spherical solutes, so it must necessarily be approximate.

n	R_n/σ	Discontinuity
2	0	$\Delta\Omega'''(R)$
3	$\frac{1}{\sqrt{3}} - \frac{1}{2}$	$\frac{\partial^6 \Delta\Omega}{\partial R^6}$
4	$\sqrt{\frac{3}{8}} - \frac{1}{2}$	$\frac{\partial^9 \Delta\Omega}{\partial R^9}$

Table A.1: First few singularities in the cost of inserting a sphere of radius R into a one-component hard sphere liquid of diameter σ in $d = 3$. $R = R_n$ is the minimum radius required for a sphere to contain n spheres, and the corresponding singularity is determined from equations (A.1) and (A.6).

Appendix B

Computational geometry for the union of many spheres

B.1 Introduction

The two curvature measures, $C_{\partial\mathcal{L}}$ and $X_{\partial\mathcal{L}}$ (integrated mean and Gaussian curvatures respectively), are required for the morphological thermodynamics used extensively in chapters 4, 5 and 6. In this section we give details on their geometric construction to aid morphological calculations. The relevant formulas for $C_{\partial\mathcal{L}}$ and $X_{\partial\mathcal{L}}$ in hard sphere systems have previously been given in references [202] and [95]. Here, we restate these formulas and extend them by computing their derivatives with respect to atomic coordinates. This technical description is only likely to be of interest to those wishing to do morphological calculations of their own.

To briefly motivate these derivative calculations, we remind the reader that derivatives were used in 5 in the calculation of the free energy of local structures along reaction paths (see also Appendix C). Gradients were required for this calculation, providing an analytic method (with perturbation theory) where the numerical method (thermodynamic integration) fails due the instability of intermediate points along the reaction path. Full details of this method are given in section 5.5 and Appendix C. It is worth stating that the usefulness of gradient calculations extends beyond this one application.

The gradient gives the mean depletion forces between (nearby) particles within the bulk liquid, which is generally a quantity of interest in liquid state theories. These solvation forces are useful for speeding up numerical minimisation procedures, and for describing the solvation forces for molecules and proteins in aqueous solution. For the latter case one requires a solvent accessible surface $\partial\mathcal{L}$ which is composed of balls of varying radii; the formulas we present allow for this generalisation.

B.2 Decomposing the solvent accessible surface into intersections

For correlations in homogeneous liquids composed of identical balls, the curvatures must be computed across the solvent accessible surface $\partial\mathcal{L}$ where

the enclosed volume is

$$\mathcal{L} = \cup_{i=1}^{n} \mathcal{B}_{\sigma}^{d}(\mathbf{r}_i),$$

where $\mathcal{B}_{\sigma}^{d}(\mathbf{r})$ is a d-dimensional ball of diameter σ centred on $\mathbf{r}$. In order to keep the formulas as general as possible, we will consider a small generalisation of this surface where the spheres are of arbitrary radii, i.e.

$$\mathcal{L} = \cup_{i=1}^{n} \mathcal{B}_{\sigma_i}^{d}(\mathbf{r}_i), \tag{B.1}$$

where σ_i is the diameter of particle i. The surface used in the main chapters for single-component hard spheres is recovered by setting $\sigma_i = \sigma$ for all i. By construction $\mathcal{L} \in \mathcal{K}^d$ and $\partial\mathcal{L} \in \mathcal{K}^{d-1}$.

If particle i is on the surface of $\mathcal{L}$, i.e.

$$S_i \cap \partial\mathcal{L} \notin \varnothing$$

where $S_i := \partial\mathcal{B}_{\sigma_i}^{d}(\mathbf{r}_i)$ is the spherical surface of particle i, then integrals over $\partial\mathcal{L}$ must carefully consider pieces S_i and intersections $\bigcap_i S_i$ separately. Intersections, e.g. $S_i \cap S_j$ for $i \neq j$, contribute zero area, but may have nonvanishing curvature; this is usually understood by considering the parallel surface $\partial(\mathcal{L} + \mathcal{B}_\epsilon)$ in the limit as $\epsilon \to 0$. Hard core interactions ensure pathological cases where spheres share a centre are excluded, so intersections of two spheres must result in a (one) lower dimensional manifold $S_i \cap S_j \in \mathcal{K}^{d-2}$. It is straightforward to extend this argument to $n \leq d$ intersections $\bigcap_{i=1}^{n} S_i \in \mathcal{K}^{d-n}$. For $n = d$ intersections the solution is a zero-dimensional manifold, i.e. a point.

Intersections between $n > d$ spherical surfaces are possible in principle, but in practice they occur with vanishing probability once a system is thermalised. To see this, consider an overlap of $n > d$ hard spheres. By the above argument one can decompose the surface of the resulting structure into k-dimensional submanifolds where $0 \leq k \leq d$. Higher order surface intersections $n > d$ requires multiple $n = d$ intersections to occur at the same point, which is overconstrained and occurs with measure zero. Thus, the probability of finding points where $n > d$ spheres intersect occurs with measure zero. This argument only applies because we considered the *boundary* of the intersections; it is more common in the physics literature to consider the Mayer function (2.54) (related to the Euler characteristic) of the intersection *volumes*, where the measure is nonzero leading to slow convergence of the virial series [12]. Despite having zero measure, there are cases where one would construct a geometry containing a higher order intersection so we will return to this topic in more detail in section B.5.

In summary, for $d = 3$ the surface $\partial\mathcal{L}$ contains the following submanifolds:

- $S_i \cap \partial\mathcal{L} \notin \varnothing$: a spherical cap from particle i.
- $S_i \cap S_j \cap \partial\mathcal{L} \notin \varnothing$ for $i \neq j$: a line, specifically a circular arc.
- Point $S_i \cap S_j \cap S_k \cap \partial\mathcal{L} \notin \varnothing$ for $i \neq j \neq k$: points where balls i, j, and k intersect. 3 intersecting spheres generally have 2 points of intersection, though usually only 1 of these coincides with the surface $\partial\mathcal{L}$ (the other is usually buried inside the volume $\mathcal{L}$).

- Intersections of more than 3 surface spheres: occurs with vanishing probability in *thermal* systems (see above).

In subsequent sections we will detail contributions to $C_{\partial\mathcal{L}}$ and $X_{\partial\mathcal{L}}$ (and their derivatives) from each of these intersections in $d = 3$. Note that for morphological thermodynamics one also requires the volume and surface area contributions, $V_{\mathcal{L}}$ and $A_{\partial\mathcal{L}}$, for which we do *not* provide computational details as there is already a wealth of literature on this subject (notably Refs. [307, 308]). In particular, we found the algorithm in Ref. [203] to be fast and robust. We extended their implementation to also compute integrated curvature measures, with the formulas given in subsequent sections.

B.3 Integrated mean curvature

B.3.1 Notation

As each line contribution in (B.2) depends on the positions of 2 central spheres, whose intersection forms a circle, together with 2 additional spheres whose intersections with the first two spheres creates terminating vertices for the circular arc. Thus the line contribution depends on the positions of up to 4 particles, so the domain and image of the gradient is (potentially) 12-dimensional. Fewer particles can be involved, and thus the dimension of the space is reduced, if:

- $\theta_l^{(1)}$ and $\theta_l^{(2)}$ are formed by intersections with the same third particle, i.e. if both the solutions (points) to $S_1 \cap S_2 \cap S_i$ $i \notin \{1, 2\}$ and the line joining them is on the surface $\partial\mathcal{S}$. In this case the space is 9-dimensional.

- $\phi_l = 2\pi$: the line forms a closed circle, uninterrupted by other particle intersections. In this case the space is 6-dimensional.

These cases are pathological and generally lines involve 4 particles so the space is 12-dimensional.

Given the large dimensionality we adopt the following notation to carefully distinguish each term in the space. We recast the coordinates as the product space $\mathbf{r}^n \in \mathbb{R}^{n\times 3}$ so we can use the following notation for basis vectors:

$$\mathbf{e}_i^\alpha = \mathbf{e}_i \otimes \mathbf{e}_\alpha,$$

where $i \in \{1, \ldots, n\}$ and $\alpha \in \{1, 2, 3\}$. We use Roman indices to denote the particle number and Greek indices for the Cartesian component.

We use suffix notation where summation is assumed over repeated indices. For example, we write the coordinates in summation convention as

$$\mathbf{r}^n = r_i^\alpha \mathbf{e}_i^\alpha := \sum_{i,\alpha} r_i^\alpha \mathbf{e}_i^\alpha.$$

One obtains the gradient from components of differentiation by summing over the basis vectors, as in

$$\nabla f = \frac{\partial f}{\partial r_i^\alpha} \mathbf{e}_i^\alpha.$$

The latter expression can be used to determine gradients from the explicit forms of differentials given in subsequent sections.

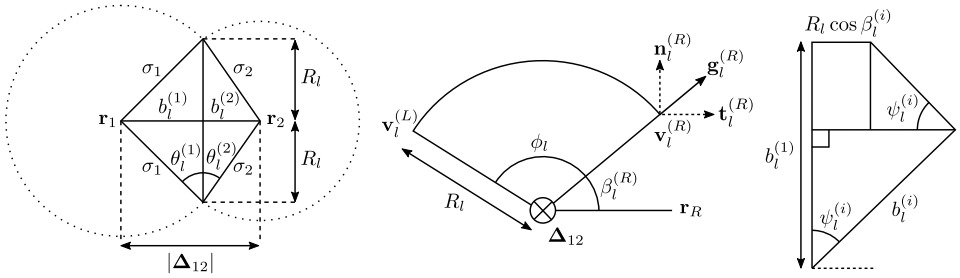

a orthogonal to intersection plane **b** plane of intersection **c** vertex tangents

Figure B.1: Geometrical quantities involved in the calculation of line curvatures.

B.3.2 Problem statement: form of the integrated mean curvature

The integrated mean curvature for the generalised solvent accessible surface $\partial\mathcal{L}$ where $\mathcal{L}$ is composed of spheres of differing radii as in (B.1) is given as [95]

$$C_{\partial\mathcal{L}} = \sum_{s\in S} \frac{A_s}{\sigma_s} - \sum_{l\in L} \frac{\phi_l R_l}{2}(\theta_l^{(1)} + \theta_l^{(2)}), \tag{B.2}$$

where A_s is the area of spherical cap s, ϕ_l is the angular length of the line l, $\phi_l R_l$ its arc length, and $\theta_l^{(1)}$ and $\theta_l^{(2)}$ are the angles between the spheres and the plane of intersection defined in Refs. [309, 310], see Fig. B.1(a). Algorithms already exist for computing the differential of the total area [203, 308], so we do not need to consider the first term in (B.2). This leaves only the line contributions for consideration. The curvature contribution from a single line differentiates to

$$\begin{aligned}\frac{\partial C_{\partial\mathcal{L}}}{\partial r_i^\alpha} =& \sum_{s\in S} \frac{1}{\sigma_s}\frac{\partial A_s}{\partial r_i^\alpha} - \frac{1}{2}\sum_{l\in L}\left(\frac{\partial\phi_l}{\partial r_i^\alpha} R_l(\theta_l^{(1)} + \theta_l^{(2)})\right. \\ &\left. + \phi_l \frac{\partial R_l}{\partial r_i^\alpha}(\theta_l^{(1)} + \theta_l^{(2)}) + (\phi_l R_l)\left(\frac{\partial\theta_l^{(1)}}{\partial r_i^\alpha} + \frac{\partial\theta_l^{(2)}}{\partial r_i^\alpha}\right)\right).\end{aligned} \tag{B.3}$$

In subsequent sections we will give explicit formulas for each differential in this expression.

To get the curvature for the surface used in the results chapters one sets $\sigma_i = \sigma \;\forall\; i \in \{1 \ldots n\}$. In this limiting case the curvature (B.2) simplifies to

$$C_{\partial\mathcal{L}} = \frac{A_{\partial\mathcal{L}}}{\sigma} - \sum_{l\in L} \frac{\phi_l R_l}{2}(\theta_l^{(1)} + \theta_l^{(2)}),$$

and many of the explicit expressions for ϕ_l, R_l, $\theta_l^{(1)}$ and $\theta_l^{(2)}$ also simplify as will be seen in subsequent sections.

Note that in the computational algorithm which we use to compute $\partial\mathcal{L}$ (c.f. Ref. [203]) the symbol θ denotes the in-plane angle $\frac{\pi}{2} - \theta_l^{(\alpha)} \;\forall\; \alpha \in \{1, 2\}$ is used instead in the construction of the surface, so formulas stated below must be adjusted in the implementation if this angle is used.

B.3.3 Particle separations

The separation between two particle centres is

$$\mathbf{\Delta}_{ij} = \mathbf{r}_i - \mathbf{r}_j \tag{B.4}$$

which differentiates to

$$\frac{\partial|\boldsymbol{\Delta}_{ij}|}{\partial r_k^\alpha} = \frac{r_i^\alpha - r_j^\alpha}{|\boldsymbol{\Delta}_{ij}|}(\delta_{ki} - \delta_{kj}) \tag{B.5}$$

where δ_{ij} is the Kronecker delta.

The basis vector for separations differentiates as

$$\frac{\partial}{\partial r_k^\alpha}\left(\frac{\boldsymbol{\Delta}_{ij}}{|\boldsymbol{\Delta}_{ij}|}\right) = \frac{(\delta_{ki} - \delta_{kj})\mathbf{e}_k^\alpha}{|\boldsymbol{\Delta}_{ij}|} - \frac{\boldsymbol{\Delta}_{ij}}{|\boldsymbol{\Delta}_{ij}|^2}\frac{\partial|\boldsymbol{\Delta}_{ij}|}{\partial r_k^\alpha}. \tag{B.6}$$

B.3.4 Quantities in the plane orthogonal to intersection

We will label the particles whose intersection creates the circle of arc as 1 and 2 for convenience. We consider the distances from these particles to the centre of the circle as $b_l^{(1)}$ and $b_l^{(2)}$, see Fig. B.1(a). Clearly $|\boldsymbol{\Delta}_{12}| = b_l^{(1)} + b_l^{(2)}$. These distances form equilateral triangles with circle radius R_l of hypotenuse σ_i for $i \in \{1, 2\}$. This geometry is sketched in Fig. B.1(a). By Pythagoras' theorem we find the unknown distances as

$$R_l = \sigma_1 \cos\theta_l^{(1)} = \sigma_2 \cos\theta_l^{(2)} = \frac{1}{2}\sqrt{2(\sigma_1^2 + \sigma_2^2) - |\boldsymbol{\Delta}_{12}|^2 - \left(\frac{\sigma_1^2 - \sigma_2^2}{|\boldsymbol{\Delta}_{12}|}\right)^2}, \tag{B.7}$$

$$b_l^{(1)} = \sigma_1 \sin\theta_l^{(1)} = \frac{|\boldsymbol{\Delta}_{12}| + \frac{\sigma_1^2 - \sigma_2^2}{|\boldsymbol{\Delta}_{12}|}}{2}, \tag{B.8}$$

$$b_l^{(2)} = \sigma_2 \sin\theta_l^{(2)} = \frac{|\boldsymbol{\Delta}_{12}| - \frac{\sigma_1^2 - \sigma_2^2}{|\boldsymbol{\Delta}_{12}|}}{2}. \tag{B.9}$$

The gradients of the angles between the planes are

$$\frac{\partial\theta_l^{(1)}}{\partial r_i^\alpha} = \frac{1 - \frac{\sigma_1^2 - \sigma_2^2}{|\boldsymbol{\Delta}_{12}|^2}}{2R_l}\frac{\partial|\boldsymbol{\Delta}_{12}|}{\partial r_i^\alpha}, \tag{B.10a}$$

$$\frac{\partial\theta_l^{(2)}}{\partial r_i^\alpha} = \frac{1 + \frac{\sigma_1^2 - \sigma_2^2}{|\boldsymbol{\Delta}_{12}|^2}}{2R_l}\frac{\partial|\boldsymbol{\Delta}_{12}|}{\partial r_i^\alpha}, \tag{B.10b}$$

and the gradients of the distances are

$$\frac{\partial R_l}{\partial r_i^\alpha} = \frac{|\boldsymbol{\Delta}_{12}|}{4R_l}\left(\left(\frac{\sigma_1^2 - \sigma_2^2}{|\boldsymbol{\Delta}_{12}|}\right)^2 - 1\right)\frac{\partial|\boldsymbol{\Delta}_{12}|}{\partial r_i^\alpha}, \tag{B.11a}$$

$$\frac{\partial b_l^{(1)}}{\partial r_i^\alpha} = \frac{1 - \frac{\sigma_1^2 - \sigma_2^2}{|\boldsymbol{\Delta}_{12}|^2}}{2}\frac{\partial|\boldsymbol{\Delta}_{12}|}{\partial r_i^\alpha}, \tag{B.11b}$$

$$\frac{\partial b_l^{(2)}}{\partial r_i^\alpha} = \frac{1 + \frac{\sigma_1^2 - \sigma_2^2}{|\boldsymbol{\Delta}_{12}|^2}}{2}\frac{\partial|\boldsymbol{\Delta}_{12}|}{\partial r_i^\alpha}. \tag{B.11c}$$

As we must calculate the angles $\theta_l^{(1)}$ and $\theta_l^{(2)}$ and their derivatives for the curvature calculation, i.e. (B.2) and (B.3), a convenient form for these latter

derivatives is

$$\frac{\partial R_l}{\partial r_i^\alpha} = -b_l^{(1)} \frac{\partial \theta_l^{(1)}}{\partial r_i^\alpha} = -b_l^{(2)} \frac{\partial \theta_l^{(2)}}{\partial r_i^\alpha}, \tag{B.12a}$$

$$\frac{\partial b_l^{(1)}}{\partial r_i^\alpha} = R_l \frac{\partial \theta_l^{(1)}}{\partial r_i^\alpha}, \tag{B.12b}$$

$$\frac{\partial b_l^{(2)}}{\partial r_i^\alpha} = R_l \frac{\partial \theta_l^{(2)}}{\partial r_i^\alpha}. \tag{B.12c}$$

The expressions in this section are the only quantities which explicitly depend on the sizes of the spheres σ_i, so we see how it is straightforward to consider the more general surface composed of arbitrarily sized spheres. The above formulas are simplified if spheres are of equal sizes i.e. $\sigma_i = \sigma$ (as in the results chapters) leading to vanishing of $\sigma_1^2 - \sigma_2^2$ terms.

B.3.5 Angular length

To complete the derivatives in (B.3) we need an explicit expression for the gradient of the angular separation ϕ_l. In general, the line consists of an arc along a circle of radius R_l, which terminates at the vertices.

We consider the 2d plane containing the intersection $S_1 \cap S_2$. The centre of the intersection circle is

$$\mathbf{c}_l = \mathbf{r}_1 + b_l^{(1)} \frac{\boldsymbol{\Delta}_{12}}{|\boldsymbol{\Delta}_{12}|} = \mathbf{r}_2 - b_l^{(2)} \frac{\boldsymbol{\Delta}_{12}}{|\boldsymbol{\Delta}_{12}|}. \tag{B.13}$$

The plane of intersection is seen by looking along $\boldsymbol{\Delta}_{12}$, making the arc $\phi_l R_l$ perfectly circular, shown in Fig. B.1(b). By convention we choose the arc to be a clockwise migration from a 'left' vertex to a 'right' vertex, which we label $v_l^{(L)}$ and $v_l^{(R)}$ accordingly. These vertices form at 3-particle intersections, so we will use the suffixes L and R to indicate the 3rd particle index (distinct from 1 and 2) where appropriate. We write the vertex coordinates as

$$\mathbf{v}_l^{(i)} = \mathbf{c}_l + R_l \, \mathbf{g}_l^{(i)} \qquad i \in \{L, R\}, \tag{B.14}$$

where the unit vectors are

$$\mathbf{g}_l^{(i)} = \frac{\mathbf{v}_l^{(i)} - \mathbf{c}_l}{|\mathbf{v}_l^{(i)} - \mathbf{c}_l|} \qquad i \in \{L, R\}. \tag{B.15}$$

The unit vectors for the 'right' component are sketched in Fig. B.1(b). The central angle is thus defined as the angle (going clockwise) between these unit vectors, i.e.

$$\cos \phi_l = \mathbf{g}_l^{(L)} \cdot \mathbf{g}_l^{(R)}, \tag{B.16}$$

which after differentiation gives

$$\frac{\partial \phi_l}{\partial r_i^\alpha} = -\frac{\frac{\partial \mathbf{g}_l^{(L)}}{\partial r_i^\alpha} \cdot \mathbf{g}_l^{(R)} + \mathbf{g}_l^{(L)} \cdot \frac{\partial \mathbf{g}_l^{(R)}}{\partial r_i^\alpha}}{\sin \phi_l}. \tag{B.17}$$

So we need explicit expressions for vectors $\mathbf{g}_l^{(L)}$ and $\mathbf{g}_l^{(R)}$ and their derivatives to proceed.

We decompose the vertex unit vectors into the following Cartesian basis:

$$\mathbf{g}_l^{(i)} = \cos\beta_l^{(i)}\,\mathbf{t}_l^{(i)} + \sin\beta_l^{(i)}\,\mathbf{n}_l^{(i)} \qquad i \in \{L, R\}, \tag{B.18}$$

where $\mathbf{t}_l^{(i)}$ is the vector tangent to the plane spanned by particles $\{1, 2, i\}$ and $\mathbf{n}_l^{(i)}$ is normal to this plane. If $\psi_l^{(i)}$ is the angle $\angle 1i2$, that is

$$\cos\psi_l^{(i)} = \frac{\boldsymbol{\Delta}_{12}\cdot\boldsymbol{\Delta}_{1i}}{|\boldsymbol{\Delta}_{12}||\boldsymbol{\Delta}_{1i}|} \qquad i \in \{L, R\} \tag{B.19}$$

then these basis vectors take the form

$$\mathbf{n}_l^{(L)} = \frac{1}{\sin\psi_l^{(L)}}\frac{\boldsymbol{\Delta}_{12}\times\boldsymbol{\Delta}_{1L}}{|\boldsymbol{\Delta}_{12}||\boldsymbol{\Delta}_{1L}|}, \tag{B.20a}$$

$$\mathbf{n}_l^{(R)} = \frac{1}{\sin\psi_l^{(R)}}\frac{\boldsymbol{\Delta}_{1R}\times\boldsymbol{\Delta}_{12}}{|\boldsymbol{\Delta}_{1R}||\boldsymbol{\Delta}_{12}|}, \tag{B.20b}$$

$$\mathbf{t}_l^{(L)} = \frac{\mathbf{n}_l^{(L)}\times\boldsymbol{\Delta}_{12}}{|\boldsymbol{\Delta}_{12}|}, \tag{B.20c}$$

$$\mathbf{t}_l^{(R)} = \frac{\boldsymbol{\Delta}_{12}\times\mathbf{n}_l^{(R)}}{|\boldsymbol{\Delta}_{12}|}. \tag{B.20d}$$

Finally, from Fig. B.1(c) we have

$$b_l^{(i)}\sin\beta_l^{(i)} - R_l\cos\beta_l^{(i)} = \frac{b_l^{(1)} - b_l^{(i)}\cos\psi_l^{(i)}}{\tan\psi_l^{(i)}} \qquad i \in \{L, R\}, \tag{B.21}$$

giving

$$\mathbf{g}_l^{(i)}\cdot\mathbf{t}_l^{(i)} = \cos\beta_l^{(i)} = \frac{1}{R_l}\left(b_l^{(i)}\sin\psi_l^{(i)} + \frac{b_l^{(i)}\cos\psi_l^{(i)} - b_l^{(1)}}{\tan\psi_l^{(i)}}\right) \qquad i \in \{L, R\}. \tag{B.22}$$

With explicit expressions for all of the vectors involved in the arc, the only remaining step is to differentiate. First, we differentiate the vertex unit vectors (B.18) in the basis defined by (B.20) to obtain

$$\frac{\partial\mathbf{g}_l^{(j)}}{\partial r_i^\alpha} = \frac{\mathbf{g}_l^{(j)}\times\boldsymbol{\Delta}_{12}}{|\boldsymbol{\Delta}_{12}|}\frac{\partial\beta_l^{(j)}}{\partial r_i^\alpha} + \cos\beta_l^{(j)}\frac{\partial\mathbf{t}_l^{(j)}}{\partial r_i^\alpha} + \sin\beta_l^{(j)}\frac{\partial\mathbf{n}_l^{(j)}}{\partial r_i^\alpha} \qquad j \in \{L, R\}. \tag{B.23}$$

Second, we take the derivatives of the basis vectors themselves (B.20) giving

$$\frac{\partial\mathbf{n}_l^{(L)}}{\partial r_i^\alpha} = \frac{\mathbf{e}_{c,j}\times\mathbf{e}_l + \mathbf{e}_c\times\mathbf{e}_{l,j}}{\sin\psi_l} - \frac{\cos\psi_l}{\sin\psi_l}\psi_{l,j}\,\mathbf{n}_l, \tag{B.24a}$$

$$\frac{\partial\mathbf{n}_l^{(R)}}{\partial r_i^\alpha} = \frac{\mathbf{e}_{r,j}\times\mathbf{e}_c + \mathbf{e}_r\times\mathbf{e}_{c,j}}{\sin\psi_r} - \frac{\cos\psi_r}{\sin\psi_r}\psi_{r,j}\,\mathbf{n}_r, \tag{B.24b}$$

Finally, we differentiate the angles from (B.19) and (B.22) to get

$$\frac{\partial \beta_l^{(j)}}{\partial r_i^\alpha} = \frac{\frac{\partial R_l}{\partial r_i^\alpha}\cos\beta_l^{(j)} - \frac{\partial}{\partial r_i^\alpha}\left(R_l\cos\beta_l^{(j)}\right)}{R_l \sin\beta_l^{(j)}}, \tag{B.25a}$$

$$\frac{\partial}{\partial r_i^\alpha}\left(R_l\cos\beta_l^{(j)}\right) = \frac{1}{\sin\psi_l^{(j)}}\frac{\partial b_l^{(j)}}{\partial r_i^\alpha} - \frac{1}{\tan\psi_l^{(j)}}\frac{\partial b_l^{(1)}}{\partial r_i^\alpha} - \frac{b_l^{(j)}\cos\psi_l^{(j)} - b_l^{(1)}}{\sin^2\psi_l^{(j)}}\frac{\partial \psi_l^{(j)}}{\partial r_i^\alpha}, \tag{B.25b}$$

$$\begin{aligned}\frac{\partial \psi_l^{(j)}}{\partial r_i^\alpha} &= -\frac{1}{\sin\psi_l^{(j)}}\frac{\partial(\cos\psi_l^{(j)})}{\partial r_i^\alpha} \\ &= -\frac{1}{\sin\psi_l^{(j)}}\left(\frac{\partial}{\partial r_i^\alpha}\left(\frac{\boldsymbol{\Delta}_{12}}{|\boldsymbol{\Delta}_{12}|}\right)\cdot\frac{\boldsymbol{\Delta}_{1j}}{|\boldsymbol{\Delta}_{1j}|} + \frac{\boldsymbol{\Delta}_{12}}{|\boldsymbol{\Delta}_{12}|}\cdot\frac{\partial}{\partial r_i^\alpha}\left(\frac{\boldsymbol{\Delta}_{1j}}{|\boldsymbol{\Delta}_{1j}|}\right)\right),\end{aligned} \tag{B.25c}$$

for $j \in \{L, R\}$ in each expression.

B.4 Integrated Gaussian curvature

$\partial\mathcal{L}$ forms a closed two-dimensional surface, so by the Gauss-Bonnet theorem (2.9) we find X is a topological constant of the surface. Thus, the derivative of X is zero everywhere except at pathological points where a topological change in the surface occurs. In practice this happens when a cavity larger than a particle size forms inside the structure, or when a particle dissociates; being interested in high densities where local structures are condensed, we can exclude both of these scenarios from consideration. Thus, for all local structures $\chi = 2$, and the gradient of X is zero everywhere.

Under the above assumptions we do not need to compute $X_{\partial\mathcal{L}}$, but nevertheless it is convenient to do so in order to check the correctness of the algorithm:

$$X_{\partial\mathcal{L}} = -\sum_{l\in L}\phi_l\left(\sin\theta_l^{(1)} + \sin\theta_l^{(2)}\right) + \sum_{(i,j,k)\in V}\Omega_{ijk} \tag{B.26}$$

where Ω_{ijk} is the solid angle spanned by the 3-vectors at vertex $S_i \cap S_j \cap S_k$ [202]. The condition that this sum must produce the same result as (2.9) provides a useful check of the numerics.

B.5 Intersections of more bodies: possible caveats with quenched geometries

A common task with computer simulations is to quench a geometry to find the minimal (or *inherent*) energy structure. Quenched geometries are inherently athermal so the argument above that intersections of $n > d$ spheres should occur with vanishing probability does not apply; it is common to find intersections of 4 or more particles at the surface in $d = 3$ *after a quench*. To investigate quenched geometries one must properly treat such intersections, as we will demonstrate below with an illustrative example.

An example of these intersections in $d = 3$ occurs where 4 particles are arranged in a perfect square (as in e.g. any outer face of the body-centred cubic unit cell). This special geometry corresponds to a bifurcation point in configuration space, where two pairs of surface vertices are simultaneously created and annihilated. The gradient is not continuous at these points *with respect to the atomic coordinates*, as the continuity of the morphological free energy is only guaranteed with respect to the set $\mathcal{L}$ according to the Hausdorff metric. In atomic coordinates derivatives can contain poles and step discontinuities.

As the example above illustrates, the gradient is not well defined at pathological points where many spheres intersect. It is thus impossible to quench these geometries using standard algorithms (which assume smooth functions) and perturbation theories (e.g. the harmonic approximation for the free energy) will fail. A proper treatment of these cases would be required for an investigation of quenched geometries. In chapter 5 we avoided these pitfalls primarily by restricting ourselves to geometries thermalised using a Monte-Carlo algorithm (Figs. 5.2 and 5.3). Construction of the reaction paths particles necessitated an analytic method which uses a quenched geometry, however the geometries for $n = 6$ and $n = 7$ are not pathological so no special consideration was needed.

Appendix C

Evaluating free energies of hard sphere structures analytically

This appendix describes analytical methods for evaluating the free energy of hard sphere structures used in chapter 5 to obtain free energies along reaction paths. We need to evaluate integrals of the form of (5.16) which we repeat here as

$$\mathcal{I} = \int_{D'} g^{(n)}(\mathbf{x}) R(\mathbf{x})\, d^l\mathbf{x},$$

where $R(\mathbf{x})$ rotational metric. In section (5.5.1) we demonstrated that it is sufficient to solve

$$Z = \int_{\mathcal{D}'} g^{(n)}(\mathbf{x})\, d^l\mathbf{x},$$

and to evaluate the effects of rotations perturbatively using (5.18) it is sufficient to determine the first few moments of the probability distribution $p(\mathbf{x})$. We restate its definition (5.22) as a reminder here as

$$\begin{aligned} p(\mathbf{x}) &= \frac{y^{(n)}(\mathbf{x})}{Z} \prod_{(i,j)\in\mathcal{M}} \mathbb{I}_{[0,\delta]}(h_{ij}) \prod_{\substack{i<j \\ (i,j)\notin\mathcal{M}}} \mathbb{I}_{[0,\infty]}(h_{ij}), \\ &\simeq \frac{y^{(n)}(\mathbf{x}^*)e^{-\mathbf{A}\cdot\Delta\mathbf{x}}}{Z} \prod_{(i,j)\in\mathcal{M}} \mathbb{I}_{[0,\delta]}(h_{ij}) \prod_{\substack{i<j \\ (i,j)\notin\mathcal{M}}} \mathbb{I}_{[0,\infty]}(h_{ij}), \end{aligned}$$

with $\int_{\mathbb{R}^l} p(\mathbf{x}) d^l\mathbf{x} = 1$, and in the final line we have used the first-order expansion of the potential of mean force (5.20) $\mathbf{A} = \nabla\beta\Omega(\mathbf{x}^*)$. Introducing the *tile distribution*

$$t_{ij}(h_{ij}) = \begin{cases} \mathbb{I}_{[0,\delta]}(h_{ij}) & \text{if } (i,j)\in\mathcal{M} \\ \mathbb{I}_{[0,\infty]}(h_{ij}) & \text{if } (i,j)\notin\mathcal{M} \end{cases} \tag{C.1}$$

then the probability distribution becomes

$$p(\mathbf{x}) = \frac{y^{(n)}(\mathbf{x}^*)e^{-\mathbf{A}\cdot\Delta\mathbf{x}}}{Z} \prod_{i<j} t_{ij}(h_{ij}). \tag{C.2}$$

Inspired by the Harmonic approximation (5.4), where the energy is expanded to second order, we will attempt to approximate the basin probability distribution $p(\mathbf{x})$ as a Gaussian. We write this approximate probability distribution as

$$q(\mathbf{x}) = Z\mathcal{N}(\mathbf{x}; \boldsymbol{\mu}, \boldsymbol{\Sigma}). \tag{C.3}$$

where we have kept it unnormalised for convenience (so it is not strictly a distribution) as our goal is to determine Z. The moments of the Gaussian $\boldsymbol{\mu}, \boldsymbol{\Sigma}$ will be determined alongside Z, giving the evaluation of I through (5.18). Some relevant properties of multivariate Gaussians, including its explicit form, are given in section C.5

Consider the free energy difference between the true and approximate distribution

$$\Delta F = -\int p(\mathbf{x}) \ln\left(\frac{q(\mathbf{x})}{Zp(\mathbf{x})}\right) d\mathbf{x}.$$

In information theory this would be called the *Kullback-Leibler divergence*, a measure of information loss from using the approximate distribution $q(\mathbf{x})/Z$. It is straightforward to prove that it is only zero when $p(\mathbf{x}) = q(\mathbf{x})/Z$ [65, 69], but this is impossible to achieve unless $p(\mathbf{x})$ is also Gaussian. However, by minimising ΔF we can optimise the parameters of $q(\mathbf{x})$ to minimise the error of the approximation. It is straightforward to show that for distributions in the exponential family this corresponds to matching the moments of $q(\mathbf{x})$ and $p(\mathbf{x})$ [236–239]. Matching the moments is still intractable because of the high dimensionality of $\mathbf{x}$. Expectation propagation (EP) is a technique to approximate this procedure, which involves matching moments along marginal distributions instead of the whole space [236–239]. This approximation scheme was inspired by the cavity method of spin glasses, for applications to approximate Bayesian inference.

In section C.1 we show how Z can be calculated exactly for the simplest case of minimally constrained geometries and where no additional hard sphere overlaps can occur over the integration domain; this approximation is valid for the smallest geometries up to $n \leq 6$, however fails for $n = 7$ where frustrated packings appear. In subsequent sections we generalise this integration to the the more general case with additional hard sphere interactions using the approximation scheme outlined above. In section C.2 we introduce the *polyhedral approximation* to the integration limits that simplifies treating the tile distributions appearing in (C.2), before we describe the EP method to obtain the optimal Gaussian parameters in section C.3. Throughout this exposition we invoke properties of multivariate Gaussians, which are summarised at the end in section C.5. As this method is a little technical, we provide an example for a simple integration on a triangle in section C.4 as an illustration.

C.1 Minimally constrained geometries

First, we consider the simplest case of *minimally constrained* geometries which have exactly $m = l$ bonds[101], so that the bond-distance space forms a natural basis for this expansion and we can set $\mathbf{x} = \{h_{a_1b_1}, \cdots, h_{a_mb_m}\}$, with the energy minimum occurring at $\mathbf{x}^* = \{0, \cdots, 0\} = \mathbf{0}$. This special case simplifies calculation in a similar way that isostaticity can be exploited

[101] As a reminder, $l = 3n - 6$ is the number of (non-rigid body) degrees of freedom.

to derive theories for systems approaching jamming, [227, 311]. However, we will have to consider the effects of additional hard sphere interactions and later using EP can generalise to the case where $m \geq l$.

As an aside, we describe how to calculate the internal metric entering into $R(\mathbf{x})$ for this choice of coordinates. This metric is defined by

$$\overline{G_{ij}} = \mathbf{J}^T\mathbf{J}$$

where the Jacobian matrix entries are given by

$$J_{ij} = \frac{\partial x_i}{\partial h_{a_j b_j}}.$$

In practice it is usually easier to calculate its inverse numerically (via e.g. finite differences) using

$$J^{-1}_{ij} = \frac{\partial h_{a_i b_i}}{\partial x_j},$$

which has linearly independent rows for a minimally constrained geometry. We can recover $\mathbf{J}$ from $\mathbf{K} := \mathbf{J}^{-1}$ using the matrix inversion formula $\mathbf{J} = (\mathbf{K}^T\mathbf{K})^{-1}\mathbf{K}^T$.

In this basis, the definition of structure (and limits of integration) is equivalent to a hypercube, i.e.

$$\int_{D'} d^l x = \int_0^\delta dx_1 \cdots \int_0^\delta dx_m.$$

Helpfully, the hard sphere interactions between particle pairs $a_k, b_k \in \mathcal{M}$ have been absorbed into the integration limits, so we only have to consider the remaining $n(n-1)/2 - m$ interactions. As our first approximation we ignore the effects of overlaps between any other particle pairs giving

$$Z = \int_0^\delta dx_1 \cdots \int_0^\delta dx_m \, y^{(n)}(\mathbf{x}) \tag{C.4a}$$

$$\langle\cdot\rangle_{\mathcal{P}} = \frac{1}{Z}\int_0^\delta dx_1 \cdots \int_0^\delta dx_m \, (\cdot) y^{(n)}(\mathbf{x}). \tag{C.4b}$$

Introducing the perturbation expansion of the cavity function (5.20) we obtain

$$\begin{aligned} Z &= y^{(n)}(\mathbf{x}^*) \prod_{i=1}^{l} \int_0^\delta \exp\left(-\mathbf{A}\cdot\mathbf{e}_i \, x_i\right) dx_i \\ &= y^{(n)}(\mathbf{x}^*) \prod_{i=1}^{l} \left[\frac{1-\exp\left(-A_i\,\delta\right)}{A_i}\right] \end{aligned} \tag{C.5}$$

with similar expressions for the first few moments. Inserting this expression into the structural partition function (5.12) yields expressions for the local structure's free energy/concentration.

The above formulae are rather simple, however the approximation is uncontrolled and we in general expect large errors for all but the most simple geometries: the hard sphere interactions should have a large effect. We find that ignoring the effect of hard sphere interactions not in $\mathcal{M}$ to be

a reasonably accurate approximation for $n \leq 6$, however it fails for $n \geq 7$ with selected geometries. In Fig. C.1 (top panel) we see that the error in this method is comparable between 4 out of the 5 possible structures, with a similar trend against density. However, one structure deviates strongly from the main trend with the error becoming substantial at high densities. The geometry in question is a variant of the frustrated pentagonal bipyramid with broken fivefold symmetry (top variant Fig. 5.1); the particles with the broken bond are almost touching so ignoring their interaction is a serious approximation. In general, we expect the majority of stable structures to require treatment of more hard sphere interactions than just the contacts.

To go beyond this approximation we will approximate the geometry of hard sphere interactions to leading order; in effect, this models the domain of integration as a polyhedron. Finally, we will use the EP technique to evaluate the integral on the resulting polyhedron.

C.2 Polyhedral approximation

The bond-distance arguments h_{ij} to the tile distributions in (C.2) are complicated functions of $\mathbf{x}$ in general. Our central simplifying approximation is to approximate them by an expansion to linear order, as in

$$h_{ij}(\mathbf{x}) \simeq h_{ij}(\mathbf{x}^*) + \nabla h_{ij}(\mathbf{x}^*) \cdot \Delta\mathbf{x} + \mathcal{O}(\Delta\mathbf{x}^2),$$

To leading order, the tile distribution (C.1) then constrains the bond distances to the regions

$$\nabla h_{ij}(\mathbf{x}^*) \cdot \Delta\mathbf{x} \in \begin{cases} [0, \delta] & \text{if } (i,j) \in \mathcal{M} \\ [-h_{ij}(\mathbf{x}^*), \infty] & \text{if } (i,j) \notin \mathcal{M}, \end{cases}$$

noting that $h_{ij}(\mathbf{x}^*) = 0$ iff $(i,j) \in \mathcal{M}$ by definition. The latter line includes the $n(n-1)/2 - m$ interactions not covered by $\mathcal{M}$; empirically, for $n \leq 7$ we find that most of these constraints are satisfied for all $\mathbf{x}$ (with $\delta \leq 0.4\sigma$) and can be safely ignored.

Within this linear approximation, the combined effect of the tile distributions is to constrain the domain of integration to a high-dimensional polyhedron. Our partition function becomes an integral of the cavity function, in the exponential family to leading order, over this polyhedron. Similar approximations have been made for hard sphere free energy calculations in the crystal [312, 313] and related systems [314]; these approximations become exact at very high densities approaching close packing.

Finally, we note that for implementations the derivatives ∇h_{ij} have to be calculated in some coordinate basis. For minimally constrained geometries with $m = l$ the natural basis is the bond-distances for pairs in $\mathcal{M}$ as outlined in the previous section. For $m \geq l$ any choice of m pairs will serve as a basis, though the choice may affect the end result.

C.3 Expectation propagation

Having introduced the relevant prerequisites, we now describe the EP algorithm which optimises the parameters of the approximate distribution $q(\mathbf{x})$ to obtain an estimate of the integral Z. Our exposition of this technique closely follows [239].

For convenience we will ignore prefactors $y^{(n)}(\mathbf{x}^*)$ in (C.2), which can be substituted back in at the end to obtain the full solution, and we assume in the chosen coordinates $\mathbf{x}^* = 0$ so that we can write $\Delta\mathbf{x} = \mathbf{x}$. Then replacing the double indices in the tile distributions with a single index $h_{ij} \to h_k$ we have

$$p(\mathbf{x}) = e^{-\mathbf{A}\cdot\mathbf{x}} \prod_{k=1}^{m^*} t_k(\mathbf{c}_k \cdot \mathbf{x})$$

where $\mathbf{c}_k = \nabla h_k(0)$ and m^* is the number of tile distributions which contribute after making the polyhedral approximation of the previous section ($m \leq m^* \leq n(n-1)/2$).

The EP algorithm constructs projections in the marginal distributions parallel to each of these constraints. The moments are then matched along these univariate distributions, which is much more tractable than for the full probability distribution. To facilitate this, a natural decomposition of $q(\mathbf{x})$ involves writing it in terms of approximate tile distributions $\widetilde{t}_i$, i.e.

$$q(\mathbf{x}) = e^{-\mathbf{A}\cdot\mathbf{x}} \prod_{i=1}^{m^*} \widetilde{t}_i(x_i) = e^{-\mathbf{A}\cdot\mathbf{x}} \prod_{i=1}^{m^*} \widetilde{Z}_i \mathcal{N}(x_i; \widetilde{\mu}_i, \widetilde{\sigma}_i^2) \tag{C.6}$$

with projected values

$$x_i = \mathbf{c}_i \cdot \mathbf{x} \tag{C.7a}$$

$$\mu_i = \mathbf{c}_i \cdot \boldsymbol{\mu} \tag{C.7b}$$

for $i \in \{1, \cdots, m\}$. From (C.28) and (C.31) we have

$$\begin{aligned} q(\mathbf{x}) &= Z_0 \exp(-\mathbf{A}\cdot\mathbf{x})\, \mathcal{N}(\mathbf{x}; \boldsymbol{\Sigma}\cdot\boldsymbol{\nu}, \boldsymbol{\Sigma}) \\ &= Z_0 \exp\left(\frac{\mathbf{A}\cdot\boldsymbol{\Sigma}\cdot\mathbf{A}}{2} - \mathbf{A}\cdot\boldsymbol{\Sigma}\cdot\boldsymbol{\nu}\right) \mathcal{N}(\mathbf{x}; \boldsymbol{\Sigma}\cdot(\boldsymbol{\nu}-\mathbf{A}), \boldsymbol{\Sigma}) \end{aligned} \tag{C.8}$$

where $\boldsymbol{\Sigma}, \boldsymbol{\nu}, Z_0$ are given by (C.29b), (C.29d) and (C.29e) respectively. We thus have

$$\boldsymbol{\mu} = \boldsymbol{\Sigma}\cdot(\boldsymbol{\nu} - \mathbf{A}) \tag{C.9a}$$

$$Z = Z_0 \exp\left(\frac{\mathbf{A}\cdot\boldsymbol{\Sigma}\cdot\mathbf{A}}{2} - \mathbf{A}\cdot\boldsymbol{\Sigma}\cdot\boldsymbol{\nu}\right) \tag{C.9b}$$

$$Z_0 = \sqrt{(2\pi)^{l-m^*} \det \boldsymbol{\Sigma}}\, \exp\left(\frac{\boldsymbol{\nu}\cdot\boldsymbol{\Sigma}\cdot\boldsymbol{\nu}}{2}\right) \prod_{i=1}^{m^*} \left(\frac{\widetilde{Z}_i}{\sqrt{\widetilde{\sigma}_i^2}} \exp\left(-\frac{\widetilde{\nu}_i\widetilde{\mu}_i}{2}\right)\right) \tag{C.9c}$$

We marginalise the full probability distribution along one direction to obtain the cavity distribution

$$q^{\setminus i}(\mathbf{x}) = \frac{\widetilde{Z}_i}{Z} \frac{q(\mathbf{x})}{\widetilde{t}_i(x_i)} = \frac{\mathcal{N}(\mathbf{x}; \boldsymbol{\mu}, \boldsymbol{\Sigma})}{\mathcal{N}(x_i; \widetilde{\mu}_i, \widetilde{\sigma}_i^2)}. \tag{C.10}$$

This particular normalisation is chosen such that

$$\int_{\mathbb{R}^l} q^{\setminus i}(\mathbf{x})\widetilde{t}_i(x_i)\,d\mathbf{x} = \widetilde{Z}_i \int_{\mathbb{R}^l} \mathcal{N}(\mathbf{x};\boldsymbol{\mu},\boldsymbol{\Sigma})\,d\mathbf{x} = \widetilde{Z}_i. \tag{C.11}$$

Integrating this cavity over the orthogonal affine space gives

$$\begin{aligned}
q_{\setminus i}(x_i) :=& \int_{\mathbb{R}^l \setminus \mathbf{c}_i} q^{\setminus i}(\mathbf{x}_{\setminus i}; x_i)\,d\mathbf{x}_{\setminus i} \\
=& \frac{1}{\mathcal{N}(x_i;\widetilde{\mu}_i,\widetilde{\sigma}_i^2)} \int_{\mathbb{R}^l \setminus \mathbf{c}_i} \mathcal{N}(\mathbf{x};\boldsymbol{\mu},\boldsymbol{\Sigma})\,d\mathbf{x}_{\setminus i} \\
=& \frac{\mathcal{N}(x_i;\mu_i,\mathbf{c}_i\cdot\boldsymbol{\Sigma}\cdot\mathbf{c}_i)}{\mathcal{N}(x_i;\widetilde{\mu}_i,\widetilde{\sigma}_i^2)} \\
=& \sqrt{\frac{\widetilde{\sigma}_i^2}{\mathbf{c}_i\cdot\boldsymbol{\Sigma}\cdot\mathbf{c}_i}} \exp\left(-\frac{(x_i-\mu_i)^2}{2\mathbf{c}_i\cdot\boldsymbol{\Sigma}\cdot\mathbf{c}_i} + \frac{(x_i-\widetilde{\mu}_i)^2}{2\widetilde{\sigma}_i^2}\right) \\
=& \sqrt{\frac{\sigma_{\setminus i}^2+\widetilde{\sigma}_i^2}{\sigma_{\setminus i}^2}} \exp\left(-\frac{(x_i-\mu_{\setminus i})^2}{2\sigma_{\setminus i}^2} + \frac{1}{2}\frac{(\mu_{\setminus i}-\widetilde{\mu}_i)^2}{\sigma_{\setminus i}^2+\widetilde{\sigma}_i^2}\right) \\
=& Z_{\setminus i}\,\mathcal{N}(x_i;\mu_{\setminus i},\sigma_{\setminus i}^2)
\end{aligned} \tag{C.12}$$

where we completed the square in the penultimate step using the cavity parameters: [238, 239]

$$Z_{\setminus i} = \sqrt{2\pi(\sigma_{\setminus i}^2+\widetilde{\sigma}_i^2)} \exp\left(\frac{1}{2}\frac{(\mu_{\setminus i}-\widetilde{\mu}_i)^2}{\sigma_{\setminus i}^2+\widetilde{\sigma}_i^2}\right) \tag{C.13}$$

$$\sigma_{\setminus i}^2 = \left(\frac{1}{\mathbf{c}_i\cdot\boldsymbol{\Sigma}\cdot\mathbf{c}_i} - \frac{1}{\widetilde{\sigma}_i^2}\right)^{-1} \tag{C.14}$$

$$\mu_{\setminus i} = \sigma_{\setminus i}^2\left(\frac{\mu_i}{\mathbf{c}_i\cdot\boldsymbol{\Sigma}\cdot\mathbf{c}_i} - \frac{\widetilde{\mu}_i}{\widetilde{\sigma}_i^2}\right). \tag{C.15}$$

Note that the cavity distribution is the properly normalised quantity $q_{\setminus i}(x_i)/Z_{\setminus i}$. The exact zeroth cavity moment is found via [239]

$$\begin{aligned}
\frac{\widehat{Z}_i}{Z_{\setminus i}} &= \frac{1}{Z_{\setminus i}} \int_{\mathbb{R}} q_{\setminus i}(x_i)t_i(x_i)\,dx_i \\
&= \frac{1}{Z_{\setminus i}} \int_{l_i}^{u_i} q_{\setminus i}(x_i)\,dx_i = \frac{1}{2}\left(\operatorname{erf}\beta_i - \operatorname{erf}\alpha_i\right)
\end{aligned} \tag{C.16}$$

where l_i, u_i are the limits imposed by the tile distribution, and where we have introduced the shorthand

$$\alpha_i = \frac{l_i-\mu_{\setminus i}}{\sqrt{2}\sigma_{\setminus i}} \tag{C.17}$$

$$\beta_i = \frac{u_i-\mu_{\setminus i}}{\sqrt{2}\sigma_{\setminus i}}. \tag{C.18}$$

The above relations are numerically unstable in the limit of small $\sigma_i^2 - \widetilde{\sigma}_i^2$, so we have to handle this case by Taylor expansion:

$$\begin{aligned}
q_{\setminus i}(x_i) &= \frac{\mathcal{N}(x_i;\mathbf{c}_i\cdot\boldsymbol{\mu},\mathbf{c}_i\cdot\boldsymbol{\Sigma}\cdot\mathbf{c}_i)}{\mathcal{N}(x_i;\widetilde{\mu}_i,\widetilde{\sigma}_i^2)} = \frac{\mathcal{N}(x_i;\mu_i,\sigma_i^2)}{\mathcal{N}(x_i;\widetilde{\mu}_i,\widetilde{\sigma}_i^2)} \\
&= \exp\left(-A_i x_i - \frac{A_i^2\sigma_i^2}{2} + A_i\mu_i\right)\frac{\mathcal{N}(x_i;\mu_i+A_i\sigma_i^2,\sigma_i^2)}{\mathcal{N}(x_i;\widetilde{\mu}_i,\widetilde{\sigma}_i^2)}
\end{aligned} \tag{C.19}$$

where $A_i = \mathbf{A} \cdot \mathbf{c}_i$, giving

$$\begin{aligned}\widehat{Z}_i =& \int_{\mathbb{R}} q_{\backslash i}(x_i) t_i(x_i)\, dx_i \\ =& \sqrt{\frac{\widetilde{\sigma}_i^2}{\mathbf{c}_i \cdot \boldsymbol{\Sigma} \cdot \mathbf{c}_i}} \int_{l_i}^{u_i} \exp\left(-\frac{(x_i - \mu_i)^2}{2\mathbf{c}_i \cdot \boldsymbol{\Sigma} \cdot \mathbf{c}_i} + \frac{(x_i - \widetilde{\mu}_i)^2}{2\widetilde{\sigma}_i^2} \right) dx_i, \end{aligned} \tag{C.20}$$

which is in a suitable form for a perturbation expansion.

In the EP algorithm an iterative scheme is constructed to obtain the parameters $\{\widetilde{Z}_i, \widetilde{\mu}_i, \widetilde{\sigma}_i^2\}$ so that the equality (C.16) is achieved along with similar equalities for the higher-order moments [236–239]. This process is simpler than before because in each iteration the parameters are univariate. After obtaining the optimal parameters, we have to bring the univariate distributions back together to obtain the final value of Z. Matching moments between (C.11) and (C.16) gives us

$$\widetilde{Z}_i = \frac{\widehat{Z}_i}{Z_{\backslash i}} \sqrt{2\pi(\sigma_{\backslash i}^2 + \widetilde{\sigma}_i^2)} \exp\left(\frac{1}{2} \frac{(\mu_{\backslash i} - \widetilde{\mu}_i)^2}{\sigma_{\backslash i}^2 + \widetilde{\sigma}_i^2} \right). \tag{C.21}$$

We calculate $\widehat{Z}_i / Z_{\backslash i}$ from (C.16) and then obtain the partition function as

$$\begin{aligned}\log \widetilde{Z}_i = \frac{1}{2} \Bigg(& \log(2\pi) + \log(\sigma_{\backslash i}^2 + \widetilde{\sigma}_i^2) + \frac{(\mu_{\backslash i} - \widetilde{\mu}_i)^2}{\sigma_{\backslash i}^2 + \widetilde{\sigma}_i^2} \\ & + \log\left(\frac{\operatorname{erf} \beta_i - \operatorname{erf} \alpha_i}{2} \right) \Bigg). \end{aligned} \tag{C.22}$$

From (C.30) the final partition function is found as

$$\begin{aligned}\log Z =& \frac{1}{2} \Big((l - m^*) \log 2\pi + \log\det \boldsymbol{\Sigma} + \boldsymbol{\nu} \cdot \boldsymbol{\Sigma} \cdot \boldsymbol{\nu} \Big) \\ & + \sum_{i=1}^{m^*} \left(\log \widetilde{Z}_i - \frac{1}{2} \left(\log \widetilde{\sigma}_i^2 + \frac{\widetilde{\mu}_i^2}{\widetilde{\sigma}_i^2} \right) \right) \end{aligned} \tag{C.23}$$

where the term inside the summation is given by [239]

$$\begin{aligned} & \log \widetilde{Z}_i - \frac{1}{2} \left(\log \widetilde{\sigma}_i^2 + \frac{\widetilde{\mu}_i^2}{\widetilde{\sigma}_i^2} \right) \\ =& \frac{1}{2} \left(\log(2\pi) + \log\left(\frac{\sigma_{\backslash i}^2 + \widetilde{\sigma}_i^2}{\widetilde{\sigma}_i^2} \right) + \frac{(\mu_{\backslash i} - \widetilde{\mu}_i)^2}{\sigma_{\backslash i}^2 + \widetilde{\sigma}_i^2} \right. \\ & \left. - \frac{\widetilde{\mu}_i^2}{\widetilde{\sigma}_i^2} + \log\left(\frac{\operatorname{erf} \beta_i - \operatorname{erf} \alpha_i}{2} \right) \right), \end{aligned} \tag{C.24}$$

from (C.22). Note that the latter quantity is numerically unstable for small $\sigma_i^2 - \widetilde{\sigma}_i^2$, so a perturbation expansion must be used instead; this ensures that this method reduces to the exact integral of section C.1 in cases where $m = l$ and no additional hard sphere overlaps are possible.

In Fig. C.1 (bottom panel) we see that this method can handle the effect of additional hard sphere interactions. There is a systematic error brought about by the approximations in this integration scheme, however this error scales similarly for all 5 of the packings available for $n = 7$ particles.

This has been a rather technical account of the method, so in the next section we show how $q(\mathbf{x})$ approximates the tile distributions in the simple case of an integration over a triangle.

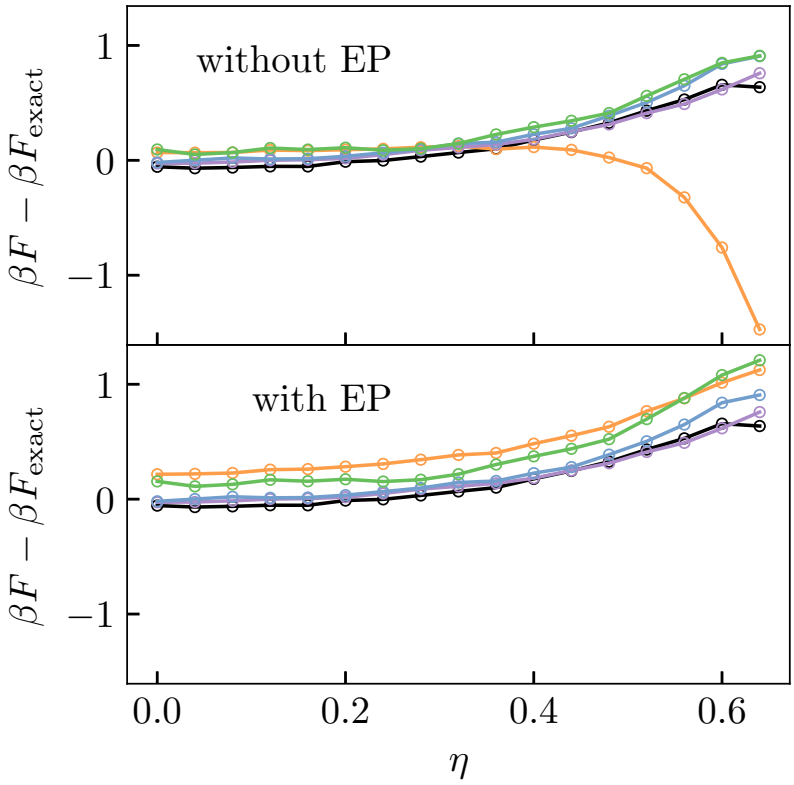

Figure C.1: Errors in analytic integration techniques for free energies of the five $n = 7$ structures in Fig. 5.1. Top panel: simple integration ignoring hard sphere interactions not explicitly captured by the boundary conditions (section C.1). Bottom panel: expectation propagation (EP) integration which approximates the combined effect of boundary conditions and hard sphere interactions using (section C.3). In each case, the numerically exact result was obtained using thermodynamic integration described in chapter 5. The orange curve which deviates from the main trend without EP is the structure corresponding to a pentagonal bipyramid with broken fivefold symmetry; treatment of the broken bond with EP corrects the deviation.

C.4 Worked example: area of a triangle

As a simple worked example we consider the area of a right-angled triangle with vertices $(0,0)$, $(1,0)$, and $(0,1)$ i.e. half of the unit square. We can write this area as the integral over a box

$$A_\Delta = \int_0^1 \int_0^1 \Theta(1-x-y)\, dxdy = \frac{1}{2} \tag{C.25}$$

where $\Theta(\cdot)$ is the Heaviside function. The exact result is fairly trivial, but it has the same form as the integrals we have been studying with e.g. x, y representing the contact particles and $\Theta(1-x-y)$ representing an additional hard sphere interaction between non-contact particles. As such, we can evaluate the area using expectation propagation giving $A_\Delta^{\text{EP}} \simeq 0.515$ for an error of about 3%. The effective probability distribution $p(x,y)$ for this integral is shown in C.2 (lower panel) which illustrates how the method builds in geometric information of additional constraints (in this case $\Theta(1-x-y)$. The distribution for the equivalent integral without this constraint is shown in the same figure (upper panel).

As an extension of the above problem we introduce an external field representing the perturbation expansion of the potential of mean force $\phi^{(n)}$. We obtain the integral

$$Z_\Delta = \int_0^1 \int_0^1 \Theta(1-x-y) e^{-A_x x A_y y}\, dxdy \tag{C.26}$$

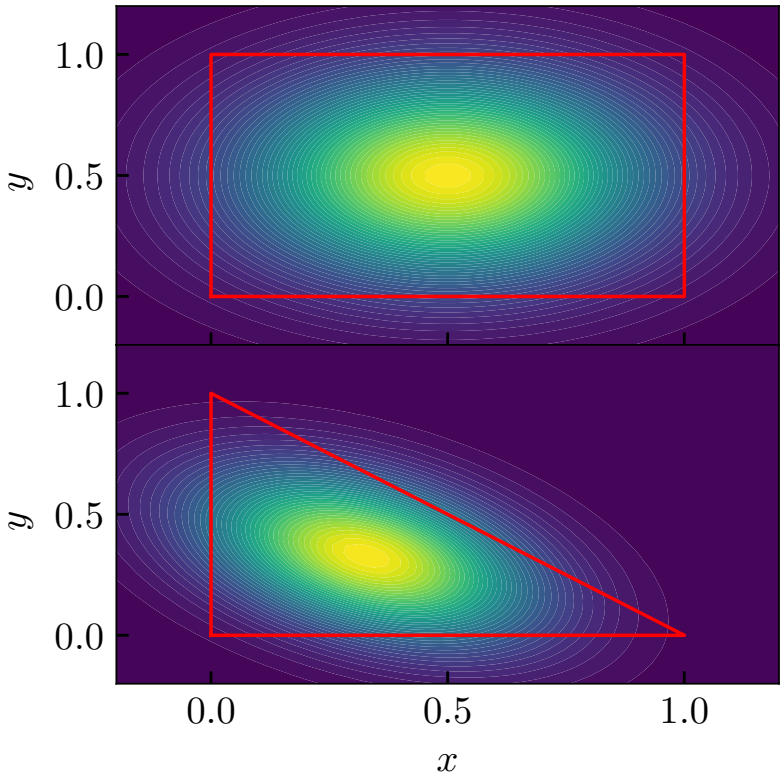

Figure C.2: Approximate (Gaussian) probability distribution $q(x, y)$ produced by expectation propagation for an integration over a square (top) and a right-angled triangle (bottom). In each panel the boundary of the true integration area is indicated by red lines, though the approximate probability distribution spans all of space.

with the errors of expectation propagation shown in Fig. C.3. The error of 3% in the area is recovered in the limit $\mathbf{A} \to 0$, which increases to a maximum of around 4% at moderate field strength. At very large field strengths the error drops to essentially zero as the effect of the extra boundary condition is not seen, and the method becomes exact.

C.5 Addendum: properties of multivariate Gaussians

The multivariate Gaussian is defined as

$$\begin{aligned}\mathcal{N}(\mathbf{x};\boldsymbol{\mu},\boldsymbol{\Sigma}) :=& \frac{1}{\sqrt{(2\pi)^l \det \boldsymbol{\Sigma}}} \exp\left(-\frac{1}{2}(\mathbf{x}-\boldsymbol{\mu})\cdot\boldsymbol{\Sigma}^{-1}\cdot(\mathbf{x}-\boldsymbol{\mu})\right) \\ =& \frac{1}{\sqrt{(2\pi)^l \det \boldsymbol{\Sigma}}} \exp\left(-\frac{\mathbf{x}\cdot\boldsymbol{\Sigma}^{-1}\cdot\mathbf{x}}{2} + \mathbf{x}\cdot\boldsymbol{\Sigma}^{-1}\cdot\boldsymbol{\mu} - \frac{\boldsymbol{\mu}\cdot\boldsymbol{\Sigma}^{-1}\cdot\boldsymbol{\mu}}{2}\right)\end{aligned} \tag{C.27}$$

where $\mathbf{x} \in \mathbb{R}^l$ is the Gaussian distributed vector in our phase space, with mean $\boldsymbol{\mu} \in \mathbb{R}^l$ and (positive-definite) covariance matrix $\boldsymbol{\Sigma} \in \mathbb{R}^{l\times l}$.

In the EP algorithm we wrote the multivariate Gaussian approximation in q as the product of univariate Gaussians from the tile distributions approximating the boundary conditions. To show this, consider the product

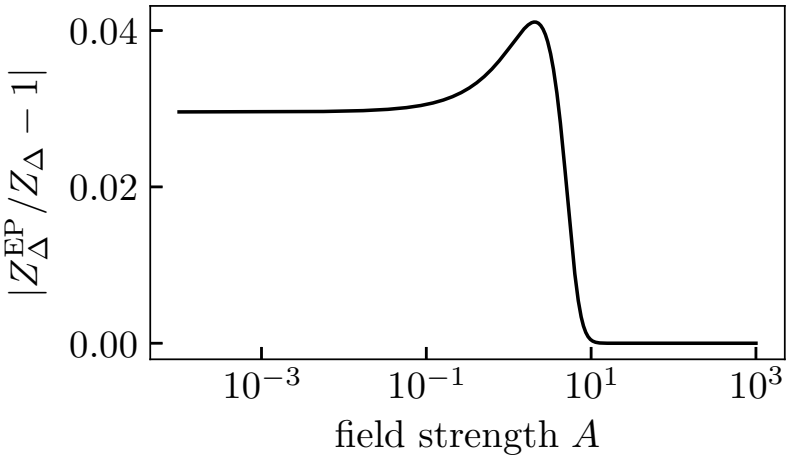

Figure C.3: Errors in expectation propagation for integrating a field over a triangle. The exact integral is given by (C.26), taking field $\mathbf{A} = (A, A)$.

of univariate Gaussians:

$$\begin{aligned}
&\prod_{i=1}^{m^*} \mathcal{N}(\mathbf{c}_i \cdot \mathbf{x}; \widetilde{\mu}_i, \widetilde{\sigma}_i^2) = \prod_{i=1}^{m^*} \left(\frac{1}{\sqrt{2\pi\widetilde{\sigma}_i^2}} \exp\left(-\frac{1}{2} \frac{(\mathbf{c}_i \cdot \mathbf{x} - \widetilde{\mu}_i)^2}{\widetilde{\sigma}_i^2} \right) \right) \\
=&\prod_{i=1}^{m^*} \left(\frac{1}{\sqrt{2\pi\widetilde{\sigma}_i^2}} \exp\left(-\frac{\widetilde{\mu}_i^2}{2\widetilde{\sigma}_i^2} \right) \right) \exp\left(\sum_{i=1}^{m^*} \left(-\frac{(\mathbf{c}_i \cdot \mathbf{x})^2}{2\widetilde{\sigma}_i^2} + \frac{\widetilde{\mu}_i (\mathbf{c}_i \cdot \mathbf{x})}{\widetilde{\sigma}_i^2} \right) \right) \\
=&\prod_{i=1}^{m^*} \left(\frac{1}{\sqrt{2\pi\widetilde{\sigma}_i^2}} \exp\left(-\frac{\widetilde{\nu}_i \widetilde{\mu}_i}{2} \right) \right) \mathcal{N}(\mathbf{x}; \boldsymbol{\mu}, \Sigma) \sqrt{(2\pi)^l \det \boldsymbol{\Sigma}} \exp\left(\frac{\boldsymbol{\nu} \cdot \boldsymbol{\Sigma} \cdot \boldsymbol{\nu}}{2} \right) \\
=&Z \mathcal{N}(\mathbf{x}; \boldsymbol{\mu}, \Sigma)
\end{aligned} \tag{C.28}$$

with

$$\widetilde{\nu}_i = \frac{\widetilde{\mu}_i}{\widetilde{\sigma}_i^2} \tag{C.29a}$$

$$\boldsymbol{\Sigma}^{-1} = \sum_{i=1}^{m^*} \frac{\mathbf{c}_i \otimes \mathbf{c}_i}{\widetilde{\sigma}_i^2} \tag{C.29b}$$

$$\boldsymbol{\mu} = \boldsymbol{\Sigma} \cdot \left(\sum_{i=1}^{m^*} \widetilde{\nu}_i \mathbf{c}_i \right) = \boldsymbol{\Sigma} \cdot \boldsymbol{\nu} \tag{C.29c}$$

$$\boldsymbol{\nu} = \sum_{i=1}^{m^*} \widetilde{\nu}_i \mathbf{c}_i \tag{C.29d}$$

$$Z = \sqrt{(2\pi)^{l-m^*} \det \boldsymbol{\Sigma}} \exp\left(\frac{\boldsymbol{\nu} \cdot \boldsymbol{\Sigma} \cdot \boldsymbol{\nu}}{2} \right) \prod_{i=1}^{m^*} \frac{1}{\sqrt{\widetilde{\sigma}_i^2}} \exp\left(-\frac{\widetilde{\nu}_i \widetilde{\mu}_i}{2} \right) \tag{C.29e}$$

From this we find that

$$\log Z = \frac{l - m^*}{2} \log 2\pi + \frac{1}{2} \log \det \boldsymbol{\Sigma} + \frac{\boldsymbol{\nu} \cdot \boldsymbol{\Sigma} \cdot \boldsymbol{\nu}}{2} - \sum_{i=1}^{m^*} \left(\frac{1}{2} \log \widetilde{\sigma}_i^2 + \frac{\widetilde{\nu}_i \widetilde{\mu}_i}{2} \right) \tag{C.30}$$

Finally, note that

$$e^{-\mathbf{A}\cdot\mathbf{x}}\mathcal{N}(\mathbf{x};\boldsymbol{\mu},\boldsymbol{\Sigma}) = \exp\left(\frac{\mathbf{A}\cdot\boldsymbol{\Sigma}\cdot\mathbf{A}}{2} - \mathbf{A}\cdot\boldsymbol{\mu}\right)\mathcal{N}(\mathbf{x};\boldsymbol{\mu}-\boldsymbol{\Sigma}\cdot\mathbf{A},\boldsymbol{\Sigma}). \quad \text{(C.31)}$$

Bibliography

[1] J. F. Robinson, F. Turci, R. Roth, and C. P. Royall, "Morphometric approach to many-body correlations in hard spheres", Phys. Rev. Lett. **122**, 068004 (2019).

[2] F. K. A. Gregson, J. F. Robinson, R. E. H. Miles, C. P. Royall, and J. P. Reid, "Drying kinetics of salt solution droplets: water evaporation rates and crystallization", J. Phys. Chem. B **123**, 266 (2019).

[3] J. F. Robinson, F. Turci, R. Roth, and C. P. Royall, "Many-body correlations from integral geometry", Phys. Rev. E **100** (2019) `10.1103/physreve.100.062126`.

[4] J. F. Robinson, R. Roth, and C. P. Royall, "Morphological thermodynamics for hard bodies from a controlled expansion", arXiv: 1910.11836 (2019), Submitted to Phil. Mag.

[5] J. F. Robinson, F. K. A. Gregson, R. E. H. Miles, J. P. Reid, and C. P. Royall, "Nucleation kinetics in drying sodium nitrate aerosols", arXiv: 1911.06212 (2019), Submitted to J. Chem. Phys.

[6] F. K. A. Gregson, J. F. Robinson, R. E. H. Miles, C. P. Royall, and J. P. Reid, "Studies on crystal nucleation rates in evaporating sodium nitrate aerosol droplets", in preparation.

[7] C. P. Royall, F. Turci, S. Tatsumi, J. Russo, and J. Robinson, "The race to the bottom: approaching the ideal glass?", J. Phys. Condens. Matter **30**, 363001 (2018).

[8] C. P. Royall, unpublished.

[9] T. Lubensky, "Soft condensed matter physics", Solid State Commun. **102**, 187 (1997).

[10] W. C. K. Poon, "Goo Galore - the Ubiquity of Soft Matter", invited talk launching the Soft Matter Network at the University of Bristol, Dec. 2018.

[11] B. Widom, "Intermolecular Forces and the Nature of the Liquid State: Liquids reflect in their bulk properties the attractions and repulsions of their constituent molecules", Science **157**, 375 (1967).

[12] J.-P. Hansen and I. R. McDonald, *Theory of Simple Liquids with Applications to Soft Matter*, Fourth Edition (Elsevier, 2013).

[13] A. Santos, *A Concise Course on the Theory of Classical Liquids*, 1st ed., Vol. 923 (Springer International Publishing, Cham, 2016).

[14] W. G. Hoover and F. H. Ree, "Melting Transition and Communal Entropy for Hard Spheres", J. Chem. Phys. **49**, 3609 (1968).

[15] N. F. Carnahan and K. E. Starling, "Equation of State for Nonattracting Rigid Spheres", J. Chem. Phys. **51**, 635 (1969).

[16] R. J. Speedy, "Pressure and entropy of hard-sphere crystals", J. Phys. Condens. Matter **10**, 4387 (1998).

[17] M. N. Bannerman, L. Lue, and L. V. Woodcock, "Thermodynamic pressures for hard spheres and closed-virial equation-of-state.", J. Chem. Phys. **132**, 084507 (2010).

[18] B. J. Alder and T. E. Wainwright, "Phase Transition for a Hard Sphere System", J. Chem. Phys. **27**, 1208 (1957).

[19] W. W. Wood and J. D. Jacobson, "Preliminary Results from a Recalculation of the Monte Carlo Equation of State of Hard Spheres", J. Chem. Phys. **27**, 1207 (1957).

[20] P. N. Pusey and W. van Megen, "Phase behaviour of concentrated suspensions of nearly hard colloidal spheres", Nature **320**, 340 (1986).

[21] M. Mareschal, "Early years of Computational Statistical Mechanics", Eur. Phys. J. H **43**, 293 (2018).

[22] N. D. Mermin and H. Wagner, "Absence of Ferromagnetism or Antiferromagnetism in One- or Two-Dimensional Isotropic Heisenberg Models", Phys. Rev. Lett. **17**, 1133 (1966).

[23] N. D. Mermin, "Crystalline Order in Two Dimensions", Phys. Rev. **176**, 250 (1968).

[24] A. González, J. A. White, F. L. Román, and R. Evans, "How the structure of a confined fluid depends on the ensemble: Hard spheres in a spherical cavity", J. Chem. Phys. **109**, 3637 (1998).

[25] Y. Rosenfeld, "Free-energy model for the inhomogeneous hard-sphere fluid mixture and density-functional theory of freezing", Phys. Rev. Lett. **63**, 980 (1989).

[26] R. Roth, "Fundamental measure theory for hard-sphere mixtures: a review", J. Phys. Condens. Matter **22**, 063102 (2010).

[27] M. P. Hobson, G. P. Efstathiou, and A. N. Lasenby, *General relativity: an introduction for physicists* (Cambridge University Press, 2006).

[28] J. Russo, A. C. Maggs, D. Bonn, and H. Tanaka, "The interplay of sedimentation and crystallization in hard-sphere suspensions", Soft Matter **9**, 7369 (2013).

[29] S. Torquato and F. H. Stillinger, "Jammed hard-particle packings: From Kepler to Bernal and beyond", Rev. Mod. Phys. **82**, 2633 (2010).

[30] H. Cohn, "Packing, coding, and ground states", arXiv: 1603.05202 (2016).

[31] J. H. Conway and N. J. A. Sloane, *Sphere packings, lattices, and groups* (Springer, New York, 1999).

[32] T. Hales, "A proof of the Kepler conjecture", Ann. Math. **162**, 1065 (2005).

[33] M. C. Holmes-Cerfon, "Enumerating Rigid Sphere Packings", SIAM Rev. **58**, 229 (2016).

[34] M. C. Holmes-Cerfon, "Sticky-Sphere Clusters", Annu. Rev. Condens. Matter Phys. **8**, 77 (2017).

[35] D. Chandler, *Introduction to modern statistical mechanics* (Oxford University Press, New York, 1987).

[36] T. Young, "III. An essay on the cohesion of fluids", Phil. Trans. R. Soc. Lon **95**, 65 (1805).

[37] P.-S. Laplace, *Traité de Mécanique Céleste*, Vol. 4 (Courcier, Paris, 1805).

[38] D. H. Everett, "The thermodynamics of frost damage to porous solids", Trans. Faraday Soc. **57**, 1541 (1961).

[39] P.-M. König, R. Roth, and K. R. Mecke, "Morphological Thermodynamics of Fluids: Shape Dependence of Free Energies", Phys. Rev. Lett. **93**, 160601 (2004).

[40] S. Asakura and F. Oosawa, "On Interaction between Two Bodies Immersed in a Solution of Macromolecules", J. Chem. Phys. **22**, 1255 (1954).

[41] S. Asakura and F. Oosawa, "Interaction between particles suspended in solutions of macromolecules", J. Polym. Sci. **33**, 183 (1958).

[42] L. A. Santaló, *Integral geometry and geometric probability*, 2nd ed, Cambridge Mathematical Library (Cambridge University Press, Cambridge, UK ; New York, 2004).

[43] R. Schneider, "Integral geometry - Measure theoretic approach and stochastic applications", Adv. Course Integral Geom., CRM (1984).

[44] R. Schneider and W. Weil, *Stochastic and integral geometry*, Probability and Its Applications (Springer, Berlin, 2008).

[45] D. A. Klain and G.-C. Rota, *Introduction to geometric probability*, Lezioni Lincee (Cambridge University Press, Cambridge, UK ; New York, 1997).

[46] S. Banach and A. Tarski, "Sur la décomposition des ensembles de points en parties respectivement congruentes", Fund Math **6**, 244 (1924).

[47] H. Hadwiger, *Vorlesungen Über Inhalt, Oberfläche und Isoperimetrie* (Springer Berlin Heidelberg, Berlin, Heidelberg, 1957).

[48] W. Blaschke, "Integralgeometrie 13. Zur Dinematik", Math. Z. **41**, 465 (1936).

[49] W. Blaschke, *Vorlesungen über Integralgeometrie*, Vol. 47 (Berlin: Tuebner, Dec. 1937).

[50] L. A. Santaló, "Integralgeometrie 5. Über das kinematische Mass im Raum", Actual. Sci. Ind. **357** (1936).

[51] M. Marechal, S. Korden, and K. Mecke, "Deriving fundamental measure theory from the virial series: Consistency with the zero-dimensional limit", Phys. Rev. E **90**, 042131 (2014).

[52] L. D. Landau, E. M. Lifšic, L. P. Pitaevskij, and L. D. Landau, *Statistical physics, Part 1*, 3. ed, Course of Theoretical Physics by L. D. Landau and E. M. Lifshitz ; Vol. 5 (Elsevier [u.a.], Amsterdam [u.a], 2008).

[53] E. T. Jaynes, "Information Theory and Statistical Mechanics", Phys. Rev. **106**, 620 (1957).

[54] E. T. Jaynes, "Information Theory and Statistical Mechanics. II", Phys. Rev. **108**, 171 (1957).

[55] G. E. Uhlenbeck, P. C. Hemmer, and M. Kac, "On the van der Waals Theory of the Vapor-Liquid Equilibrium. II. Discussion of the Distribution Functions", J. Math. Phys. **4**, 229 (1963).

[56] H. D. Ursell, "The evaluation of Gibbs' phase-integral for imperfect gases", Math. Proc. Camb. Phil. Soc. **23**, 685 (1927).

[57] J. E. Mayer and E. Montroll, "Molecular Distribution", J. Chem. Phys. **9**, 2 (1941).

[58] E. W. Montroll and J. E. Mayer, "Statistical Mechanics of Imperfect Gases", J. Chem. Phys. **9**, 626 (1941).

[59] G. Leithall and M. Schmidt, "Density functional for hard hyperspheres from a tensorial-diagrammatic series", Phys. Rev. E **83**, 021201 (2011).

[60] S. Korden, "Deriving the Rosenfeld functional from the virial expansion", Phys. Rev. E **85**, 041150 (2012).

[61] J. A. Gualtieri, J. M. Kincaid, and G. Morrison, "Phase equilibria in polydisperse fluids", J. Chem. Phys. **77**, 521 (1982).

[62] P. B. Warren, "Combinatorial entropy and the statistical mechanics of polydispersity", Phys. Rev. Lett. **80**, 1369 (1998).

[63] P. Sollich and M. E. Cates, "Projected Free Energies for Polydisperse Phase Equilibria", Phys. Rev. Lett. **80**, 1365 (1998).

[64] P. Sollich, P. B. Warren, and M. E. Cates, "Moment Free Energies for Polydisperse Systems", in *Advances in Chemical Physics*, edited by I. Prigogine and S. A. Rice (John Wiley & Sons, Inc., Hoboken, NJ, USA, Jan. 2001), pp. 265–336.

[65] R. Evans, "The nature of the liquid-vapour interface and other topics in the statistical mechanics of non-uniform, classical fluids", Adv. Phys. **28**, 143 (1979).

[66] R. Evans, *Microscopic theories of simple fluids and their interfaces*, 1989.

[67] R. Evans, "Density Functionals in the Theory of Non-Uniform Fluids", in *Fundamentals of Inhomogeneous Fluids*, edited by D. Henderson (Marcel Dekker, 1992), pp. 85–175.

[68] N. Ashcroft, "Density Functional Descriptions of Classical Inhomogeneous Fluids", Aust. J. Phys. **49**, 3 (1996).

[69] N. D. Mermin, "Thermal properties of the inhomogeneous electron gas", Phys. Rev. **137**, 1 (1965).

[70] W. S. B. Dwandaru and M. Schmidt, "Variational principle of classical density functional theory via Levy's constrained search method", Phys. Rev. E **83**, 061133 (2011).

[71] L. S. Ornstein and F. Zernike, "Accidental deviations of density and opalescence at the critical point of a single substance", Proc Acad Sci Amst. **17**, 793 (1914).

[72] Y. Rosenfeld, "Density functional theory of molecular fluids: Free-energy model for the inhomogeneous hard-body fluid", Phys. Rev. E **50**, R3318 (1994).

[73] Y. Rosenfeld, "Free energy model for the inhomogeneous hard-body fluid: application of the Gauss-Bonnet theorem", Mol. Phys. **86**, 637 (1995).

[74] H. Hansen-Goos and K. Mecke, "Fundamental Measure Theory for Inhomogeneous Fluids of Nonspherical Hard Particles", Phys. Rev. Lett. **102**, 018302 (2009).

[75] H. Hansen-Goos and K. Mecke, "Tensorial density functional theory for non-spherical hard-body fluids", J. Phys. Condens. Matter **22**, 364107 (2010).

[76] R. Wittmann, M. Marechal, and K. Mecke, "Fundamental mixed measure theory for non-spherical colloids", Europhys. Lett. **109**, 26003 (2015).

[77] R. Wittmann, M. Marechal, and K. Mecke, "Elasticity of nematic phases with fundamental measure theory", Phys. Rev. E **91**, 052501 (2015).

[78] R. Wittmann, M. Marechal, and K. Mecke, "Fundamental measure theory for non-spherical hard particles: predicting liquid crystal properties from the particle shape", J. Phys.: Condens. Matter **28**, 244003 (2016).

[79] A. Santos, "Class of consistent fundamental-measure free energies for hard-sphere mixtures", Phys. Rev. E **86**, 040102(R) (2012).

[80] J. F. Lutsko, "Recent Developments in Classical Density Functional Theory", in *Advances in Chemical Physics*, edited by S. A. Rice (John Wiley & Sons, Inc., Hoboken, NJ, USA, Jan. 2010), pp. 1–92.

[81] F. H. Stillinger and F. P. Buff, "Equilibrium Statistical Mechanics of Inhomogeneous Fluids", J. Chem. Phys. **37**, 1 (1962).

[82] J. S. Rowlinson, "Virial Expansions in an Inhomogeneous System", Proc. R. Soc. A **402**, 67 (1985).

[83] J. K. Percus, "Free energy models for nonuniform classical fluids", J. Stat. Phys. **52**, 1157 (1988).

[84] R. Roth, R. Evans, A. Lang, and G. Kahl, "Fundamental measure theory for hard-sphere mixtures revisited: the White Bear version", J. Phys. Condens. Matter **14**, 12063 (2002).

[85] H. Reiss, H. L. Frisch, E. Helfand, and J. L. Lebowitz, "Aspects of the Statistical Thermodynamics of Real Fluids", J. Chem. Phys. **32**, 119 (1960).

[86] A. Santos, "Note: An exact scaling relation for truncatable free energies of polydisperse hard-sphere mixtures", J. Chem. Phys. **136**, 136102 (2012).

[87] J. L. Lebowitz, E. Helfand, and E. Praestgaard, "Scaled Particle Theory of Fluid Mixtures", J. Chem. Phys. **43**, 774 (1965).

[88] Y. Rosenfeld, D. Levesque, and J. J. Weis, "Free-energy model for the inhomogeneous hard-sphere fluid mixture: Triplet and higher-order direct correlation functions in dense fluids", J. Chem. Phys. **92**, 6818 (1990).

[89] Y. Rosenfeld, "Scaled field particle theory of the structure and the thermodynamics of isotropic hard particle fluids", J. Chem. Phys. **89**, 4272 (1988).

[90] M. S. Wertheim, "Exact solution of the percus-yevick integral equation for hard spheres", Phys. Rev. Lett. **10**, 321 (1963).

[91] L. Berthier, D. Coslovich, A. Ninarello, and M. Ozawa, "Equilibrium Sampling of Hard Spheres up to the Jamming Density and Beyond", Phys. Rev. Lett. **116**, 238002 (2016).

[92] T. Boublik, "Hard-Sphere Equation of State", J. Chem. Phys. **53**, 471 (1970).

[93] G. A. Mansoori, N. F. Carnahan, K. E. Starling, and T. W. Leland, "Equilibrium Thermodynamic Properties of the Mixture of Hard Spheres", J. Chem. Phys. **54**, 1523 (1971).

[94] Y.-X. Yu and J. Wu, "Structures of hard-sphere fluids from a modified fundamental-measure theory", J. Chem. Phys. **117**, 10156 (2002).

[95] R. Roth, Y. Harano, and M. Kinoshita, "Morphometric Approach to the Solvation Free Energy of Complex Molecules", Phys. Rev. Lett. **97**, 078101 (2006).

[96] H. Hansen-Goos and R. Roth, "Density functional theory for hard-sphere mixtures: the White Bear version mark II", J. Phys. Condens. Matter **18**, 8413 (2006).

[97] H. Hansen-Goos and R. Roth, "A new generalization of the Carnahan-Starling equation of state to additive mixtures of hard spheres", J. Chem. Phys. **124**, 154506 (2006).

[98] M. N. Bannerman, R. Sargant, and L. Lue, "DynamO: a free O(N) general event-driven molecular dynamics simulator", J. Comput. Chem. **32**, 3329 (2011).

[99] J. E. Hallett, F. Turci, and C. P. Royall, "Local structure in deeply supercooled liquids exhibits growing lengthscales and dynamical correlations", Nat. Commun. **9**, 3272 (2018).

[100] L. M. C. Janssen, "Mode-Coupling Theory of the Glass Transition: A Primer", Front. Phys. **6**, 97 (2018).

[101] J. S. Langer, "Statistical theory of the decay of metastable states", Ann. Phys. **54**, 258 (1969).

[102] A. Cavagna, "Supercooled liquids for pedestrians", Phys. Rep. **476**, 51 (2009).

[103] P. K. Bommineni, N. R. Varela-Rosales, M. Klement, and M. Engel, "Complex Crystals from Size-Disperse Spheres", Phys. Rev. Lett. **122**, 128005 (2019).

[104] E. Sanz, C. Valeriani, E. Zaccarelli, W. C. K. Poon, P. N. Pusey, and M. E. Cates, "Crystallization Mechanism of Hard Sphere Glasses", Phys. Rev. Lett. **106** (2011) 10.1103/physrevlett.106.215701.

[105] C. A. Angell, "Formation of Glasses from Liquids and Biopolymers", Science **267**, 1924 (1995).

[106] C. Angell, "Structural instability and relaxation in liquid and glassy phases near the fragile liquid limit", J. Non-Cryst. Solids **102**, 205 (1988).

[107] L. Berthier and T. A. Witten, "Glass transition of dense fluids of hard and compressible spheres", Phys. Rev. E **80**, 021502 (2009).

[108] C. P. Royall and W. Kob, "Locally favoured structures and dynamic length scales in a simple glass-former", J. Stat. Mech. **2017**, 024001 (2017).

[109] C. P. Royall and S. R. Williams, "The role of local structure in dynamical arrest", Phys. Rep. **560**, 1 (2015).

[110] L. Berthier and G. Biroli, "Theoretical perspective on the glass transition and amorphous materials", Rev. Mod. Phys. **83**, 587 (2011).

[111] M. D. Ediger, "Spatially heterogeneous dynamics in supercooled liquids.", Annu. Rev. Phys. Chem. **51**, 99 (2000).

[112] A. Widmer-Cooper and P. Harrowell, "On the relationship between structure and dynamics in a supercooled liquid", J. Phys. Condens. Matter **17**, S4025 (2005).

[113] G. Biroli and J. P. Garrahan, "Perspective: The glass transition", J. Chem. Phys. **138**, 12A301 (2013).

[114] D. R. Reichman and P. Charbonneau, "Mode-coupling theory", J. Stat. Mech. **2005**, P05013 (2005).

[115] E. Flenner, M. Zhang, and G. Szamel, "Analysis of a growing dynamic length scale in a glass-forming binary hard-sphere mixture", Phys. Rev. E **83**, 051501 (2011).

[116] G. Brambilla, D. El Masri, M. Pierno, L. Berthier, L. Cipelletti, G. Petekidis, and A. B. Schofield, "Probing the Equilibrium Dynamics of Colloidal Hard Spheres above the Mode-Coupling Glass Transition", Phys. Rev. Lett. **102**, 085703 (2009).

[117] W. van Megen and S. M. Underwood, "Glass transition in colloidal hard spheres: Measurement and mode-coupling-theory analysis of the coherent intermediate scattering function", Phys. Rev. E **49**, 4206 (1994).

[118] T. Maimbourg, J. Kurchan, and F. Zamponi, "Solution of the Dynamics of Liquids in the Large-Dimensional Limit", Phys. Rev. Lett. **116**, 015902 (2016).

[119] G. Szamel, "Mode-coupling theory and beyond: A diagrammatic approach", Prog. Theor. Exp. Phys. **2013**, 1 (2013).

[120] G. Biroli, J.-P. Bouchaud, K. Miyazaki, and D. R. Reichman, "Inhomogeneous Mode-Coupling Theory and Growing Dynamic Length in Supercooled Liquids", Phys. Rev. Lett. **97**, 195701 (2006).

[121] L. M. Janssen and D. R. Reichman, "Microscopic Dynamics of Supercooled Liquids from First Principles", Phys. Rev. Lett. **115**, 205701 (2015).

[122] G. Parisi and F. Zamponi, "Mean-field theory of hard sphere glasses and jamming", Rev. Mod. Phys. **82**, 789 (2010).

[123] J. Kurchan, G. Parisi, and F. Zamponi, "Exact theory of dense amorphous hard spheres in high dimension I. The free energy", J. Stat. Mech. **2012**, P10012 (2012).

[124] J. Kurchan, G. Parisi, P. Urbani, and F. Zamponi, "Exact Theory of Dense Amorphous Hard Spheres in High Dimension. II. The High Density Regime and the Gardner Transition", J. Phys. Chem. B **117**, 12979 (2013).

[125] P. Charbonneau, J. Kurchan, G. Parisi, P. Urbani, and F. Zamponi, "Fractal free energy landscapes in structural glasses.", Nat. Commun. **5**, 3725 (2014).

[126] P. Charbonneau, J. Kurchan, G. Parisi, P. Urbani, and F. Zamponi, "Exact theory of dense amorphous hard spheres in high dimension. III. The full replica symmetry breaking solution", J. Stat. Mech. **2014**, P10009 (2014).

[127] F. H. Stillinger, "A Topographic View of Supercooled Liquids and Glass Formation", Science **267**, 1935 (1995).

[128] J. Kurchan, T. Maimbourg, and F. Zamponi, "Statics and dynamics of infinite-dimensional liquids and glasses: a parallel and compact derivation", J. Stat. Mech. **2016**, 033210 (2016).

[129] P. Charbonneau, J. Kurchan, G. Parisi, P. Urbani, and F. Zamponi, "Glass and Jamming Transitions: From Exact Results to Finite-Dimensional Descriptions", Annu. Rev. Condens. Matter Phys. **8**, 265 (2017).

[130] T. R. Kirkpatrick and P. G. Wolynes, "Stable and metastable states in mean-field Potts and structural glasses", Phys. Rev. B **36**, 8552 (1987).

[131] T. R. Kirkpatrick, D. Thirumalai, and P. G. Wolynes, "Scaling concepts for the dynamics of viscous liquids near an ideal glassy state", Phys. Rev. A **40**, 1045 (1989).

[132] W. Kauzmann, "The Nature of the Glassy State and the Behavior of Liquids at Low Temperatures.", Chem. Rev. **43**, 219 (1948).

[133] R. W. Hall and P. G. Wolynes, "The aperiodic crystal picture and free energy barriers in glasses", J. Chem. Phys. **86**, 2943 (1987).

[134] A. J. Liu and S. R. Nagel, "Jamming is not just cool any more", Nature **396**, 21 (1998).

[135] M. Wyart, "Marginal Stability Constrains Force and Pair Distributions at Random Close Packing", Phys. Rev. Lett. **109**, 125502 (2012).

[136] E. Lerner, G. Düring, and M. Wyart, "Low-energy non-linear excitations in sphere packings", Soft Matter **9**, 8252 (2013).

[137] E. DeGiuli, E. Lerner, C. Brito, and M. Wyart, "Force distribution affects vibrational properties in hard-sphere glasses", Proc. Natl. Acad. Sci. **111**, 17054 (2014).

[138] L. Berthier, G. Biroli, P. Charbonneau, E. I. Corwin, S. Franz, and F. Zamponi, "Gardner physics in amorphous solids and beyond", J. Chem. Phys. **151**, 010901 (2019).

[139] L. Berthier, P. Charbonneau, D. Coslovich, A. Ninarello, M. Ozawa, and S. Yaida, "Configurational entropy measurements in extremely supercooled liquids that break the glass ceiling", Proc. Natl. Acad. Sci. **114**, 11356 (2017).

[140] G. Adam and J. H. Gibbs, "On the Temperature Dependence of Cooperative Relaxation Properties in Glass-Forming Liquids", J. Chem. Phys. **43**, 139 (1965).

[141] J.-P. Bouchaud and G. Biroli, "On the Adam-Gibbs-Kirkpatrick-Thirumalai-Wolynes scenario for the viscosity increase in glasses", J. Chem. Phys. **121**, 7347 (2004).

[142] A. Montanari and G. Semerjian, "Rigorous Inequalities Between Length and Time Scales in Glassy Systems", J. Stat. Phys. **125**, 23 (2006).

[143] M. Ozawa and L. Berthier, "Does the configurational entropy of polydisperse particles exist?", J. Chem. Phys. **146**, 014502 (2017).

[144] M. Ozawa, G. Parisi, and L. Berthier, "Configurational entropy of polydisperse supercooled liquids", J. Chem. Phys. **149**, 154501 (2018).

[145] M. Ozawa, A. Ikeda, K. Miyazaki, and W. Kob, "Ideal Glass States Are Not Purely Vibrational: Insight from Randomly Pinned Glasses", Phys. Rev. Lett. **121**, 205501 (2018).

[146] D. J. Wales, *Energy Landscapes: Applications to Clusters, Biomolecules and Glasses* (Cambridge University Press, Cambridge, United Kingdom, 2004).

[147] M. Dzero, J. Schmalian, and P. G. Wolynes, "Activated events in glasses: The structure of entropic droplets", Phys. Rev. B **72**, 100201 (2005).

[148] S. Franz, "First steps of a nucleation theory in disordered systems", J. Stat. Mech. **2005**, P04001 (2005).

[149] M. C. Angelini and G. Biroli, "Real Space Migdal–Kadanoff Renormalisation of Glassy Systems: Recent Results and a Critical Assessment", J. Stat. Phys. **167**, 476 (2017).

[150] C. Rulquin, P. Urbani, G. Biroli, G. Tarjus, and M. Tarzia, "Nonperturbative fluctuations and metastability in a simple model: from observables to microscopic theory and back", J. Stat. Mech. **2016**, 023209 (2016).

[151] G. Biroli, C. Cammarota, G. Tarjus, and M. Tarzia, "Random-field Ising-like effective theory of the glass transition. I. Mean-field models", Phys. Rev. B **98**, 174205 (2018).

[152] G. Biroli, C. Cammarota, G. Tarjus, and M. Tarzia, "Random field Ising-like effective theory of the glass transition. II. Finite-dimensional models", Phys. Rev. B **98**, 174206 (2018).

[153] L. Berthier, P. Charbonneau, A. Ninarello, M. Ozawa, and S. Yaida, "Zero-temperature glass transition in two dimensions", Nat. Commun. **10**, 1508 (2019).

[154] M. Wyart and M. E. Cates, "Does a Growing Static Length Scale Control the Glass Transition?", Phys. Rev. Lett. **119**, 195501 (2017).

[155] F. C. Frank, "Supercooling of Liquids", Proc. R. Soc. **215**, 43 (1952).

[156] D. Kivelson, S. A. Kivelson, X. Zhao, Z. Nussinov, and G. Tarjus, "A thermodynamic theory of supercooled liquids", Phys. A **219**, 27 (1995).

[157] G. Tarjus, S. A. Kivelson, Z. Nussinov, and P. Viot, "The frustration-based approach of supercooled liquids and the glass transition: a review and critical assessment", J. Phys. Condens. Matter **17**, R1143 (2005).

[158] E. G. Teich, G. van Anders, and S. C. Glotzer, "Identity crisis in alchemical space drives the entropic colloidal glass transition", Nat. Commun. **10**, 64 (2019).

[159] B. Charbonneau, P. Charbonneau, and G. Tarjus, "Geometrical Frustration and Static Correlations in a Simple Glass Former", Phys. Rev. Lett. **108**, 035701 (2012).

[160] P. Charbonneau and G. Tarjus, "Decorrelation of the static and dynamic length scales in hard-sphere glass formers", Phys. Rev. E **87**, 042305 (2013).

[161] F. Turci, G. Tarjus, and C. P. Royall, "From Glass Formation to Icosahedral Ordering by Curving Three-Dimensional Space", Phys. Rev. Lett. **118**, 215501 (2017).

[162] C. P. Royall, S. R. Williams, T. Ohtsuka, and H. Tanaka, "Direct observation of a local structural mechanism for dynamic arrest", Nat. Mater. **7**, 556 (2008).

[163] D. Coslovich and G. Pastore, "Understanding fragility in supercooled Lennard-Jones mixtures. II. Potential energy surface", J. Chem. Phys. **127**, 124505 (2007).

[164] D. Coslovich and G. Pastore, "Understanding fragility in supercooled Lennard-Jones mixtures. I. Locally preferred structures", J. Chem. Phys. **127**, 124504 (2007).

[165] M. Leocmach and H. Tanaka, "Roles of icosahedral and crystal-like order in the hard spheres glass transition", Nat. Commun. **3**, 1974 (2012).

[166] G. M. Hocky, D. Coslovich, A. Ikeda, and D. R. Reichman, "Correlation of Local Order with Particle Mobility in Supercooled Liquids Is Highly System Dependent", Phys. Rev. Lett. **113**, 157801 (2014).

[167] J. Kurchan and D. Levine, "Order in glassy systems", J. Phys. Math. Theor. **44**, 035001 (2011).

[168] T. Speck, "Dynamic facilitation theory: a statistical mechanics approach to dynamic arrest", J. Stat. Mech. **2019**, 084015 (2019).

[169] D. Chandler and J. P. Garrahan, "Dynamics on the Way to Forming Glass: Bubbles in Space-Time", Annu. Rev. Phys. Chem. **61**, 191 (2010).

[170] R. Evans, private communication.

[171] D. C. Wallace, "On the role of density fluctuations in the entropy of a fluid", J. Chem. Phys. **87**, 2282 (1987).

[172] J. G. Kirkwood, "Statistical Mechanics of Fluid Mixtures", J. Chem. Phys. **3**, 300 (1935).

[173] R. P. Sear, "Nucleation: Theory and applications to protein solutions and colloidal suspensions", J. Phys. Condens. Matter **19**, 033101 (2007).

[174] V. Lubchenko and P. G. Wolynes, "Theory of structural glasses and supercooled liquids.", Annu. Rev. Phys. Chem. **58**, 235 (2007).

[175] C. Brito and M. Wyart, "Geometric interpretation of previtrification in hard sphere liquids", J. Chem. Phys. **131**, 024504 (2009).

[176] H. Hansen-Goos, R. Roth, K. R. Mecke, and S. Dietrich, "Solvation of Proteins: Linking Thermodynamics to Geometry", Phys. Rev. Lett. **99**, 128101 (2007).

[177] M. Oettel, H. Hansen-Goos, P. Bryk, and R. Roth, "Depletion interaction of two spheres —Full density functional theory vs. morphometric results", Europhys. Lett. **85**, 36003 (2009).

[178] D. J. Ashton, N. B. Wilding, R. Roth, and R. Evans, "Depletion potentials in highly size-asymmetric binary hard-sphere mixtures: Comparison of simulation results with theory", Phys. Rev. E **84**, 061136 (2011).

[179] B. B. Laird, A. Hunter, and R. L. Davidchack, "Interfacial free energy of a hard-sphere fluid in contact with curved hard surfaces", Phys. Rev. E **86**, 060602(R) (2012).

[180] E. M. Blokhuis, "Existence of a bending rigidity for a hard-sphere liquid near a curved hard wall: Validity of the Hadwiger theorem", Phys. Rev. E **87**, 022401 (2013).

[181] I. Urrutia, "Bending rigidity and higher-order curvature terms for the hard-sphere fluid near a curved wall", Phys. Rev. E **89**, 032122 (2014).

[182] H. Hansen-Goos, "Communication: Non-Hadwiger terms in morphological thermodynamics of fluids", J. Chem. Phys. **141**, 171101 (2014).

[183] H. Reiss, H. L. Frisch, and J. L. Lebowitz, "Statistical Mechanics of Rigid Spheres", J. Chem. Phys. **31**, 369 (1959).

[184] E. Helfand, H. Reiss, H. L. Frisch, and J. L. Lebowitz, "Scaled Particle Theory of Fluids", J. Chem. Phys. **33**, 1379 (1960).

[185] H. Reiss and S. W. Mayer, "Theory of the Surface Tension of Molten Salts", J. Chem. Phys. **34**, 2001 (1961).

[186] R. Gibbons, "The scaled particle theory for particles of arbitrary shape", Mol. Phys. **17**, 81 (1969).

[187] R. Gibbons, "The scaled particle theory for mixtures of hard convex particles", Mol. Phys. **18**, 809 (1970).

[188] F. H. Stillinger, P. G. Debenedetti, and S. Chatterjee, "Scaled particle theory for hard sphere pairs. I. Mathematical structure", J. Chem. Phys. **125**, 204504 (2006).

[189] S. Chatterjee, P. G. Debenedetti, and F. H. Stillinger, "Scaled particle theory for hard sphere pairs. II. Numerical analysis", J. Chem. Phys. **125**, 204505 (2006).

[190] E. Helfand, H. L. Frisch, and J. L. Lebowitz, "Theory of the Two- and One-Dimensional Rigid Sphere Fluids", J. Chem. Phys. **34**, 1037 (1961).

[191] S. C. Martin, B. B. Laird, R. Roth, and H. Hansen-Goos, "Thermodynamics of the hard-disk fluid at a planar hard wall: Generalized scaled-particle theory and Monte Carlo simulation", J. Chem. Phys. **149**, 084701 (2018).

[192] H. Hansen-Goos, "Scaling with a fractional power: Overcoming the shortage of scaled-particle variables for the hard-disk fluid", J. Chem. Phys. **150**, 011101 (2019).

[193] B. Widom, "Some Topics in the Theory of Fluids", J. Chem. Phys. **39**, 2808 (1963).

[194] B. Widom, "Potential-distribution theory and the statistical mechanics of fluids", J. Phys. Chem. **86**, 869 (1982).

[195] J. S. Rowlinson and B. Widom, *Molecular Theory of Capillarity* (Dover Publications, 2002).

[196] R. Evans, R. Roth, and P. Bryk, "Wetting at curved substrates: Non-analytic behavior of interfacial properties", Europhys. Lett. EPL **62**, 815 (2003).

[197] R. Evans, J. R. Henderson, and R. Roth, "Nonanalytic curvature contributions to solvation free energies: Influence of drying", J. Chem. Phys. **121**, 12074 (2004).

[198] B. Lee and F. M. Richards, "The interpretation of protein structures: Estimation of static accessibility", J. Mol. Biol. **55**, 379 (1971).

[199] F. M. Richards, "Areas, Volumes, Packing, and Protein Structure", Annu. Rev. Biophys. Bioeng. **6**, 151 (1977).

[200] P. Bryk, R. Roth, K. R. Mecke, and S. Dietrich, "Hard-sphere fluids in contact with curved substrates", Phys. Rev. E **68**, 031602 (2003).

[201] J. K. Percus, "Approximation Methods in Classical Statistical Mechanics", Phys. Rev. Lett. **8**, 462 (1962).

[202] K. R. Mecke, T. Buchert, and H. Wagner, "Robust Morphological Measures for Large-Scale Structure", Astron. Astrophys. **288**, 697 (1994).

[203] K. V. Klenin, F. Tristram, T. Strunk, and W. Wenzel, "Derivatives of molecular surface area and volume: Simple and exact analytical formulas", J. Comput. Chem. **32**, 2647 (2011).

[204] J. A. Krumhansl and S. S. Wang, "Triplet correlation in liquid argon by monte carlo method: low densities", J. Chem. Phys. **56**, 2034 (1972).

[205] R. L. Davidchack, B. B. Laird, and R. Roth, "Parameterising the surface free energy and excess adsorption of a hard-sphere fluid at a planar hard wall", Mol. Phys. **113**, 1091 (2015).

[206] S. Yaida, L. Berthier, P. Charbonneau, and G. Tarjus, "Point-to-set lengths, local structure, and glassiness", Phys. Rev. E **94**, 032605 (2016).

[207] C. N. Likos, "Effective interactions in soft condensed matter physics", Phys. Rep. **348**, 267 (2001).

[208] A. Ivlev, H. Löwen, G. Morfill, and C. P. Royall, *Complex Plasmas and Colloidal Dispersions: Particle-Resolved Studies of Classical Liquids and Solids*, Vol. 5, Series in Soft Condensed Matter (World Scientific Publishing Co, July 2012).

[209] J. Russo and H. Tanaka, "The microscopic pathway to crystallization in supercooled liquids", Sci. Rep. **2**, 505 (2012).

[210] W. Götze, *Complex dynamics of glass-forming liquids: a mode-coupling theory*, International Series of Monographs on Physics 143 (Oxford University Press, Oxford ; New York, 2009).

[211] N. Arkus, V. N. Manoharan, and M. P. Brenner, "Minimal Energy Clusters of Hard Spheres with Short Range Attractions", Phys. Rev. Lett. **103**, 118303 (2009).

[212] S. Mossa and G. Tarjus, "Locally preferred structure in simple atomic liquids", J. Chem. Phys. **119**, 8069 (2003).

[213] S. Mossa and G. Tarjus, "An operational scheme to determine the locally preferred structure of model liquids", J. Non-Cryst. Solids **352**, 4847 (2006).

[214] F. H. Stillinger and T. A. Weber, "Hidden structure in liquids", Phys. Rev. A **25**, 978 (1982).

[215] D. J. Wales, "Rearrangements of 55-atom Lennard-Jones and (C60)55 clusters", J. Chem. Phys. **101**, 3750 (1994).

[216] J. P. K. Doye, D. J. Wales, W. Branz, and F. Calvo, "Modeling the structure of clusters of C60 molecules", Phys. Rev. B **64**, 235409 (2001).

[217] J. P. K. Doye, D. J. Wales, and R. S. Berry, "The effect of the range of the potential on the structures of clusters", J. Chem. Phys. **103**, 4234 (1995).

[218] J. P. K. Doye and D. J. Wales, "The effect of the range of the potential on the structure and stability of simple liquids: from clusters to bulk, from sodium to", J. Phys. B **29**, 4859 (1996).

[219] D. J. Wales, M. A. Miller, and T. R. Walsh, "Archetypal energy landscapes", Nature **394**, 758 (1998).

[220] N. Arkus, V. N. Manoharan, and M. P. Brenner, "Deriving Finite Sphere Packings", SIAM J. Discrete Math. **25**, 1860 (2011).

[221] R. Connelly and W. Whiteley, "Second-Order Rigidity and Prestress Stability for Tensegrity Frameworks", SIAM J. Discrete Math. **9**, 453 (1996).

[222] J. C. Maxwell, "On the calculation of the equilibrium and stiffness of frames", Philos. Mag. Ser. 4 **27**, 294 (1864).

[223] C. Calladine, "Buckminster Fuller's "Tensegrity" structures and Clerk Maxwell's rules for the construction of stiff frames", Int. J. Solids Struct. **14**, 161 (1978).

[224] C. Brito, H. Ikeda, P. Urbani, M. Wyart, and F. Zamponi, "Universality of jamming of nonspherical particles", Proc. Natl. Acad. Sci. **115**, 11736 (2018).

[225] Y. Kallus and M. C. Holmes-Cerfon, "Free energy of singular sticky-sphere clusters", Phys. Rev. E **95**, 1 (2017).

[226] M. Holmes-Cerfon, S. J. Gortler, and M. P. Brenner, "A geometrical approach to computing free-energy landscapes from short-ranged potentials", Proc. Natl. Acad. Sci. **110**, E5 (2013).

[227] C. Brito and M. Wyart, "On the rigidity of a hard-sphere glass near random close packing", EPL Europhys. Lett. **76**, 149 (2006).

[228] M. E. Cates and V. N. Manoharan, "Celebrating Soft Matter's 10th anniversary: Testing the foundations of classical entropy: colloid experiments", Soft Matter **11**, 6538 (2015).

[229] D. Frenkel and B. Smit, *Understanding molecular simulation: from algorithms to applications*, 2nd ed, Computational Science Series 1 (Academic Press, San Diego, 2002).

[230] T. Schilling and F. Schmid, "Computing absolute free energies of disordered structures by molecular simulation", J. Chem. Phys. **131**, 231102 (2009).

[231] A. Malins, S. R. Williams, J. Eggers, and C. P. Royall, "Identification of structure in condensed matter with the topological cluster classification.", J. Chem. Phys. **139**, 234506 (2013).

[232] A. Malins, S. R. Williams, J. Eggers, H. Tanaka, and C. P. Royall, "Geometric frustration in small colloidal clusters", J. Phys. Condens. Matter **21**, 425103 (2009).

[233] G. Meng, N. Arkus, M. P. Brenner, V. N. Manoharan, and S. O. Material, "The Free-Energy Landscape of Clusters of Attractive Hard Spheres", Science **327**, 560 (2010).

[234] A. J. Dunleavy, K. Wiesner, R. Yamamoto, and C. P. Royall, "Mutual information reveals multiple structural relaxation mechanisms in a model glass former.", Nat. Commun. **6**, 6089 (2015).

[235] L. Trombach, R. S. Hoy, D. J. Wales, and P. Schwerdtfeger, "From sticky-hard-sphere to Lennard-Jones-type clusters", Phys. Rev. E **97**, 043309 (2018).

[236] T. P. Minka, "A family of algorithms for approximate bayesian inference", PhD thesis (2001).

[237] T. P. Minka, "Expectation Propagation for Approximate Bayesian Inference", Uncertain. Artif. Intell. **17**, 362 (2001).

[238] C. E. Rasmussen and C. K. I. Williams, *Gaussian Processes for Machine Learning* (2006).

[239] J. P. Cunningham, P. Hennig, and S. Lacoste-Julien, "Gaussian probabilities and expectation propagation", arXiv: 1111.6832 (2011).

[240] D. Coslovich, M. Ozawa, and L. Berthier, "Local order and crystallization of dense polydisperse hard spheres", J. Phys. Condens. Matter **30**, 144004 (2018).

[241] R. Kodama, R. Roth, Y. Harano, and M. Kinoshita, "Morphometric approach to thermodynamic quantities of solvation of complex molecules: Extension to multicomponent solvent", J. Chem. Phys. **135**, 045103 (2011).

[242] W. Helfrich, "Elastic Properties of Lipid Bilayers: Theory and Possible Experiments", Z. Für Naturforschung C **28**, 693 (1973).

[243] L. Tonks, "The Complete Equation of State of One, Two and Three-Dimensional Gases of Hard Elastic Spheres", Phys. Rev. **50**, 955 (1936).

[244] M. S. Wertheim, "Fluids of hard convex molecules", Mol. Phys. **83**, 519 (1994).

[245] A. Isihara, "Determination of Molecular Shape by Osmotic Measurement", J. Chem. Phys. **18**, 1446 (1950).

[246] F. H. Ree and W. G. Hoover, "Fifth and Sixth Virial Coefficients for Hard Spheres and Hard Disks", J. Chem. Phys. **40**, 939 (1964).

[247] Y. Rosenfeld, M. Schmidt, H. Löwen, and P. Tarazona, "Dimensional crossover and the freezing transition in density functional theory", J. Phys. Condens. Matter **8**, L577 (1996).

[248] P. Tarazona and Y. Rosenfeld, "From zero-dimension cavities to free-energy functionals for hard disks and hard spheres", Phys. Rev. E **55**, R4873 (1997).

[249] M. S. Wertheim, "Fluids of hard convex molecules II. Two-point measures", Mol. Phys. **89**, 989 (1996).

[250] M. S. Wertheim, "Fluids of hard convex molecules III. The third virial coefficient", Mol. Phys. **89**, 1005 (1996).

[251] G. Parisi, P. Urbani, and F. Zamponi, *Theory of Simple Glasses: Exact Solutions in Infinite Dimensions* (Cambridge University Press, New York, 2020).

[252] O. Boucher, D. Randall, P. Artaxo, C. Bretherton, G. Feingold, P. Forster, V.-M. Kerminen, Y. Kondo, H. Liao, U. Lohmann, P. Rasch, S. K. Satheesh, S. Sherwood, B. Stevens, and X. Y. Zhang, "Clouds and aerosols", in *Climate Change 2013: The Physical Science Basis. Contribution of Working Group I to the Fifth Assessment Report of the Intergovernmental Panel on Climate Change*, edited by T. F. Stocker, D. Qin, G.-K. Plattner, M. Tignor, S. K. Allen, J. Doschung, A. Nauels, Y. Xia, V. Bex, and P. M. Midgley (Cambridge University Press, Cambridge, UK, 2013), pp. 571–657.

[253] K. S. Carslaw, L. A. Lee, C. L. Reddington, K. J. Pringle, A. Rap, P. M. Forster, G. W. Mann, D. V. Spracklen, M. T. Woodhouse, L. A. Regayre, and J. R. Pierce, "Large contribution of natural aerosols to uncertainty in indirect forcing", Nature **503**, 67 (2013).

[254] L. A. Lee, C. L. Reddington, and K. S. Carslaw, "On the relationship between aerosol model uncertainty and radiative forcing uncertainty", Proc. Natl. Acad. Sci. **113**, 5820 (2016).

[255] L. A. Regayre, J. S. Johnson, M. Yoshioka, K. J. Pringle, D. M. H. Sexton, B. B. B. Booth, L. A. Lee, N. Bellouin, and K. S. Carslaw, "Aerosol and physical atmosphere model parameters are both important sources of uncertainty in aerosol ERF", Atmospheric Chem. Phys. **18**, 9975 (2018).

[256] K. J. Pringle, K. S. Carslaw, T. Fan, G. Mann, A. Hill, P. Stier, K. Zhang, and H. Tost, "A multi-model assessment of the impact of sea spray geoengineering on cloud droplet number", Atmospheric Chem. Phys. **12**, 11647 (2012).

[257] N. Hodas, A. Zuend, W. Mui, R. C. Flagan, and J. H. Seinfeld, "Influence of particle-phase state on the hygroscopic behavior of mixed organic–inorganic aerosols", Atmospheric Chem. Phys. **15**, 5027 (2015).

[258] M. I. Cotterell, R. E. Willoughby, B. R. Bzdek, A. J. Orr-Ewing, and J. P. Reid, "A complete parameterisation of the relative humidity and wavelength dependence of the refractive index of hygroscopic inorganic aerosol particles", Atmospheric Chem. Phys. **17**, 9837 (2017).

[259] G. W. Mann, K. S. Carslaw, C. L. Reddington, K. J. Pringle, M. Schulz, A. Asmi, D. V. Spracklen, D. A. Ridley, M. T. Woodhouse, L. A. Lee, K. Zhang, S. J. Ghan, R. C. Easter, X. Liu, P. Stier, Y. H. Lee, P. J. Adams, H. Tost, J. Lelieveld, S. E. Bauer, K. Tsigaridis, T. P. C. van Noije, A. Strunk, E. Vignati, N. Bellouin, M. Dalvi, C. E. Johnson, T. Bergman, H. Kokkola, K. von Salzen, F. Yu, G. Luo, A. Petzold, J. Heintzenberg, A. Clarke, J. A. Ogren, J. Gras, U. Baltensperger, U. Kaminski, S. G. Jennings, C. D. O'Dowd, R. M. Harrison, D. C. S. Beddows, M. Kulmala, Y. Viisanen, V. Ulevicius, N. Mihalopoulos, V. Zdimal, M. Fiebig, H.-C. Hansson, E. Swietlicki, and J. S. Henzing, "Intercomparison and evaluation of global aerosol microphysical properties among AeroCom models of a range of complexity", Atmospheric Chem. Phys. **14**, 4679 (2014).

[260] J. Zhu, J. E. Penner, F. Yu, S. Sillman, M. O. Andreae, and H. Coe, "Decrease in radiative forcing by organic aerosol nucleation, climate, and land use change", Nat. Commun. **10**, 423 (2019).

[261] W. C. Keene, R. Sander, A. A. Pszenny, R. Vogt, P. J. Crutzen, and J. N. Galloway, "Aerosol pH in the marine boundary layer", J. Aerosol Sci. **29**, 339 (1998).

[262] M. P. Tolocka, T. D. Saul, and M. V. Johnston, "Reactive Uptake of Nitric Acid into Aqueous Sodium Chloride Droplets Using Real-Time Single-Particle Mass Spectrometry", J. Phys. Chem. A **108**, 2659 (2004).

[263] C. E. Scott, A. Rap, D. V. Spracklen, P. M. Forster, K. S. Carslaw, G. W. Mann, K. J. Pringle, N. Kivekäs, M. Kulmala, H. Lihavainen, and P. Tunved, "The direct and indirect radiative effects of biogenic secondary organic aerosol", Atmospheric Chem. Phys. **14**, 447 (2014).

[264] U. Pöschl and M. Shiraiwa, "Multiphase Chemistry at the Atmosphere–Biosphere Interface Influencing Climate and Public Health in the Anthropocene", Chem. Rev. **115**, 4440 (2015).

[265] K. M. Carver and R. C. Snyder, "Unexpected Polymorphism and Unique Particle Morphologies from Monodisperse Droplet Evaporation", Ind. Eng. Chem. Res. **51**, 15720 (2012).

[266] E. Lintingre, F. Lequeux, L. Talini, and N. Tsapis, "Control of particle morphology in the spray drying of colloidal suspensions", Soft Matter **12**, 7435 (2016).

[267] J. W. Ivey, P. Bhambri, T. K. Church, D. A. Lewis, and R. Vehring, "Experimental investigations of particle formation from propellant and solvent droplets using a monodisperse spray dryer", Aerosol Sci. Technol. **52**, 702 (2018).

[268] X. You, Z. Zhou, Z. Liao, L. Che, X. D. Chen, W. D. Wu, M. Woo, and C. Selomulya, "Dairy Milk Particles Made with a Mono-Disperse Droplet Spray Dryer (MDDSD) Investigated for the Effect of Fat", Dry. Technol. **32**, 528 (2014).

[269] R. Lin, W. Liu, M. W. Woo, X. D. Chen, and C. Selomulya, "On the formation of "coral-like" spherical α-glycine crystalline particles", Powder Technol. **279**, 310 (2015).

[270] L. Yu and K. Ng, "Glycine Crystallization during Spray Drying: The pH Effect on Salt and Polymorphic Forms", J. Pharm. Sci. **91**, 2367 (2002).

[271] A. Dubbini, R. Censi, V. Martena, E. Hoti, M. Ricciutelli, L. Malaj, and P. Di Martino, "Influence of pH and method of crystallization on the solid physical form of indomethacin", Int. J. Pharm. **473**, 536 (2014).

[272] Q. Zhong, "Co-Spray Dried Mannitol/Poly(amidoamine)-Doxorubicin Dry-Powder Inhaler Formulations for Lung Adenocarcinoma: Morphology, In Vitro Evaluation, and Aerodynamic Performance", AAPS PharmSciTech **19**, 531 (2018).

[273] A. B. D. Nandiyanto and K. Okuyama, "Progress in developing spray-drying methods for the production of controlled morphology particles: From the nanometer to submicrometer size ranges", Adv. Powder Technol. **22**, 1 (2011).

[274] F. Lyu, J. J. Liu, Y. Zhang, and X. Z. Wang, "Combined control of morphology and polymorph in spray drying of mannitol for dry powder inhalation", J. Cryst. Growth **467**, 155 (2017).

[275] R. Vehring, W. R. Foss, and D. Lechuga-Ballesteros, "Particle formation in spray drying", J. Aerosol Sci. **38**, 728 (2007).

[276] H. R. Costantino, J. D. Andya, P.-A. Nguyen, N. Dasovich, T. D. Sweeney, S. J. Shire, C. C. Hsu, and Y.-F. Maa, "Effect of Mannitol Crystallization on the Stability and Aerosol Performance of a Spray-Dried Pharmaceutical Protein, Recombinant Humanized anti-IgE Monoclonal Antibody", J. Pharm. Sci. **87**, 1406 (1998).

[277] E. Amstad, F. Spaepen, and D. A. Weitz, "Stabilization of the Amorphous Structure of Spray-Dried Drug Nanoparticles", J. Phys. Chem. B **120**, 9161 (2016).

[278] C. Brough and R. Williams, "Amorphous solid dispersions and nano-crystal technologies for poorly water-soluble drug delivery", Int. J. Pharm. **453**, 157 (2013).

[279] J. F. Davies, A. E. Haddrell, and J. P. Reid, "Time-Resolved Measurements of the Evaporation of Volatile Components from Single Aerosol Droplets", Aerosol Sci. Technol. **46**, 666 (2012).

[280] C. Handscomb, M. Kraft, and A. Bayly, "A new model for the drying of droplets containing suspended solids", Chem. Eng. Sci. **64**, 628 (2009).

[281] R. M. Power, S. H. Simpson, J. P. Reid, and A. J. Hudson, "The transition from liquid to solid-like behaviour in ultrahigh viscosity aerosol particles", Chem. Sci. **4**, 2597 (2013).

[282] A. Baldelli, R. M. Power, R. E. H. Miles, J. P. Reid, and R. Vehring, "Effect of crystallization kinetics on the properties of spray dried microparticles", Aerosol Sci. Technol. **50**, 693 (2016).

[283] A. P. Lyubartsev and A. Laaksonen, "Concentration Effects in Aqueous NaCl Solutions. A Molecular Dynamics Simulation", J. Phys. Chem. **100**, 16410 (1996).

[284] H. S. Yeh and G. B. Wills, "Diffusion coefficient of sodium nitrate in aqueous solution at 25.deg. as a function of concentration from 0.1 to 1.0M", J. Chem. Eng. Data **15**, 187 (1970).

[285] S. L. Clegg, P. Brimblecombe, and A. S. Wexler, "Thermodynamic Model of the System H^+-NH_4^+-Na^+-SO_4^{2-}-NO_3^--Cl^--H_2O at 298.15 K", J. Phys. Chem. A **102**, 2155 (1998).

[286] I. N. Tang and H. R. Munkelwitz, "Water activities, densities, and refractive indices of aqueous sulfates and sodium nitrate droplets of atmospheric importance", J. Geophys. Res. **99**, 18801 (1994).

[287] G. Rovelli, R. E. H. Miles, J. P. Reid, and S. L. Clegg, "Accurate Measurements of Aerosol Hygroscopic Growth over a Wide Range in Relative Humidity", J. Phys. Chem. A **120**, 4376 (2016).

[288] J. C. Slattery, *Advanced Transport Phenomena* (Cambridge University Press, Cambridge, 1999).

[289] W. A. Sirignano, *Fluid dynamics and transport of droplets and sprays*, 2nd ed (Cambridge University Press, New York, 2010).

[290] W. Thomson, "4. On the Equilibrium of Vapour at a Curved Surface of Liquid", Proc. R. Soc. Edinb. **7**, 63 (1872).

[291] M. Kulmala, T. Vesala, and P. Wagner, "An analytical expression for the rate of binary condensational particle growth: Comparison with numerical results", J. Aerosol Sci. **23**, 133 (1992).

[292] J. Crank, P. Nicolson, and D. R. Hartree, "A practical method for numerical evaluation of solutions of partial differential equations of the heat-conduction type", Math. Proc. Camb. Philos. Soc. **43**, 50 (1947).

[293] C. Valeriani, E. Sanz, and D. Frenkel, "Rate of homogeneous crystal nucleation in molten NaCl", J. Chem. Phys. **122**, 194501 (2005).

[294] J. Desarnaud, H. Derluyn, J. Carmeliet, D. Bonn, and N. Shahidzadeh, "Metastability limit for the nucleation of NaCl crystals in confinement", J. Phys. Chem. Lett. **5**, 890 (2014).

[295] P. F. Damasceno, M. Engel, and S. C. Glotzer, "Predictive Self-Assembly of Polyhedra into Complex Structures", Science **337**, 453 (2012).

[296] P. F. Damasceno, M. Engel, and S. C. Glotzer, "Crystalline Assemblies and Densest Packings of a Family of Truncated Tetrahedra and the Role of Directional Entropic Forces", ACS Nano **6**, 609 (2012).

[297] K. L. Young, M. L. Personick, M. Engel, P. F. Damasceno, S. N. Barnaby, R. Bleher, T. Li, S. C. Glotzer, B. Lee, and C. A. Mirkin, "A Directional Entropic Force Approach to Assemble Anisotropic Nanoparticles into Superlattices", Angew. Chem. Int. Ed. **52**, 13980 (2013).

[298] B. A. Schultz, P. F. Damasceno, M. Engel, and S. C. Glotzer, "Symmetry Considerations for the Targeted Assembly of Entropically Stabilized Colloidal Crystals via Voronoi Particles", ACS Nano **9**, 2336 (2015).

[299] G. van Anders, D. Klotsa, A. S. Karas, P. M. Dodd, and S. C. Glotzer, "Digital Alchemy for Materials Design: Colloids and Beyond", ACS Nano **9**, 9542 (2015).

[300] K. Miszta, J. de Graaf, G. Bertoni, D. Dorfs, R. Brescia, S. Marras, L. Ceseracciu, R. Cingolani, R. van Roij, M. Dijkstra, and L. Manna, "Hierarchical self-assembly of suspended branched colloidal nanocrystals into superlattice structures", Nat. Mater. **10**, 872 (2011).

[301] J. Henzie, M. Grünwald, A. Widmer-Cooper, P. L. Geissler, and P. Yang, "Self-assembly of uniform polyhedral silver nanocrystals into densest packings and exotic superlattices", Nat. Mater. **11**, 131 (2012).

[302] W. Qi, J. de Graaf, F. Qiao, S. Marras, L. Manna, and M. Dijkstra, "Phase diagram of octapod-shaped nanocrystals in a quasi-two-dimensional planar geometry", J. Chem. Phys. **138**, 154504 (2013).

[303] Y. Harano and M. Kinoshita, "Large gain in translational entropy of water is a major driving force in protein folding", Chem. Phys. Lett. **399**, 342 (2004).

[304] Y. Harano and M. Kinoshita, "Translational-Entropy Gain of Solvent upon Protein Folding", Biophys. J. **89**, 2701 (2005).

[305] M. Kinoshita, "Roles of entropic excluded-volume effects in colloidal and biological systems: Analyses using the three-dimensional integral equation theory", Chem. Eng. Sci. **61**, 2150 (2006).

[306] Y. Harano, R. Roth, and M. Kinoshita, "On the energetics of protein folding in aqueous solution", Chem. Phys. Lett. **432**, 275 (2006).

[307] H. Edelsbrunner and P. Koehl, "The weighted-volume derivative of a space-filling diagram", Proc. Natl. Acad. Sci. **100**, 2203 (2003).

[308] R. Bryant, H. Edelsbrunner, P. Koehl, and M. Levitt, "The Area Derivative of a Space-Filling Diagram", Discrete Comput. Geom. **32**, 293 (2004).

[309] M. L. Connolly, "Analytical molecular surface calculation", J. Appl. Crystallogr. **16**, 548 (1983).

[310] M. L. Connolly, "Computation of molecular volume", J. Am. Chem. Soc. **107**, 1118 (1985).

[311] M. Wyart, "On the rigidity of amorphous solids", Ann. Phys. **30**, 1 (2005).

[312] C. Radin and L. Sadun, "Structure of the Hard Sphere Solid", Phys. Rev. Lett. **94**, 015502 (2005).

[313] H. Koch, C. Radin, and L. Sadun, "Most stable structure for hard spheres", Phys. Rev. E **72**, 016708 (2005).

[314] F. Leoni and Y. Shokef, "Attraction Controls the Inversion of Order by Disorder in Buckled Colloidal Monolayers", Phys. Rev. Lett. **118**, 218002 (2017).